Study of gas-liquid mass transfer in bubble and spray column adding solid media
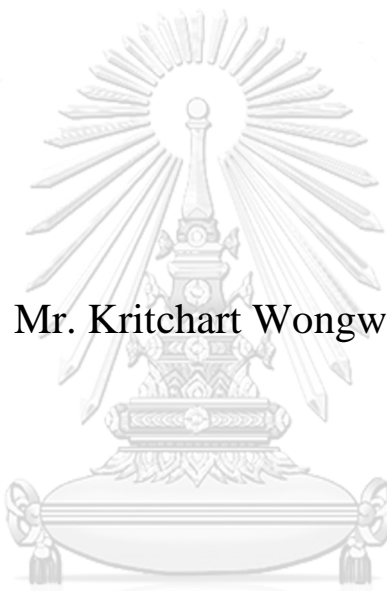
Mr. Kritchart Wongwailikhit

การวิเคราะห์กลไกการดูดซึมระหว่างก๊าซและของเหลวในคอลัมน์แบบเป่าฟองและแบบโปรยที่มีตัวกลางของแข็ง

นายกริชชาติ ว่องไวลิขิต

วิทยานิพนธ์นี้เป็นส่วนหนึ่งของการศึกษาตามหลักสูตรปริญญาวิศวกรรมศาสตรดุษฎีบัณฑิต
สาขาวิชาวิศวกรรมสิ่งแวดล้อม ภาควิชาวิศวกรรมสิ่งแวดล้อม
คณะวิศวกรรมศาสตร์ จุฬาลงกรณ์มหาวิทยาลัย
ปีการศึกษา 2561

Thesis Title	Study of gas-liquid mass transfer in bubble and spray column adding solid media
By	Mr. Kritchart Wongwailikhit
Field of Study	Environmental Engineering
Thesis Advisor	Associate Professor Pisut Painmanakul, Ph.D.

Accepted by the Faculty of Engineering, Chulalongkorn University in Partial Fulfillment of the Requirement for the Doctor of Philosophy

.... Dean of the Faculty of Engineering
(Professor Bundhit Eua-arporn, Ph.D.)

DISSERTATION COMMITTEE

.... Chairman
(Associate Professor SIRIMA PANYAMETHEEKUL, Ph.D.)

.... Thesis Advisor
(Associate Professor Pisut Painmanakul, Ph.D.)

.... Examiner
(Assistant Professor CHAIYAPORN PUPRASERT, Ph.D.)

.... Examiner
(Associate Professor Patiparn Punyapalakul, Ph.D.)

.... External Examiner
(Marupatch Jamnongwong, Ph.D.)

กริชชาติ ว่องไวลิขิต : การวิเคราะห์กลไกการดูดซึมระหว่างก๊าซและของเหลวในคอลัมน์แบบเป่าฟองและแบบโปรยที่มีตัวกลางของแข็ง.
(Study of gas-liquid mass transfer in bubble and spray column adding solid media) อ.ที่
ปรึกษาหลัก : รศ. ดร.พิสุทธิ์ เพียรมนกุล

     การดูดซึมแก๊สเป็นกระบวนการแยกที่ใช้หลักการความแตกต่างของความเข้มข้นในการถ่ายเทมวลสารจากวัฏภาคแก๊สสู่วัฏภาคของเหลว โดยกระบวนการนี้ใช้กันอย่างแพร่หลายในการบำบัดมลพิษทางอากาศ หรือ เพิ่มความบริสุทธิ์ให้กับแก๊ส เช่น การดูดซึมแก๊สคาร์บอนไดออกไซด์จากแก๊สชีวภาพ (Biogas) หรือ การดูดซึมสารอินทรีย์ระเหยง่าย (Volatile organic compounds, VOCs) จากอากาศเสียปนเปื้อนจากกระบวนการปิโตรเคมี โดยทั่วไปแล้วกระบวนการดูดซึมของแก๊สมักใช้คอลัมน์แบบเป่าฟอง (Bubble column) หรือ คอลัมน์แบบโปรย (Spray column) ในการดำเนินการ ซึ่งมีงานวิจัยที่เกี่ยวข้องกับทั้งสองคอลัมน์นี้เป็นจำนวนมากแต่อย่างไรก็ตามงานวิจัยดังกล่าว ไม่ได้ศึกษาคอลัมน์ทั้งสองชนิดเปรียบเทียบกันโดยตรง ดังนั้นในงานวิจัยนี้จึงได้มีจุดประสงค์เพื่อเปรียบเทียบพลศาสตร์การไหลและการถ่ายเทมวลสารของคอลัมน์แบบเป่าฟองและแบบโปรย พร้อมทำการเปรียบเทียบกำลังงานจำเพาะ (Specific power consumption) ที่ใช้ในการดำเนินการของคอลัมน์ทั้งสองชนิด เพื่อใช้เป็นแนวทางในการเลือกอุปกรณ์ที่เหมาะสมสำหรับกระบวนการการดูดซึมในอุตสาหกรรม โดยจากการทดลอง คอลัมน์แบบเป่าฟองมีพื้นที่ผิวสัมผัสจำเพาะ (specific interfacial area) ที่มากกว่าคอลัมน์แบบโปรยเมื่อดำเนินการที่อัตราการไหลของแก๊สที่ต่ำ โดยในสภาวะการดำเนินการดังกล่าว คอลัมน์แบบเป่าฟองมีค่าสัมประสิทธิ์การถ่ายเทมวลสารรวม (overall mass transfer coefficient) ที่มากกว่าคอลัมน์แบบโปรยเมื่อทำการเปรียบเทียบที่พลังงานจำเพาะเท่ากัน แต่อย่างไรก็ตาม เมื่อดำเนินการที่อัตราการไหลแก๊สที่สูง คอลัมน์แบบโปรยจะมีความเหมาะสมมากกว่าคอลัมน์แบบเป่าฟองเนื่องจากคอลัมน์แบบเป่าฟองใช้กำลังงานในการผลิตฟองสูงกว่าที่อัตราการไหลของแก๊สที่สูงเมื่อเทียบกับคอลัมน์แบบโปรย

     นอกจากนี้ งานวิจัยนี้ยังได้ทำการศึกษาผลของตัวกลางของแข็งที่มีต่อพลศาสตร์การไหลและการถ่ายเทมวลสารในคอลัมน์แบบเป่าฟองและแบบโปรย โดยได้ใช้กระบวนการวิเคราะห์สี (Colorimetric method) แบบสีแดง (Red bottle) ภายในคอลัมน์แบบเป่าฟองขนาดเล็ก โดยพบว่า การชนกันระหว่างฟองอากาศและตัวกลางของแข็งจะทำให้การถ่ายเทมวลสารของฟองอากาศนั้นๆลดลง อันเนื่องมาจากความเร็วที่ลดลงของฟองอากาศโดยเฉพาะฟองอากาศขนาดเล็กที่สามารถสูญเสียความเร็วได้ง่ายจากการชนกับของแข็ง แต่อย่างไรก็ตาม การลดความเร็วลงของฟองอากาศทำให้ฟองอากาศอยู่ภายในคอลัมน์นานยิ่งขึ้น ซึ่งเป็นการเพิ่มเวลาสัมผัสให้กับฟองอากาศ ส่งผลให้มีสัดส่วนแก๊ส (gas holdup) และพื้นที่ผิวสัมผัสจำเพาะขึ้นเมื่อเพิ่มตัวกลางของแข็งเข้าไปในระบบ ดังนั้น การเติมตัวกลางของแข็งในสภาวะที่เหมาะสมจะทำให้มีการเพิ่มพื้นที่ผิวสัมผัสมากกว่าการลดลงของการถ่ายเทมวลสาร ซึ่งในงานวิจัยนี้พบว่า สภาวะดังกล่าวเกิดขึ้นเมื่อใช้ของแข็งแบบเคลื่อนที่ได้รูปร่างวงแหวนในคอลัมน์แบบเป่าฟองที่มีหัวจ่ายอากาศที่มีรูจ่ายอากาศ (orifice) ขนาดใหญ่

     ไม่เพียงเท่านี้ งานวิจัยนี้ยังได้พัฒนาการใช้ระบบการวิเคราะห์สีเพื่อใช้สำหรับการคำนวณค่าสัมประสิทธิ์การถ่ายเทมวลสารของออกซิเจน (oxygen) ภายในคอลัมน์แบบเป่าฟองโดยใช้วิธีการตรวจวัดเวลาที่ใช้ในการเปลี่ยนสีของสารจากไม่มีสีเป็นสีแดง ซึ่งกระบวนการดังกล่าวเป็นกระบวนการที่เหมาะสมในการประยุกต์ใช้ในกระบวนการศึกษา เนื่องจากเป็นตัวอย่างที่เห็นได้ชัดจากการถ่ายเทมวลสารและไม่จำเป็นต้องใช้อุปกรณ์ใดๆเพิ่มเติม นอกจากนี้ งานวิจัยนี้ยังได้ทำการศึกษาความแม่นยำของโพรบเส้นใยนำแสง (Optical fiber probe) ที่สามารถใช้ตรวจวัดความเร็วและขนาดของหยดน้ำในกระบวนการแบบโปรยอีกด้วย

สาขาวิชา	วิศวกรรมสิ่งแวดล้อม	ลายมือชื่อนิสิต ....
ปีการศึกษา	2561	ลายมือชื่อ อ.ที่ปรึกษาหลัก ....

5771459121 : MAJOR ENVIRONMENTAL ENGINEERING

KEYWORD: absorption, mass transfer, hydrodynamics, bubble column, spray column, three-phase

Kritchart Wongwailikhit : Study of gas-liquid mass transfer in bubble and spray column adding solid media. Advisor: Assoc. Prof. Pisut Painmanakul, Ph.D.

Gas absorption is a separation process that transfers substances from gas phase to liquid phases due to the different concentrations. The operation can be applied in many treatments or purifying processes e.g. CO_2 absorption from biogas or volatile organic compounds (VOCs) recovery from petroleum emission air. The conventional unit operation using for the gas absorption process are bubble column and spray column. Although there are several literatures reporting the efficiency of spray columns and bubble columns, those were done separately. Therefore, this research projected to investigate both hydrodynamics and mass transfer in both spray and bubble columns and comparing their specific power consumptions in order to develop the selection a guideline for industrial usages. The results indicated that the bubble column had larger specific interfacial area than the spray column when using at small gas loading rate. At this range of operation, the bubble column yielded higher overall mass transfer coefficient with the same specific power consumption. However, when operating at high gas loading rate, the spray column was the one better than the bubble column since the bubble column consumed larger power consumption as the pressure drop of the bubble column was mostly due to the gas flow.

In addition, this research also studied the effect of solid phase on the hydrodynamics and mass transfer in the bubble column and spray column. By using the colorimetric method of "red bottle" experiment, it was found that the bubble-particles collision diminished the mass transfer of bubbles because the collision slowed down the bubbles especially for the small bubbles due to the fact that the small bubble simply lost their velocities from the collision. However, there was an advantage of introducing the particles since solid particles could obstruct the rising bubble and reduced its rising velocity. Consequently, the contact time between gas and liquid is increased and resulted in higher gas hold up and specific interfacial area. Therefore, with the appropriate conditions for which solid promoted specific interfacial area higher than diminished the mass transfer coefficient, the higher mass transfer rate was achieved. For the experimental setup using in this research, the enhance of mass transfer rate was occurred when the movable ring-shaped particles were introduced into the column that had large orifice sizes of gas sparger.

In addition, this thesis also developed a colorimetric method to determine the overall mass transfer coefficient of oxygen without using other equipment rather than measuring the time which color of the solution changed from colorless to saturated red. This technique is very useful in the aspect of education since it does not require another equipment for measurement rather than visually observation. Nevertheless, the performance of optical fiber probes for hydrodynamics determination of droplets were also investigated.

Field of Study:	Environmental Engineering	Student's Signature	....
Academic Year:	2018	Advisor's Signature	....

ACKNOWLEDGEMENTS

A lot of things happened when I was doing this thesis. For the whole 4 years, I experienced many new things: living in the different country, speak French, working with people from different countries. In the beginning, it was very hard. I had to push myself a lot in order to learn and get used to it. Eventually, I managed to do it and in my point of view, I satisfied with that. However, these all things could not be happened if I did not get the supports from my supervisors, Pisut Painmanakul, Gilles Hébrard and Nicolas Dietrich. The opportunities that these professors gave me were one of the greatest in my life. I would like to say "thank you" again and again as the things I got were the one created my future and this fact lives in my memory.

Besides, my family is one of the key to become this far. Everyone knows that becoming a PhD candidate is a real deal. It is a long-term hard working to achieve the PhD. So, it required to have a very good mentality support. Thanks to my family especially my mom and my dad who always have my back. With they were there for me all the time, I can look back and find my comfort zone whenever I need. The mentality help from you might seem to be a little, but it was important to me. In the end, I came back home and finished this PhD. I can say that without your supports, I cannot stand here. I could not say thanks more to you. I love you. Moreover, a little support from the others like my brothers were also kept in my mind. Even though it was just joking around, I really appreciated that.

For the whole two years in France, inside and outside the laboratory I would like to thank my co-worker and friends. Thank you, Claude and José, for your support for my experiment. Till this date, I am still thinking of the Saturday parties that helped me for both mentality and living, P'Tee, P'Ploy, P'Hor, Benz, Ping, and Yee. Hope we can have some time together again. Moreover, Paul, Xiaomin, Aida, Lixia, Quiming, Feishi, Mei Mei, Allan, Prantik, Elsa, Naïla, David and the others whom I did not mentioned, you all also made my years. My life in France should never been this good without you all. Fernfern, Gag, Tie, Tarn, Science, Xia, M and the rest of my gang, thanks for cheering me up and calling me when I was alone. Last but not least, I would like to thank the one who stayed beside me all the time when I was doing my thesis especially in this last year, Fah. You somehow made the hard time easier and were one of the key for this success.

Kritchart Wongwailikhit

TABLE OF CONTENTS

จุฬาลงกรณ์มหาวิทยาลัย

CHULALONGKORN UNIVERSITY

LIST OF FIGURES

LIST OF TABLES

NOMENCLATURE

Latin letters

a	area of transfer and different	[m^{-1}]
A	column cross-sectional area	[m^2]
A$_B$	projected area of bubble	[mm^2]
a$_d$	specific interfacial area of non-collision droplet	[m^{-1}]
A$_D$	projected area of droplet	[mm^2]
A$_L$	light absorbance	[-]
a$_p$	packing specific interfacial area	[m^{-1}]
a$_{total}$	total specific interfacial area of packed bed spray column	[m^{-1}]
a$_w$	effective specific interfacial area of packing	[m^{-1}]
b, c	stoichiometry of the reaction	[-]
C$_A$	concentration of A in liquid phase	[mol/L]
C$_A^*$	saturated concentration of A in liquid phase	[mol/L]
C$_{AI}$	concentration of A at gas-liquid layer	[mol/L]
C$_{AL}$	concentration of A in bulk liquid phase	[mol/L]
C$_D$	drag coefficient	[-]
C$_{e,O2}$	oxygen equivalent concentration	[mg/L]
$\bar{C}$	average concentration	[mol/L]
$\Delta C_{ln,mean}$	log-mean different concentration	[-]
d	distance	[mm]
d$_{32}$	Sauter mean diameter	[mm]
d$_B$	bubble diameter	[mm]
d$_{B,max}$	maximum bubble diameter	[mm]
d$_c$	effect size	[~]
d$_D$	droplet diameter	[mm]
d$_{D,max}$	maximum droplet diameter	[mm]
d$_e$	equivalent diameter	[mm]
D$_i$	diffusion coefficient	[m^2/s]
d$_o$	orifice diameter	[mm]
E	enhancement factor	[-]
E$_i$	enhancement parameter	[-]
f	interference frequency	[Hz]
f$_{aq}$	acquisition frequency	[Hz]
f$_L$	droplet frequency	[Hz]
g	gravity constant	[m/s^2]
H$_A$	Henry constant	[mol/L.Pa]
h$_A$	height of the liquid surface without gas phase	[cm]
h$_B$	height of the liquid surface with gas phase	[cm]
I	light intensity	[Cd]
k$_1$	pseudo-first order reaction coefficient	[s^{-1}]
k$_g$	gas mass transfer coefficient	[m/s]
K$_g$	overall gas side mass transfer coefficient	[m/s]
K$_H$	Henry constant	[Pa.L/mol]

k_L	liquid mass transfer coefficient	[m/s]
K_L	overall liquid side mass transfer coefficient	[m/s]
L	path length of light travel	[cm]
L_c	droplet chord length	[mm]
L_s	optical probe constant	[nm]
M_H	Hatta Number	[-]
N	number of data	[-]
N_b	number of bubbles	[-]
N_I	number of points in interference signal	[-]
N_I	number of points in liquid fraction determination	[-]
n_{o2}	mole of oxygen	[mole]
P	power	[W]
P/V	specific power consumption	[W/m^3]
p_A	partial pressure of A in gas phase	[Pa]
p_{A*}	saturated partial pressure of A in gas phase	[Pa]
p_{AG}	partial pressure of A in bulk gas phase	[Pa]
p_{AI}	partial pressure of A at gas-liquid layer	[Pa]
P_B	perimeter of bubble	[mm]
P_D	perimeter of droplet	[mm]
Pe	Peglect number	[-]
ΔP_g	gas pressure drop	[Pa]
ΔP_L	liquid pressure drop	[Pa]
Q_g	gas flow rate	[L/min]
Q_L	liquid flow rate	[L/min]
R	radius	[cm]
R_A	mass transfer rate of A	[mol/s]
Re	Reynolds number	[-]
Re_0	Orifice Reynolds number	[-]
S_b	interfacial surface area of bubble	[m^2]
Sc	Schmidt number	[-]
Sh	Sherwood number	[-]
S_i^2	variance of the sample	[~]
t	time	[s]
t_0	t-score	[-]
t_e	time of exposure	[-]
T_L	liquid presenting time on probe tip	[ms]
T_R	liquid de-wetting time	[ms]
T_{total}	total time of measurement	[ms]
U^*	surface friction velocity	[m/s]
u_b	bubble rising velocity	[cm/s]
u_D	droplet velocity	[m/s]
$u_{D,i}$	droplet initial velocity	[m/s]
u_E	relative droplet velocity	[m/s]
u_o	orifice velocity	[m/s]
u_{rel}	relative velocity	[m/s]
u_{sg}	superficial gas velocity	[cm/s]

V	system volume	[m^3]
V$_b$	volume of bubble	[mm^3]
V$_g$	gas volume	[L]
V$_L$	liquid volume	[L]
V$_s$	solid volume	[L]
We	Weber number	[-]
$\bar{X}_i$	mean of the sample	[~]
x	position in x-axis	[m]
x$_A$	mole fraction of A in liquid phase	[-]
y	position in y-axis	[m]
y$_A$	mole fraction of A in gas phase	[-]
z	position in z-axis	[m]

Greek symbols

δ	phase shift between waves	[-]
σ$_c$	critical surface tension of material	[N/m]
ρ$_g$	gas density	[kg/m^3]
σ$_g$	gas surface tension	[N/m]
ε	power dissipation	[W/kg]
ε$_g$	gas fraction	[-]
ε$_I$	molar absorptivity (L/mol.cm)	[L/mol.cm]
ρ$_L$	liquid density	[kg/m^3]
σ$_L$	liquid surface tension	[N/m]
ε$_L$	liquid fraction	[-]
ε$_{L,avg}$	average liquid fraction	[-]
ε$_{L,local}$	local liquid fraction	[-]
ε$_s$	solid fraction	[-]
$\emptyset_i$	phase shift	[-]
ε_d	volume fraction of non-collision droplets	[-]
ε_w	volume fraction of collision droplets on packing	[-]
τ_s	shear stress	[N/m^2]
μ$_g$	gas viscosity	[Pa.s]
μ$_L$	liquid viscosity	[Pa.s]
λ	wavelength of optical probe light	[nm]
φ	mass flux	[mol/m^2.s]

Abbreviation

HSC	high-speed camera
OFP	optical fiber probe
AARD	Absolute average relative deviation
BCR	bubble column reactor
SPR	spray column reactor

Introduction

Gas absorption is now a frequently applied process in various applications, including the removal of volatile organic compounds (VOCs), hydrogen sulfide (H_2S), nitrogen oxide (NO_X), sulfur dioxide (SO_2), and carbon dioxide (CO_2) from contaminated gases. There are several types of equipment that can be used for the absorption process: tray columns, packed columns, spray columns and bubble columns. Every equipment provides the interfacial area between the gas and liquid phase in order to make the mass transfer happened. In general, bubble column and spray column are used for the gas treatment processes due to their low operating and maintenance costs, compactness, and high mass transfer rate (Kantarci et al., 2005; Tatin et al., 2015).

Bubble column is a gas-liquid contactor having the liquid phase as its continuous phase while the gas phase as the disperse phase in the form of bubbles. Bubbles can be produced using several types of sparger including membranes, perforated plates, and rigid sparger. Commonly, the sparger with small orifice diameters and a large number of orifices provided a high mass transfer rate but the corresponding power consumption is increased (Bouaifi et al., 2001; Luo et al., 2011). The bubble columns are very adaptable; various designs are available for this equipment. Most of the designs were done intending to improve the specific interfacial area and the mass transfer in the column. It is the most suitable in common applications since it provides a large contact time of liquid phases.

Spray column is another gas-liquid contactor that the liquid phase is dispersed phase (as droplets) and the gas phase is continuous phase. The liquid is fed into nozzle orifice where the small droplets are produced from the top of the column. The gas phase is fed at the bottom in the countercurrent regime and contact with moving down liquid droplet in order to transfer substance. The spray column dominates applications where a quick quench is needed, and the spray column is preferred when the solute is very soluble in the liquid. For the spray, the hydrodynamics of droplets play an important role in controlling the absorption efficiency of the sprays because the droplet sizes and velocities directly affect the interfacial area available for absorption (Roustan, 2003). If a spray system is to be understood and utilized efficiently, droplet size and velocity distributions need to be characterized (Hariz et al., 2017; Tatin et al., 2015). Various studies have proposed their mechanisms of droplet formation, including droplet sizes and velocities (Jones and Watkins, 2012; Nicholas P. Cheremisinoff, 1986) and have been further used for the purposes of simulation, optimization, and design of the processes (Bandyopadhyay and Biswas, 2007; Darake et al., 2016).

Several works of literature reporting the efficiency of spray columns and bubble columns for each solute and absorbent (Bandyopadhyay and Biswas, 2007; Bouaifi et al., 2001). Roustan, (2003) summarized that the mass transfer efficiency of both bubble column and spray column are close to each other. Their interfacial areas are between 50-300 and 10-100 m^{-1} for bubble column and spray column, respectively; while their

mass transfer coefficients (k_L) are both between 1-4 x 10^{-4} m/s. Even though the bubble column seems to be superior, it still cannot be concluded since the power consumption using by both columns have not been compared. However, the comparison is not so convenient since most experimental setups were done separately, and it was difficult to directly compare especially in terms of the mass transfer coefficient, specific interfacial area, and the specific power consumption.

Furthermore, there were several researchers working on the enhancement of the mass transfer rate in both the bubble column and spray column. For the bubble column, the addition of surfactant in the liquid phase is one alternative for increasing the gas-liquid interfacial area by decreasing bubble diameters (García-Abuín et al., 2012). However, the presence of surfactants can also decrease the liquid side mass transfer coefficient, it was found that the addition of surfactants decreased the mass transfer coefficient more than promoting the specific interfacial area (Painmanakul et al., 2005; Sardeing et al., 2006). Therefore, the modification of a bubble column using surfactant is not an effective method. Another approach is to introduce a solid phase in the bubble column. There were various works applying packed beds into their bubble column. Both positive and negative effects on bubble hydrodynamics and mass transfer were achieved (Maldonado et al., 2008). Besides, several works also applied movable solids into their bubble columns but there were discrepancies observed from their works. Ferreira et al., (2010) and Mena et al., (2011) applied different solid particles in their bubble column and mostly found the negative effect on the mass transfer coefficient ($k_L.a$); whereas, some works observed the positive effect on their $k_L.a$. The differences between the physical properties of solid particles such as size, density, and loading were suggested to be responsible for these differences. Various works had been done investigated the effect of solid size, density and loading rate on the $k_L.a$. However, none of them had investigated the relative effect of orifice size as well as the particle shape on the hydrodynamic and mass transfer in a bubble column. Moreover, the explanation of the bubble hydrodynamics and mass transfer due to the presence of the solid phase is still unclear. Therefore, the study of phenomena after adding solid in the reactor was still required in order to better understand and further used for applications. For the spray column, so far, most of the spray system enhancement have done by developing the orifice that is suitable in each application. Therefore, various types of orifices for spraying system have been pioneered. However, the enhancement of the mass transfer rate using the solid phase have not widely done.

Therefore, in order to fulfill the gap, this research projected to determine the effect of solid investigated the interaction of solid phases on the bubble or droplet hydrodynamics as well as its effect on mass transfer efficiency. An effective colorimetric method will be used to visually determine the collision effect between bubbles and particles. Besides, this research also aimed to globally investigate both hydrodynamics and mass transfer in both spray and bubble columns and comparing their specific power consumptions in order to develop the selection guideline for industrial usages. A high-void packing and ring-shaped particles were introduced into the columns to further determine the effect of the solid phase on the mass transfer rate.

Research objectives

- To determine the interaction between solid particles and bubble and its effect on mass transfer efficiency of a bubble column
- To determine the interaction between solid packing media and liquid droplet as well as its effect on mass transfer efficiency for a spray column
- To identify the parameters which control the mass transfer in solid adding system absorption
- To compare bubble and spraying system with and without solid for absorption, by experimental and modeling approaches

Research hypothesis

- Solid particles adding into bubble column increase mass transfer contact time by breaking up large bubbles into smaller bubbles which increasing gas hold up and interfacial area
- Solid particles adding into spray column increase mass transfer contact time by reducing the settling velocity of liquid droplets and result in raising liquid hold up

Expected outcome

- Understand liquid and gas flow phenomena after adding solid in bubble column and spray column
- Obtain appropriate mass transfer parameters to be the guideline for achieving the optimum bubble and spray columns.

Manuscript structure

This thesis consists of 5 chapters. In chapter 1, the review of gas absorption is summarized. It shows that the gas absorption can be operated in different gas-liquid contactors. Bubble column and spray column are ones of the contactors that can be used for the purpose. However, most of the literature did not report the power consumption that requires to achieve mass transfer performance. Moreover, the mass transfer performance can be improved by the addition of solid phase. To fulfill this gap, the mass transfer performances of a bubble column and a spray column were studied. Initially, an optical probe which is one of the equipment that used for characterizing the droplet hydrodynamics was studied in terms of its accuracy. This equipment is one of the tools using for characterizing the spray in Chapter 3 where the hydrodynamics of fluid in both columns as described were investigated. Afterward, the effect of the solid adding into a bubble column on the mass transfer was investigated locally by a colorimetric method in Chapter 4. The mass transfer of CO_2 in both bubble and spray columns adding solid media were then studied globally in Chapter 5. The detail of each chapter can be expressed as follow:

Chapter 1 (Gas absorption review) contains the review according to the gas absorption. Firstly, the basic knowledge, Henry's law, and absorption mechanism are

summarized. Equipment and design equation using for absorption processes are also included along with the fundamental of chemical absorption. Secondly, the carbon dioxide capture processes are introduced including its storage and utilization. Lastly, the hydrodynamics and mass transfer in bubble columns and spray columns are reviewed. The gap of literature is presented in this chapter.

Chapter 2 (Optical fiber probe for spray characteristics) presents the performance of optical probes on the characterization of spray droplets. In this work, two types of optical probes were used in the study: the de-wetting probe and light interference probe. These probes have capabilities to determine droplet velocity and size where their results were compared with a high-speed camera. Two regimes of sprays were studied; the series of droplets produced with a syringe and the full-cone spray regime produced by industrial nozzles. The experimental setup, material and method, the result and discussion, as well as the chapter's conclusion are included in this chapter.

Chapter 3 (Three-phase spray and bubble columns: hydrodynamics) is the chapter where the global hydrodynamics parameters of spray and bubble columns were determined. The droplet and bubble diameters, droplet and bubble velocities, gas and liquid fractions, and specific interfacial areas of each column were observed in the same range of gas and liquid flow rates. A high-void packing and ring-shaped particles were also added in the columns in order to study their effects on the hydrodynamics of droplets and bubbles. In addition, pressure drops and power consumption of each column were determined and compared in order to determine their advantages and drawbacks.

Chapter 4 (Colorimetric method for characterizing mass transfer in bubble column) consists of two parts. The first part utilizes the "red bottle" reaction as the colorimetric method to develop a technique to determine the mass transfer coefficient visually. This technique overcomes other techniques as it does not require other measuring equipment rather than to record the time that the solution changes from colorless to saturated red. The latter part uses the colorimetric method to observe the mass transfer of bubbles when the bubbles collide with particles. The effect of bubble-particle collision on the mass transfer is depicted in this part. Note that, there were two experimental setups in this chapter since each part has different experimental setup as well as material and method.

Chapter 5 (Three-phase spray and bubble columns: mass transfer) compares bubble and spray columns in the mass transfer aspect. The overall mass transfer coefficient (k_La) and the liquid side mass transfer coefficient (k_L) were determined and compared between the bubble and spray columns. The high-void packing and the ring-shaped particles were also added in the column in order to determine its effect on the mass transfer. The specific power consumptions (P/V) of each column were also investigated as a function of k_La and compared between both columns. Lastly, the summary of advantages and drawbacks for each column was proposed.

Finally, overall research conclusion of this thesis is presented after Chapter 5 along with references and Appendix.

Chapter 1
Gas absorption review

1.1 Absorption

1.1.1 Basic knowledge

Absorption is a transfer process where substances from gas phase transfer to liquid phase. It was occurred due to the different fugacity between gas phase and liquid phase, inducing each substance to transfer from gas phase having high concentration to liquid phase that contains lower concentration. The rate of absorption depends on properties of gas-liquid fluid dynamics, interfacial area between phases, concentration difference, temperature, and pressure. The absorption can be applied in many processes; separate gas mixtures. remove impurities, contaminants, pollutants, or catalyst poisons from a gas; and recover valuable chemicals (Seader et al., 2010). The oxygenation in aerobic wastewater treatment and carbon dioxide capture from electricity generation process, sulfur dioxide removal and recovery of n-hexane are the example of the processes utilizing the absorption theory (Bouaifi et al., 2001; Kothandaraman, 2010; Xiao et al., 2015).

There were two major types of absorption: physical absorption and chemical absorption. Physical absorption or non-reactive absorption is a process of mass transfer that doesn't involve with chemical reaction occurring in liquid phase; the aeration process, for instance. This mass transfer takes place at the interface between the liquid and the gas. This type of absorption depends on the solubility of gases, pressure, temperature as well as surface area of the interface and its duration time of contact.

Chemical absorption or reactive absorption is a chemical reaction between the absorbed and the absorbing substances. It is the combination between physical absorption and chemical reaction. Rather than the surface area and the time of contact, this type of absorption depends upon the stoichiometry of the reaction and the concentration of its reactants. Commonly, this type of absorption uses in industrial application due to its higher mass transfer rate comparing to physical absorption, leading smaller absorption equipment required.

1.1.2 Solubility and Henry's law

One of most important factors for absorption is the solubility of gas in liquid. Generally, solubility of gas depends on temperature, pressure and characteristic of the substance itself. The solubility of gas in liquid can be identified by feeding the gas into close vessel. After reaching equilibrium, which is the point that both gas and liquid phases transfer rate are equal, the concentrations of the component in both gas and liquid phases are constant.

The gas-liquid equilibrium is related to gas and liquid fugacity balance. When perfect gas law can be applied and liquid solution can be assumed as ideal, the gas-liquid equilibrium can be described with Henry's Law which is the relationship between concentrations of the substance in gas phase and liquid phase as expressed in Equation (1.1), where p_A, H_A and C_A are the partial pressure of A in gas phase, Henry constant of the gas at a certain temperature, and the concentration of A in liquid phase, respectively.

$$p_A = H_A C_A \tag{1.1}$$

The Henry's law is commonly used in the gas absorption process. It has a good capability to predict the gas-liquid equilibrium especially in a dilute condition which is the common condition that the absorption process is used for ideal solutions. Rather than Equation (1.1), Henry's law can be expressed in various forms. Each form has different Henry constant due to different units as shown in Table 1.1.

Table 1.1 Henry's law constants for various gases in water at 25°C (Sander, 2015)

Equation:	$K_{Hc} = \frac{p_A}{C_A}$	$H_A = \frac{C_A}{P_A}$	$K_{Hx} = \frac{p_A}{x_A}$	$K_{Hxy} = \frac{y_A}{x_A}$
Unit:	$\left(\frac{L \cdot atm}{mol}\right)$	$\left(\frac{mol}{L \cdot atm}\right)$	(atm)	(dimensionless)
O_2	770	1.3×10^{-3}	4.3×10^4	3.2×10^{-2}
H_2	1300	7.8×10^{-4}	7.1×10^4	1.9×10^{-2}
CO_2	29	3.4×10^{-2}	1.6×10^3	8.3×10^{-1}
N_2	1600	6.1×10^{-4}	9.1×10^4	1.5×10^{-2}
He	2700	3.7×10^{-4}	1.5×10^5	9.1×10^{-3}
Ne	2200	4.5×10^{-4}	1.2×10^5	1.1×10^{-2}
Ar	710	1.4×10^{-3}	4.0×10^4	3.4×10^{-2}
CO	1100	9.5×10^{-4}	5.8×10^4	2.3×10^{-2}

* x_A and y_A are the mole fraction of substance A in liquid phase and gas phase, respectively.

1.1.3 Mechanism of absorption

The basic theory of mass transfer with absorption is the two-film theory, Figure 1.1. In the figure, interface of gas and liquid is illustrated with assumption of laminar film. The gas contains substance A with the bulk concentration of gas phase, P_{AG}, transfers to liquid phase at its bulk concentration, C_{AL}. At the interfaces of both phases, there are two films, gas film and liquid film connecting to each other. At the gas interface, the substance A is not able to transfer to liquid phase rapidly due to their different density, diffusivity and surface tension between both phases. As it is limited at the interface, the substance A forms the gas-liquid equilibrium at the interface between the gas and liquid layer, and the concentrations of A at the gas and liquid interfaces are corresponding to Henry's law. It should be noticed that the concentration of A reduced along its trajectory from the gas phase to the liquid phase.
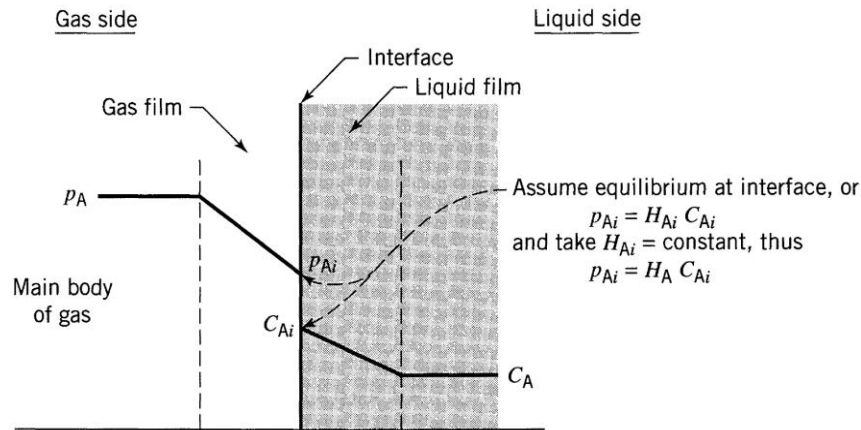
Figure 1.1 Two-Film Theory (Levenspiel, 1999)

From the transfer mechanism of the two-film theory, rate of mass transfer per volume
(R_A, mol/L.s) from gas phase to gas-liquid layer can be described as in Equation (1.2) which is the function of gas mass transfer coefficient (k_g, m/s), area of transfer (a, m^{-1}) and different concentration between bulk gas (p_{AG}, mol/L) and gas-liquid layer (p_{AI}, mol/L). For liquid, as well as gas transfer, the transfer rate in the liquid phase is equal to multiply of liquid transfer coefficient, area of transfer (a, m^{-1}) and difference in concentration between layer of gas-liquid (C_{AI}, mol/L) and bulk phase (C_{AL}, mol/L) as expressed in Equation (1.3)

$$R_A = k_{Ag}a\,(p_{AG} - p_{AI}) \qquad (1.2)$$
$$R_A = k_{Al}a\,(C_{AI} - C_{AL}) \qquad (1.3)$$

In practical, the concentration of substances at the interface cannot be directly measured. Hence, the overall mass transfer coefficient for gas phase and liquid phase (K_L, K_G) are utilized instead. The overall mass transfer coefficients are considered transfer between bulk solution and saturated film. Thus, Equation (1.2) and (1.3) convert into Equation (1.4) and (1.5) respectively, where p_A^* is the saturated pressure calculated at equilibrium with the liquid bulk concentration and C_A^* is the calculated concentration at equilibrium with the gas concentration. Both p_A^* and C_A^* can be estimated using the Henry's law.

$$R_A = K_G a\,(p_{AG} - p_A^*) \qquad (1.4)$$
$$R_A = K_L a\,(C_A^* - C_{AL}) \qquad (1.5)$$

At equilibrium, the relationship between overall mass transfer coefficient (K_i, m/s) and minor mass transfer coefficient (k_i, m/s) can be described as in Equation (1.6) and (1.7) for gas and liquid respectively.

$$\frac{1}{K_G} = \frac{1}{k_g} + \frac{H_A}{k_L} \qquad (1.6)$$

$$\frac{1}{K_L} = \frac{1}{k_L} + \frac{1}{H_A k_g} \qquad\qquad (1.7)$$

In case that H_A is very low (high solubility of gas in liquid), $K_G \approx k_g$ and mass transfer will be limiting on gas phase. While for high value of Henry's constant (Low solubility of gas), $K_L \approx k_L$ which indicates that mass transfer limiting step will be depending on liquid phase. For example, in a case of CO_2 absorption, since its solubility is low (H = 2,980 $Pa.m^3$/mole at 25ºC), its mass transfer rate is limited at liquid film and Equation (1.5) can be utilized to determine $k_L a$ value of the process. Note that turbulent liquid flow is desirable to reduce thickness of liquid film if mass transfer is limiting in the liquid phase, while a continuous turbulent gas flow is desirable if mass transfer is limiting in the gas phase (Levenspiel, 1999).

1.1.4   Absorption equipment

There are several types of equipment used for the absorption process. Every equipment provides the interfacial area between the gas and liquid phase, so-called gas-liquid contactors, in order to make the mass transfer happened. Common equipment for absorption process consists of tray columns, packed columns, spray columns and bubble columns.

(a) Bubble column

Bubble column is a gas-liquid contactor having the liquid phase as its continuous phase while the gas phase as the disperse phase in the form of bubbles. The bubble columns are very adaptable; various designs are available for this equipment as shown in Figure 1.2. The simplest form of bubble column (Fig. A) consists of a vertical tube with no internals part. Gas is fed in at the bottom while liquid is led through with co-current or counter-current regime. From these basic configurations, a number of modifications are employed. The back-mixing of gas and liquid phases in the simple bubble column and the non-uniform distribution of gas bubbles over the cross section can be reduced by the installation of trays (Fig. B), packing (Fig. C), or shafts (Fig. D). All these devices can operate either co-currently or counter-currently. To set up the most homogeneous bubble flow, static mixer elements can also be placed in the ascending flow section (Fig. E).
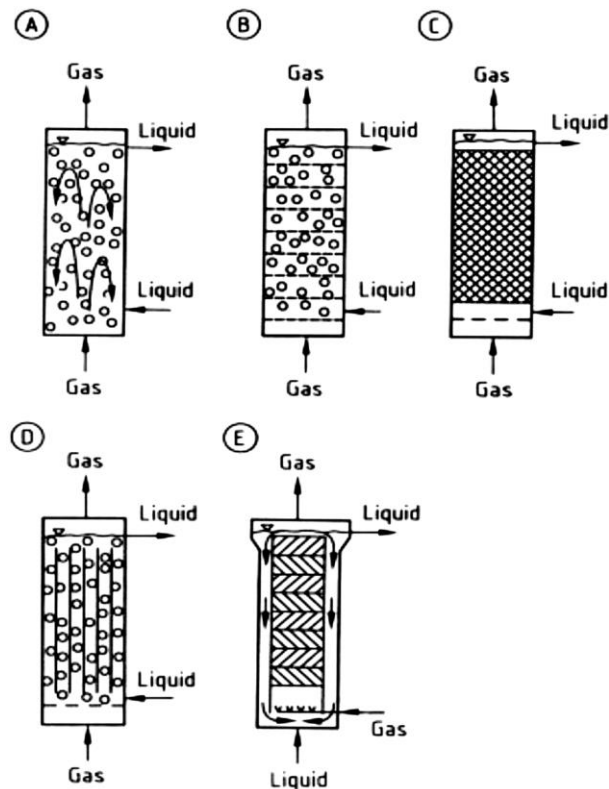
Figure 1.2 Types of bubble-column reactors
(A) Simple bubble column (B) Cascade bubble column with sieve trays (C) Packed
bubble column (D) Multi-shaft bubble column (E) Bubble column with static mixers
(Deckwer and Field, 1992)

(b) Tray column

A plate column or tray column, Figure 1.3, is a gas-liquid contactor that the gas
comes in contact with liquid through different stages in counter current regime. The
liquid is fed at the top of the column while the gas phase was throughput at the bottom.
There are a number of holes in each stage to let the gas and liquid phase contact with
each other. Plate columns can be designed to handle a wider range of liquid and gas
flow rates This type of column is commonly applied for distillation, gas-liquid
absorption and liquid-liquid extraction. Both continuous and batch operations can be
performed by the tray column.
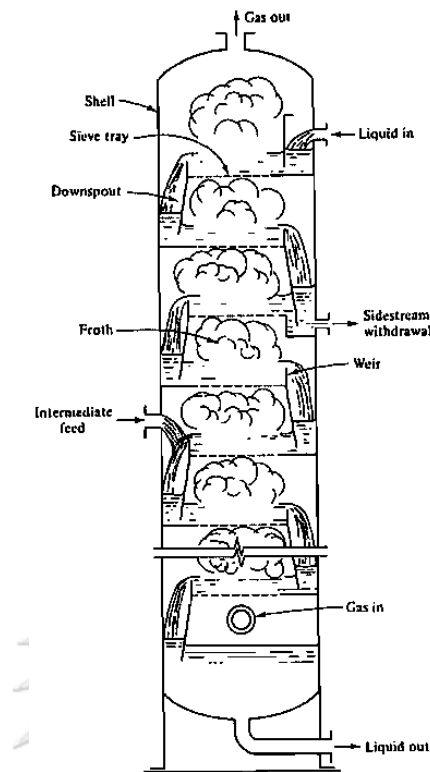
Figure 1.3 Tray column (Treybal, 1980)

(c) Packed column

Packed columns, Figure 1.4, are used in various purposes: distillation, gas absorption and liquid-liquid extraction. The liquid flows down in the column over the packing surface where the surface is designed to be covered by the liquid film. The gas phase moves counter-currently, upward the column. The mass transfer process occurs at the interface of the liquid film covering the packing. The performance of the packed column depends on the hold up of liquid and gas distribution through the packed bed. There are some advantages and disadvantages for the plate and the packed columns. However, the packed columns are not suitable for very low liquid flow rates since the packing will not be fully covered leading to lower interfacial area. However, this type of contactor is commonly used when the corrosive, toxic, or flammable liquids are used since its liquid fraction in the column was low.
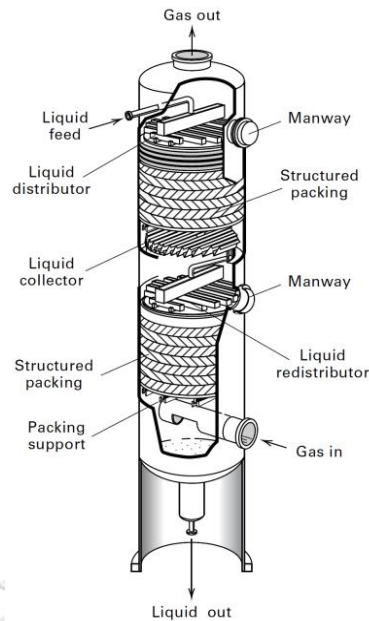
Figure 1.4 Packed Column (Green and Perry, 2007)

The packing types (Figure 1.5) can be divided into two broad classes: structured and random packing. The random packings are more commonly used in the industry (Raschig-, Pall- and HyPack rings, and Berl- and Intallox saddles).
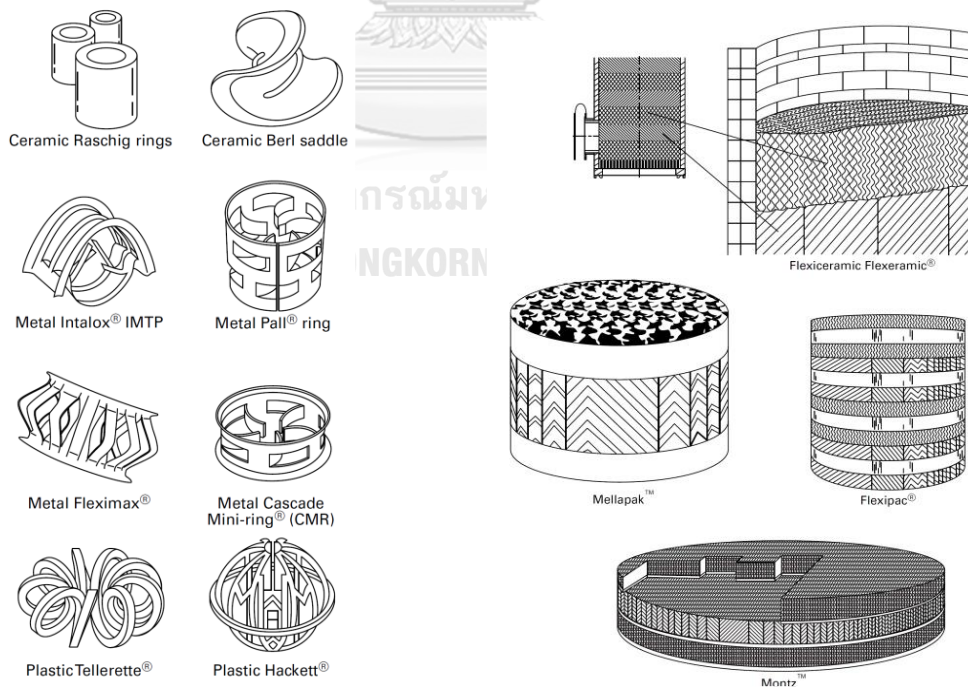
Figure 1.5 Packing characteristic for
(Left) dumped packing or random packing (Right) structured packing
(Seader et al., 2010)

(d) Spray column

Spray column is one of absorption operating unit which contrast with bubble column. The liquid is fed into nozzle orifice where the small droplets are produced from top of column. Gas phase is fed at the bottom in counter current regime and contact with moving down liquid droplet in order to transfer substance. The schematic diagram for spray tower can be illustrated as in Figure 1.6.
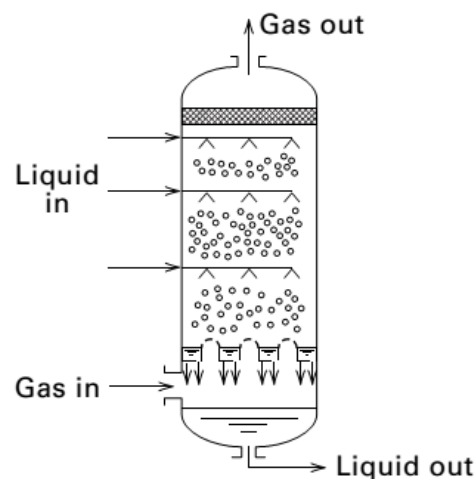
Figure 1.6 Spray Tower (Seader et al., 2010)

(e) Stirred Tank
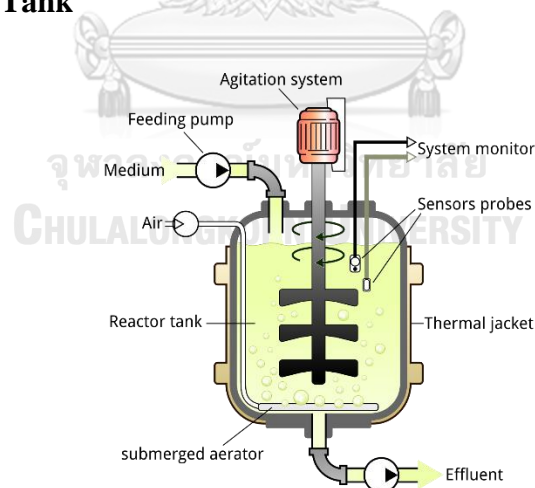
Figure 1.7 Continuous stirred-tank contactor (Nič et al., 2009)

Stirred tank, Figure 1.7, is a vessel that contains an agitation system along with the submerged aerator at the bottom of the tank. The aeration system produces bubbles from the bottom and the bubbles contacts with the liquid phase inside the column. The agitation system enhances the liquid mixing regime and velocity in order to promote

the mass transfer inside the tank. This type of equipment is commonly used in biological processes which involves organisms or biochemically active substances.

(f) Equipment selection

For the normal absorption operation, a packed column is commonly used. The dumped packing is favored when column diameter is less than 0.6 m with the height less than 6 m. It is normally used especially when dealing with high liquid flow rate or corrosive substances, where ceramic or plastic material are suitable than metals. The packed column is also preferred when foaming is severe or low liquid holdup is desirable. Note that the structured packing is one of the best choices when the dumped packing pressure drop is too high. It provides a better degree of separation when comparing with dumped packing. However, the price for the installation cost is significantly higher. For other operations, trayed columns are more preferred especially for low flow rate. Usually, the (continuous) gas phase is mass transfer-limiting in packed columns and the (continuous) liquid phase is mass-transfer-limiting in tray columns. (Seader et al., 2010)

For absorption of low solubility gases, the bubble column is the most favored since it provides large contact time of liquid phases. Bubble systems tend to have much higher interfacial area than the spray one. However, the droplet systems can enable much higher energy input than the bubble column and, as a result, dominate applications where a quick quench is needed. This higher transfer rate is one of the advantage for the spray system since it might require smaller equipment size (Kunesh, 1993) and it also requires low gas pressure drop and also tend to be non-fouling (Green and Perry, 2007). Moreover, the spray column is preferred when the solute is very soluble in the liquid. Although there are several literatures reporting the efficiency of spray columns and bubble columns, those were done separately.

1.1.5 Design equations for absorption process

The general design equation for physical absorption process uses the mass balance equation in order to determine the column. For continuous regime, the mass balance can be derived as in Equation (1.8), where the R_A can be expressed as in Equation (1.9).

$$\text{Accumulation} + \text{Outlet} = \text{Inlet} + \text{mass transfer} \qquad (1.8)$$

$$R_A = K_L a \Delta C_{ln,mean} \qquad (1.9)$$

In the equation, R_A is the mass transfer rate, K_L is the overall liquid mass transfer coefficient, a is the specific interfacial area, and $\Delta C_{ln,mean}$ is the log-mean different concentration. Here, the design equations for each absorption equipment are different depending on their hydrodynamics of both gas phase and liquid phase. When considering the possible outcomes for continuous regime, it can be summarized as in Figure 1.8.
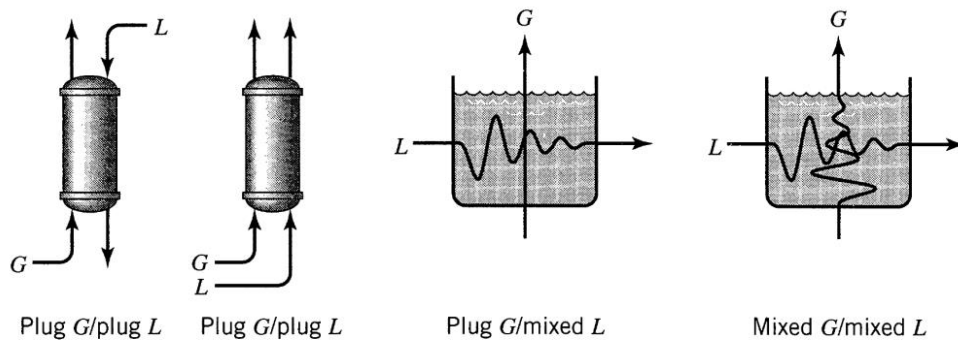
Figure 1.8 Contacting patterns for gas-liquid contactor (Levenspiel, 1999)

Four types of the patterns are consisted of (1) Counter-current of plug flows in both gas and liquid phases (2) Co-current of plug flows in both gas and liquid phases (3) Plug flow in gas phase and mixed flow in liquid phase, and (4) Both mixed flows in both gas and liquid phase. When paring the flow patterns with the different types of contactors, type (1) should represent spray columns, packed columns, and tray columns. The log-mean different concentration of the type (1) can be expressed as in Equation (1.10) for low solubility gases. Since the mass transfer is limited in the liquid phase, the driving force is the difference of concentration between the gas-liquid interface, which is represented by C^*, and the concentrations at the inlet and the outlet.

$$\Delta C_{ln,mean} = \left[\frac{(C_{in}^* - C_{out}) - (C_{out}^* - C_{in})}{\ln\left(\frac{C_{in}^* - C_{out}}{C_{out}^* - C_{in}}\right)} \right] \tag{1.10}$$

However, for the bubble column, type (3) is the preferred one since the gas phase slips through the column as a plug flow regime while the liquid phase can be mixed rapidly inside the column. Therefore, the concentration of the substance in the liquid phase should be identical and equal to the outlet concentration as depicted in Equation (1.11).

$$\Delta C_{ln,mean} = \left[\frac{(C_{in}^* - C_{out}) - (C_{out}^* - C_{out})}{\ln\left(\frac{C_{,in}^* - C_{out}}{C_{out}^* - C_{out}}\right)} \right] \tag{1.11}$$

1.1.6 Chemical absorption

Chemical absorption is one of the absorption processes where the dissolved substance transfers into liquid phase and reacts with another substance in the liquid phase. The example of chemical reaction of first order reaction can be expressed as in Equation (1.12).

$$A_{(g \to l)} + bB_{(l)} \to P_{(s,l,g)} \tag{1.12}$$

In reaction, A is substance that transfer from gas phase and dissolves in the liquid phase and reacts with the substance B in the liquid phase to form P which is the product of the reaction. The chemical reaction can occur since A and B are in contact in the liquid phase, including the interface of gas-liquid and in bulk liquid. As mentioned earlier, mass transfer equation for physical absorption can be defined as in Equation (1.13).

$$R_A = k_{Ag}a(p_A - p_{Ai}) = k_{Al}a(C_{Ai} - C_A) \qquad (1.13)$$

However, for chemical absorption which combined between physical absorption and chemical reaction the rate of absorption equation can be described as in equation (1.14), where E represents the ratio of mass transfer coefficient with chemical reaction to mass transfer coefficient without chemical reaction, Equation (1.15). For physical absorption, E is equal to 1 but for chemical absorption the E value is larger than 1 where the mass transfer rate in reactor is increased. The difference in concentration profiles can be illustrated as in Figure 1.9.

$$R_A = k_{Ag}a(p_A - p_{Ai}) = Ek_{Al}a(C_{Ai} - C_A) \qquad (1.14)$$

$$E = \frac{K_L a \text{ with chemical reaction}}{K_L a \text{ without chemical reaction}} \qquad (1.15)$$
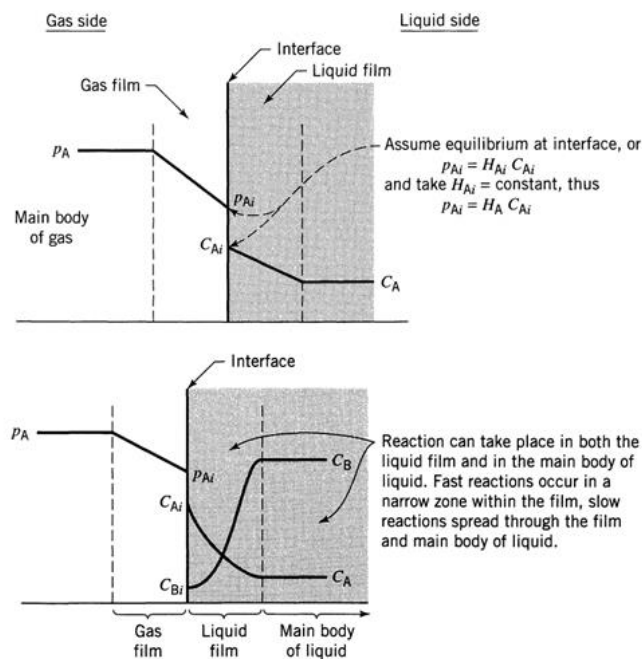
Figure 1.9 Two-Film Theory for physical absorption (Above figure) and Chemical absorption (below figure) (Levenspiel, 1999)

In order to estimate the enhancement factor (E), two variables are introduced, Hatta number (M_H) and E_i. The Hatta number can be calculated with Equation (1.16), which consist of rate of reaction (k_1), diffusion coefficient (D_A) and mass transfer coefficient (k_{Al}) while E_i is the function of diffusion coefficient of both substances (D_A, D_B), concentration of substance B, partial pressure of A (P_{Ai}), Henry constant (H_A) and the stoichiometry of the reaction (b), as expressed in Equation (1.17).

$$M_H = \frac{\sqrt{kC_B D_A}}{k_{Al}} = \frac{\sqrt{k_1 D_A}}{k_{Al}} \tag{1.16}$$

$$E_i = 1 + \frac{D_B C_B H_A}{b D_A p_{Ai}} \tag{1.17}$$

Afterwards, the value of E can be estimated from the correlation of the Modified van Krevelens and Hoftijzer as shown in Figure 1.10 (Levenspiel, 1999). From the correlation, for M_H lower than 0.02 with regardless of the E_i, the E can be considered as equal to 1 due to the fact that the rate of reaction is very low, and the chemical absorption is insignificant. Eventually, the physical absorption controls the mass transfer. However, for the process having Hatta number (M_H) higher than 2, there is a significant change of E related to the value the E_i and M_H. In case that the $E_i > 5M_H$, the pseudo first order reaction occurred at the gas-liquid interface and $E \cong M_H$. Whilst, for the case where $5E_i < M_H$, the reaction is instantaneously occurred at the liquid film and $E \cong E_i$. Note that for the case where $5E_i > M_H > E_i/5$, the value of E can be estimated from Figure 1.10. Lastly, for M_H between 0.02 and 2, it can be considered as the intermediate reaction where the E can be estimated from $E \cong 1+M_H^2/3$ as described in the figure.
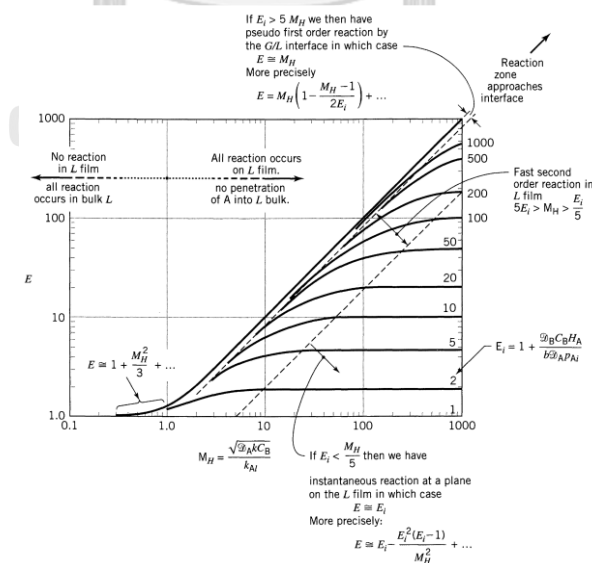
Figure 1.10 The enhancement factor for fluid-fluid reactions as a function of M_H and Ei, modified from the numerical solution of van Krevelens and Hoftijzer (Levenspiel, 1999).

1.1.7 General consideration parameters for absorption

(a) Interface characteristic

Interface characteristic depends on the equipment used for the absorption. For packing column, the interface of mass transfer is the layer of liquid that covered the packing as shown in Figure 1.11. The slip velocity through the interface as well as the thickness of the layer is one of the factors controlling the mass transfer in the packing system.
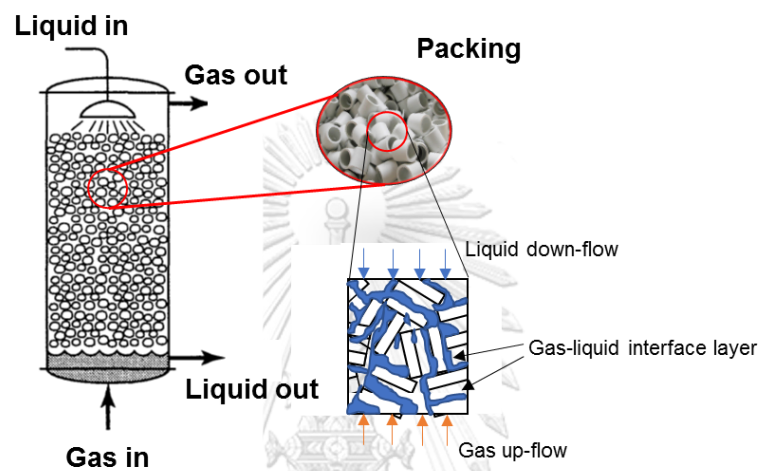
Figure 1.11 Gas-liquid interface layer of packing column

For bubble column and spray column, their interfaces for mass transfer are bubbles and droplets, respectively. Bubble/droplet characteristic can be described in two major parts, geometry and dynamic. The geometry is size and shape which affects the surface area of bubble/droplet as well as dynamic of bubble/droplet which were force and velocity, since shape and size affect amount of drag force acting on bubble surface. The bubble/droplet size and shape are mostly depending on size of orifice, gas flow rate, liquid properties as well as pressure and temperature of operation.

(b) Gas holdup/Liquid holdup (ε_g, ε_L)

Gas hold up, Equation (1.18), is fraction of gas volume presenting in reactor at contacting zone. It is unitless variables for mass transfer which can correlate to interfacial area between gas and liquid interface. High amount of gas holdup represents amount of gas presenting in the column which imply that there are a lot of interfacial area in reactor. For common operation, gas hold up usually depends on the gas phase characteristic, gas flow rate, size of column, pressure, temperature, size of orifice and also properties of liquid and solid in the system.

$$\varepsilon_g = \frac{Gas\ volume\ in\ contactor}{Total\ volume\ of\ contactor} \tag{1.18}$$

Liquid holds up, Equation (1.19), is vice versa from gas hold up and usually utilize to identify fraction of liquid presenting in the column. As liquid presenting more in the column, amount of liquid holdup is increasing. The liquid holdup is as well depending on the liquid phase characteristic, liquid flow rate, size of column, temperature, size of liquid feed nozzle and also properties of gas-liquid.

$$\varepsilon_L = \frac{Liquid\ volume\ in\ contactor}{Total\ volume\ of\ contactor} \qquad (1.19)$$

(c) Interfacial area (a)

Interfacial area is the area where the gas and liquid phases are in contact with each other. It is one of the important mass transfer parameters controlling by the fluid dynamic in the column. For absorption aspect, the specific interfacial area (a), which defined as the total interfacial area per unit volume of column, is normally used as shown in Equation (1.20).

$$a = \frac{Gas - liquid\ interfacial\ area\ (m^2)}{Volume\ of\ continuous\ phase\ in\ the\ column} \qquad (1.20)$$

The specific interfacial areas of each contactor are different depending on their interface characteristics. For the packed column, its interfacial area is the interfacial area of the wetted packed solid while, for bubble column, the interfacial area is the total interface area of bubbles in the column. The droplets total surface area is the one that represents the interfacial area of the spray column. Normally, the specific interfacial area is proportional to the discrete phase holdup and the interface between the discrete phase and the continuous phase.

(d) Mass transfer coefficient (K_L, K_G)

Mass transfer coefficient is one of mass transfer variables; it represents the rate of transferring through the interfacial area, which already described in Section 1.1.3. As mentioned earlier, in case of high solubility gases in liquid, the K_G is normally the one represents the mass transfer in the contactors while the K_L usually represents the mass transfer for low solubility gases. Moreover, the mass transfer coefficient is the function of various variables including properties between gas and liquid, fluid velocities, cross-sectional area of fluid flows, fluid flow regimes, surface shear forces, mixing regime in the column, chemical reactions, for instance (Green and Perry, 2007; Seader et al., 2010).

(e) Pressure drop and power consumption

Pressure drop is the pressure loss due to the flow of fluids inside the contactors. It commonly depends on the gas flow rate, liquid flow rate, and also the contactors configuration. The sudden expansion and contraction of fluids are normally the ones that contribute to the pressure loss inside the contactors, leading to a large power

consumption to operate the system. Therefore, the pressure drop is one of the parameters that should be taken into account when selecting a suitable contactor. The relations between the pressure drop of the fluid flow and the specific power consumption, which is the power consumption per volume of the contactor, are shown in the Equation (1.21) and (1.22) for the gas and liquid phases, respectively. In the equations, *P/V* is the specific power consumption, Q_i is the flow rate of the fluid, ΔP_i is the pressure drop of the fluid, and V is the volume of the contactor.

$$(P/V)_{gas} = Q_g \cdot \Delta P_g/V \tag{1.21}$$
$$(P/V)_{Liquid} = Q_L \cdot \Delta P_L/V \tag{1.22}$$

(f) Comparison of parameters for various gas-liquid contactors

When considering each parameter that controlling the mass transfer in the contactors, it can be summarized as shown in Table 1.2, where the gas-liquid interface characteristics, dispersed phase holdups, interfacial areas, and mass transfer coefficients (K_L) are compared.

Table 1.2 Gas-liquid contactor comparison in terms of mass transfer performance (Roustan, 2003)

Contactor	Dispersed phase	Gas-liquid Interface	Interfacial area (m²/m³)	Dispersed phase holdup (%)	Mass transfer coefficient, K_L (m/s)
Bubble Column	Gas	Bubbles	50-400	1-30	$1\text{-}5 \times 10^{-4}$
Stirred Tank	Gas	Bubbles	50-300	1-20	$2\text{-}5 \times 10^{-4}$
Packed Column	Liquid	Wetted packing interface	50-300	4-15	$0.5\text{-}4 \times 10^{-4}$
Spray Column	Liquid	Droplets	10-100	1-10	$1\text{-}4 \times 10^{-4}$

From the table, it can be seen that the dispersed phases of each contactor are different due to the different interface characteristics and flow regimes inside each contactor. Among all contactors, the bubble column is the one that provides the maximum specific interfacial area and the holdup at around 50-400 m^{-1} and 1-30 %, respectively. The stirred tank reactor gave a slightly lower holdup at 1-20 % and 50-300 m^{-1} for the interfacial area. The packed column has the same range of the interfacial area as the stirred tank but slight lower holdup. The spray column is the one having the lowest interfacial area range and the holdup. For the mass transfer, the liquid-side mass transfer coefficients (K_L) are almost the same for all types of contactors. Even though the bubble column seems to be the best one, it still cannot be settled since the power

consumptions using by each contactor have not been compared. Therefore, this summary can be improved by adding two other issues as described in the following:

Firstly, the pressure drop and power consumption of each contactor should also be taken into account as some contactors might possibly provide an equivalent interfacial area and mass transfer but requires a larger power consumption. Hence, by comparing both interfacial area and mass transfer coefficient in terms of the power consumption, a suitable equipment will be able to optimally be selected. Secondly, the parameters controlling each contactor have not been mentioned. As shown in the table, the dispersed phase and gas-liquid interfaces of each contactor are different and therefore the parameters that control their holdups, interfacial areas, and mass transfer are unavoidably different. Therefore, in order to comprehensively create a guideline for the contactor selection, these parameters that control the mass transfer as well as the power consumption should be studied. In this study, the bubble column and spray column were selected to compare as both equipment have the very similar regime that can be simply compared in terms of their discrete phase hydrodynamics and the power consumption.

1.2 Bubble column

1.2.1 Fluid dynamic in bubble column

Fluid dynamic affects significantly to efficiency of bubble column. The flow regime is mostly depending on size of column and superficial gas velocity as shown in Figure 1.12 and Figure 1.13. Noted that the superficial gas velocity is calculated by the gas flow rate divided by the flow cross-sectional area. As seen in the figures, 3 types of regimes are occurring in bubble column which are

1. Homogeneous or Bubbly flow regime

2. Heterogeneous or Churn-turbulent regime

3. Slug flow regime
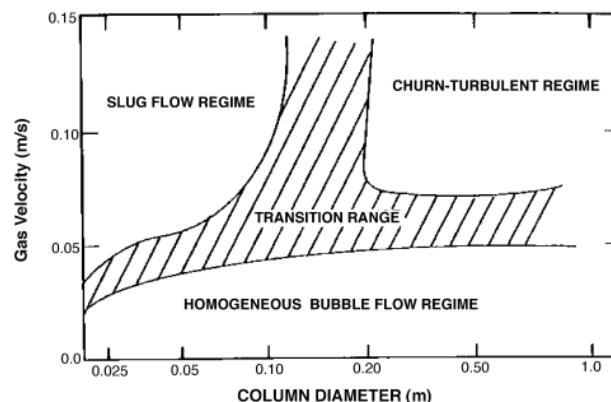
Figure 1.12 Flow Regime as function of column diameter and gas velocity (Kantarci et al., 2005)

For bubble flow regime which occurs when gas velocity is lower than 5 cm/s, the gas bubble size will be small and uniformly throughout column. The bubble flow in this regime has low chance to coalesce into larger size of bubble. This regime is the most required for the real application.

For Churn-Turbulent regime which is the regime of bubble perform at higher superficial velocity, the bubbles flow inside reactor with turbulent and circulation. As the result for turbulent and circulation, the bubble has higher chance to coalesce into larger bubble but also increase chance of bubble break up into smaller bubble. Most of industrial absorption can only work on this regime due to requirement of high superficial gas velocity.

Slug flow regime is the regime that bubbles coalesce into large slug due to very high gas velocity or low diameter of columns. This regime is not appropriate for absorption process due to low interfacial area between gas and liquid phase. Figure 1.13 illustrates flow regime occurring in bubble column.
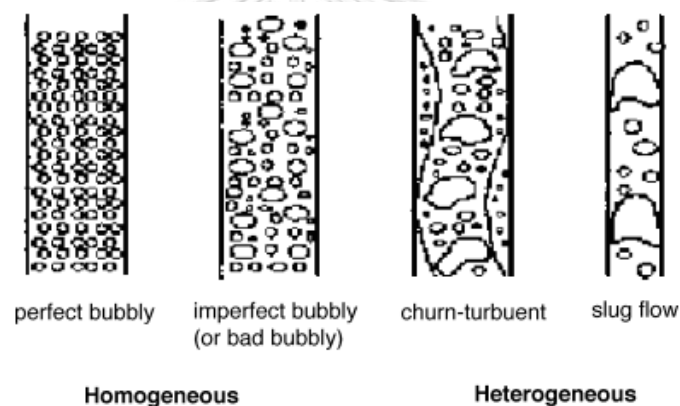
Figure 1.13 Flow Regime in bubble column (Hébrard et al., 1996)

1.2.2 Bubble hydrodynamics

(a) Characterizing methods

Various methods have been pioneered for characterizing bubble hydrodynamics in the bubble column. Among the techniques, the optical technique is the mostly used one due to its reliability and simplicity. The use of charge coupled device (CCD) and complementary metal oxide semiconductor (CMOS) camera have been widely used along with various image processing techniques to computationally determined bubble sizes and velocity (De Swart et al., 1996; Kulkarni and Joshi, 2005; Loubière et al., 2003). However, the optical technique cannot individually determine the gas holdup in the column. The utilization of the gas-liquid height relative to the gas-free liquid level along with the optical techniques or the pressure taps are required in order to acquire the information (Bouaifi et al., 2001; Kantarci et al., 2005; Maldonado et al., 2008).

Besides of the common optical techniques, phase detection probe technique is one of the techniques that commonly uses to determine the bubble hydrodynamics especially for the gas holdup. The phase detection probe is an equipment using the different properties of the gas and liquid phases to characterize the bubble hydrodynamics. Among the types of the phase detection probes, the optical probe is the commonly used one as due to its high frequency acquisition rate and the stability of the signal (Barrau et al., 1999; Cartellier and Barrau, 1998). Various works utilized the optical probe to determine their gas holdup in their gas-liquid contactors (Bouaifi et al., 2001; Schweitzer et al., 2001). Some researchers also applied the signal change due to phase changing for estimation of bubble sizes and velocities (Mena et al., 2008; Pjontek et al., 2014). However, the bubble sizes and velocities determination using the optical probes have not been widely used because the probes have a drawback in terms of size measurement as it requires each bubble to collide to the probe tip where most of the bubbles do not pierce through the probe at the center of the bubble and the sizes determined by the probe are their chords not their diameter (Vejražka et al., 2010). Hence, for the bubble sizes and velocities the optical techniques are more preferable except for the conditions where the visibility is very low (Husted et al., 2009).

(b) Bubble sizes produced at orifices

There were several studies that determined bubble sizes generated at orifices. The force balance on a bubble when generated at a single orifice was the balance between buoyancy force and liquid surface tension force acting on the bubble. The balance was attributed to Tate, (1864), where derived the solution of the force balance. Afterwards, various literatures studied bubble formations and sizes at the orifice. Luo et al., (1998) added several forces for bubble growth at the orifice as shown in Figure 1.14, where the effective buoyancy force, F_B, and gas momentum force, F_M, and liquid drag, F_D, surface tension force, F_σ, bubble inertial force, $F_{l,g}$, and Basset force, $FBA)$ were considered. This study also concerned the effect of particles on the formation of the bubble that were the particle–bubble collision force, F_C, and the suspension inertial force, $F_{l,m.}$ The suspension inertial force is due to the acceleration of the liquid and particles surrounding the bubble.
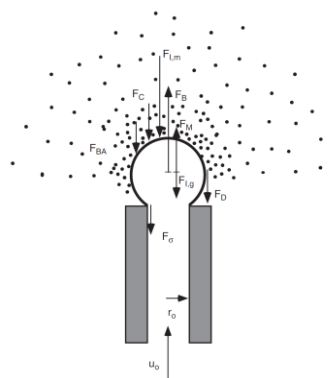
Figure 1.14 The balance of all the forces acting on a growing bubble (Yang et al., 2007)

However, the force balance derived as shown in Figure 1.14, is somehow difficult to use for the design purpose due to its complexity (Loubière et al., 2003; Loubière and Hébrard, 2004). According to Loubière and Hébrard (2004) and Loubière et al., (2003), bubble sizes depend on orifice type like flexible or solid, bubbling gas regime and liquid characteristics like surface tension and dynamic viscosity. For practical usage, several correlations are normally selected and used, depending on the condition.

Table 1.3 summarized correlations and their suitable conditions in bubble columns.

Table 1.3 Correlations for the size of bubbles produced at an orifice

Literature	Correlation	Suitable condition
Miller, (1974)	$d_b = \left[\dfrac{6\sigma d_0}{g(\rho_L - \rho_L)}\right]^{\frac{1}{3}}$	Low gas flow rate Viscosity around 1 cP
Davidson et al., (1960)	$d_b = 0.19 d_0^{0.48} Re_0^{0.32}$	Moderate to high gas flow rate Aqueous system d_0 is between 0.1 – 1 cm
Leibson et al., (1956)	$d_b = 0.18 d_0^{0.5} Re_0^{\frac{1}{3}}$	$Re_0 < 2000$
Kumar and Kuloor, (1970)	$V_b = \left(\dfrac{4\pi}{3}\right)^{\frac{1}{3}} \left(\dfrac{15\mu_L Q_g}{2\rho_L g}\right)^{\frac{3}{4}}$	Low gas flow rate (0.2-2.5 cm³/s)
Bhavaraju et al., (1978)	$\dfrac{d_b}{d_0} = 3.23 \left(\dfrac{4\rho_L Q_g}{\pi \mu_L d_0}\right)^{-0.1} \left(\dfrac{Q_g^2}{d_0^5 g}\right)^{0.21}$	Low to high gas flow rate μ_L = 1-1000 cp Good for design purpose
Park et al., (1977)	$V_b = \dfrac{\pi d_0 \sigma}{\Delta\rho g}$	Low gas flow rate
Gaddis and Vogelpohl, (1986)	$d_b = \left[\left(\dfrac{6d_0\sigma}{\rho_L g}\right) + \left(\dfrac{81\upsilon V_T}{\pi g}\right) + \left(\dfrac{135V_T^2}{4\pi^2 g}\right)^{\frac{5}{3}}\right]^{0.25}$	Moderate to high gas flow rate No obstruction in column
Pamperin and Rath, (1995)	$d_b = d_0 \sqrt{\Delta\rho \cdot \left(\dfrac{We}{We - 8}\right)} \sqrt{\dfrac{4}{Re_o} + \dfrac{0.124}{Re_o^{0.5}}}$	Moderate to high gas flow rate

Note that $Re_0 = \dfrac{4Q_g \rho_g}{\pi d_0 \mu_g}$

(c) Bubble size in the column

At the position far from the orifice, bubble sizes might be changed according to the liquid motions, liquid properties. The change of bubble sizes appears when the turbulence occurs in the column. Their sizes might be increased with liquid height due to bubble coalescence or reduced due to bubble break-up. There is an equilibrium size of bubbles which occurred due to the equality of coalescence rate and break-up rate. Note that the liquid motion is occurred due to the power dissipation of rising gas stream.

Three steps are presented in the bubble coalescence process: approach of two bubbles, thinning liquid film and rupture (Chaudhari and Hofmann, 1994). The film thinning is the rate controlling step since takes the longest time among all the steps. Pressure bubble sizes in the system and are one of the important factors. Larger sizes of bubbles have lower rate of film thinning as well as for the increase of pressure.

For bubble break-up, there are two causes, leading to the break-up of bubbles: instability of bubbles and bubble-solid collision. For the instability, Hinze, (1955) proposed the cause of bubble break-up via the dynamic pressure and the shear stresses on the bubble surface made by different liquid flow patterns, e.g., shear flow and turbulence. When the maximum hydrodynamic force in the liquid is larger than the surface tension force, the bubble breaks into smaller bubbles. This mechanism can be quantified using the liquid Weber number (We), represented as in Equation (1.23). When the Weber number (We) is larger than a critical value, the bubble is not stable and disintegrates.

$$We = \frac{\rho_L u_b d_B}{\sigma} \qquad (1.23)$$

When using dynamic pressure force to determine the size of the stable bubble in the column, it can be found that the equilibrium size of bubbles can be estimated from the following relation (Hughmark, 1967);

$$d_{Be} = 0.7 \frac{\sigma^{0.6}}{\left(\frac{P}{V}\right)^{0.4} \rho_L^{0.2}} \left(\frac{\mu_L}{\mu_g}\right)^{0.1} \quad (d_{Be} \ in \ m) \qquad (1.24)$$

With increasing gas flow, the liquid circulated by the power input from the gas phase will become turbulent and the break-up of bubbles will occur. The bubbles larger than the size predicted by Equation (1.24) will break up. However, at very high gas flow rates, equilibrium between break-up and coalescence will exist, and the equilibrium bubble size is in general larger than that of predicted.

Luo et al., (1999) considered the shear force by the centrifugal force in the column and proposed a criterion for bubble instability leading to correlation for bubble sizes as shown in Equation (1.25) and (1.26), for liquid and liquid-solid suspension conditions, respectively.

$$d_{b,max} = 2.53 \sqrt{\frac{\sigma}{g\rho_g}} \quad for \ liquid \ phase \qquad (1.25)$$

$$d_{b,max} = 3.27 \sqrt{\frac{\sigma}{g\rho_g}} \quad for \ liquid - solid \ suspension \qquad (1.26)$$

Bhavaraju et al., (1978) also found the equilibrium diameter differently depending on the liquid phase properties, Figure 1.15. When water was used as the liquid phase, when the gas flow rate increased, the bubble diameters were rose until a

point where the turbulence in the column was sharply raised by the liquid circulation. The bubble diameters were reduced due to the break-up of the bubble at high flow rate. However, when adding Carbopol that reduced the turbulence in the column, the break-up regime did not occur.
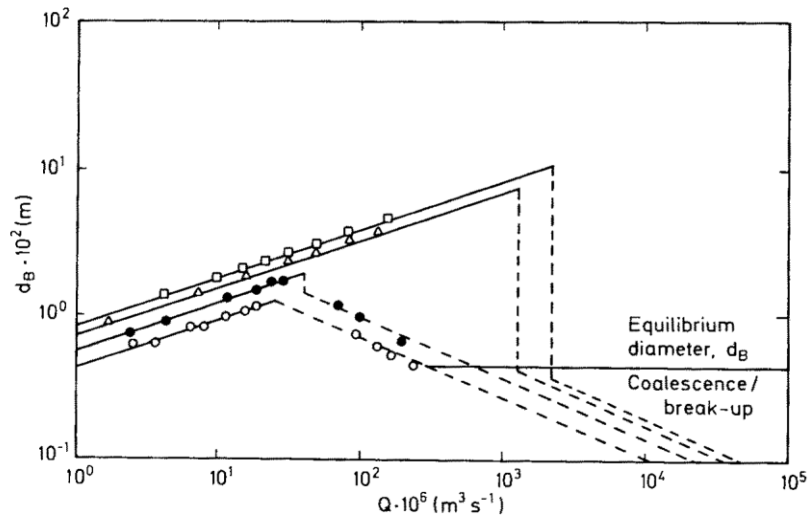
Figure 1.15 Bubble size far from the orifice in a bubble column
○ Water ● 0.10% Carbopol △ 0.15% Carbopol, □ 0.20% Carbopol
(Bhavaraju et al., 1978b)

Kumar et al., (1976) proposed a correlation for describing bubble diameter at the conditions approaching constant pressure at the orifice entrance, which simulates most industrial applications. For air at near atmospheric pressure sparged into inviscid liquids (11 ~ 100 cP), the correlation of Kumar et al. fits experimental data well. Their correlation is presented shown in Figure 1.16.
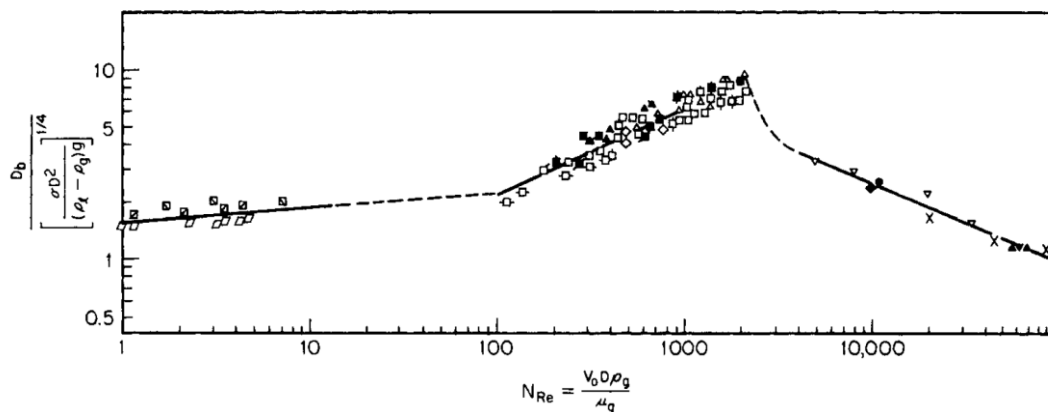
Figure 1.16 Bubble diameter correlation for air-liquid system
(Kumar et al., 1976)

Rather than the bubble instability itself, the bubble break-up could also occur due to the solid-bubble collision. The collisions have two different consequences: the

particle is ejected from the bubble surface, or the particle penetrates the bubble leading to either bubble breakage or non-breakage.

Clift et al., (2013) indicted that bubble–particle collisions generate perturbations on the bubble surface. After the bubble–particle collision, three factors become crucial in determining the breakage characteristics of the bubble: (1) shear stress, which depends on the liquid velocity gradient and the relative bubble–particle impact speed, and tends to break the bubble; (2) surface tension force, which tends to stabilize the bubble and causes it to recover the bubble's original shape; (3) viscous force, which slows the growth rate of the surface perturbation, and tends to stabilize the bubble.

When neglecting the shear effects due to the liquid flow, three criteria for particle penetration through a bubble were also proposed (Chen and Liang-Shin, 1989). The particle will penetrate the bubble when any of the following three criteria is satisfied. (1) the acceleration of the particle is downward; (2) the particle velocity relative to the bubble is downward; (3) the particle penetration depth is larger than the deformed bubble height. It was also analyzed by Boys' instability analysis (Boys, 1890) that when the particle diameter is larger than the height of the doughnut shape bubble, the bubble will breakup, When none of these criteria are satisfied, the particle will be ejected from the bubble surface upon contact with the bubble.

Hong et al., (1999) also showed that the bubble breakage mechanism due to solid collision depended on the liquid flow regime. For laminar regime, the bubble recovers its original shape; while in turbulence regime, bubbles were broken down. Hence, the bubble in water is disintegrated by the surface perturbations induced by the turbulent shear stress when the particle penetrates. This finding was also simulated and has a good agreement with the numerical simulation. Their simulation also shows a large resulting pressure oscillation, which could also contribute to bubble surface instability leading to its breakage.

(d) Bubble dynamics in a bubble column

(i) Bubble velocity

Bubble velocity is a crucial factor for the mass transfer in bubble columns since it represents the time that bubble spends in the column where the mass transfer is occurring. Several correlations were proposed at different conditions.

The basic correlation was developed using the force balance around a single spherical bubble. The buoyancy force, gravitation force, and drag force were included in the derivation. The force balance on a droplet was developed as shown in Equation (1.27). The equation consists of 3 terms: Accumulate momentum, gravity force along with buoyancy force, and drag force as shown in the equation below:

$$\left(\rho_g + \frac{1}{2}\rho_L\right)\left(\frac{\pi d_b^3}{6}\right)\left(\frac{dU_{rel}}{dt}\right) = \frac{\pi d_b^3}{6}\Delta\rho g - \frac{\pi d_b^2}{4}\frac{1}{2}\rho_L C_D U_{rel}^2 \qquad (1.27)$$

Where ρ_g and ρ_L are the density of gas and liquid, respectively, while d_b represents bubble diameter and C_D the drag coefficient. After rearranging the terms, the bubble relative velocity (U_{rel}) can be written as shown in Equation (1.28).

$$\left(\frac{dU_{rel}}{dt}\right) = \frac{U_{rel,t+\Delta t} - U_{rel,t}}{\Delta t} = \frac{\frac{\pi d_b^3}{6}\Delta\rho g - \frac{\pi d_b^2}{4}\frac{1}{2}\rho_L C_D U_{rel,t}^2}{\left(\rho_g + \frac{1}{2}\rho_L\right)\left(\frac{\pi d_b^3}{6}\right)} \tag{1.28}$$

By using explicit differential equation solving method, the velocity droplets at the considered time can be calculated. However, in order to perform velocity and distance analysis, the relation between distance, time, and droplet velocity can be calculated using Equation (1.29).

$$U_{rel,t} = \frac{\Delta x}{\Delta t} \tag{1.29}$$

When the bubble is flowing at laminar regime where Re <1, the bubble velocity can be estimated using Stoke's Equation, where;

$$C_d = \frac{24}{Re} \tag{1.30}$$

Where Re, is the Reynolds number represented by Equation (1.31).

$$Re = \frac{\rho_L u_b d_b}{\mu_L} \tag{1.31}$$

And the bubble velocity can be written as in Equation (1.32);

$$u_b = \frac{g\left(\rho_L - \rho_g\right)d_b^2}{18\mu_L} \tag{1.32}$$

This equation is very used when determining the small bubble where its shape is normally rigid and viscous effects are major. The drag force calculated by this equation assumed to be similar to those of small spherical solids where the drag coefficient is represented by Equation (1.24). However, when using with other condition, other drag coefficient correlation needed to be used instead of Stoke's Equation especially when non-rigid bubbles or large bubbles were presented in the system.

Table 1.4 Drag coefficient correlations

Researcher	Drag correlation	Comment
Schiller and Naumann, (1935)	$C_D = \begin{cases} 24\left(1+0.15Re^{0.687}\right)/Re & Re \le 1000 \\ 0.44 & Re > 1000 \end{cases}$	General use for all fluid-fluid pairs of phases
Morsi and Alexander, (1972)	$C_D = a_1 + \dfrac{a_2}{Re} + \dfrac{a_3}{Re^2}$ $a_1, a_2, a_3 = \begin{cases} 0, 24, 0 & 0 < Re < 0.1 \\ 3.690, 22.73, 0.0903 & 0.1 < Re < 1 \\ 1.222, 29.1667, -3.8889 & 1 < Re < 10 \\ 0.6167, 46.50, -116.67 & 10 < Re < 100 \\ 0.3644, 98.33, -2778 & 100 < Re < 1000 \\ 0.357, 148.62, -47500 & 1000 < Re < 5000 \\ 0.46, -490.546, 578700 & 5000 < Re < 10000 \\ 0.5191, -1662.5, 5416700 & Re \ge 10000 \end{cases}$	Covered all the range but less stable than other models
Grace et al. (1978)	$C_D = \max\left(\min\left(C_{D_{ellipse}}, C_{D_{cap}}\right), C_{D_{sphere}}\right)$ $C_{D_{sphere}} = \begin{cases} 24/Re & Re < 0.01 \\ 24\left(1+0.15Re^{0.687}\right)/Re & Re \ge 0.01 \end{cases}$ $C_{D_{cap}} = \dfrac{8}{3}$ $C_{D_{ellipse}} = \dfrac{4}{3} \dfrac{g d_p}{U_t^2} \dfrac{\left(\rho_q - \rho_p\right)}{\rho_q}$	well suited to gas-liquid flows
Tomiyama et al. (1999)	$C_D = \max\left(\min\left(\dfrac{24}{Re}\left(1+0.15Re^{0.687}\right), \dfrac{72}{Re}\right), \dfrac{8}{3}\dfrac{Eo}{Eo+4}\right)$ $Eo = \dfrac{g(\rho_q - \rho_p)d_p^2}{\sigma}$	well suited to gas-liquid flows
Ishii, (1979)	$C_D = \min\left(C_D^{vis}, C_D^{dis}\right)$ $C_D^{vis} = \dfrac{24}{Re}\left(1+0.15Re^{0.75}\right)$ $C_D^{dis} = \dfrac{2}{3}\dfrac{d_p}{\sqrt{\frac{\sigma}{g(\rho_q - \rho_p)}}}$	Boiling flow

Moreover, several works also focus on the empirical equation for the bubble velocity. Hadamard-Rybczynskil, Schugerl equation, Wilkinson Equation, Li and Prakash equation, for example (Kantarci et al., 2005). Furthermore, for liquid solid suspension, the rising velocity of bubbles can be estimated from Davies-Taylor equation;

$$u_b = \left(\frac{1.6\sigma g}{\rho_g}\right)^{\frac{1}{4}} \tag{1.33}$$

(ii) Gas holdup

Gas holdup is the fraction of gas volume in the column as shown in Equation (1.34).

$$\varepsilon_g = \frac{V_g}{V_g + V_L + V_s} \tag{1.34}$$

The gas holdup in bubble column has been investigated frequently by many researchers. Correlations were proposed based on the condition used in the researcher experiments. Kantarci et al., (2005) summarized these correlations in their review. Among the correlations, Equation (1.35) is a crucial equation that has a promising agreement with the experiment (Green and Perry, 2007) where the gas holdup can be estimated using gas superficial velocity (u_{sg}), bubble rising velocity (u_b), and liquid velocity (u_L). Note that Equation (1.35) imitates the correlation of Wallis (Isbin, 1970).

$$\varepsilon_g = \frac{Q_g}{A(u_b + u_L)} = \frac{u_{sg}}{u_b + u_L} \tag{1.35}$$

(iii) Specific interfacial area

The specific interfacial area (a) is the summation of interfacial area between bubbles and liquid phase. It can be represented as shown in Equation (1.36).

$$a = \frac{N_B \cdot S_B}{V_L} \tag{1.36}$$

Various approaches can be used to estimate the specific interfacial area. When the gas holdup is known, Equation (1.37) is normally used.

$$a = \frac{6}{d_b} \cdot \frac{\varepsilon_g}{1 - \varepsilon_g - \varepsilon_s} \tag{1.37}$$

The other approach is based on the bubble size, velocity, and the time that bubble spends in the column. The equation can be expressed as in Equation (1.38), where the specific interfacial area is the function of gas flow rate (Q_g), the bubble velocity (U_b), bubble diameter (d_b), and the column cross-sectional area (A).

$$a = \frac{6}{d_b} \frac{Q_g}{u_b A} \tag{1.38}$$

1.2.3 Improvement of bubble column hydrodynamics

(i) Solid phase addition

Moustiri et al., (2002) studied the effect of solid media on hydrodynamic parameters, which were gas hold up and bubble size. It was found that at gas velocity lower than 1 cm/s, gas hold up in absorption system was lower after adding solid comparing to conventional column. But for gas velocity over than 1 cm/s, the results were in contrast. The gas hold up was higher as solids were presented in the system. Moustiri explained that at low velocity of gas, solid was performed as contaminated in

system which reducing cross-sectional area of flow and increasing superficial velocity. However, for high velocity of gas, the solids were performed as the obstacles to rising bubble and made them stay longer in reactor which increases gas hold up. Nevertheless, Moustiri also found that solid media adding to absorption system delayed flow regime of fluid of homogeneous regime. It was found that without solid, the flow regime would convert from homogeneous to heterogeneous regime at velocity more than 4 cm/s. However, with presenting of solid, the heterogeneous regime was found when velocity was above than 6 cm/s.

Bhatia et al., (2004) researched similar to Moustiri et al., (2002) but including effect of solid media on mass transfer parameters. The researchers found that, with media presenting in the system, the rising velocity of bubbles were lower and result in higher value of gas hold up. In this work, the interfacial area (a) for media presenting system was higher but, however, mass transfer coefficient didn't change significantly.

There were others work involving with solid adding absorption system. Table 1.5 displays others researches work on adding solid into bubble column. In the table, operating condition are presented as well as the effect of solid media to percent change of hydrodynamic parameters and mass transfer coefficient.

Table 1.5 Summarized of literature review for solid media absorption

Researcher	Gas Superficial Velocity (m/s)	Solid Media Type	Solid Media Density (kg/m³)	Solid Media Size (mm)	Solid Media Conc (%v/v)	Change in Gas Hold Up (%)	Change in overall mass transfer coefficient (%)
Choi et al., (1996)	0.08	Glass beads	2517	0.069	0-5	-6 to 0 %	-
Garcia-Ochoa et al., (1997)	0.004-0.132	Glass beads and Pyrite	2400 and 4500	0.039-0.160	-	-10 to +42 %	-
Behkish et al., (2002)	0.01-0.16	Glass beads	2500	0.011	0-36	-	-72 to 0 %
Moustiri et al., (2002)	0.005-0.10	High-void Packing	-	-	0.092	-5 to + 45%	-
Bhatia et al., (2004)	0.005-0.10	High-void Packing	-	-	0.092	0 to +70%	0% to +5 %
Maldonado et al., (2008)	0.0012-0.0033	Glass cells	65-1576	1.8-10	Packed	Positive and Negative	-
Ferreira et al., (2010)	0-0.0072	EPS, PVC	1040,1350	0.210-0.549	0-5	-	-42 to 0 %
Mena et al., (2011)	0-0.0027	EPS	1040	0.5-1.1	0-30	-	-80 to 0%

As seen in table 1.5, most of work indicated that adding solid media into reactor reduced gas hold up or mass transfer coefficient which contrasted with Moustiri et al (2002) and Bhatia et al (2004) works where larger solid media are involved.

Maldonado et al., (2008) also researched on characteristic of packing media that affected on hydrodynamic and mass transfer parameters. This work used air-water as the representative of absorption system. It was found that, gas hold up was raise as solid media presenting in the system. However, gas hold up was lower as function of void fraction of media or size of media. Maldonado claimed that, porosity and size provided more contact area between media and bubble and also forms surface tension force as illustrated in Figure 1.17. The surface tension force which occurring when bubble contact with solid would have the direction opposite to rising velocity which will reduce their rising velocity and result in higher gas hold up.
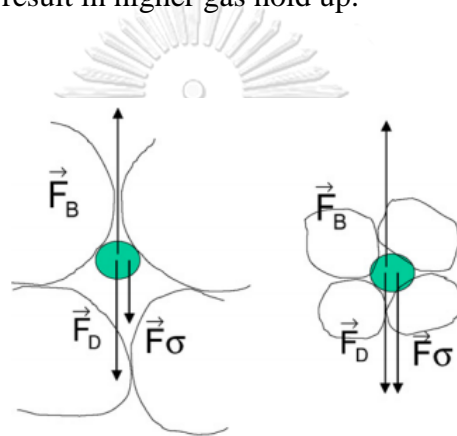
Figure 1.17 Surface Force acting on bubble surface comparing between
high void fraction (Left) and low void fraction (Right)
(Maldonado et al, 2008)

Maldonado either claimed that media presenting in this research didn't affect the size of bubble diameter, but overall mass transfer coefficient was higher as superficial of gas velocity increase. However, for small media (Low void fraction) would lower the mass transfer coefficient because media would affect rising velocity and resulted in lower mass transfer coefficient following Higbie equation, which will be detailed in Equation (1.45).

1.2.4 Mass transfer

Mass transfer from bubbles can be classified into two classes. Mass transfer from small bubbles, which their surfaces are rigid, and from large bubbles where their surfaces are oscillating while moving in bubble columns (Sardeing et al., 2006).

For bubble smaller than 1.5 mm, their surfaces are still rigid due to the pressure inside the bubbles. Therefore, the mass transfer can be estimated via Frossling, (1938) and Calderbank and Moo-Young, (1961) as desbribed in Equation (1.39) and (1.40),

respectively. Note that the Sc in the equation represents Schmidt number which can be computed using Equation (1.41), where D is the diffusion coefficient.

$$k_L = \frac{D}{d_b}\left(2 + 0.6Re^{1/2}Sc^{1/3}\right) \tag{1.39}$$

$$k_L = 0.31\left(\frac{g\mu_L}{\rho_L}\right)^{1/3} Sc^{-2/3} \tag{1.40}$$

$$Sc = \frac{\mu}{\rho D} \tag{1.41}$$

For larger bubbles (more than 3.5 mm), the surfaces of those bubbles are movable and less sphere-like. The oscillating regime is occurred when the bubbles are rising in the column. The mass transfer coefficient of bubbles in this regime can be estimated using several equations.

$$Sh = \frac{k_L d_b}{D} \tag{1.42}$$

Hadamard, (1911) proposed a set of equation where the Sherwood number (Sh), Equation (1.42), are derived as a function of Re and Sc and summarized in Table 1.6.

Table 1.6 Hadamard correlation of mass transfer of mobile-case bubbles

Reynolds number	Correlation
Re <1	$0.65\,Pe^{0.5}$
10 < Re < 100	$Sh = 0.65Pe^{0.5}\left(1 + \dfrac{Re}{2}\right)^{0.5}$
100 < Re < 1000	$Sh = 1.13\left(1 - \dfrac{2.9}{Re^{0.5}}\right)^{0.5} Pe^{0.5}$
Re > 1000	$Sh = 1.13Pe^{0.5}$

In addition, Hughmark, (1967) proposed a useful equation for determining the k_L for bubbles in case of both single bubble and bubble swarms. The equation can be expressed in Equation (1.43), where C_1 is equal to 0.061 and 0.0187, for a single bubble and bubble swarm, respectively.

$$Sh = 2 + C_1\left[Re^{0.484}Sc^{0.339}\left(\frac{d_b g^{1/3}}{D^{2/3}}\right)^{0.072}\right]^{1.61} \tag{1.43}$$

Calderbank and Moo-Young, (1961) also proposed the mass transfer coefficient correlation for the mobile case. It is the function of liquid and gas density, viscosity, and Sc as shown in Equation (1.44).

$$k_L = 0.42 \left(\frac{(\rho_L - \rho_g)\mu_L g}{\rho_L^2} \right)^{1/3} Sc^{-1/2} \qquad (1.44)$$

In addition, the Higbie penetration model (Higbie, 1935) can also be applied for the estimation of k_L as shown in Equation (1.45), where t_e is the time of exposure which expressed in Equation (1.46).

$$k_L = 2\sqrt{\frac{D}{\pi t_e}} \qquad (1.45)$$

$$t_e = d_b/u_b \qquad (1.46)$$

1.2.5 Pressure drop in bubble column

Pressure drop in the bubble column is mostly dominated by the formation of bubbles at the bubble column's orifices and the liquid pressure on top of the orifices as can be expressed as in Equation (1.47).

$$\Delta p_{Total} = \Delta p_w + \rho_L g H_L \qquad (1.47)$$

The orifice pressure drop (Δp_w) or wet plate pressure drop is mostly depending on the configuration of orifices, gas properties, and gas flow rate. According to Thorat et al., (2001), the Δp_w is the function of gas flow rate, orifice size diameter, gas density, surface tension, and orifice arrangement which are orifice diameter to orifice thickness ratio and pitch to orifice diameter ratio.

1.3 Spray column

1.3.1 Fluid dynamics in spray column

The fluid dynamics in spray column can be depicted as in Figure 1.18. The liquid is fed into column by a nozzle where there is a reduction in cross-sectional area. The energy loss in from the reduction causes the turbulence to occur in the near region where the liquid is break-down into several droplets.
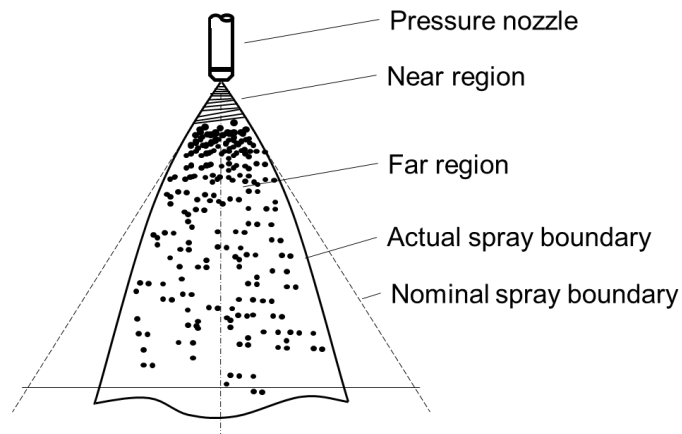
Figure 1.18 Fluid dynamic notation in spray system

      The droplets settled downwards in the column in the counter-current regime to the gas phase moving up in the column. In the far region, droplets have an actual boundary depending on the types of the nozzle used in the system. Figure 1.19 shows the type of nozzle that used for sprays. For the mass transfer purpose, the full-cone type is preferred since it requires as much as possible droplets to cover the column area.
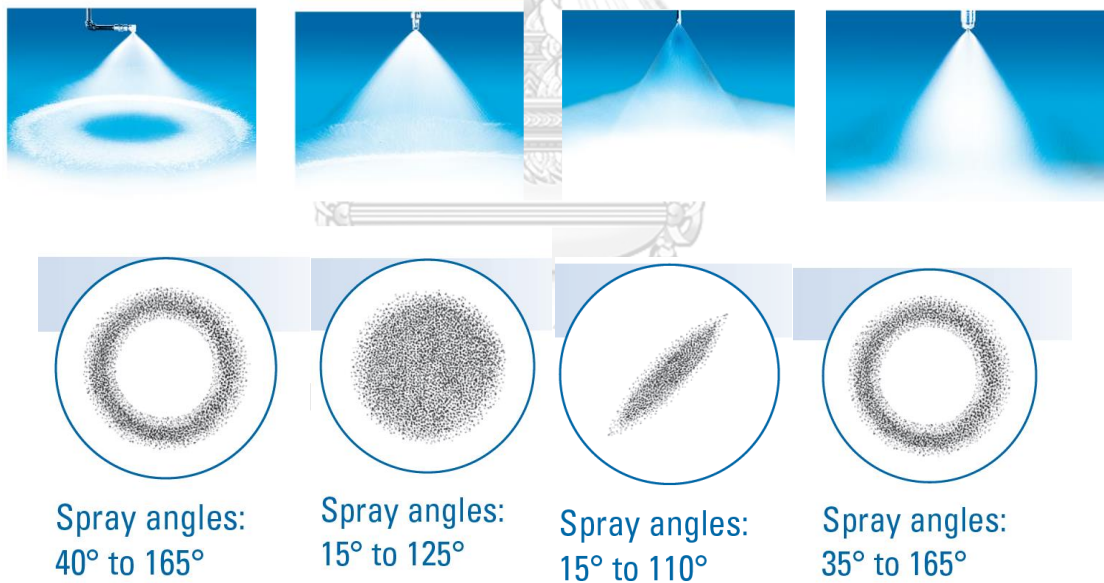
Figure 1.19 Types of nozzles for spray systems
(Left to right) Hollow cone, full cone, flat cone, and atomization
("Experts in Spray Technology | Spraying Systems Co.," n.d.)

1.3.2 Droplet hydrodynamics

(a) Characterizing methods

There are various techniques that can be used to determine droplet hydrodynamics in spray conditions. The common optical techniques are the basic one that widely used to determine both droplet sizes and velocities using CCD or CMOS camera. However, there are specific conditions rather than the bubble hydrodynamics since the droplets are mostly smaller and move faster than the bubbles. Hence, the cameras and their setups that able to use for this purpose required a very high capture framerate and high resolutions. Furthermore, various image processing techniques were also developed based on the captured images from the cameras. Droplet Tracking Velocimetry (DTV) is one of the image processing techniques that commonly uses to determine both droplet sizes and velocity for each consecutive frame captured by the camera (Hess and L'Esperance, 2009; Husted et al., 2009; Stevenin et al., 2016a).

Besides of the optical techniques, a phase-doppler based technique using the light scattering principle or Phase Doppler Anemometry (PDA) is also one of the preferred techniques that widely used for the determination of droplet sizes and velocities. The PDA measurements are performed on single particles and statistically determine the size and velocity of each droplets as well as particle concentration and local size-velocity correlation. Various of researches use this technique to determine droplet sizes and velocities in their works (Bhatia et al., 1988; Edwards and Rudoff, 1991; Pitcher et al., 1991; Sommerfeld, 1998). It should be noted that the PDA and most of the optical techniques encounter difficulties when used with dense spray or in conditions of poor visibility (Husted et al., 2009).

Phase detection probe is one of the techniques that can overcome such difficulties when used with dense spray or in conditions of poor visibility (Husted et al., 2009). It was first pioneered by (Neal and Bankoff, 1963) as a technique for measuring multiphase flow characteristics. Since then, the probe has been widely used for the characterization of both gas phase dispersed in a liquid phase (Cartellier and Achard, 1991). Various works utilized the phase detection probes to determine the hydrodynamic of the air-water system, especially for high-velocity free surface flow (Felder and Chanson, 2015; Felder and Pfister, 2017; Zhang and Chanson, 2018).
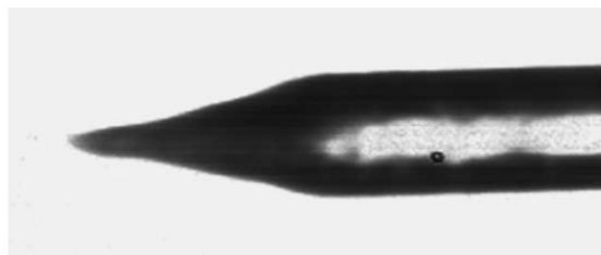
Figure 1.20 Image of the tip of a conical optical probe
(Hong et al., 2004)

However, these probes have rarely been used in spray systems since responding to small, high velocity droplets in such conditions requires an extremely high acquisition rate. However, the optical probes have now overcome the difficulty. Various types of the optical probes have been considered for observing droplet hydrodynamics and the most suitable type for using in spray systems has been found to be the monofiber probe, as shown on Figure 1.21, as its small size extends its ability to detect small droplets (Hong et al., 2004; Saito, 2017).
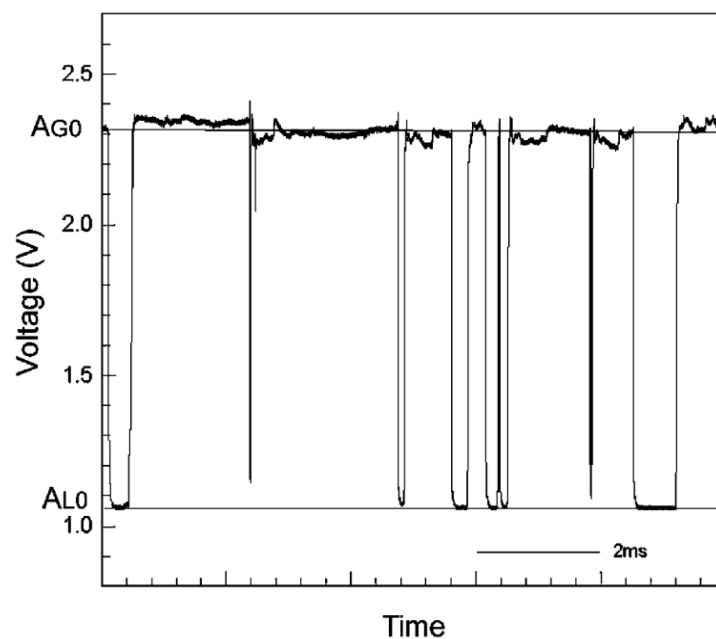
Figure 1.21 Raw signal delivered by a conical probe in a spray
(Hong et al., 2004)

The principle of the probe for determining the droplet hydrodynamics is based on the refractive index of the phase where the probe is located (Abuaf et al., 1978); different light intensity is sent back to a detector when the probe is exposed to different phases. Therefore, when a droplet collides with the probe, the detected light intensity changes due to the change in the phase covering the probe, as shown in Figure 1.21. Consequently, the droplet velocity and size can be determined from the change of the light intensity over the time that the droplet spends on the probe.

There are two types of optical probes that can be used for spray systems: dewetting probe and light interference probe. For the dewetting probe, the velocity is proportional to the liquid dewetting time (T_R) that is the time the voltage rises from the liquid level (A_{L0}) to gas level (A_{G0}) as shown in Figure 1.21. For the interference probe, the light reflection and interference are used to determine to droplet velocity. These methodologies will be detailed in Chapter 2.

A major advantage of the probe is that it not only delivers velocity and size distributions but can also be used to directly determine the dispersed phase

characteristics of sprays, such as liquid fraction or droplet density. Most of the utilizations of optical probes on sprays nowadays concern only the liquid fraction. Although the methodology exists, few works have used the technique to measure droplet sizes or velocities (Marty et al., 2013; Valero and Bung, 2017), especially in cases of gas absorption; the optical probe is rarely used to determine the droplet hydrodynamics in actual spray conditions.

(b) Droplet size generated at nozzles

There are four mechanisms for generating droplets from liquid: (1) droplet in a field with high turbulence, (2) simple jets at low velocity (3) expanding sheets of liquid at relatively low velocity, and (4) droplet in a steady field of high relative velocity (droplet-solid collision).

Among all the mechanism, the breaking up in a highly turbulent field is the dominant process in spray regime since this mechanism is the one that gives the smallest drop size (Green and Perry, 2007). Many applications for sprays involve a three-step process with high velocity first tearing wave crests away from liquid sheets, followed by breakup of ligaments into large droplets, followed by breakup of the large droplets.
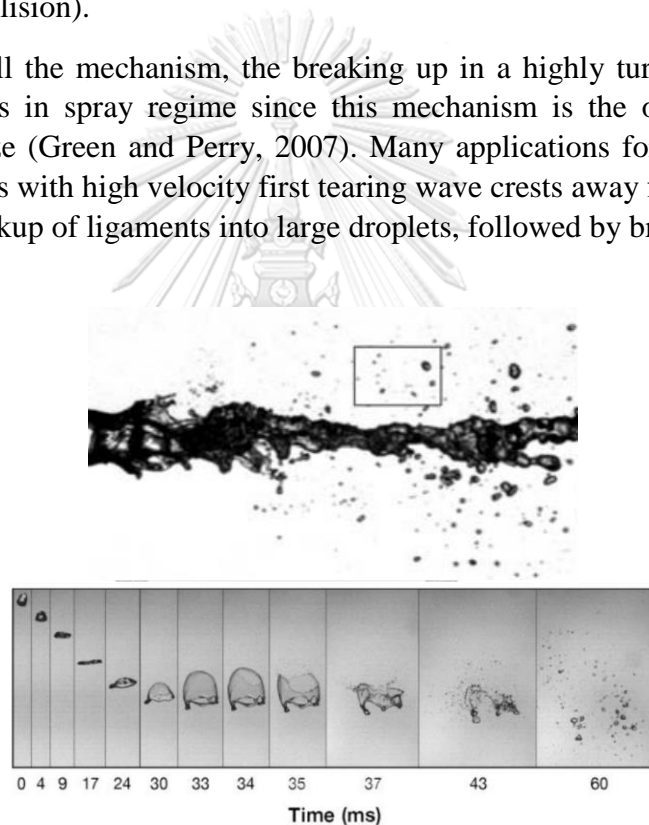
Figure 1.22 (Left) Ligament breakup into small droplets (Marmottant and Villermaux, 2004) and (Right) Breakup of a 5 mm droplet into smaller droplets (Villermaux, 2007)

Hinze, (1955) applied turbulence theory to obtain Equation (1.48) and took liquid-liquid data to define the coefficient, where ε is power dissipation (W/kg), σ is surface tension (N/m), and ρ_g is gas density(kg/m^3).

$$d_{D,max}(m) = 0.725 \frac{\left(\frac{\sigma}{\rho_g}\right)^{0.6}}{\varepsilon^{0.4}}$$

(1.48)

Lehrer, (1975) also proposed another correlation that can be used for estimation of maximum droplet size.

$$d_{D,max} = \left[\frac{16\sigma}{(\rho_L - \rho_g)g}\right]^{0.5} \tag{1.49}$$

(c) Droplet size far from the nozzle

Since a spectrum of droplets are produced at the orifice. It is recommended to have a value that represents the entire droplets. For the spray regime, the Sauter mean diameter (d_{32}) is normally used. D_{32} is the ratio of surface to volume of total drop population. Walzel (1993) proposed that, the size of droplets can be estimated from the d_{max} that calculated from power/mass relationship as shown in Equation (1.50).

$$d_{D,32} = 0.3 \cdot d_{D,max} \tag{1.50}$$

In addition to the Walzel correlation, there are various correlations published the droplet size as summarized in Table 1.7, where most of the droplet correlations relate with liquid Reynolds number and the orifice sizes.

Table 1.7 Droplet size correlations

Researcher	Correlation
Murty's correlation (Roustan, 2003)	$d_D = 57 Re_j^{-0.48} We^{-0.18} d_{nozzle}$
Duffie and Marshall (Nicholas P. Cheremisinoff, 1986)	$d_D = 36 d_0^{0.56} Re_j^{-0.10}$
Kataoka-Ishii correlation (Kataoka et al., 1983)	$d_D = 0.28 \frac{\sigma}{\rho_g}\left(\frac{A}{Q_g}\right)^2 Re_L^{-\frac{1}{6}} Re_g^{\frac{2}{3}} \left(\frac{\rho_g}{\rho_L}\right)^{-\frac{1}{3}} \left(\frac{\mu_g}{\mu_L}\right)^{2/3}$

Note: $Re_j = \frac{u_o D_o \rho_L}{\mu_L}$, $We = \frac{u_o \mu_L}{\sigma_L}$ and A is cross-sectional area of the column

(d) Droplet dynamics in spray column

(i) Droplet velocity

In order to determine droplet velocity, the force balance similar to those of represented in Equation (1.27)-(1.29) are also applied. However, the drag coefficient (C_d) is different from the bubble cases. Table 1.8 shows the correlations that typically used in the droplet system.

Table 1.8 Different air drag coefficient (C_d) of droplets

Researcher		Correlation
Bird et al., (2007)	Re ≤ 0.1	$C_d = \frac{24}{Re}$
	2 < Re ≤ 500	$C_d = \frac{18.5}{Re^{3/5}}$
	500 < Re ≤ 20,000	$C_d = 0.44$
Park et al., (1983)	Re ≤ 1000	$C_d = \frac{24}{Re}(1 + 0.15Re^{0.687})$
	Re > 1000	$C_d = 0.438\left(1.0 + 0.21\left[\left(\frac{Re}{1000}\right) - 1\right]^{1.25}\right)$
Fukui et al., (1980)	Re ≤ 128	$C_d = \frac{33.3}{Re} - 0.0033Re + 1.2$
	128 < Re ≤ 1440	$C_d = \frac{72.2}{Re} - 0.0000556Re + 0.48$
	Re > 1440	$C_d = 0.45$
Yevgeny Isa, (1976)	Re ≤ 1.0	$C_d = 0.45$
	1.0 < Re ≤ 800	$C_d = \frac{12.5}{\sqrt{Re}}$
	800 < Re ≤ 1600	$C_d = 0.50 - 0.55$
	Re > 1600	$C_d = 3\ x\ 10^{-4}Re$
Isbin, (1970)	Re ≤ 1000	$C_d = \frac{24}{Re}(1 + 0.15Re^{0.687})$
	Re > 1000	$C_d = 0.44$
Yan et al., (2010).	Re ≤ 800	$C_D = \frac{24}{Re}\Big(1 + 0.15Re^{0.687} + \frac{0.0175}{1+4.25x10^4Re^{-1.16}}\Big)$
	800 < Re ≤ 1600	$C_D = 0.5$
	Re > 1600	$C_D = 3\ x\ 10^{-4}Re$

(ii) Liquid holdup or liquid fraction

The liquid fraction (ε_L) is the fraction of liquid volume (V_l) in respected to the summation of itself, gas volume (V_f) and solid volume (V_s) as shown in Equation (1.51).

$$\varepsilon_L = \frac{V_l}{V_g + V_l + V_s} \tag{1.51}$$

In order to estimate the liquid fraction in spray columns, unlike bubble columns, it requires a phase detection probe in order to determine the liquid fraction of spray column. One of the phase detection probes that normally uses in spray system is the optical fiber probe. It could determine if it is covered by the liquid phase or the gas phase. Hence, by measuring for a certain time that can represent the steady fluid dynamics in the column, the local liquid fraction at the point placing the optical probe can be estimated using Equation (1.52), where T_L is the time that liquid covered the probe tip while T_{total} is the total time used for the measurement. Various authors have utilized this advantage for the determination of the liquid fraction in their works (Stevenin et al., 2016a, 2016b).

$$\varepsilon_{L,local} = \frac{\sum T_L}{T_{total}} \tag{1.52}$$

This liquid fraction was further used to determine the specific interfacial area of the spray column. The average liquid fraction can be obtained by integrating the value throughout the cross-sectional area of the column which can be expressed as in Equation (1.53).

$$\varepsilon_{L,Avg} = \frac{1}{\pi R^2} \int_0^R \varepsilon_L(r) \, 2\pi r \, dr \tag{1.53}$$

where r in the equation refers to the radius from the center of cross-sectional area of the column while R represents the radius of column. The ε_L is the local liquid fraction at the distance r from the center. Note that the symmetry of spray cone was assumed for this calculation.

(iii) Specific interfacial area

Normal spray condition

For the spray column, there were 2 equations that can be used to represent the specific interfacial area of the column. The first methodology was based on the same approach used for the interfacial area calculation of bubble column, Equation. The mimic of the equation is expressed in Equation (1.54), where d_d is the droplet Sauter mean diameter.

$$a = \frac{6}{d_d} \cdot \frac{\varepsilon_L}{1 - \varepsilon_l - \varepsilon_s} \tag{1.54}$$

The other approach is based on the droplet size, velocity, and the time it spends in the column. The equation can be expressed as in Equation, where the specific interfacial area is the function of liquid flow rate (Q_L), the relative droplet velocity (U_E), droplet diameter (d_d), and the column cross-sectional area (A).

$$a = \frac{6}{d_d} \frac{Q_L}{U_E A} \tag{1.55}$$

Both approaches were used in order to determine the specific interfacial area of the spray system.

Packing spray condition

For the specific interfacial area of packing, the effective area is not the same value since the liquid does not cover the full packing surface. In order to estimate the effective area of packing, the Onda's method is used (Onda et al., 1968). After calculated the effective specific interfacial area of packing (a_w) and non-collision droplets (a_d), the total interfacial area (a_{Total}) can be determined using Equation (1.56).

Their correlation was based on large amount of data on gas absorption and distillation. The equation for the effective area is:

$$\frac{a_w}{a} = 1 - \exp[-1.45 \left(\frac{\sigma_c}{\sigma_L}\right)^{0.75} \left(\frac{L_w^*}{a\mu_L}\right)^{0.1} \left(\frac{L_w^{*\,2}a}{\rho_L^2 g}\right)^{-0.05} \left(\frac{L_w^{*\,2}}{\rho_L \sigma_L a}\right)^{0.2} \qquad (1.56)$$

Where L_w^* is liquid mass flow per unit cross-sectional area (kg/m^2.s), ρ_L is liquid density (kg/m^3), μ_L is liquid viscosity (Pa s), σ_L is liquid surface tension (N/m), σ_C is critical surface tension of packing material, which equals to 75 mN/m for steel packing, a is actual specific interfacial area (m^{-1}), and a_w is effective specific interfacial area (m^{-1}).

1.3.3 Mass transfer

Similar to those of bubbles, the mass transfer in the spray column occurs at the interface between droplets and the gas phase. Hadamard, (1911), Table 1.6, can also be applied for the gas-liquid dispersion in case of droplets. Moreover, Saboni (1991) also proposed a correlation for liquid phase used in droplet system, which represented by Equation (1.57).

$$Sh_L = 0.8 Re_i^{0.5} Sc_L^{0.5} \qquad (1.57)$$

Where:

$$Sh_L = \frac{k_L d_d}{D} \qquad (1.58)$$

$$Sc_L = \frac{\mu_L}{\rho_L D} \qquad (1.59)$$

$$Re_i = \frac{U^* d_D \rho_L}{\mu_L} \qquad (1.60)$$

The surface friction velocity (U^*) can be calculated using Equation (1.61), where the shear stress (τ_s) is represented by Equation (1.62).

$$U^* = \sqrt{\frac{\tau_s}{\rho_L}} \qquad (1.61)$$

$$\tau_s = \frac{1}{2}\rho_g u_D^2 C_D \qquad (1.62)$$

Moreover, several correlations also published by researchers as summarized in Table 1.9.

Table 1.9 Correlations for mass transfer of droplets (Nicholas P. Cheremisinoff, 1986)

Researcher	Correlation
Froessling	$Sh = 2 + 0.552Re^{0.5}Sc^{0.33}$
Ranz and Marshall	$Sh = 2 + 0.6Re^{0.5}Sc^{0.33}$
Ahmadzadeh and Harker	$Sh = 3(0.345d_D - 0.744)Re$
Srikrishna et al.	$Sh = 2 + 0.37Re^{0.577}Sc^{0.333}$

1.3.4 Pressure drop in spray column

Pressure drop in the spray column is mostly occurred at the nozzle of the spray. According to Bernoulli's formula, the pressure loss was due to the energy conservation that occurring when the liquid flow from a large to small cross-sectional area which results in higher velocity of liquid flow. Consequently, from the energy conservation, the pressure is converted to the velocity leading to the lower pressure which can be implied as the pressure drop (PNR, 2007). Moreover, the sudden contraction at the orifice also causes a minor head loss for the fluid. When integrating the pressure loss and the minor head loss, the total pressure drop due to the liquid flow through the nozzle can be estimated. Equation (1.63) and (1.64) show the Bernoulli's formula that included the energy loss due to the sudden contraction ($K\rho V^2/2$) and the contraction coefficient (K) calculation, respectively (McCabe et al., 2005).

$$p_1 - p_2 = \frac{\rho V_2^2}{2} - \frac{\rho V_1^2}{2} + \rho g(z_2 - z_1) + \frac{K\rho V^2}{2} \tag{1.63}$$

$$K = 0.5\left(1 - \frac{A_2}{A_1}\right) \tag{1.64}$$

From the equation, it can be summarized that the pressure drop occurring due to the liquid flow through the nozzle depends on the liquid flow rate, which corresponding to liquid velocity; liquid density, orifice diameter to pipe diameter ratio (A_2/A_1), as well as the contraction regime inside the orifice diameter.

1.4 Absorption of CO_2

1.4.1 General information

Gas absorption is commonly used in various purposes. The frequently-used application for the gas absorption is the aeration in aerobic wastewater treatment, the recovery of the valuable chemical and the removal of the impurities from a valuable gas such as sulfur dioxide removal or n-hexane recovery from industrial exhaust gas. Carbon dioxide capture from electricity generation process or the natural gas stream is also one of the main applications of the absorption using in the industrial process (Seader et al., 2010).

Carbon dioxide capture and storage is the process that prevents waste carbon dioxide (CO_2) from exposing to atmosphere (Fanchi and Fanchi, 2016). Normally, CO_2 is the reaction product from combustion, which is used to create energy from fossil fuel; the emission of the waste CO_2 causes global warming as well ocean acidification. In order to avoid these problems, the CO_2 is then captured before exposes to the atmosphere and stored in suitable sites, preventing from contact with the atmosphere.

Absorption is the process that transfers substances from gas phase to liquid phase thanks to the difference concentration between both phases. Nowadays, absorption process is the most dominant technology using for carbon capture. The process flow diagram of absorption process is as shown in Figure 1.23.
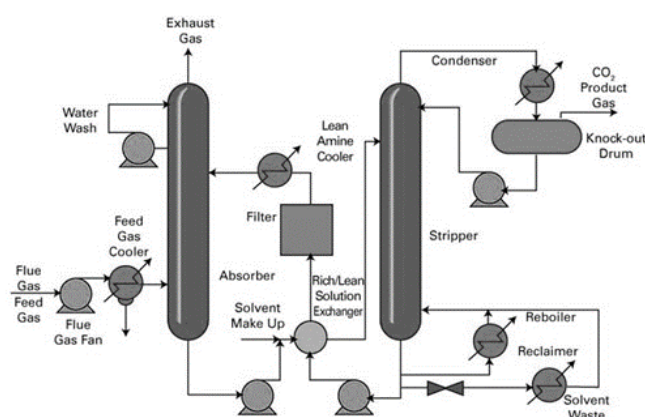
Figure 1.23 Process flow diagram of absorption process using amine as absorber (Dsong, 2013)

Normally, absorption process contains two units, absorber and stripper. The absorber is used to transfer CO_2 from gas phase to liquid phase in order to purify flue gas. The liquid that absorbed the CO_2 is then transport to the stripper, which is the process using the change of CO_2 solubility in liquid phase when the temperature is changed, to separate CO_2 from the liquid phase. The CO_2-free liquid phase is consecutively use as solvent again for the absorber.

Several liquid phases can be used to absorb CO_2 from flue gas. Among all of the liquid, amines derivatives are the most dominant solvent using for CO_2 absorption due to its efficiency and ability to regenerate (Kohl and Nielsen, 1997).

1.4.2 Liquid solvent for chemical absorption of CO_2

There are various liquid solvents that can be used to absorb CO_2. The absorption of CO_2 is normally a chemical absorption; however, the rate of the reactions might be too slow and can be considered as a physical absorption, depending on the solvents used. Water, hydroxide, carbonate, ammonia and alkanolamines are commonly used as solvents for CO_2 absorption. In the industrial application, the alkanolamines, carbonate, and hydroxide are the major chemical that used for the CO_2 capture. Both physical and chemical absorptions can be undergone in the absorption process depending on types

of solvents and their concentration. Generally, for water or low concentration chemical, the physical absorption is dominant in the system.

When considering the chemical absorption rate of CO_2, Vázquez et al., (2000) applied Danckwerts method, Equation (1.65), to analyze interfacial area and mass transfer coefficient. The carbon dioxide was absorbed using sodium Carbonate-Bicarbonate (Na_2CO_3-$NaHCO_3$) solution. Vázquez found that, mass transfer coefficient as well as interfacial area were incrased as function of gas flow rate, surface tension as well as decrasing orifice or bubble diameter. Note that, in the equation, R_A is absorption rate, C^* is concentration at equilibrium, a is the specific interfacial area, k_L is the mass transfer coefficient, k_1 is Pseudo-first order reaction coefficient and D_A is the diffusion coefficient of CO_2.

$$R_A = C^* a \sqrt{k_L^2 + k_1 D_A} \tag{1.65}$$

Wei-rong et al., (2004) also applied Danckwerts equation for studied interfacial area, mass transfer coefficient and overall mass transfer coefficient of CO_2 in Na_2CO_3-$NaHCO_3$. This research added catalyst sodium arsenite ($NaAsO_2$) as well as surfactant Dodecyl Benzene sulfonate (DBS) in the absorption process. The experiments were conducted in different temperature conditions and was found that at high velocity of gas, interfacial, mass transfer coefficient, and overall mass transfer coefficient were increased. Moreover, it also found that at higher temperature, the interfacial area of absorption was decreased due to lower surface tension force. The increasing in temperature resulted in increasing mass transfer coefficient because high temperature increased molecule activities and resulted in higher velocity of transfer. Moreover, at higher concentration of surfactant, mass transfer coefficient was lower due to layer of surfactant was surround bubble and obstructed diffusing gas in absorption process.

1.5 Conclusion

According to the review, information regarding hydrodynamics and mass transfer in bubble column and spray column exits for both local and global scales. However, the direct comparison between bubble and spray column in terms of hydrodynamics, mass transfer and specific power consumption is still in needed in order to select an appropriate equipment to use in the industrial processes. In addition, the presence of solid phase in bubble and spray column has a great potential to promote the mass transfer in the column. Hence, this thesis aims to manipulate a new experiment and techniques to better characterize the hydrodynamic and the mass transfer of these contactors.

Chapter 2

Optical fiber probe for spray characteristics

2.1 Abstract

This chapter describes the performance of an optical fiber probe on hydrodynamics parameters investigation of sprays. Two types of optical probes were studied: a de-wetting probe and an interference probe. Both probes had different methodologies to determine droplet hydrodynamics. The results were compared with a high-speed camera in order to visualize and analyze advantages and drawbacks of each equipment. A part of this chapter had been presented and published in the GLS-13 conference in Bruxelles in 2017. Moreover, the results of the performance determination of the de-wetting probe, have been submitted in the Industrial & Engineering Chemistry Research Journal.

2.2 Introduction

Optical fiber probe is one of a technique that nowadays able to apply for determination of droplet hydrodynamics. Although the optical fiber probe has already been used for the investigation of bubble hydrodynamics, the utilization on droplets has lately developed. Several literatures studied on the optical fiber probe performance, but the actual spray condition has not been investigated. Hence, the objective of the work presented here is to identify the performance of two types of optical probes, which use different methodologies, in an actual spray system, compared with that of a high-speed camera in order to verify the probe performance and methodology visually. The two types of optical probes used in this study were a de-wetting probe and a light interference probe. In the first section, a series of droplets produced by a syringe as a nozzle was investigated. The objective of this part is to compare the accuracy of the optical probes when the same droplets are observed with a high-speed camera. Afterwards, a comparison experiment will be conducted in actual spray conditions using two orifice sizes of industrial nozzles. The limits of the probes, including the maximum velocity they can measure, the smallest size of droplets that can be detected as well as droplet frequency approaching the probe, are analyzed and discussed.

2.3 Methodology

The experiment consisted of two parts: the investigation of the series of droplets, and the investigation of actual sprays. Note that the "investigation" refers to the recording of information about the hydrodynamics of droplet using a high-speed camera or an optical probe. The details of each part are described as the following.

2.3.1 Experimental setup

(a) Acquisition of series of droplets
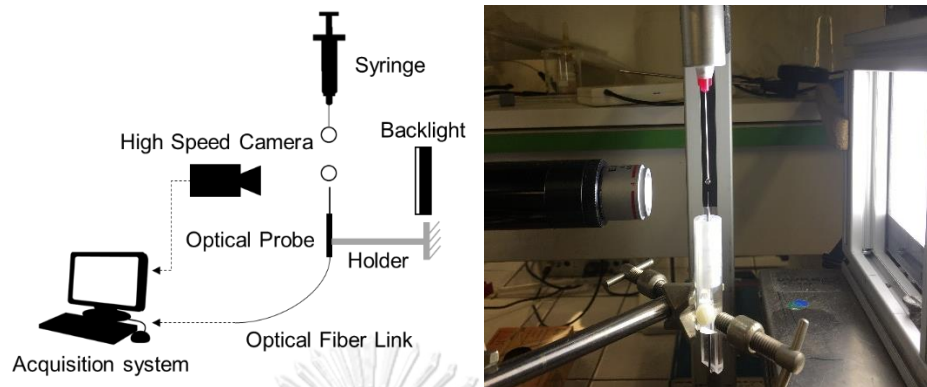
Figure 2.1 Experimental setup for acquisition of the same droplets

The experiment was set up as shown in Figure 2.1. A syringe with a 0.5 mm tip size was positioned above a monofiber optical probe (A2 Photonic Sensors, France). The syringe was filled with tap water and it could produce thanks to syringe pump, droplet sizes between 0.5 and 1.0 mm at a flow rate of 0.128 mL/s. After the injections, the droplets produced with the syringe settled and came into contact with an optical probe. The signal from the probe was sent to the data acquisition system and analyzed by its software. Two types of optical probes from A2 Photonic Sensors, (France) were assessed: de-wetting probe and light interference probe. A high-speed camera (Vision Research, Miro – M110, USA) was also set up to capture the trajectories of droplets, including their contacts with the optical probe. The detail of photo capturing will be detailed later in Section 2.3.3. The signal from the optical probe and the photos of each droplet as it moved were then analyzed to determine its size and velocity. The results from the two techniques were compared to evaluate the probe accuracy.

(b) Acquisition of sprays
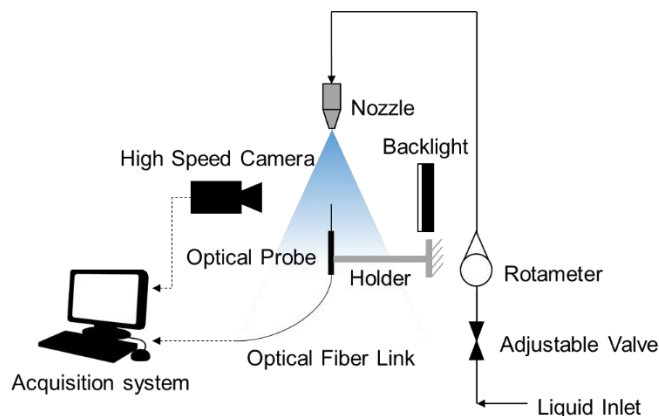
Figure 2.2 Experimental setup for acquisition of a spray condition

The experimental setup is schematically depicted in Figure 2.2 and visually illustrates in Figure 2.3. The water was fed through a spray nozzle at a flow rate that could be adjusted using the valve and rotameter. The optical probe and the high-speed camera were set up under the injection zone. Both camera and optical sensor were situated 5 and 25 cm below the nozzle. The distance between the camera and the center line of the nozzle was 20 cm. In this experiment, 0.89 and 1.50 mm, full-cone spray nozzle from Spraying System Co. (USA) were used. Figure 2.4 shows the photo of nozzles used in the experiment. The liquid flow rate was controlled at range of 0.19-0.59 LPM. Note that, in this experiment, many thousands of droplets were measured to ensure statistical accuracy of the results.
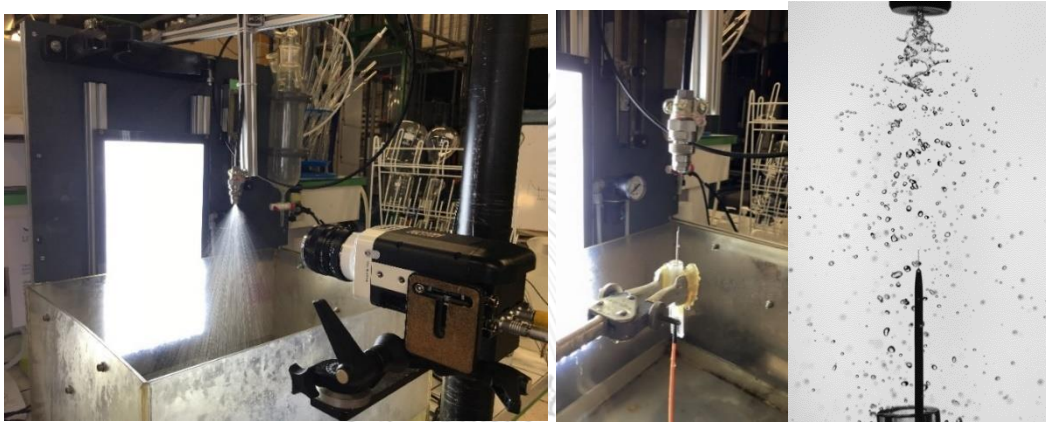
Figure 2.3 Experimental setup for acquisition of sprays

Figure 2.4 Full-cone spray nozzles (left) 0.89 mm (right) 1.50 mm

2.3.2 Optical probe

(a) Overall probe methodology

Figure 2.5 shows the methodology of the probe used in this experiment. The light source equipped within the module transmits light to the optical probe via the optical fiber wire. Once the light reaches the tip of the probe, the light reflects back to the optical fiber wire and consecutively transmits to the light sensor in the module. The intensity of the light reflected changes according to the fluid phase covering the probe tip. This change can be differently used to determine the velocity and size of the droplet. Until now, there are two methods developed to apply for the droplet hydrodynamics using a monofiber probe: de-wetting time and light interference, where their methodology will be described in the next section.
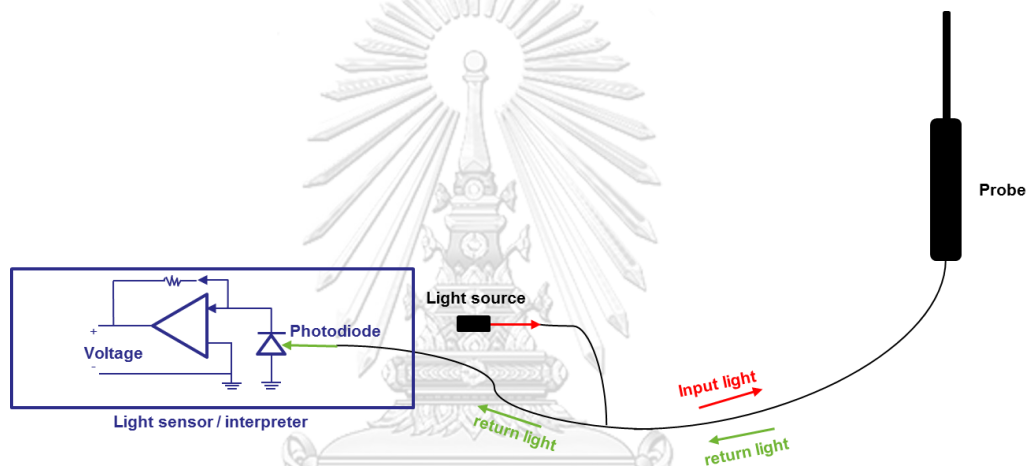
Figure 2.5 Optical probe used in the experiment

(b) De-wetting probe

(i) Signal acquisition of a droplet
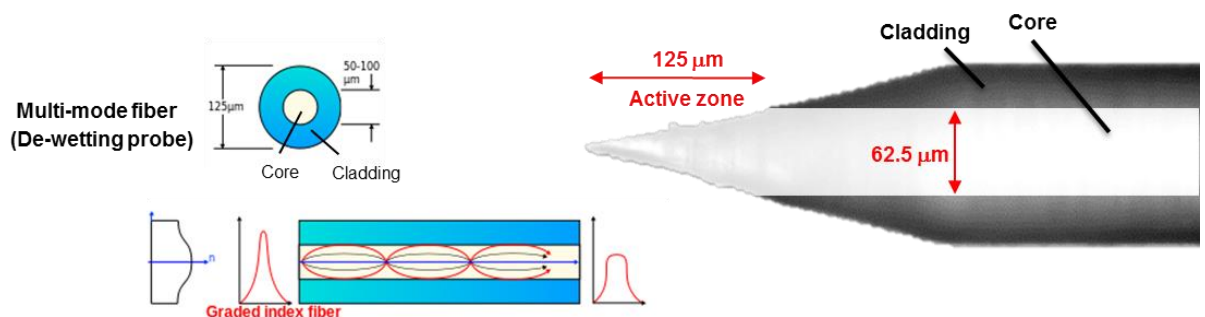
Figure 2.6 De-wetting probe characteristic

A monofiber optical probe from A2 Photonic Sensors (France) was used in this work. The optical fiber wire used for this probe is a multi-mode fiber that has the size of 125 µm in diameter and 62.5 µm size of its core, as illustrated in Figure 2.6. The

light transmits within the core has moderate intensity that does not equally distributed. The maximum intensity is at the center of the core and gradually reduced with the core radius.

In order to use it for characterization of sprays, the probe was set up as to be exposed to the spraying system and connected to its module. The minimum and maximum voltages were adjusted to -8 and +8 V, respectively. The probe measured the maximum voltage value (V_G) when it was exposed to air, and the minimum value (V_L) when covered by water.
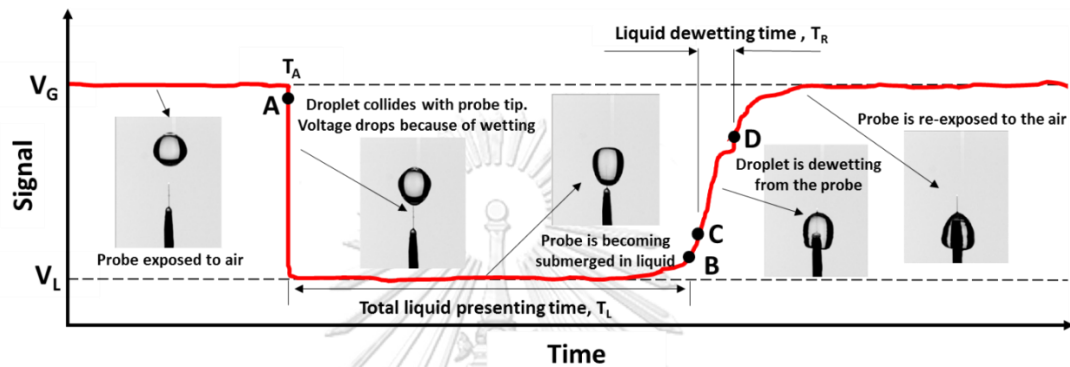
Figure 2.7 Voltage signal from a droplet colliding with an optical probe

Normally, as shown in Figure 2.7, the signal from the probe that is exposed to the air is constantly at V_G. Once a droplet collides with the probe tip (point A), the signal drops instantly to V_L because the tip is surrounded by water. The signal stays at V_L until the droplet starts becoming isolated from the probe tip (point B). When the droplet is about to leave, the probe signal starts to rise linearly from V_L to V_G. The total time the droplet spends on the probe tip, from point A to point B, is defined as the liquid presenting time (T_L) while the time taken for the signal to rise from V_L to V_G is defined as the liquid de-wetting time (T_R). However, according to (Hong et al., 2004), T_R can be suitably evaluated between point C (which represents 10% of the difference between V_G and V_L) and point D (which represents 70% of this difference) as the signal rise is linear and stable between these points. The T_L and T_R measured for each droplet could be used to compile its size and velocity.

(ii) Data interpretation

According to (Hong et al., 2004), droplet velocity is proportional to its dewetting time (T_R). The relation between T_R and a droplet velocity (u_d) is described in Equation (2.1) where L_s and b are the equation constants. These constants depend on the characteristics of each probe, which can be determined experimentally. In this experiment, L_s and b for the probe were equal to 17 μm and -1, respectively.

$$u_D = L_S \cdot T_R^{-b} \tag{2.1}$$

Droplet size is calculated by multiplying the liquid presenting time (T_L) and the droplet's velocity (u_D) as expressed in Equation (2.2); where L_C is the chord length of a droplet that collides with the probe. Note that the size determined with this algorithm is the droplet chord length not the droplet diameter.

$$L_C = u_D \cdot T_L \tag{2.2}$$

(iii) Velocity limitation

The limitation of velocity measurement with the de-wetting optical probe is calculated based on the methodology of the probe. The velocity of the droplet is calculated using the droplet dewetting time (T_R) and applying it to Equation (2.1). Normally, the constant b in the equation is -1, so Equation (2.1) can be expressed as;

$$u_D = \left(\frac{L_s}{T_R}\right) \tag{2.3}$$

Since L_s is the constant parameter of the probe, the maximum velocity would occur when T_R is at its minimum value. The minimum value of T_R depends on the acquisition rate of the probe as well as the number of minimum points that can be recorded on the experimental curve, as shown in Equation (2.4).

$$T_{R,min} = \left(\frac{No.\,of\,mimimum\,points}{Aquisition\,rate}\right) \tag{2.4}$$

By combining with Equation (2.3), the maximum velocity that could be determined by the probe becomes;

$$u_{D,Max} = \left(\frac{L_s}{T_{R,min}}\right) = \left(\frac{L_s\,x\,Acquisition\,rate}{No.\,of\,minimum\,points}\right) \tag{2.5}$$

Note that the minimum number of points should be more than 3 points in order to clearly observe the trend of rising. The acquisition rate used throughout this experiment was 2.5 MHz while the maximum acquisition rate for the probe was 4 MHz.

(iv) Size limitation

The droplet size limits of the optical probe could be determined in the same way as the velocity limits. The size of the droplet determined by the optical probe corresponds to Equation (2.2), and is the product of the liquid presenting time (T_L) by its velocity (u_D). Therefore, the minimum size limit would be acquired when the minimum T_L is considered. The minimum T_L is determined using the same approach as for the minimum T_R from Equation (2.4), i.e.

$$T_{L,min} = \left(\frac{No.\,of\,mimimum\,points}{Aquisition\,rate}\right) \tag{2.6}$$

By combining with Equation (2.2), the minimum size that could be determined by the optical probe can be expressed as in Equation (2.7).

$$L_{c,min} = u_D \; x \; T_{L,min} = u_D \; x \left(\frac{No.\, of\, mimimum\, points}{Aquisition\, rate} \right) \hspace{2cm} (2.7)$$

From this equation, the minimum size ($L_{c,\, min}$) is a function of the droplet's velocity (u_D), the acquisition rate, the probe constant value, and the number of minimum points of T_L. When considering the maximum velocity for a certain acquisition rate and minimum number of points, Equation (2.7) becomes;

$$L_{c,min}\, at\, u_{D,max} = \left(\frac{No.\; of\, minimum\, points}{Acquisition\, rate} \right) x \left(\frac{L_s \; x \; Acquisition\, rate}{No.\, of\, minimum\, points} \right) \hspace{0.5cm} (2.8)$$
$$= L_s$$

When the same number of minimum points is considered for both T_L and T_R, the minimum sizes are equal to the probe constant (L_s), regardless of the acquisition rates. However, it should be noted that the maximum velocity is different for different acquisition rates, which leads to the significantly different size limits at a certain velocity. Moreover, when the velocity of the measured droplet is lower than the maximum velocity, the size limit decreases following Equation (2.8). The results for the calculation are shown in Section 2.4.3.

(v) Droplet frequency limit for approaching the probe

In this experiment, the concept to determine the droplet frequency limit that approaches a probe is developed based on the interval distance between each droplet. The pre-experiment indicated that there was a discrepancy between the probe and the high-speed camera when the number of droplets approaching the probe was high. This discrepancy occurred because the droplets are too close to each other; therefore, the chance of the droplet coalescence on the probe increased, leading to the large discrepancy between the two techniques.

In order to obtain the droplet frequency limit theoretically, the assumption of the droplets was set up as follow: (1) the droplet sizes and velocities of each droplet are the same (2) the interval distance between each droplet is equal and at least equal to their own diameter, *d*, to avoid the coalescence of each droplet. The distance, *d*, is presumed to avoid the deceleration of the droplet on the probe as well as their oscillations that possibly causes the droplets to contact with each other. The conceptual diagram is as shown in Figure 2.8.
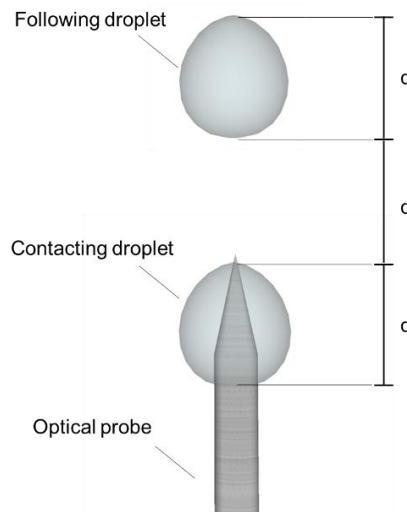
Figure 2.8 Minimum interval distance between each droplet for avoiding droplet coalescence

From the above concept, the time until the following droplet has to spend in order to collide with the probe (T_i) is:

$$T_i = \frac{distance}{velocity} = \frac{d}{u_D}$$ (2.9)

and the time each droplet spends from contacting until leaving the probe or so-called the liquid presenting time (T_L), as shown in Figure 2.7, is:

$$T_L = \frac{distance}{velocity} = \frac{d}{u_D}$$ (2.10)

Therefore, the total time of each droplet until the same cycle is repeated is the summation of T_i and T_L and the droplet frequency can be calculated from Equation (2.11)

$$f_L = \frac{1}{T_i + T_L} = \frac{u_D}{2d}$$ (2.11)

Table 2.1 shows the droplet frequency limit of each size and velocity of the droplets. The higher frequency beyond this table would have a large possibility to induce the droplet coalescence that leads to a discrepancy. In this work, it was found that the droplet frequencies were in the range between 100 to 2,500 Hz; therefore, the use of the droplet frequency limit filter from the values in Table 2.1 is mandatory, depending on the size of the droplets. In addition, with this assumption, the probe limit can be easily determined using the value of the local liquid fraction obtained in the experiment. When the local liquid fraction is higher than 50%, the limit according to Table 2.1 is achieved, thus the chance of the droplet coalescence on the probe increases and the discrepancy of the probe becomes larger. On the other hand, the accurate droplet velocity and size could be obtained when the local liquid fraction is below 50%. Note

that the calculation of the local liquid fraction could be performed according to Equation (2.12) where the liquid fraction (ε_L) can be simply calculated by summing all the droplets presenting times (T_L) and dividing by the total time of acquisition.

$$\varepsilon_L = \left(\frac{\sum T_L}{Total\ time\ of\ acquisition} \right) \tag{2.12}$$

Table 2.1 Droplet frequency limit for approaching the probe at various droplet velocities and sizes

Droplet velocity (m/s)	Droplet frequency limit (Hz)										
	Droplet diameter (mm)										
	0.5	1.0	2.0	3.0	4.0	5.0	6.0	7.0	8.0	9.0	10
0.5	500	250	125	83	63	50	42	36	31	28	25
1.0	1,000	500	250	167	125	100	83	71	63	56	50
1.5	1,500	750	375	250	188	150	125	107	94	83	75
2.0	2,000	1,000	500	333	250	200	167	143	125	111	100
2.5	2,500	1,250	625	417	313	250	208	179	156	139	125
3.0	3,000	1,500	750	500	375	300	250	214	188	167	150
4.0	4,000	2,000	1,000	667	500	400	333	286	250	222	200
5.0	5,000	2,500	1,250	833	625	500	417	357	313	278	250
6.0	6,000	3,000	1,500	1,000	750	600	500	429	375	333	300
7.0	7,000	3,500	1,750	1,167	875	700	583	500	438	389	350
8.0	8,000	4,000	2,000	1,333	1,000	800	667	571	500	444	400
9.0	9,000	4,500	2,250	1,500	1,125	900	750	643	563	500	450
10.0	10,000	5,000	2,500	1,667	1,250	1,000	833	714	625	556	500

(c) Interference probe

(i) Signal acquisition of a droplet
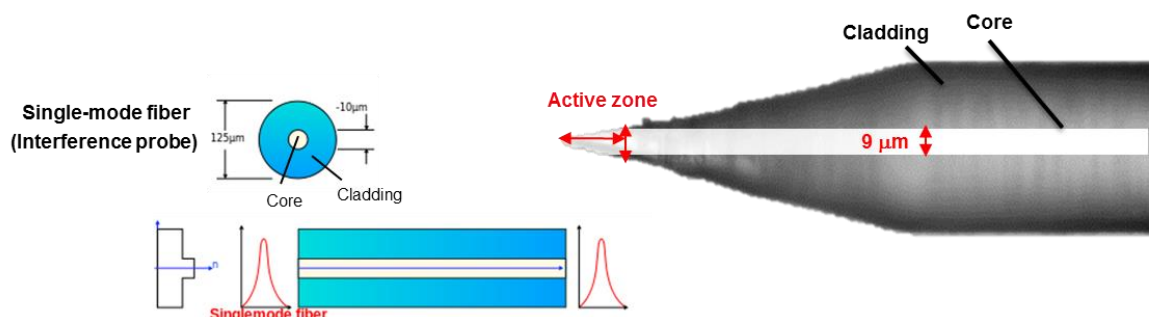
Figure 2.9 Light interference probe characteristic

Figure 2.9 shows the optical wire type used for the light interference optical probe. The single-mode fiber is normally used in order to increase light intensity for

light reflection and interference purpose, which is totally different method from the de-wetting probe. The method is based on light phenomenon induced a droplet before the droplet touches the tip of the probe. Hence, the change of droplet velocity due to the collision with the probe can be avoided.
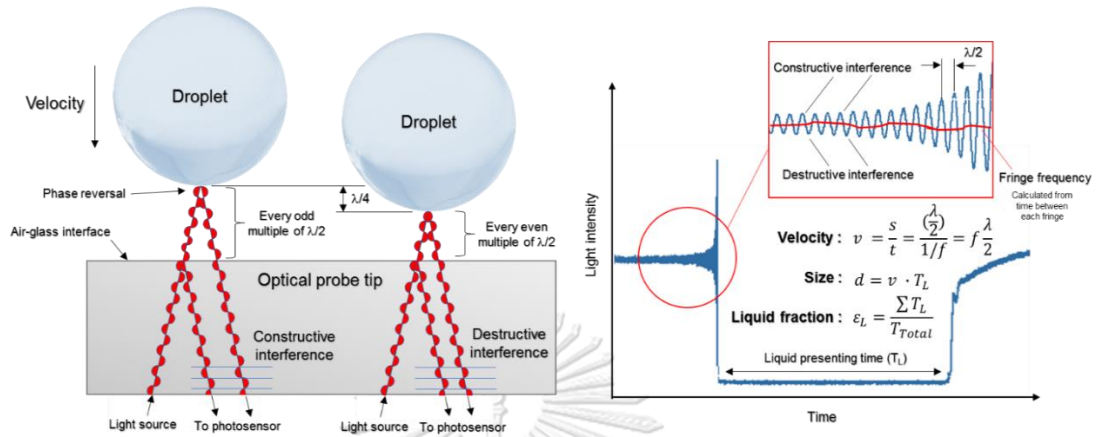
Figure 2.10 Methodology of the optical interference probe

The methodology of the optical interference probe, as shown in Figure 2.10, is based on the interference of light rays from a monochromatic source. The light rays from the light source pass through the optical fiber glass and reflect off both the air-glass interface at the optical probe tip and the gas-liquid interface of a droplet, and eventually the reflected rays combine and superpose. However, the reflected ray from the droplet has the additional path from the gap between the droplet and the optical probe tip; it also encounters a 180° phase reversal due to lower to higher reflective index of the mediums. According to the electric field of the light ray, the intensity of the superposed rays with the assumption of equal in their intensities could be mathematically derived as in Equation (2.13), where I is the light intensity of a light ray and $\emptyset_1$ and $\emptyset_2$ are the phase shift of the wave reflected at the air-glass interface and the droplet respectively [2]. Noted that the 180° phase reversal from the droplet, is already added into the equation in term of π.

$$I_{Total} = 4I cos^2 \left(\frac{\emptyset_1 - (\emptyset_2 - \pi)}{2} \right) = 4I cos^2 \left[\frac{(\delta + \pi)}{2} \right] \tag{2.13}$$

The equation indicates that when the difference of the phase shift of both waves (δ) is equal to odd multiples of $\pi/2$, the light intensity of the superposed light is at its maximum or in constructive interference, while the destructive interference or its minimum intensity occurred when the difference is equal to even multiples of $\pi/2$.

(ii) Data interpretation

According to the concept explained in the previous section, by knowing the time that the droplet traveled, its velocity can be determined by the derivative of the traveled distance with respect to the time, where the distance considering is equal to half of the

phase shift distance, which is half of the transmitted light wave length $\left(\frac{\lambda}{2}\right)$ and the time can be considered from each successive constructive interference (or so-called fringe) which can be expressed as in Equation (2.14).

$$u_D = \frac{s}{t} = \frac{\left(\frac{\lambda}{2}\right)}{\frac{1}{f}} = f\frac{\lambda}{2} \qquad (2.14)$$

In the equation, f is the interference frequency between each successive constructive interference or fringe calculated from the inverse of time between each fringe and λ is the light frequency from the source which is 1.55 µm. Note that after obtained the droplet velocity, the methodology to determine its size follows the same procedure as the de-wetting probe, where the detail was described in Equation (2.2).

In this work, the "M2 analyzer for spray" program, which is shown in Figure 2.11, was used to determine droplet velocities and sizes. The methodology of the program had 3 steps: acquisition, data interpretation, and data treatment process. In the acquisition process, the number of droplets to be recorded is able to specify. A large number of droplets were recommended since some of droplets could not be used for the determination, off-center droplets for example. After the acquisition, the program interprets the signal and calculates the frequency between each fringe of each droplet and plots the frequency between each fringe as a function of time (red line). The average frequency is used to calculate the droplet velocity.
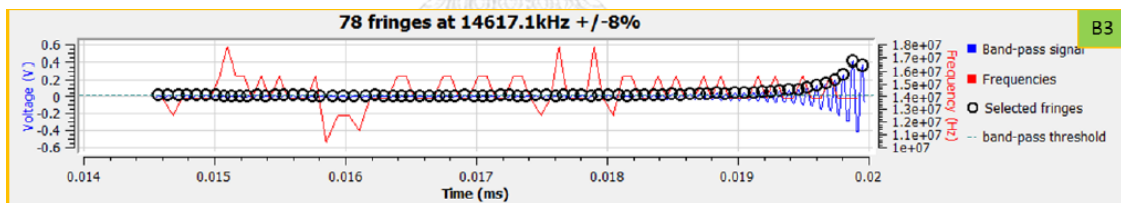
Figure 2.11 M2 analyzer for spray program used for droplet velocity and size determination

At this point, in the data treatment process, two parameters can be used to screen some flawed droplets out: minimum number of fringes and maximum standard deviation of fringe frequency. The minimum number of fringes is used to screen out the droplet having lower fringes than the criteria and the maximum standard deviation is calculated based on the well-known standard deviation of the fringe frequency. The number of points used for the standard deviation calculation is equal to the number of minimum fringes specified earlier. When the deviation is larger than the constrain, the droplet is screened out. The effect of each parameter will be studied by comparing the velocity and size obtained by the high-speed camera and the optical probe.

(iii) Velocity limitation

According to the methodology to determine a droplet velocity described in Equation (2.14), the crucial variable that can be changed is the frequency of the interference (f). In order to obtain a good interference frequency, a minimum acquisition frequency of the probe has to be identified. The minimum acquisition frequency depends on the minimum of points needs to be used to determine the interference frequency. In this work, the minimum of 10 points are recommended in order to obtain a good shape of the interference signal and fringes. The number of points can be determined by Equation (2.15), where f is the frequency of the interference signal, f_{aq} is the acquisition frequency of the probe, and N_I is the number of points in the inference signal from one fringe to the consecutive fringe.

$$\text{Number of points} = N_I = \frac{f_{aq}}{f} \tag{2.15}$$

When combined the Equation (2.15) with Equation (2.14), the equation can be expressed as in Equation (2.16).

$$u_d = \frac{f_{aq}}{N_I} \frac{\lambda}{2} \tag{2.16}$$

Hence, the number of points at each droplet velocity and acquisition frequency can be calculated using Equation (2.17).

$$N_I = \frac{f_{aq}}{u_d} \frac{\lambda}{2} \tag{2.17}$$

From the equation, when the droplet velocity is high, a high acquisition frequency is needed to be used to obtain at least 10 points of the interference signal. Therefore, the minimum acquisition frequency can be identified using this equation.

(iv) Size limitation

Since the probe used the methodology as mentioned in Equation (2.2) to determine the size of every droplet, the minimum theoretical size of the droplet that can be detected by the probe can be expressed as in Equation (2.18), where N_L is the number of points used to determine the liquid presenting time (T_L).

$$L_{C,min} = u_d \cdot T_L = u_d \cdot \frac{N_L}{f_{aq}} \tag{2.18}$$

Hence, the minimum size of droplet can be obtained by identified the minimum N_L where at least 10 points are also recommended in order to have a good accuracy.

(v) Droplet coalescence filter

In order to filter the coalescence droplets out, the droplet acquisition frequency approaching the probe should not as well excess the values from

Table 2.1. For example, when the size of droplets is around 0.5 mm and its velocity is 1 m/s, the droplet frequency between each droplet should not excess 1,000 fps to eliminate the coalescence droplets in the calculation.

Fortunately, with the maximum standard deviation and minimum number of fringes used for determination droplet velocities and sizes, those high frequency droplets can be screened out due to the large standard deviation of fringe frequency and too low number of fringes.

2.3.3 Image acquisition and treatment methodology

(a) Image acquisition
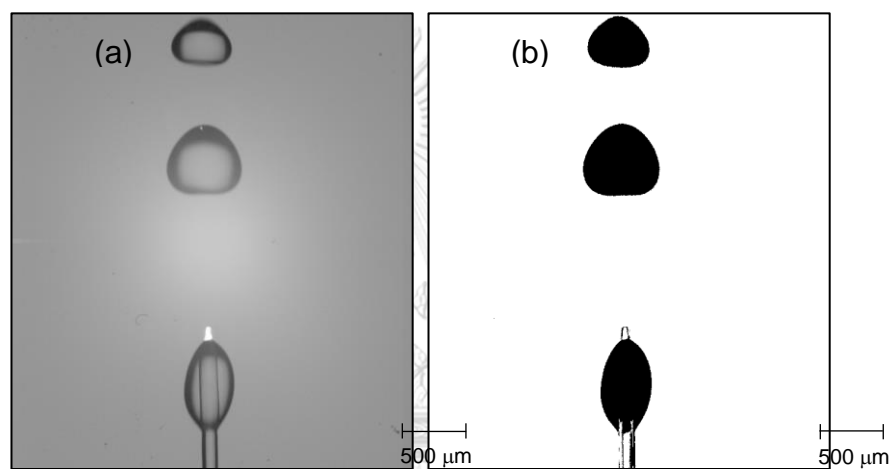
Figure 2.12 (a) Image captured with the camera and (b) Image processed with ImageJ® software for the same droplet observation

A high‑speed camera from Vision Research, Phantom Miro – M110, was used for image acquisition. A backlight from PHLOX with a luminance of 30383 cd/m^2 and a uniformity of 93.65 % was set up as the image background. The photos were captured by National Optical, 704-155 DIN 4x Objective Lens at a framerate of 2,900 fps for the acquisition described in section 2.3.1 and by Carl Zeiss 50mm f/1.4 Planar at 32,000 fps and for the second part (industrial spray). An example of an image captured is shown in Figure 2.12 (a) for the same droplet observation and Figure 2.13 for spray. The images were captured in an 8-bit grayscale format.
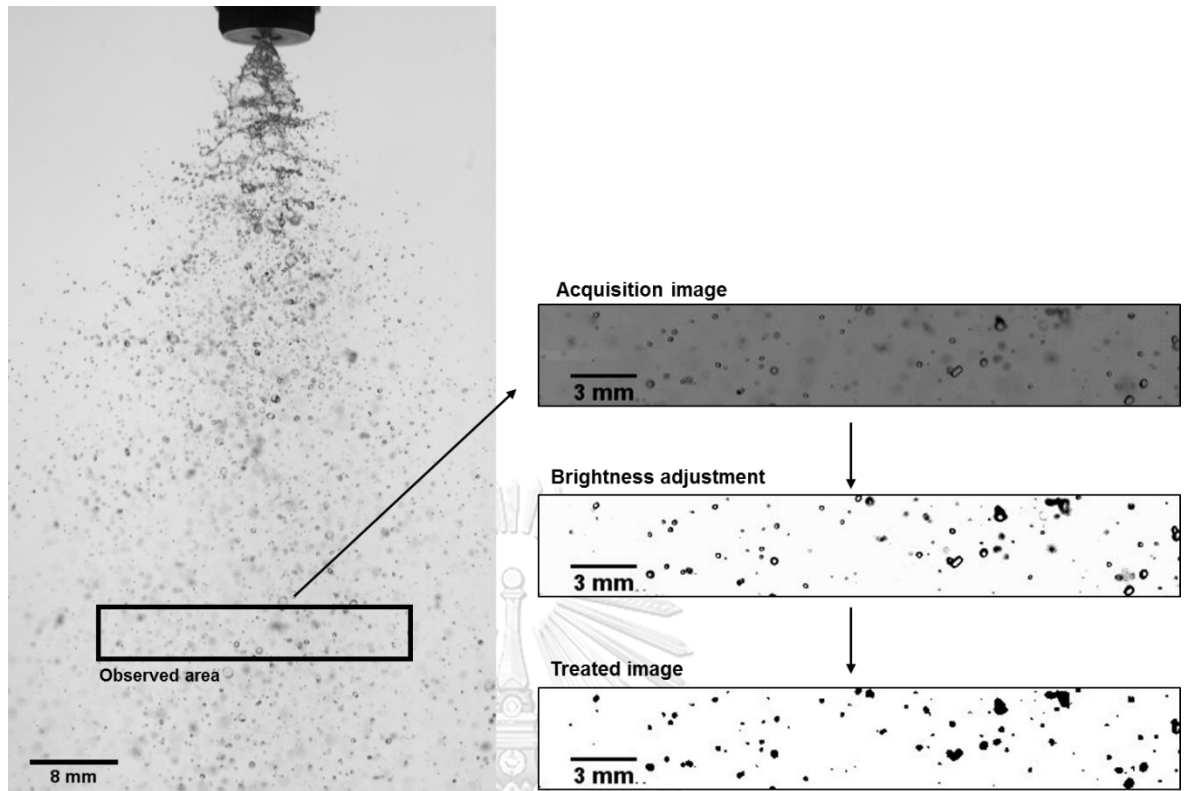
Figure 2.13 Image captured of a spray with 0.89 mm nozzle size when operating at
0.59 LPM and treated image

(b) Determination of droplet size and velocity

The captured images were processed and analyzed with ImageJ® software. The most
suitable level of gray (threshold) for each image was selected and the images were then
converted into binary images as shown in Figure 2.12 (b) and Figure 2.13 for the same
droplet observation and a spray, respectively. These binary images were used to
determine properties including projected area (A_D) and perimeter (P_D). In this work, the
equivalent spherical diameter for each droplet was used with the assumption that the
projected shape of any droplet could be treated as an ellipse. This equivalent diameter
could be determined with the correlation of (Heyt and Diaz, 1975) as shown in Equation
(2.19), where d_e is the equivalent spherical diameter.

$$d_e = 1.55 \, A_D^{0.625} / P_D^{0.25} \tag{2.19}$$

To determine droplet velocity, the "wrmtrack" plugin of ImageJ® was used. This plugin
tracked each droplet settling in the subsequent images. With the framerate used when
capturing the images in the spray system with the industrial nozzle, droplet velocities
of up to 25 m/s could be detected. However, the camera could detect only droplets
larger than 0.1 mm because of the resolution limits of the camera and its lens.

2.3.4 Performance estimators

In order to compare and discuss the results from the high-speed camera and the optical probe equitably, the statistical parameter and methodologies were applied based on the comparing data of droplet velocities and their sizes.

For the comparison of the series of droplets produced by the syringe, the average absolute relative deviation (AARD) was used to determine the average deviation of every droplet velocity and size observed from different methods. AARD can be calculated from Equation (2.20) and Equation (2.21) for the velocity and size, respectively, where u_i, d_i and N refer to the velocity obtained by each technique, the droplet size obtained by each technique, and the number of droplets used in the experiment. The number of points used for each condition was more than 1,000 droplets. The subscription of HSC represents for the high-speed camera, and OFP for the optical fiber probe.

$$\text{AARD of velocity} = \frac{1}{N}\left(\sum_{i}^{N}\left|\frac{u_{OFP} - u_{HSC}}{u_{HSC}}\right|\right)x100\ \% \tag{2.20}$$

$$\text{AARD of size} = \frac{1}{N}\left(\sum_{i}^{N}\left|\frac{d_{OFP} - d_{HSC}}{d_{HSC}}\right|\right)x100\ \% \tag{2.21}$$

For comparing the average velocities and sizes obtained from both techniques, the t-test, one of the most widely used hypothesis tests for small number of samples, was applied (Montgomery and Runger, 2010). The Welch's t-test was used due to the different variances of each droplet velocity and size from each technique. The equations for the t-test are expressed in Equation (2.22) and Equation (2.23), where t_0 is t-score while $\bar{X}_i$ and S_i^2 are mean and variance of the sample from each technique, respectively.

$$t_0 = \frac{\bar{X}_{OFP} - \bar{X}_{HSC}}{S_t} \tag{2.22}$$

$$S_t = \sqrt{\frac{S_{OFP}^2}{n} + \frac{S_{HSC}^2}{n}} \tag{2.23}$$

To perform the hypothesis test, the p-value was introduced. The p-value can be calculated from the probability of the sample that lies outside the range between $-|t_0|$ and $+|t_0|$ from its mean, which refers to the probability of the sample which deviated from its mean larger than t_0. When comparing the p-value with the significance level (α), which is the boundary level that statistically determines the statistical difference; if the p-value is larger than α, the means of the samples are not statistically significantly different. In contrast, when the p-value is smaller than α, it is remarked as statistically significantly different. Note that the exact value of the α is not identified and typically

set between 0.01 to 0.05, where the value of 0.05 is normally used. Moreover, the p-values using in this work were entirely calculated via data analysis function of Microsoft-Excel.

For the spray case used the industrial nozzle, the Cohen's effect size method was used due to the very large number of droplets observed. As mentioned above, many thousand droplets were detected by both techniques where the comparison using Z-test or T-test would lead to a false determination (Sullivan and Feinn, 2012). Therefore, the Cohen's effect size method is suitable for this comparison, where the effect size (d_c) can be determined using Equation (2.24).

$$d_c = \frac{\bar{X}_1 - \bar{X}_2}{S_t}$$

(2.24)

In the equation, $\bar{X}_i$ is the mean of data group i and S_t is the standard deviation of either group. When the effect size is 0.2 or below, the deviation can be considered as small where only 15 % of data was not overlap. While 0.5, 0.8, and 1.3 are considered as medium, large, and very large deviations with the non-overlap percentage of 33, 47, and 66 %, respectively.

2.4 Result and discussions

In this section, two regimes were studied: droplet series and sprays. Both regimes were investigated using two types of optical probes and the high-speed camera. Firstly, the series of droplets were observed in order to understand the optical probe performance for droplets that known their hydrodynamics properties (i.e. sizes and velocities). Later, sprays using nozzles were investigated.

2.4.1 Acquisition of the droplet series

This this part, two types of optical probes, which were de-wetting probe and interference probe, were used to study the droplet hydrodynamics of droplet series produced by a syringe.

(a) De-wetting probe

(i) Droplet velocity

The droplet velocities obtained from both high-speed camera and optical probe data are illustrated in Figure 2.14. A point in the figure represents a droplet velocity for the same droplet; the x-axis and y-axis are the droplet velocity determined with the high-speed camera and the optical probe, respectively. From the figure, it can be seen that the droplet velocities determined by both methods gave the same trend for very low velocities; however, as the droplet velocity increased, the discrepancies became larger; both positive and negative deviations were observed simultaneously. The droplet oscillation and droplet coalescence were responsible for the deviation as discussed below.
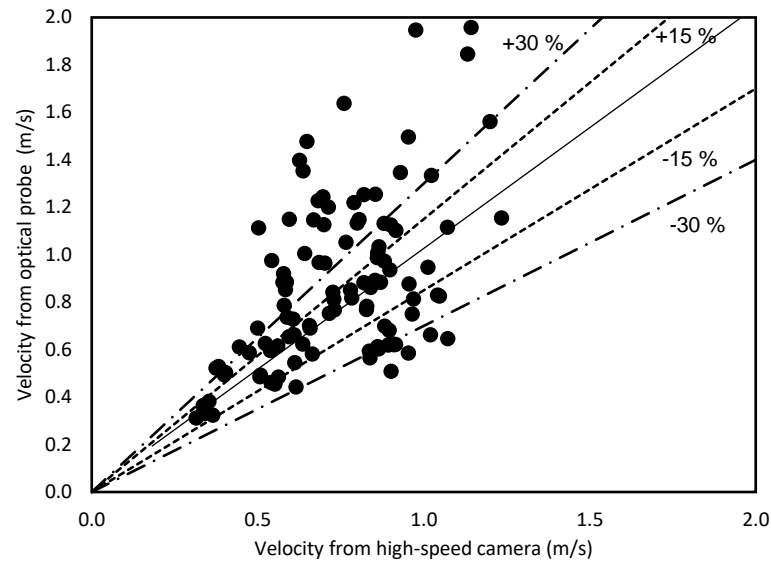
Figure 2.14 Velocities of the same droplets obtained with different methods

According to the probe methodology to determine droplet velocity, the probe examines the droplet velocity at the interface of the droplet when it is leaving the probe (Hong et al., 2004). Therefore, because of the oscillation of droplets that occurred since their formation process, when they came into contact with the optical probe as shown in Figure 2.15, the droplet velocities could be recorded as faster or slower than the actual velocity, depending on the oscillating regime occurring at the time it was leaving the probe. Figure 2.16 shows the droplet interfacial velocity determined by the high-speed camera versus its position before the droplets contacted the optical probe tip.
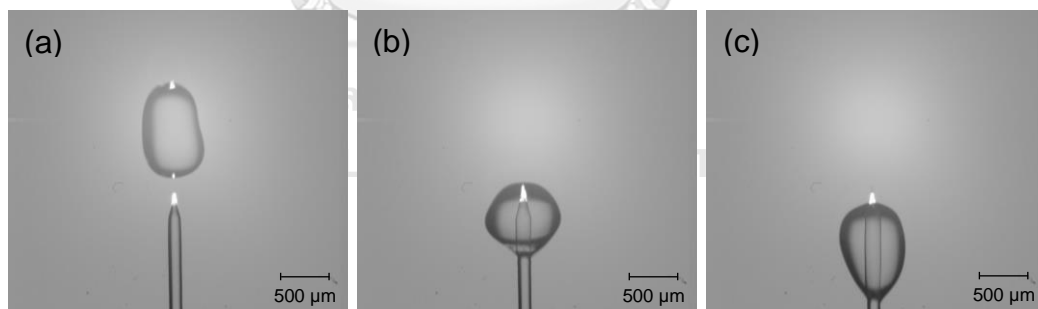
Figure 2.15 Droplet oscillation at the optical probe tip
(a) Stretching before collision (b) Shrinking during collision (c) Re-stretching after collision

As seen in Figure 2.16, the interfacial velocity of the droplets varied around its average value (dashed line) due to the oscillation effect which occurred from the droplet formation. Therefore, the velocities of the droplets determined by the optical probe were dependent on their oscillating regime when they were leaving the probe. For droplets that were expanding, the velocities obtained from the probe would be smaller than the average velocity as shown in Figure 2.16(a). On the other hand, the shrinking regime droplets would show faster velocities than their average, Figure 2.16(b). This

finding supports the experiment of Valero and Bung (2017) regarding their non-linear calibrations for high-velocity estimations with monofiber probes on multiphase flows (Valero and Bung, 2017). Note that the values of the average velocities were the values determined by the high-speed camera using the image processing methodology.
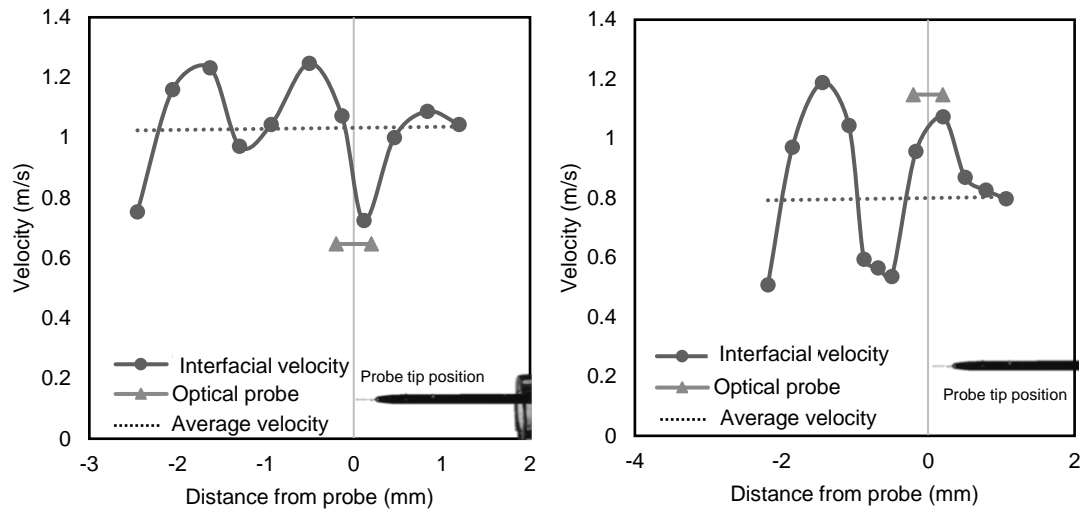
Figure 2.16 Effect of droplet oscillation on the droplet interfacial velocity according to distance from the probe at a water injection rate of 0.128 mL/s (a) Expanding oscillation (b) Shrinking oscillation

In addition to the droplet oscillation effect, the droplet coalescence at the probe tip should be considered in the deviation mentioned earlier. This phenomenon occurred when two or more droplets arrived at the probe at the same time. As shown in Figure 2.17, coalescence between droplets gave a larger droplet; the droplet arriving slightly later would undergo a change in velocity due to the surface tension of water, which dragged it down rapidly.
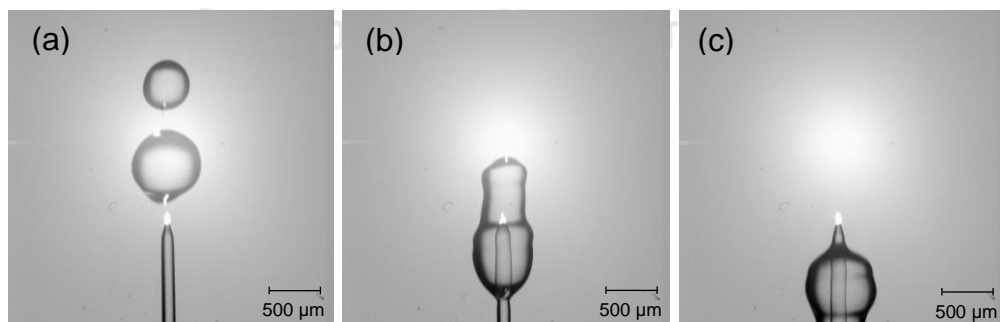
Figure 2.17 Droplet coalescence at the probe tip
(a) droplets before collision (b) coalescence on collision (c) combined droplet after collision

Figure 2.18 represents the interfacial velocity of the coalesced droplets at the probe tip as a function of distance from the probe. It can be seen that, at distances of more than 0.5 mm, the droplet moved at a velocity of around 1 m/s on average.

However, at the instant of contact, the arriving droplet coalesced with the other droplet as shown in Figure 2.17, and was dragged down by it, which increased its velocity dramatically.
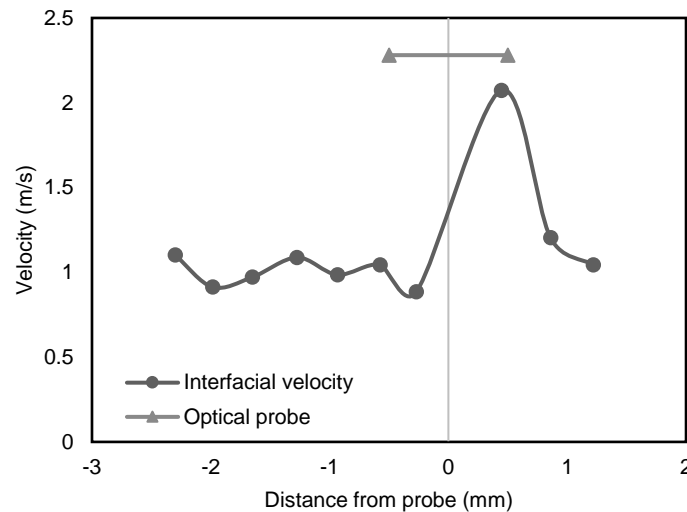
Figure 2.18 Effect of droplet coalescence on the droplet interfacial velocity as a function of distance from the probe

In order to avoid the discrepancy due to the droplet coalescence, the filter on the data obtained by the optical probe is included. The principle of the filter is based on the droplet frequency which is the number of droplets observed by the probe per second, where the detail is mentioned previously in Section 2.3.2(b). The screening out eliminated the droplets that tend to cause the coalescence regime. In this experiment, the time interval of droplets that contacted with the probe was between 0.4 to 10 milliseconds which corresponding to the droplet frequency of 100 to 2500 droplets/second. According to Table 2.1, since the majority of velocities and sizes of droplets were around 1 m/s and 0.5 mm, respectively, the droplets having higher than 1,000 Hz was screened out. Figure 2.19 shows the velocities of the droplets as shown in Figure 2.14 after screening out the droplet frequency that higher than 1,000 droplets per second.
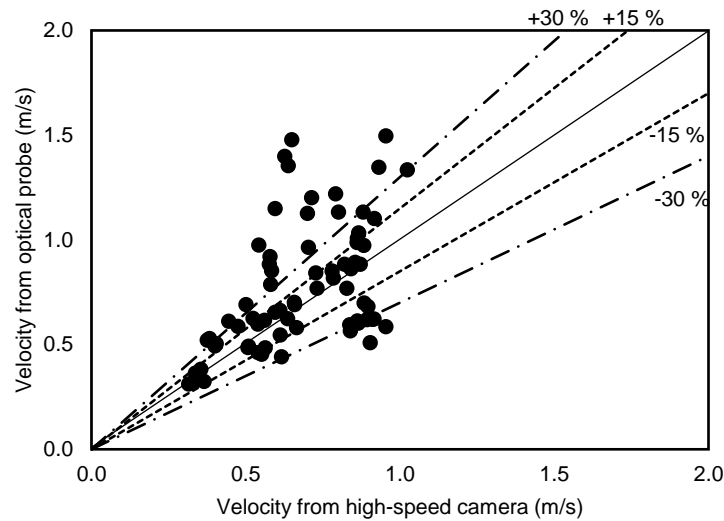
Figure 2.19 Velocities of the same droplets obtained with different methods after screening out droplets having higher frequency for approaching the probe than 1,000 droplets/second

After applying the filter, Figure 2.19 shows a better result as comparing with Figure 2.14, where no filter was applied. The droplets screened out were mostly the droplets having too high droplet frequency approaching the probe. However, with the filter, the droplet oscillation could not be eliminated and therefore the discrepancy still existed. From this point, it is obvious that one of the limits of the optical probe was the droplet frequency approaching the probe. The droplet coalescence tends to occur when too high droplet frequency or too dense spray was occurred. In order to avoid this regime, the data filter has to be applied or the optical probe should be used only in the suitable conditions. Section 2.3.2(b) describes the limit of the optical probe and the appropriate range that the optical probe can perform accurately.

In summary, the droplet velocities obtained by the high-speed camera and the optical probe had discrepancies due to the difference in approach between the two techniques; the high-speed camera determined droplet velocities from their centroids, while the optical probe acquired the velocity at the droplet interface. Therefore, the deviation between both techniques due to the droplet oscillation was unavoidable. In addition, the droplet coalescence on the probe also caused the probe to overestimate the droplet velocities. This incident indicated that the probe has its own limit on the dense regime of the spray and therefore the data filter based on the droplet frequency should be performed.

(ii) Droplet size
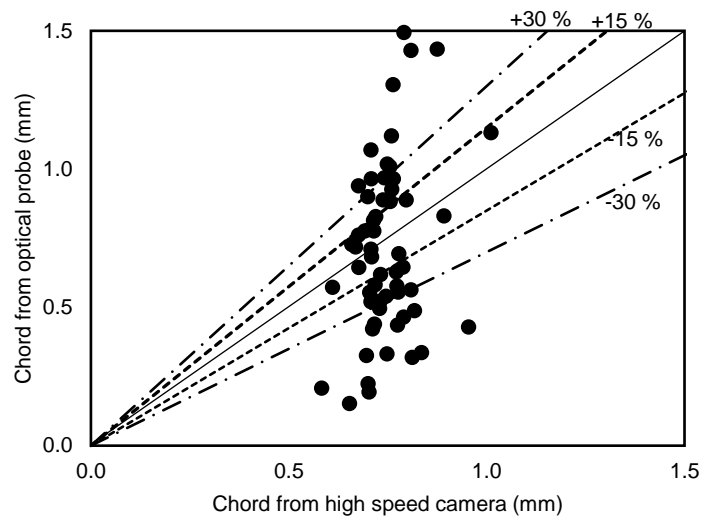
Figure 2.20 Droplet chords of the same droplets obtained with different methods after applying frequency filter

Figure 2.20 shows the sizes in terms of chord for the same droplets determined with the high-speed camera (x-axis) and the optical probe (y-axis) after screening out the high acquisition frequency droplets. It can be seen from the figure that the diameters determined by the optical probe showed a remarkable difference between them. This difference was due to the methodology for droplet size determination in which each droplet size was determined by multiplying its velocity by its liquid presenting time. Consequently, the size deviation also resulted from the deviation of both the velocity and the liquid presenting time. In conclusion, regardless of the droplet coalescence which had already been screened out, the deviation was due to both (1) the deviation of droplet velocity caused by the droplet oscillation and (2) the liquid presenting time, that is, the time the droplet used to cover the probe tip, which could be modified by various causes.
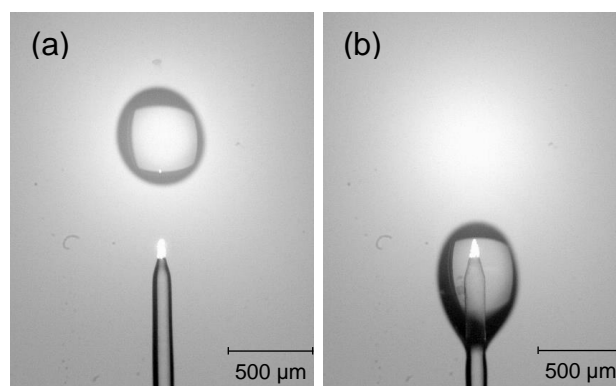
Figure 2.21 Droplet deformation
(a) Before collision (b) After collision

In this experiment, there were two major deviations relating to the liquid presenting time: the droplet oscillation and the droplet deformation. As shown in Figure 2.15, the droplet oscillation can also cause the deviation in the droplet size determination since both expanding and shrinking could lead to an overestimation or underestimation of the size. In addition, the droplet deformation as shown in Figure 2.21 also influenced the determination of size as it changed its shape after making contacted with the probe because of the adhesive force (intermolecular force) between the droplet and the optical probe. Figure 2.22 plots the droplet stream-wise diameter as a function of its distance from the probe. Before collision with the probe, the droplet diameter fluctuated around 0.65 mm. However, once the droplet collided with the probe, its diameter increased intensely due to the adhesive force. Consequently, the liquid presenting time was increased and the chord was overestimated.
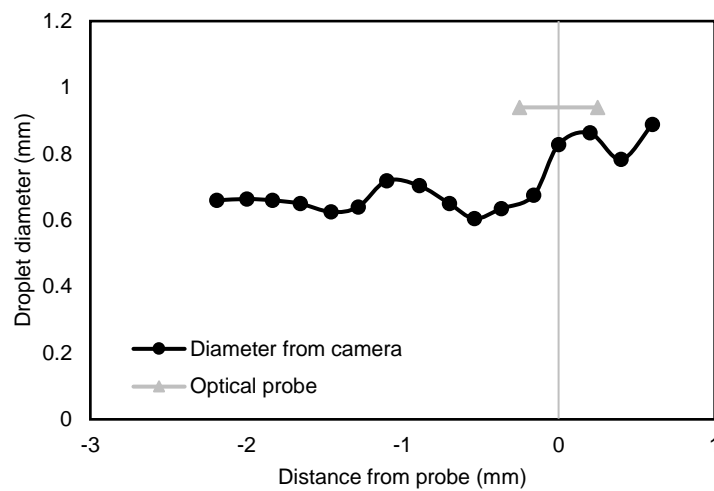
Figure 2.22 Effect of droplet deformation on the droplet diameter as a function of distance from the probe

In summary, the droplet size and velocity determined from both techniques showed an agreement with the explainable deviations. The major discrepancy was caused by the different approaches of the two techniques. Therefore, when involved with the droplet oscillation, both methods gave velocities and sizes of the oscillating droplets differently. In addition, the droplet deformation and the limit of the probe that causes the droplet coalescence on the probe were observed.

Table 2.2 Average diameter, velocity, and statistic estimator for the droplet series produced by the syringe

Variable	High speed camera	Optical probe (Before filter)	Optical probe (After filter)	AARD (%)	P-Value
Average velocity (m/s)	0.725 ± 0.16	0.909 ± 0.33	-	35.44	0.0002
		-	0.818 ± 0.28	33.29	0.0372
Average diameter (mm)	0.788 ± 0.24	0.776 ± 0.46	-	32.42	0.3000
		-	0.792 ± 0.49	28.79	0.5324

Nevertheless, Table 2.2 shows the average diameter and average velocity of all the droplets measured. It can be seen that the optical probe reported the average velocity slightly larger than that of the high-speed camera, while the average diameters were fairly close. The AARD of the average velocity and diameter were at 35.44 % and 32.42 %, respectively, where can be considered as high deviation. Furthermore, the t-test used to indicate the difference between the average values of both techniques indicated that the p-value of the average velocity and diameter were at 0.0002 and 0.3000, respectively, which referred to high significant difference in the case of the average velocity comparison.

When the high acquisition frequency was screened out, the average velocity obtained from the probe reduced and became closer to the one obtained from the high-speed camera. The AARD of both average velocity and diameter were slightly smaller comparing to the without screen out process. The p-values obtained from the test were 0.0372 and 0.5324 for the average velocity and size, respectively, indicating that the average velocity and size between both techniques were closer than without using the screen out process. At this point, the results statistically showed a better agreement since the p-value is 0.0246 which lies between the α of 0.01-0.05 that normally used as significant level of t-test. It also presented that when the comparison was made statistically, especially after using the screen out process, the deviation did not seem to be extremely high as when comparing one by one which represented by the AARD.

It should be noted that the droplet velocity obtained from the syringe was lower than that in the actual spray system. When operating with the spray system, the oscillation velocity would be significantly lower and the effect of the oscillation might be diminished as droplet are smaller. Moreover, the droplet coalescence on the probe would be reduced since the droplet frequency of the spray was lower, averagely 353.3 droplets per second when using the syringe and 35.6 droplets per second when using the spray. This incident occurred because the position of the probe according to the syringe was very smaller (5 mm) comparing to the spray (5 cm); Hence, most of the droplets injected by the syringe collided with the probe whereas only some droplets contacted with the probe in the spray case leading to smaller amounts and lower droplet

frequency. Therefore, in order to understand the potential of the optical probe better, an experiment performed to determine the droplet size and velocity in a spray system is reported in the next section.

(b)   Interference probe

(i)   *Effect of minimum fringes*

Figure 2.23 shows the droplet velocities from a series of droplets characterized by both high-speed camera and the interference probe for the same droplets at various minimum number of fringes using to determine droplet velocity. In the figure, both techniques gave the droplet velocities in the close range, 0.6-0.9 m/s for the high-speed camera and 0.2-1.2 m/s for the interference probe. The discrepancy of the interference probe was according to the droplet oscillation that also found when using the de-wetting probe. However, with the increase of the minimum number of fringes, the discrepancy decreased.
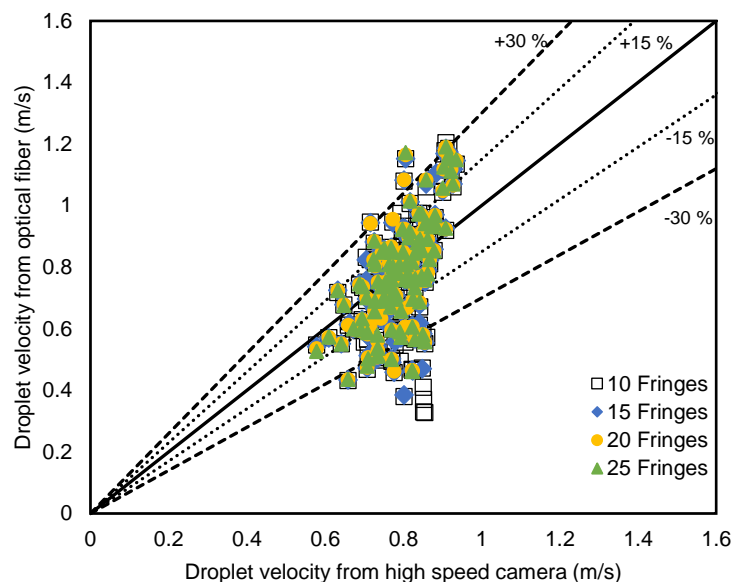
Figure 2.23 Droplet velocities of a droplet series when determining the same droplets using the high-speed camera and interference probe at various minimum numbers of fringes.

As mentioned above, the discrepancy between both techniques was due to the droplet oscillation occurred since the droplet formation. Figure 2.24(a) and (b) shows the frequency according to time of the signal obtained by the low oscillating droplet and highly oscillating droplet, respectively. The low oscillating droplet showed a frequency trend (red line) fluctuated around the mean 1.158×10^6 Hz while highly oscillating droplet showed an increasing trend of the frequency, indicating that the droplet was increasing its velocity before piercing the probe (See Figure 2.15 for detail). This finding showed that, as well as the de-wetting probe, the discrepancy due to the droplet oscillation was unavoidable. However, when using large number of fringes to

determine a droplet velocity, the droplet velocity that observed by the interference probe was the average of the velocity when the droplet was oscillating before collision with the probe, hence, with larger minimum number of fringes, the better agreement with the high-speed camera was obtained as the observed velocity by the optical probe was closer to the average velocity determined by the high-speed camera.
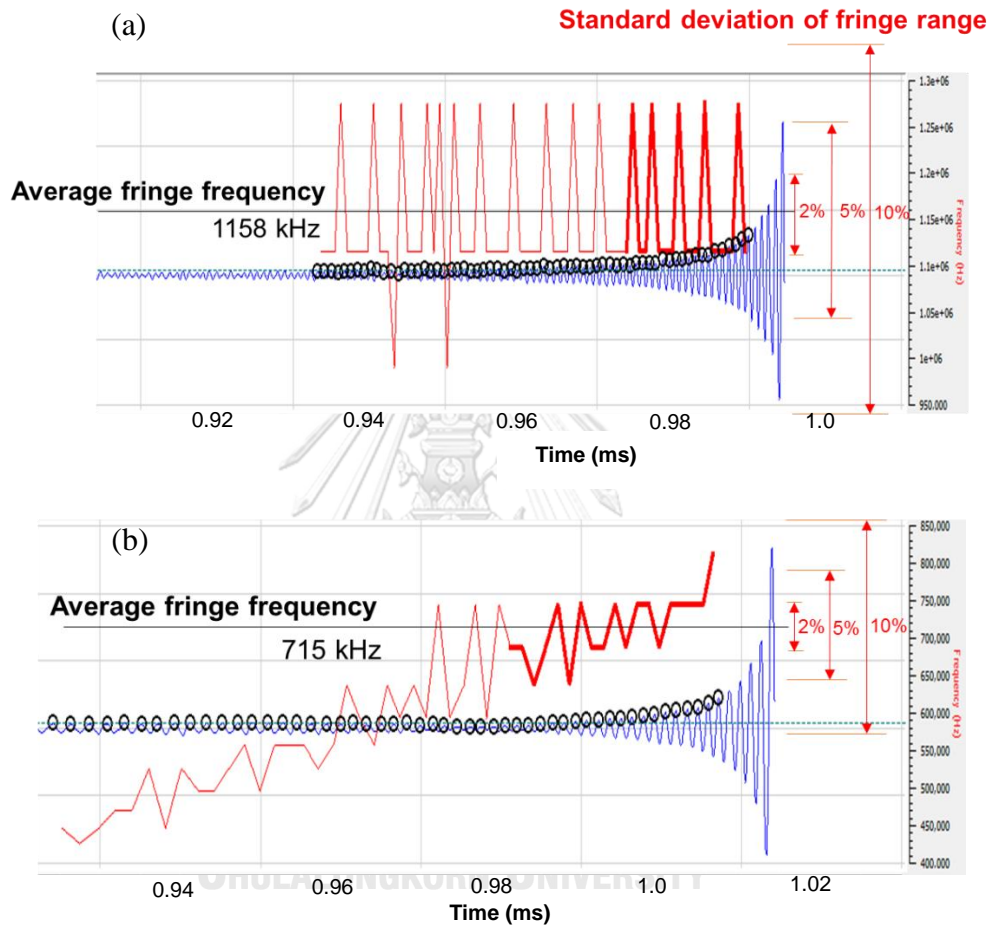
Figure 2.24 Droplet oscillation effect on the interference probe acquisition
methodology
(a) low oscillating droplet (b) Highly oscillating droplet

According to the probe methodology, the interference probe determines a droplet velocity before the droplet pierces the probe. Hence, the discrepancy due to the droplet coalescence on the probe, as found in Figure 2.18, can be neglected since it characterizes the droplet velocity before the incident happened. In addition, the increase of the minimum number of fringes used to determine droplet velocity can screen out some coalesced droplets because the increase of minimum fringes refers to an increase of the distance before collision of each droplet. Therefore, the droplet coalescence can be screen out by using a large number of minimum fringes where a certain distance between each droplet is needed in order to determine droplet velocities.
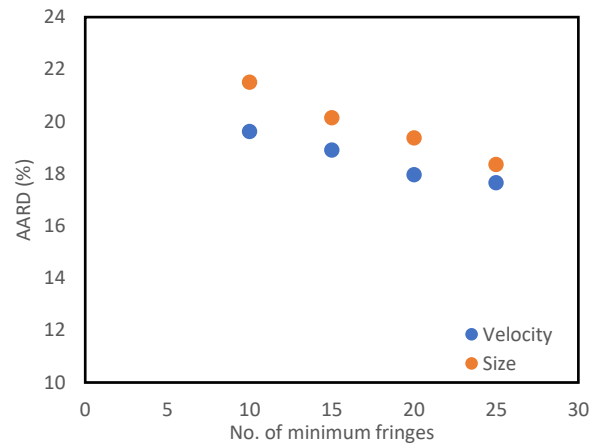
Figure 2.25 AARD of velocities and sizes comparing between the high-speed camera and interference probe at different minimum number of fringes at standard deviation of fringe frequency at 10 %

Figure 2.25 shows the AARD as the function of minimum number of fringes used to determine droplet velocities of a series of droplets. In the figure, it can be clearly seen that, the increase of the minimum number of fringes, the lower of the AARD, indicating that the better accuracy was obtained. The screen out of coalescence droplets due to increasing of the minimum fringes as well as the determination of droplet velocity by its average interference frequency was responsible for this occurrence. However, it should be noted that, the increase of the minimum number of fringes screened out a number of droplets. Thus, a large sample should be collected in order to ensure the accuracy of the data.
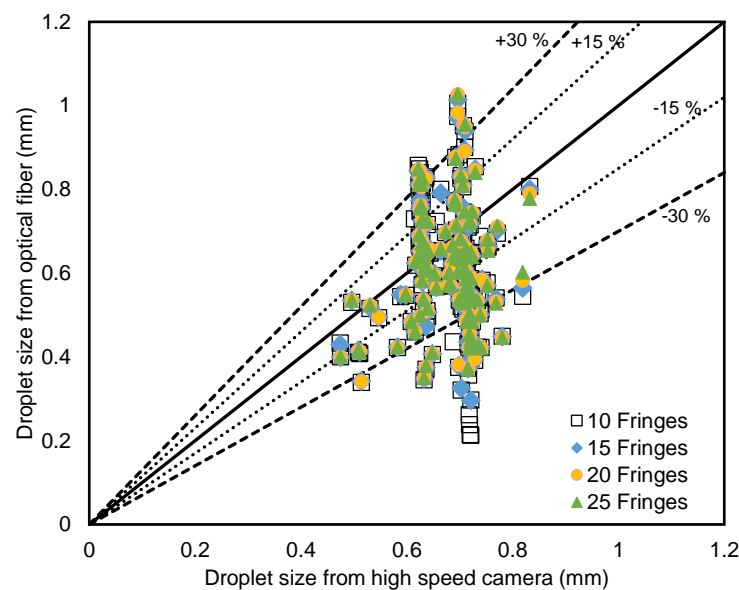
Figure 2.26 Droplet sizes of a droplet series when determining the same droplets using the high-speed camera and interference probe at various minimum numbers of fringes.

For the determination of droplet size, Figure 2.26 shows the droplet sizes from a series of droplets determined by both high-speed camera and the interference probe. The figure indicated an agreement between the techniques with a discrepancy, which caused by the error of velocities due to droplet oscillation as mentioned earlier. When the minimum number of fringes was increased, the accuracy of the probe according to the high-speed camera was improved, indicating that the better accuracy of each droplet velocity was achieved. Figure 2.25 also confirms that the AARD of the probe for the size was reduced with the increase of number of fringes.

(ii) Effect of standard deviation of fringe frequency
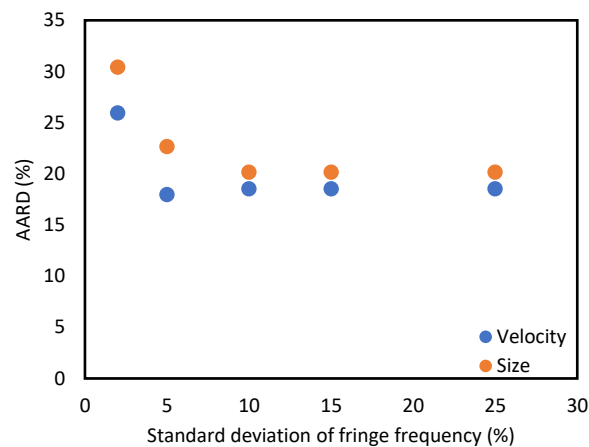
Figure 2.27 AARD of velocities and sizes comparing between the high-speed camera and interference probe at different standard deviation of fringe frequency for 25 minimum number of fringes

Standard deviation of fringe frequency is one of the factors that can be used in data treatment process in order to filter bad droplet out. Figure 2.27 shows the effect of standard deviation of fringe frequency using for droplet velocity and size determination on the AARD. It can be seen that the AARDs were high for at 2 % standard deviation and decreased when the standard deviation was larger. The optimum standard deviation of fringe frequency for the velocity determination was at 5%. However, the AARD of size at standard deviation of 5 % was larger than at standard deviation of 10 %. Hence, it can be concluded here that the appropriate standard deviation of fringe frequency for both velocity and size was 10 %. It was due to the fact that when large standard deviation of fringe frequency was concerned, the oscillating velocity of a droplet was included when calculating a droplet velocity, as shown in Figure 2.24, where 2%, 5%, and 10 % of standard deviation were illustrated. Therefore, when comparing with the high-speed camera, which determined a droplet velocity by its average velocity, the deviation in term of AARD was small. However, when small standard deviation of fringe frequency was used, the oscillating velocity determined by the probe was not included in its velocity calculation, leading to large deviation comparing with using high standard deviation.

Hence, it can be concluded that, in order to obtain an accurate result, an optimum standard deviation of fringe frequency is required as too low and too high standard deviation leaded to a discrepancy. The 10 % maximum standard deviation is recommended to use in normal operations.

(c) Comparison and summary

Table 2.3 AARD of velocities and sizes of both de-wetting probe and interference probe when compared with the high-speed camera.

Variable	Probe type	AARD (%)	p-value
Average velocity (m/s)	De-wetting probe	33.29	0.0372
	Interference probe	17.65	0.4670
Average diameter (mm)	De-wetting probe	28.79	0.5324
	Interference probe	18.36	0.0001

Table 2.3 shows the AARD of both de-wetting optical probe and light interference probe in comparing with the high-speed camera at the same condition. The AARD of de-wetting probe was significantly larger than the interference probe for both velocity and size determination at 33.29 and 28.79 % to 17.65 and 18.36 % for the de-wetting probe and the interference probe, respectively. In addition, the p-value calculated with the t-test also confirmed the fact that the interference probe yielded the same results by giving that the p-value for the velocity is larger than 0.05, where the de-wetting probe was only 0.372. However, for the sizes, the p-value of the de-wetting probe was larger and higher than 0.05, while the interference probe was at 0.0001. This occurrence was due to the standard deviation of the average droplet diameter for the interference probe that was very low comparing to the de-wetting probe. This incident confirmed that the t-test should not be used as the standalone method for hypothesis test as can be clearly seen that the AARD of the interference probe was significantly smaller.

In summary, it can be clearly seen that, both optical fiber probes can be used to determine droplet hydrodynamics. The optical fiber probes determine a droplet velocity and size via its interfacial velocity. The de-wetting probe used the behind interfacial velocity while the light interference uses the front interfacial velocity. The advantage of the interference probe is that, it does not require the collision between the probe and droplets in order to determine the droplet velocity. This advantage can reduce the effect of shear force on droplet crossing the tip of the probe.

2.4.2 Acquisition of sprays

(a) De-wetting probe

The experimental setup in this part was the one described in section 2.3.1. In this section, velocity and size distributions obtained with the de-wetting optical probe

and the high-speed camera, were compared. Note that, in this experiment, droplets were not necessarily pierced by the probe along their diameter; they were pierced at random positions. Therefore, the size measured by the optical probe was often along a chord, not a diameter. The data post processing proposed by (Clark and Turton, 1988) was therefore applied so that the sizes could be compared.

(i) Velocity distribution

Figure 2.28 shows the velocity distributions observed by the high-speed camera and by the optical probe at different flow rates and nozzle orifice sizes. In the figure, both high-speed camera and optical probe observed the increase of droplet velocities when the liquid flow rate increased. It can be seen in the figure that the droplet velocities characterized by both techniques show good agreements. Slightly higher velocities from the high-speed camera were reported, especially at high flow rates. The negative skewness was obtained by the high-speed camera while the normal distribution was observed from the optical probe, which can be indicated that the high-speed camera encountered a limitation when characterized droplets with low velocities those were typically small size droplets.
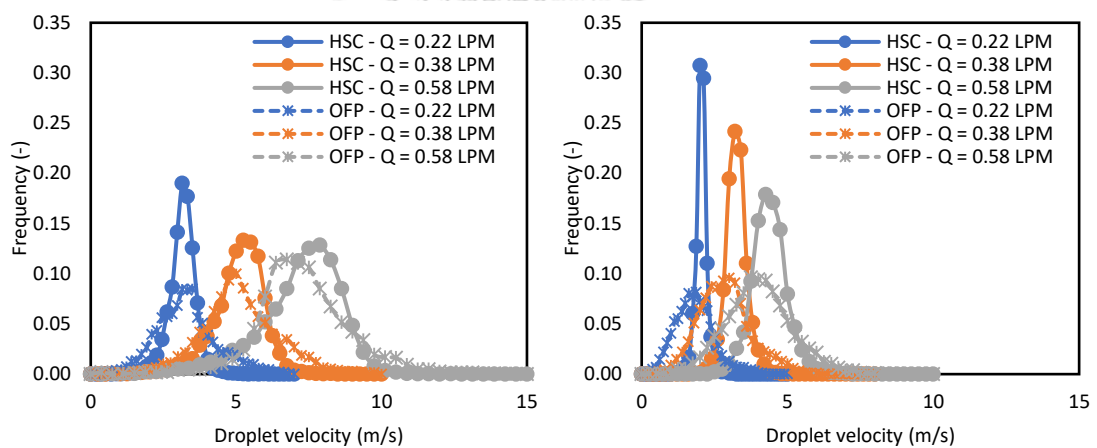
Figure 2.28 Velocity distribution of a spray system determined by high-speed camera (HSC) and de-wetting probe (OFP) at different liquid flow rates and orifice sizes (left) 0.89 mm orifice (right) 1.50 mm orifice

Table 2.4 shows the average velocity of each technique along with its statistical values. The average velocity supported the finding from Figure 2.28 where indicated that the droplets determined by the high-speed camera had smaller velocities. According to Cohen's effect size, Equation (2.24), the effect sizes between both methods were varied between 0.24-0.79 which corresponds to the non-overlapping percent of 17.0-46.6%. It can be seen that the large deviation was observed when higher flow rates, where the significant difference was observed. The different in size limitation was presumed to responsible for this difference.

The smallest diameter limit of the high-speed camera was approximately 0.1 mm, while the optical probe was capable to detect droplets with smaller diameters. The velocities of larger droplets are normally higher than those of smaller droplets, so the

velocity distribution measured by the high-speed camera would shift toward the slightly higher values and appear in the negative skewness shape as shown in the result. In addition, the optical probe did not always pierce the droplets along their center line, which led to underestimated measurements of the velocities. This phenomenon was originally reported by Hong et al., (2004).

Table 2.4 Average velocity and sizes of droplets including their performance estimators

Variable	Nozzle size	Liquid flow rate (LPM)	High speed camera	De-wetting optical probe	Cohen's Effect size	Estimated Percent of non-overlap
Average velocity (m/s)	0.89	0.22	3.07 ± 0.46	2.89 ± 1.02	0.24	17.0
		0.38	4.96 ± 0.88	4.15 ± 1.47	0.69	41.7
		0.58	7.02 ± 1.42	5.79 ± 1.69	0.79	46.6
	1.50	0.22	1.87 ± 0.26	1.75 ± 0.65	0.26	18.3
		0.38	3.10 ± 0.43	2.75 ± 0.91	0.52	33.2
		0.58	4.49 ± 0.76	4.04 ± 1.14	0.47	30.1
Average diameter (mm)	0.89	0.22	0.72 ± 0.37	0.65 ± 0.33	0.20	14.3
		0.38	0.46 ± 0.25	0.28 ± 0.17	0.86	49.5
		0.58	0.37 ± 0.17	0.21 ± 0.13	1.07	58.1
	1.50	0.22	1.18 ± 0.73	0.98 ± 0.42	0.35	23.5
		0.38	0.73 ± 0.44	0.83 ± 0.40	0.25	17.2
		0.58	0.57 ± 0.34	0.43 ± 0.26	0.48	31.0

Noted that the large deviation found in section 2.4.1(a) did not occur here and it is apparent that the effects of droplet oscillation and coalescence became less significant when the probe was used in the real-world spray system where the droplets are smaller, moving faster, and less dense (the average droplet frequency of droplets produced by the syringe was 353.3 droplets per second comparing to 35.6 droplets per second when used the industrial nozzle) and the statistics are based on large numbers of droplets.

(b) Interference probe

Figure 2.29 shows the velocity distribution obtained from both high-speed camera and the interference probe for different orifice size. The trends obtained by both

techniques were the same. However, the velocity distributions determined by the high-speed camera were slightly larger than those of the interference probe in every case.
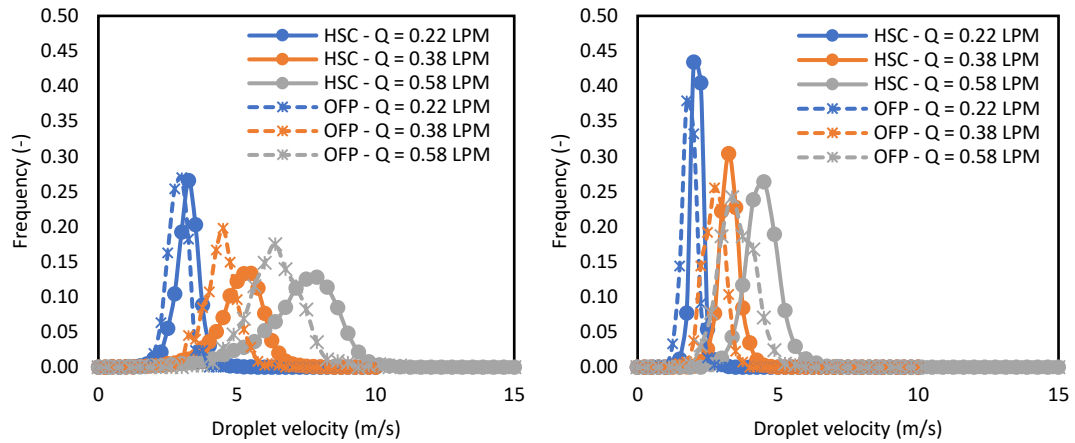
Figure 2.29 Velocity distribution of interference probe for different liquid flow rates and nozzle size comparing with high-speed camera (Left) 0.89 mm orifice (Right) 1.50 mm orifice

When using the results from Figure 2.29 to determine average droplet velocities of each technique, their averages can be illustrated as in Figure 2.30. In the figure, it can be seen that the average velocities obtained from the high-speed camera were slightly higher than those obtained by the light interference probe. The large deviation was significantly observed when higher liquid flow rates were used indicating that when the droplet sizes were smaller, the larger discrepancy was achieved. The difference in size limitation was presumed to responsible for the difference as same as in the case of the de-wetting probe.
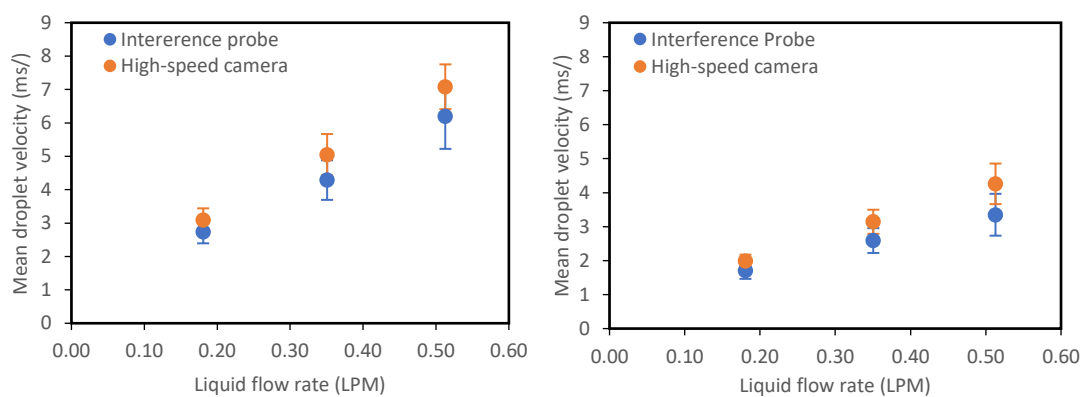
Figure 2.30 Average droplet velocity of interference probe for different liquid flow rates and nozzle size comparing with high-speed camera (Left) 0.89 mm orifice (Right) 1.50 mm orifice

Figure 2.31 shows that the average droplet sizes determined by the interference probe especially for the 0.89 mm orifice, Figure 2.31(Left), were smaller than those characterized by the high-speed camera especially at high flow rate. This difference

supported the explanation according to the size different limit mentioned earlier. In addition, it can be clearly seen that the average droplet size in case of 1.50 mm orifice, which produced larger droplets than 0.89 mm orifice, determined by both techniques were in a good agreement as the standard deviations of the results were moderately high and could be considered that the results obtained by both techniques were not significantly different.
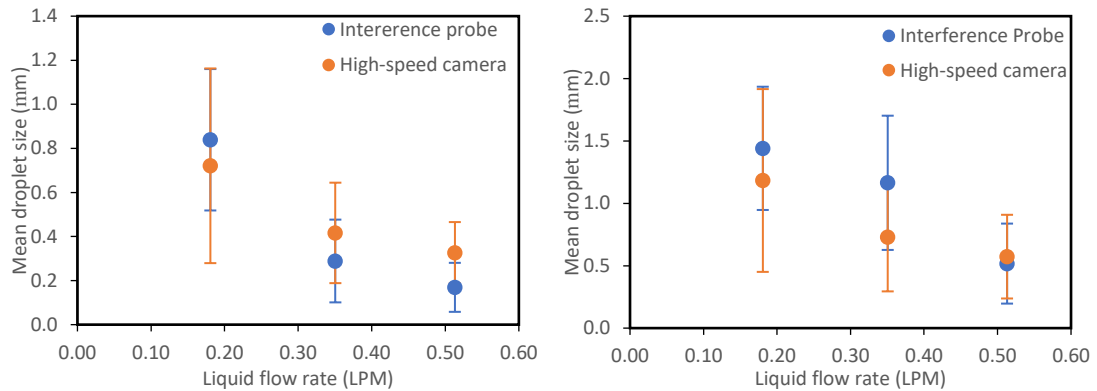
Figure 2.31 Average droplet sizes of interference probe for different liquid flow rates and nozzle size comparing with high-speed camera (Left) 0.89 mm orifice (Right) 1.50 mm orifice

In conclusion, it can be seen that the interference probe and the high-speed camera had a better agreement than the de-wetting probe. However, in order to clearly identify this assessment, the comparison of all techniques is conducted in the next section.

(c) Comparison and summary

Figure 2.32 shows the average droplet velocity and size at different horizontal position from the nozzle center. It can be seen that the average droplet velocities determined by every technique show the same trend. The droplet velocity obtained from the high-speed camera was larger than the other techniques where the limit on the droplet size was presume to responsible for this occurrence. For the size and average sizes, all techniques gave the same trend but a large deviation was found when the distance from the center of the cone of spray was large especially for the de-wetting probe which confirmed the finding of Hong et al., (2004). However, in case of the interference probe, as mentioned earlier, the probe normally determines droplet sizes approximately at near their diameters, due to the fact that the reflected light can only be detected when the droplet approaches the probe at its center line, where the angle of contact is almost perpendicular. When droplets approach the probe at other positions, the light reflected out of the probe tip and therefore the droplet is not count for the velocity and size determination.
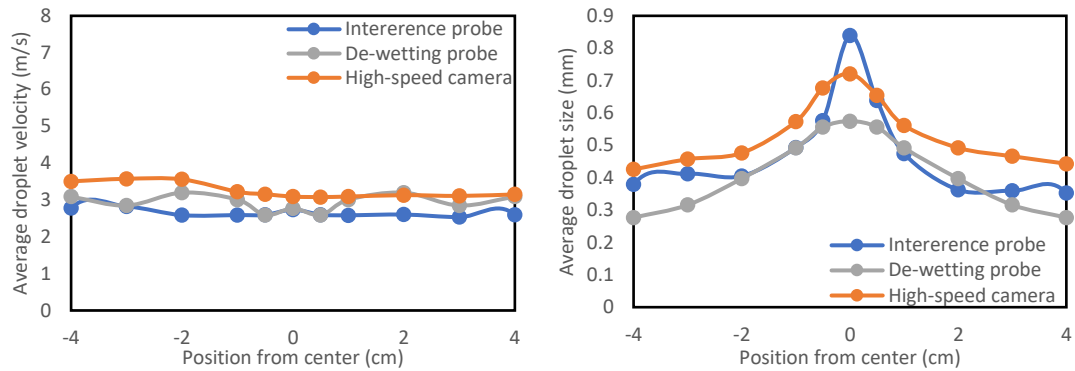
Figure 2.32 (Left) Average droplet velocity and (Right) average sizes at different position from center at 5 cm underneath 0.89 mm orifice for the liquid flow rate of 0.22 LPM

When compared average velocities of the high-speed camera, the de-wetting probe, and the light interference probe at position underneath the nozzle of 0.89 mm; it can be seen in Figure 2.33 that the same trend for every technique was achieved. The average velocities determined by the high-speed camera were the highest in every case; the minimum size limit at 0.1 mm of the high-speed camera was responsible for the incident. It can be confirmed that when using both optical probes to determine average droplet velocity in every condition, the average velocities were the same. This finding supported the minimum size limit of the high-speed camera and supported that both optical probes can be used to determine droplet velocities accurately.
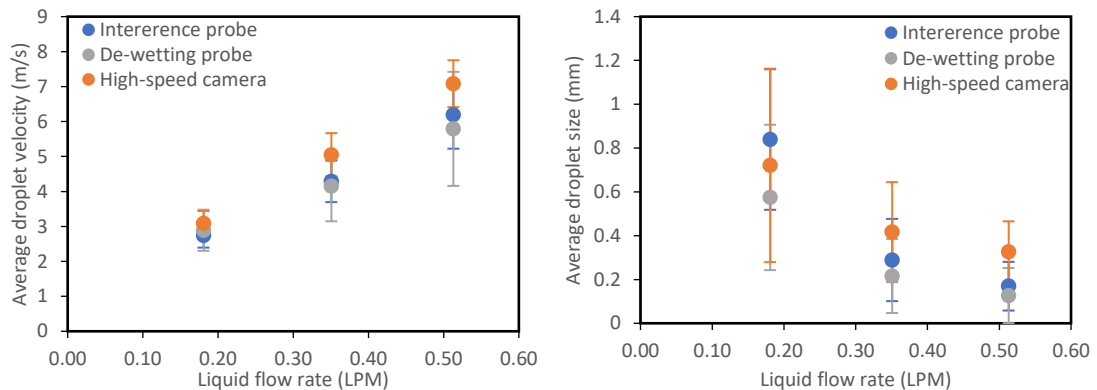
Figure 2.33 (Left) Average velocity and (Right) Average droplet size determined by different techniques at various liquid flow rates for 0.89 mm orifice

For the droplet sizes, all techniques also gave the same trend. The average sizes determined by the high-speed camera were mostly the highest among all other results except for the lowest flow rate where the interference probe gave a slightly larger size. At higher flow rates, the optical probes both gave the smaller sizes comparing with the high-speed camera. However, it can be seen that the average droplet sizes determined by the light interference probe were slightly larger than the de-wetting probe because

the interference probe determines droplet sizes only at the center position where the sizes determined by the probe were very near to their actual diameter.

Hence, it can be concluded here that the light interference probe had an advantage over the de-wetting probe as it did not require the probability data treatment in order to obtain the size distribution of a spray, where is one of the most disadvantage of the de-wetting probe. In addition, the light interference probe has lower size limitation, comparing with the high-speed camera. However, the limitation of the probes should be further discussed in order to use them properly. The next section determined the limit of both de-wetting probe and light interference probe.

2.4.3 Probe potentials and limitations

(a) De-wetting probe

(i) Velocity limit

From Equation (2.5), it is clear that the maximum velocity limit depends on three variables: the probe constant (L_s), the number of minimum points possibly recorded on the experimental curve, and the acquisition rate. By using L_s of the probe and varying its acquisition rate, the maximum velocity limit can be expressed as shown in Table 2.5 as a function of the number of minimum points. The number of minimum points usually ranges between 3 and 10 and the acquisition rate was varied from 1 to 6 MHz.

Table 2.5 Velocity and size limits of the de-wetting optical probe

Acquisition Rate (MHz)	Max velocity (m/s)				Min chord (μm)				
	3 points	5 points	7 points	10 points	V_{max}	$0.8V_{max}$	$0.5V_{max}$	$0.3V_{max}$	$0.1V_{max}$
1	5.7	3.4	2.4	1.7	17.0	13.6	8.5	5.1	1.7
2	11.3	6.8	4.9	3.4	17.0	13.6	8.5	5.1	1.7
3	17.0	10.2	7.3	5.1	17.0	13.6	8.5	5.1	1.7
4	22.7	13.6	9.7	6.8	17.0	13.6	8.5	5.1	1.7
5	28.3	17.0	12.1	8.5	17.0	13.6	8.5	5.1	1.7
6	34.0	20.4	14.6	10.2	17.0	13.6	8.5	5.1	1.7

In the table, increasing the acquisition rate raises the maximum velocity limit for each number of minimum points. The difference of number of minimum points also changes the maximum velocity: the more numerous the points used for T_R, the lower the limit for the maximum velocity that can be observed by the probe. With higher numbers of points, higher signal accuracy is obtained. Therefore, in order to obtain the best result for the velocity determined by the optical probe, the highest possible acquisition rate is recommended. However, the amount of memory consumed by the acquisition system should also be considered.

Figure 2.34 shows the effect of the acquisition rate on the droplet velocity determination by the optical probe and compares the results with that from the high-speed camera. The result from the high-speed camera indicates that the range of droplet velocities with the spray system was 5-12 m/s. The results from the optical probe for acquisition rates higher than 2 MHz show the same trends as the result from the high-speed camera. However, the result for 1 MHz acquisition rate is deviated. According to Table 2.5, the maximum velocity that can be determined with the 1 MHz acquisition rate is lower than 5.7 m/s even for 3 minimum points. This result confirms the calculation used for the determination of the maximum velocity limit.
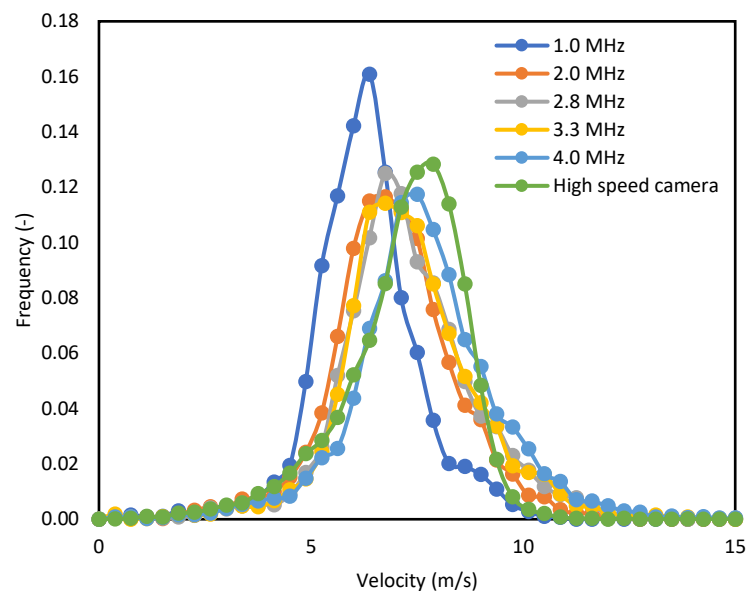
Figure 2.34 Effect of optical probe acquisition rate in a spray system with 0.89 mm nozzle size operating at 0.59 LPM, and comparison with the high-speed camera results

(ii) Size limits

Table 2.5 indicates the minimum chord that can be measured with the optical probe used in this experiment. It shows that, when operating at 10 % of the maximum velocity, the minimum size that the probe can determine is 1.7 μm, which is very much smaller than with the high-speed camera. However, it should be noted that the size limit mentioned in Table 2.5 was calculated theoretically.

In the actual regime, the very small droplets may have been destroyed by collisions and, moreover, the probability of small droplets coming into contact with the probe is extremely small. In addition, since the probe used the light reflected at the probe tip to determine every droplet size, the minimum size that can be truly determined by the distance that liquid needs to cover the probe from the probe tip in order to change the probe signal from gas phase to liquid phase (See Figure 2.7 for detail). Figure 2.35 shows the accumulated voltage change from gas phase to liquid phase according to the distance that liquid covered from the probe tip. It can be seen that, the liquid needs to

cover at least around 50 µm in order to change the signal 90 %, which was fairly enough to address the changed voltage as liquid signal (V_L in Figure 2.7). Figure 2.36 illustrates the previous explanation that 90 % of the active zone was within the range of 50 µm from the probe tip; therefore, it can be presumed that a droplet has to be larger than 50 µm in order to avoid the voltage to change back to gas phase before it reaches the liquid voltage level (V_L). It should be noted again that this approach was based on the voltage change when the liquid covers the probe tip. For such small droplets, droplets rebounds and strong viscous dissipation can probably affect the dynamics and the size limitation might be larger than 50 µm.
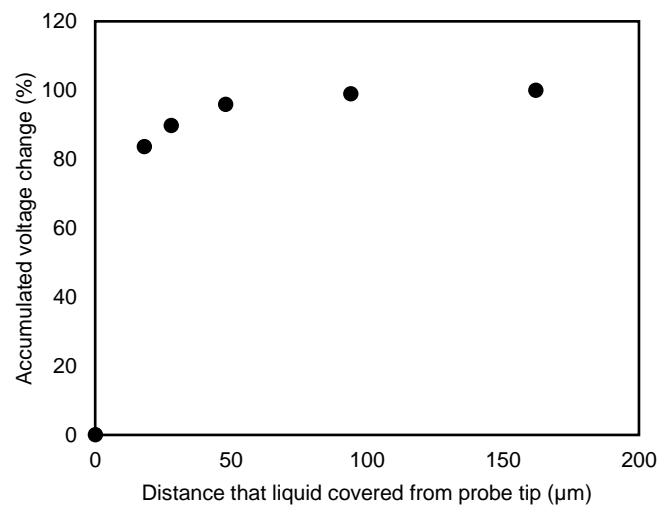
Figure 2.35 Accumulated voltage change as a function of distance that liquid covered the probe from the probe tip
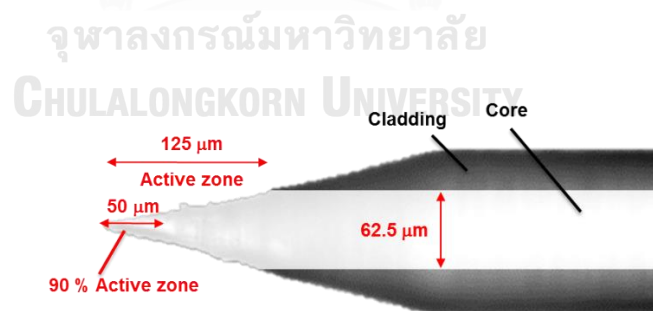
Figure 2.36 De-wetting probe characteristic and its active zone

In summary, the minimum theoretical size limit of the optical probe depends on the ratio between droplet velocity and the maximum velocity (V/V_{max}). With the lowest ratio of V/V_{max}, the smallest size limit can be reached at 17 µm. However, in order to avoid the unstable signal from the shortage of liquid coverage from the probe tip, the probe should not be used with droplets having their diameter smaller than 50 µm.

(b) Interference probe

(i) Velocity limits

Table 2.6 shows the number of points detected by the light interference probe calculated by Equation (2.17). When the acquisition frequency is high, the number of points is large where higher accuracy can be guaranteed. Moreover, a droplet having high velocity needs a higher acquisition frequency in order to have enough number of points, where at least 10 points are recommended. Therefore, with high acquisition frequency, droplets having very high velocity up to 15 m/s can be easily determined by the probe even using the acquisition frequency of 250,000 kHz. However, the amount of data consumed by the acquisition should also be concerned.

Table 2.6 Number of points detected by the probe at various acquisition frequencies

V (m/s)	Number of points detected by the interference probe					
	10,000 kHz	50,000 kHz	100,000 kHz	200,000 kHz	250,000 kHz	500,000 kHz
0.5	16	78	155	310	388	775
1	8	39	78	155	194	388
2	4	19	39	78	97	194
3	3	13	26	52	65	129
4	2	10	19	39	48	97
5	2	8	16	31	39	78
6	1	6	13	26	32	65
7	1	6	11	22	28	55
8	1	5	10	19	24	48
9	1	4	9	17	22	43
10	1	4	8	16	19	39
11	1	4	7	14	18	35
12	1	3	6	13	16	32
13	1	3	6	12	15	30
14	1	3	6	11	14	28
15	1	3	5	10	13	26

(ii) Size limits

Table 2.7 shows the minimum detectable droplet size of the interference probe using Equation (2.18) at the acquisition frequency of 10,000 kHz. The frequency of 10,000 kHz was selected to represent the minimum size due to it was the lowest one used in the interference probe. In the table, although the minimum acquisition frequency was used, the minimum sizes at the very high velocity are still very small, approximately 30 µm when used 20 points. Therefore, when uses with the normal acquisition frequency (more than 100,000 kHz), the minimum limit of the probe is significantly smaller that in Table 2.7.

Table 2.7 Minimum detectable size of the interference probe at aqusition frequency of 10,000 kHz

V (m/s)	Minimum detectable size by the light interference probe (µm)				
	3 points	5 points	7 points	10 points	20 points
0	0.0	0.0	0.0	0.0	0.0
0.5	0.2	0.3	0.4	0.5	1.0
1	0.3	0.5	0.7	1.0	2.0
2	0.6	1.0	1.4	2.0	4.0
3	0.9	1.5	2.1	3.0	6.0
4	1.2	2.0	2.8	4.0	8.0
5	1.5	2.5	3.5	5.0	10.0
6	1.8	3.0	4.2	6.0	12.0
7	2.1	3.5	4.9	7.0	14.0
8	2.4	4.0	5.6	8.0	16.0
9	2.7	4.5	6.3	9.0	18.0
10	3.0	5.0	7.0	10.0	20.0
11	3.3	5.5	7.7	11.0	22.0
12	3.6	6.0	8.4	12.0	24.0
13	3.9	6.5	9.1	13.0	26.0
14	4.2	7.0	9.8	14.0	28.0
15	4.5	7.5	10.5	15.0	30.0

However, when used the same approach as the de-wetting probe, the active zone of the light interference probe is 25 µm as shown in Figure 2.37. Hence, smaller droplet sizes than 25 µm should lead to the incomplete voltage change from gas phase to liquid phase and, therefore, the practical size limit of the probe should be at least 25 µm. Nevertheless, it should be taken in to account that, for such small droplets, droplets rebounds and strong viscous dissipation can probably affect the dynamics and the size limitation might be larger than this theoretical approach.
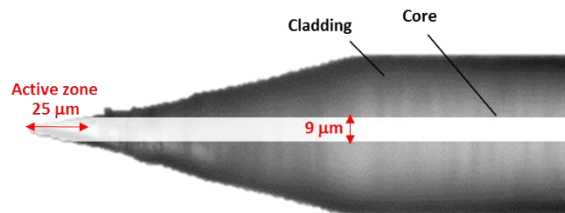
Figure 2.37 Light interference probe and its active zone

(c) Advantages and drawbacks

With the results shown in the previous section, it is clear that both optical probes have the potential to determine the hydrodynamics of spray systems. However, to reach its full potential, the optical probe should be used in the right conditions. Table 2.8

summarizes the advantages and disadvantages of optical probes and high-speed cameras.

Table 2.8 Advantages and disadvantages of optical probes and high-speed camera for determination of droplet size and velocity

High speed camera	De-wetting optical probe	Light interference probe
Advantages	**Advantages**	**Advantages**
• Can be visualized • Determines droplet size and velocity directly • Plane measurement	• Able to detect very small droplet sizes (Theoretically > 50 µm) • Liquid fraction determination • Can be used in mildly dense spray conditions	• Able to detect very small droplet sizes (Theoretically > 25 µm) • Liquid fraction determination • Can be used in dense spray conditions • Roughly measure droplet diameter
Disadvantages	**Disadvantages**	**Disadvantages**
• Requires a camera setup with high resolution and frame rate • Requires an accurate and effective image processing method • Can be used only in visible conditions i.e. not good with dense spraying	• Cannot measure droplet diameter directly • High deviation if used with small numbers of droplets • Measures interfacial velocities of droplets (Oscillation velocities are included) • Point measurement • Requires calibration	• High deviation if used with small numbers of droplets • Measures interfacial velocities of droplets (Oscillation velocities are included) • Point measurement

One of the major advantages of the optical probes is that it can be used in mildly dense spraying conditions, which are difficult to capture and process accurately with high-speed cameras. Moreover, the probe can determine the local liquid fraction directly, which the high-speed camera is not able to do. However, it was found that the de-wetting probe should not be used at highly dense spray conditions without screening process since the droplet coalescence would lead to a large discrepancy. However, the methodology of the light interference probe can overcome this problem.

In addition, the optical probe size and velocity limits are more favorable to those of high-speed cameras for both type of the optical probe. The camera requires a very high acquisition rate and also high resolution in order to provide good accuracy. However, for the de-wetting probe, the probe has the great disadvantage of not being able to measure droplet sizes directly and requires a probability-based method in order to obtain the predicted diameter distribution result. Moreover, the probe requires a calibration method from the manufacturer in order to obtain the constant for calculation, which are L_s and b. Nevertheless, this disadvantage was disregarded when using the light interference probe; nonetheless, the discrepancy due to the droplet trajectory should also be concerned.

Although there are a lot of advantages of the optical probes, the probes are handicapped by the effect of droplet oscillation when determining low droplet velocities because of their methodologies of measuring droplet velocities by their interfacial velocity. Fortunately, the effect of droplet oscillation and coalescence are less significant when operating with usual spraying systems.

2.5 Conclusion

The experiment was set up in the aim of identifying the potential of two optical probes, a de-wetting probe and a light interference probe that used to determine the hydrodynamics of spray systems. The accuracy of the probe was assessed by comparing its results with those from a high-speed camera.

When comparing the series of droplets produced by a syringe as the nozzle, it was found that the both optical probes gave an explainable discrepancy comparing with that of the high-speed camera. The deviation was caused by the different methodologies because the optical probe determined droplet velocities and sizes at the interface of droplets, while the high-speed camera determined them from the displacement of droplet centroids. Therefore, when observing oscillating droplets, the optical probes and the high-speed camera gave different results. The values could be overestimated or underestimated by the optical probe depending on the oscillating regime of droplets when contacting the probe. For the de-wetting probe, droplet coalescence also influenced the probe results; whilst for the light interference probe, the coalescence was insignificant. Fortunately, the acquisition frequency data treatment can be performed to eliminate the effect of droplet coalescence for the de-wetting probe. In addition, it also found that the comparing velocity and size results between the optical probes and the high-speed camera were in good agreement especially for the light interference probe.

When operating in the industrial spray conditions, consistent results, especially for the velocity distributions, were achieved with both optical probes and the high-speed camera. The oscillation and coalescence effects were significantly diminished because the droplets in the spray had smaller sizes, higher velocities, and less dense when compared to the droplets produced using the syringe. The deviation, especially in the size of the droplets, was logically presumed to arise from the off-center contact between

the probe and the droplets, the post-processing methodology, and the size limits of the techniques.

In addition, the probe limits in the velocity and size measurement were calculated theoretically and the results showed that the velocity and size limits were strongly dependent on the acquisition rate for both types of the probes. With the higher acquisition frequency, the higher velocity limits both of the probes can be reached. However, for both probes, when using their active zones to determine the smallest droplet size they abled to observe, the 50 µm and 25 µm were the limit for the de-wetting probe and the light interference probe, respectively.

Furthermore, one of the advantages of the optical probe is that it can directly measure the liquid fraction of the spray system and, moreover, able to determine droplet velocities and sizes in mildly dense spray conditions, which is hard to perform using a high-speed camera or other optical techniques. However, it should be noted that, when the local liquid fraction is larger than 50%, the discrepancy of the probe is highly induced by the droplet coalescence. Therefore, the accurate droplet velocity, as well as the size, could be obtained when the local liquid fraction is below 50%.

From this chapter, the performance of optical fiber probe has been confirmed to use in the actual spray condition. Therefore, in the next chapter, the optical probe will be used as one of the equipment for characterization of hydrodynamics of spray column. The droplet sizes, velocities as well as liquid fraction were studied using the de-wetting optical probe along with the high-speed camera. The hydrodynamics of spray in terms of specific interfacial area were compared with a bubble column in order to determine the suitable one in the mass transfer purpose.

Chapter 3

Three-phases spray and bubble columns: Hydrodynamics

3.1 Abstract

The hydrodynamics comparison between a bubble column and a spray column was investigated in this chapter. A high-void packing and ring-shaped particles were introduced into the column in order to study the effect of the solids on the hydrodynamics. A significant change was acquired depending on the conditions of the orifice size used in the column. This chapter planned to combine with Chapter 5 to publish not only the effect of solids but also the comparison of mass transfer in terms of power consumption. The finding is expected to be a guideline for consideration of suitable equipment that should be used in industrial processes.

3.2 Introduction

In this chapter, the hydrodynamics of gas-liquid bubble column and spray column including the gas-liquid-solid ones were investigated. One of the equipment used for the consideration of the spray hydrodynamics was the de-wetting optical fiber, which its performance was described and analyzed in Chapter 2. The liquid and gas phases used in this study were sodium hydroxide solution and carbon dioxide, respectively. In addition, two types of solid phase were introduced, high void packing and movable particles. The effect of the solid phases on the hydrodynamics, which including the size, velocity, and fraction, was examined, analyzed, and compared in terms of the power consumption.

3.3 Methodology

3.3.1 Experimental setup

(a) Bubble column setup

The experimental setup of bubble column using for absorption of CO_2 is shown in Figure 3.1. The solution of sodium hydroxide 0.05%wt in the storage tank was fed to the top of a 19 cm cylinder glass column. The height of the liquid phase in the column was fixed at 65 cm while the free-board height was 5 cm. The flow rate of the liquid was regulated by a rotameter equipped after a pumping system. A pressure gauge was placed before the column in order to measure the pressure drop. In this work, the liquid flow rate between 0.19 – 1.06 LPM was used. For the gas phase, CO_2 at the concentration of 99.998% was fed from a CO_2 vessel (Air liquide, France) and mixed with air before fed into the column via a gas sparger. A pressure sensor was equipped before the gas sparger to determine the gas pressure drop. The gas flow rate was regulated at the range of 2.0-10.8 LPM. The concentration of CO_2 at the inlet was regulated constantly at 15.5%vol, which mimicking the concentration of fuel

combustion for electrical production (Spigarelli, 2013). A high-speed camera (Vision research, Miro - 110, USA) connecting to a computer was placed at the center of the column in order to investigate bubble sizes as well as their velocity.
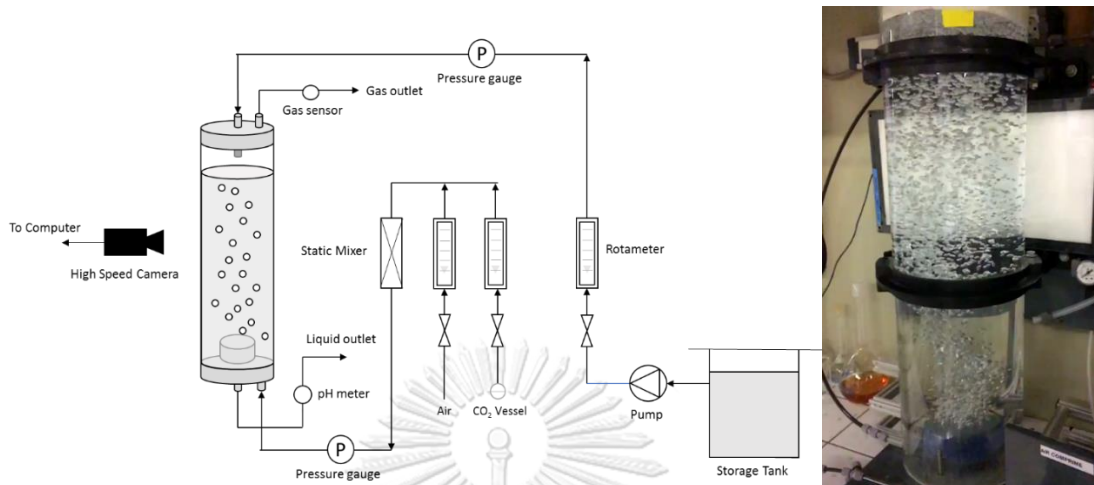
Figure 3.1 Experiment setup of CO_2 absorption with bubble column

The structure of the gas sparger used in this work is illustrated in Figure 3.2. The gas sparger having the diameter of 11 cm and 4.3 cm height were used. Each gas sparger contained 21 holes with 1.414 cm interval distance between each hole. There were 3 sizes of the orifice used in this work: 0.5, 0.8, and 1.2 mm.
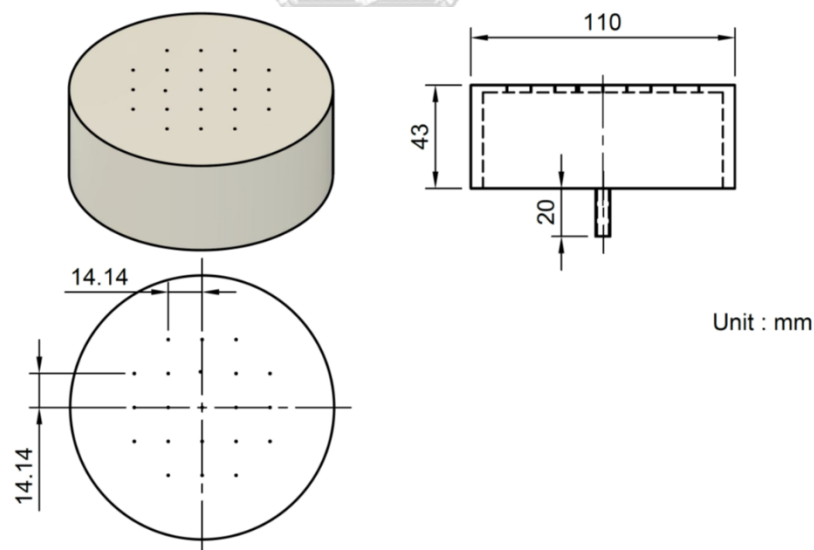
Figure 3.2 Perforate gas sparger equipped at the bottom of the bubble column

(b) Spray column setup

The experiment setup for gas-liquid absorption via spray column was setup according to Figure 3.3. Most of the experimental setup was the same as the bubble column. The liquid phase (solution of 0.05%wt NaOH) was fed via pump to the top of

the column and injected in a spray regime via a full-cone spray nozzle having the orifice sizes of 0.89, 1.20, 1.50, and 2.00 mm from Spray system. Co, USA. The characteristics of the spray nozzle are shown in Figure 3.4.
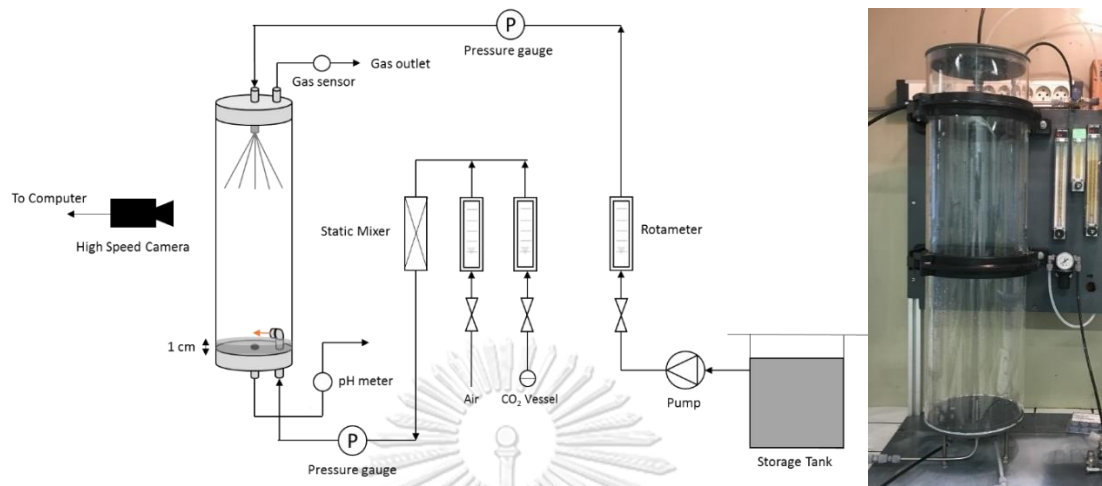
Figure 3.3 Experimental setup of CO_2 absorption with spray column

For the gas phase, the gas inlet was mixed between air and CO_2 from a vessel where the concentration of 15.5% of CO_2 was fixed. The pressure used to flow the gas at a certain flow rate was measured by a pressure sensor. Furthermore, a portion of liquid phase having a height of 1 cm was continually preserved at the bottom of the column to avoid the gas phase to leak out. The high-speed camera (Vision research, Miro – 110, USA) was placed at the position of 5, 25, and 60 cm from nozzle in order to investigate droplet sizes and velocity for hydrodynamic study of spray system. Noted that the gas flow rate used in this work was in the range of 2.0-10.8 LPM.

Figure 3.4 Full cone spray nozzle at different orifice sizes
(Left to right) 0.89 mm, 1.20 mm, 1.50 mm, and 2.00 mm

(c) Liquid phase

In this work, the absorption of CO_2 was performed using the solution of NaOH at 0.05%wt as the absorption agent. The dilute concentration was selected in order to investigate the performance of CO_2 absorption using as least chemical as possible. However, the utilization of only water could not yield a promising result. Therefore, the base solution was used in order to accelerate the mass transfer rate as well as its capacity.

The physical properties of the NaOH solution in comparing with tap water are shown in Table 3.1. The liquid densities were measured using a weigh scale while the surface tension and viscosity were determined using Wilhelmy plate method and viscometer (RM180 Rheomat Rheometric Scientific), respectively. For the alkalinity, the titration method was performed according to the method of Bridgewater et al., (2017) .

Table 3.1 Physical properties of NaOH solution comparing with tap water

Property	Tap water	NaOH 0.05%wt
Density (kg/m^3)	994.73	996.26
Surface Tension (mN/m)	71.4 ± 0.5	71.7 ± 0.5
Viscosity (mPa s) @ 20°C	0.965	0.975
pH	7.7	12.15
Alkalinity (mg/L as CaCO$_3$)	100.0	100.0

(d) Solid phase

(i) Moving particles
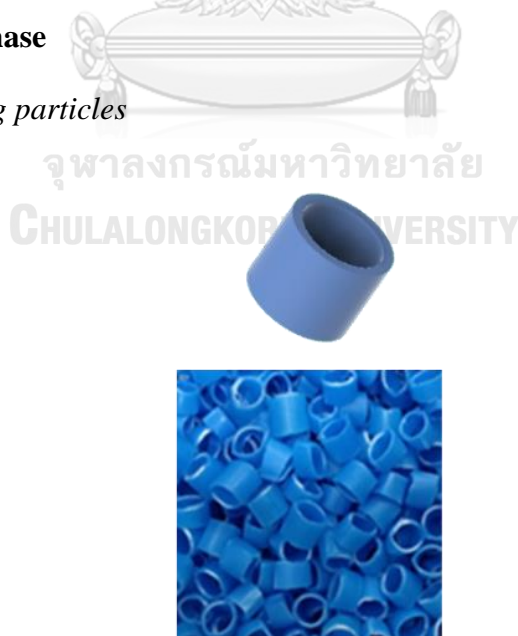
Figure 3.5 Ring-shaped movable solid particles made of polypropylene

According to Appendix D and in Wongwailikhit et al., (2018), the ring shaped solid, as shown in Figure 3.5 and detailed in Table 3.2, was the optimal particle shaped

that have a capability to enhance the mass transfer in the bubble column without spending extra power consumption. Although the suitable loading concentration of the particles was between 5 to 10 % by volume, the concentration of the particles was specified as 5 % by volume. The loading of 10 % was not used since the total liquid height was fixed constantly at 65 cm. The use of more than 5 % should be avoided as it would reduce the volume of liquid phase in the column and the mass transfer performance would be diminished.

Table 3.2 Solid particles physical properties.

Properties	Value
Material	Polypropylene (PP)
Density (kg/m^3)	946
Shape	Ring
Particle Equivalent Diameter (mm)	4.15
Bulk Porosity (-)	0.78
Shape Factor (-)	0.35

(ii) Packing

Figure 3.6 shows the characteristic of the high void packing used in this experiment. The packing had the diameter of 19 cm and the height of 57 cm. It was made from the stainless-steel wire mesh that consisted of 6,116 units of square meshes where each unit had the dimension of 1.3 cm x 1.3 cm. The properties of the packing are expressed in Table 3.3.
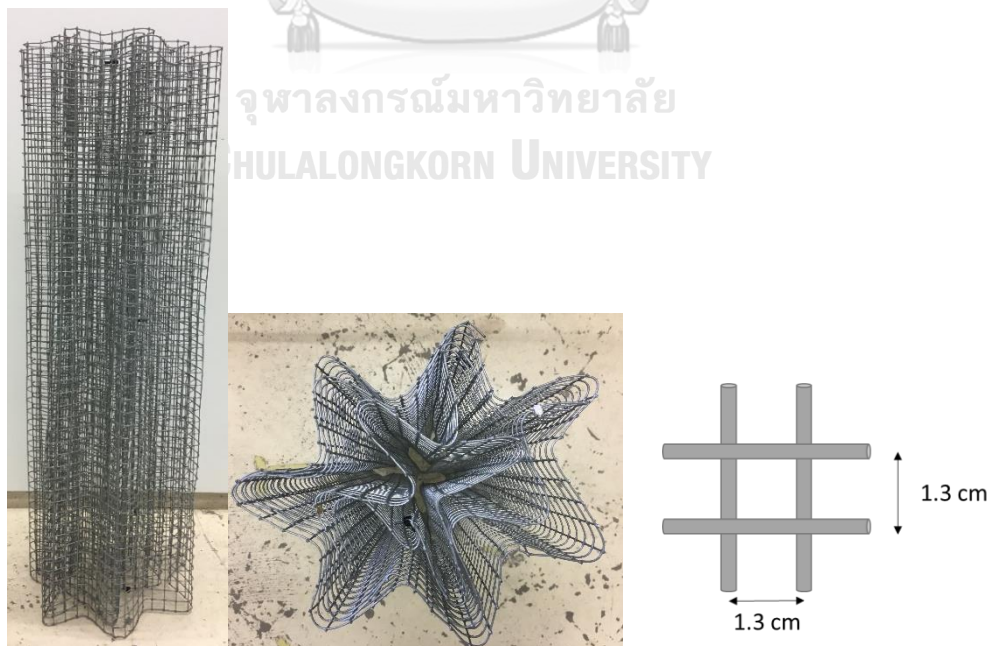
Figure 3.6 High void packing
(Left to right) Side view, top view, and diagram of each mesh in the packing

The high-void packing has the bulk volume of 0.016 m^3 and estimated total surface area of 0.507 m^3. By calculating the specific interfacial area for mass transfer, total specific interfacial area was equal to 31.69 m^{-1}. Although its specific interfacial area was not enormously high, the solid fraction of the packing was extremely low, leading to lower pressure was needed comparing with the conventional packing.

Table 3.3 Properties of high-void packing

Property	Value
Overall diameter (cm)	19
Height (cm)	57
Mesh dimension (cm x cm)	1.3 x 1.3
Number of meshes (-)	6,116
Material thickness (mm)	1
Bulk volume (m^3)	0.016
Total surface area (m^2)	0.507
Specific interfacial area (m^{-1})	31.69
Solid fraction (-)	0.0092

3.3.2 Hydrodynamics parameters

(a) Image acquisition and processing

(i) Bubble column

A high-speed camera from Vision Research, Phantom Miro – M110, was used for image acquisition. A backlight from PHLOX with a luminance of 30383 cd/m^2 and a uniformity of 93.65 % was set up as the image background. The photos were captured by Carl Zeiss 50mm f/1.4 Planar at 1,600 fps.
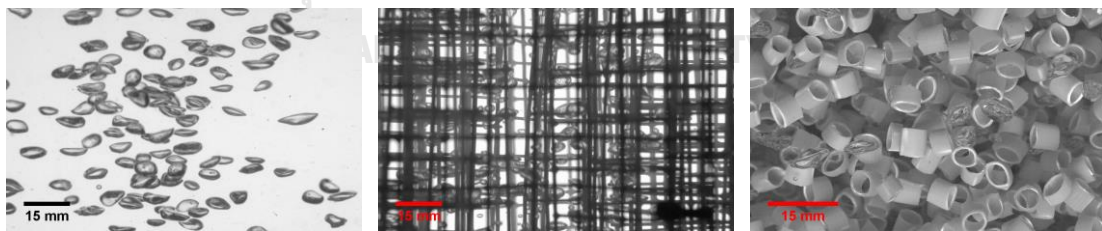
Figure 3.7 Bubbles captured with the high-speed camera in various conditions
(Left to right) No solid, packing, and ring shape particle

The examples of the captured images of bubble in the bubble column at different conditions are shown in Figure 3.7. It can be seen that in the case of bubble where no solid was presented, the bubble sizes as well as velocities were able to determine simply. However, with the presences of the wire packing and the ring shape particles, bubbles were concealed by the solids. Therefore, the bubble sizes and velocities were difficult to obtain programmatically. Consequently, in order to avoid the bias from

using different techniques, the bubble sizes and velocities in any cases were determined manually using the tools in the ImageJ® program.

(ii) Spray column

The same technique as in Chapter 2 was used for acquisition and processing of the droplet images. However, the photos were captured at 32,000 fps due to extremely larger velocity of droplets than bubbles. An example of the captured and image processing at 5 cm from the nozzle position is described already in Chapter 2 as shown in Figure 2.13. The images were captured in an 8-bit grayscale format. The captured images were processed and analyzed with ImageJ® software. The most suitable level of gray (threshold) for each image was selected and the images were then converted into binary images as shown in Figure 2.13. These binary images were used to determine properties including projected area (A) and perimeter (P).

(b) Hydrodynamics determination of bubble column

(i) Bubble diameter

Bubble diameter and bubble rising velocity were determined with the ImageJ® program. Samples of 200-300 bubbles were randomly chosen from each experiment and their equivalent diameters were measured. In this work, the equivalent spherical diameter for each bubble was used with the assumption that the projected shape of any droplet could be treated as an ellipse. This equivalent diameter could be determined with the correlation of Heyt and Diaz, (1975) as shown in Equation (3.1), where d_e is the equivalent spherical diameter.

$$d_e = 1.55 \, A_B^{0.625} / P_B^{0.25} \tag{3.1}$$

The Sauter mean diameter or the surface-to-volume diameter (d_{32}) was used to represent the average diameter ($d_{B, avg}$) for each experiment as shown in Equation (3.2).

$$d_{B,avg} = d_{32} = \frac{\sum_i n_i d_i^3}{\sum_i n_i d_i^2} \tag{3.2}$$

where n_i is the number of bubbles that have an equivalent diameter d_i.

(ii) Bubble rising velocity

The bubble rising velocity can be estimated from the distance covered by a rising bubble between two frames as in Equation (3.3).

$$u_B = \frac{\Delta D}{T_{frame}} \tag{3.3}$$

where ΔD is the bubble displacement between times $t = 0$ and t, and T_{frame} is the time between frames. The frame rate of 1,600 frames per second was used for all experiments.

(iii) Gas holdup

The gas holdup is the gas fraction present in the gas-liquid system or the gas-liquid-solid system (when solids are used). It was calculated from the gas volume (V_g), liquid volume (V_l) and solid volume (V_s) by Equation (3.4):

$$\varepsilon_g = \frac{V_g}{V_g + V_l + V_s} \tag{3.4}$$

Normally, the value of gas holdup could be directly measured experimentally and calculated by comparing the height of the liquid surface levels before (h_B) and after gas flow (h_A) as defined in Equation (3.5).

$$\varepsilon_g = \frac{(h_A - h_B)}{h_A} \tag{3.5}$$

However, since the operation of the bubble column was in the continuous regime and the liquid level in the column was controlled to be constant. It was not possible to measure the change of liquid level before and after gas flow as in Equation (3.5). Therefore, the pressure method was used instead of the conventional method for the determination of the gas holdup. The methodology and validation of the method is described in Appendix A.

In addition, the gas holdup can also be estimated from gas flow rate (Q_g), bubble rising velocity (u_B), and column cross-sectional area (A) which can be expressed as in Equation (3.6).

$$\varepsilon_g = \frac{Q_g}{u_B A} = \frac{u_{sg}}{u_B} \tag{3.6}$$

(iv) Specific interfacial area

With the assumption of spherical bubble shape, the gas/liquid interfacial area was estimated from gas holdup, solid holdup and bubble diameter with Equation (3.7).

$$a = \frac{6}{d_B} \cdot \frac{\varepsilon_g}{1 - \varepsilon_g - \varepsilon_s} \tag{3.7}$$

while the solid holdup (ε_s) was calculated from Equation (3.8).

$$\varepsilon_s = \frac{V_s}{V_g + V_l + V_s} \tag{3.8}$$

(v) Power consumption

The total specific power consumption (*P/V*) is the power consumption per unit volume of liquid in the reactor (*V*), which equal to the summation of *P/V* of gas phase

and liquid phase. *P/V* was calculated with respect to the total pressure drop (ΔP) and the volumetric flow rate (Q) of each phase as shown in Equation (3.9).

$$P/V_{total} = (P/V)_{gas} + (P/V)_{liquid}$$
$$(P/V)_{gas} = Q_g \cdot \Delta P_g / V \qquad (3.9)$$
$$(P/V)_{liquid} = Q_L \cdot \Delta P_L / V$$

(c) Hydrodynamics determination of spray column

(i) Droplet diameter

These binary images were used to determine properties including projected area (A) and perimeter (P). These values were then used to determine droplet diameter according to Equation (3.1). The Sauter mean diameter (d_{32}) is also determined using Equation (3.2).

In addition, an optical fiber probe, de-wetting type, was also used to characterize droplet diameter. The determination of droplet diameter was followed the same method as mentioned in Chapter 2 for the de-wetting probe case. The cross-validation between two techniques, which are the high-speed camera and the optical probe, were determined.

(ii) Droplet settling velocity

To determine droplet velocity using image processing, the "wrmtrack" plugin of ImageJ® was used. This plugin tracked each droplet settling in the subsequent images. Each droplet velocity was determined using the same equation as in the bubble case, Equation (3.3). With the framerate used when capturing the images, droplet velocities of up to 25 m/s could be detected. However, the camera could detect only droplets larger than 0.1 mm because of the resolution limits of the camera and its lens. Hence, in addition to the image processing, the de-wetting optical probe was parallelly used to determine droplet velocity. The methodology for droplet velocity determination is detailed in Chapter 2.

(iii) Liquid fraction

The liquid fraction (ε_L) is the fraction of liquid volume (V_l) in respected to the summation of itself, gas volume (V_f) and solid volume (V_s) as shown in Equation (3.10).

$$\varepsilon_L = \frac{V_l}{V_g + V_l + V_s} \qquad (3.10)$$

In this work, the optical fiber probe was used to determine the local liquid fraction according to the methodology described in Chapter 2. This liquid fraction was further used to determine the specific interfacial area of the spray column by integrating

the value throughout the cross-sectional area of the column which can be expressed as in Equation (3.11).

$$\varepsilon_{L,Avg} = \frac{1}{\pi R^2} \int_0^R \varepsilon_L(r) \, 2\pi r \, dr \tag{3.11}$$

Where r in the equation refers to the radius from the center of cross-sectional area of the column while R represents the radius of column. The ε_L is the local liquid fraction at the distance r from the center. Noted that the symmetry of spray cone was assumed for this calculation.

(iv) Specific interfacial area

Normal spray condition

For the spray column, there were 2 equations that can be used to represent the specific interfacial area of the column. The first methodology was based on the same approach used for the interfacial area calculation of bubble column, Equation (3.7). The mimic of the equation is expressed in Equation (3.12), where d_D is the droplet Sauter mean diameter.

$$a = \frac{6}{d_D} \cdot \frac{\varepsilon_L}{1 - \varepsilon_l - \varepsilon_s} \tag{3.12}$$

The other approach is based on the droplet size, velocity, and the time it spends in the column. The equation can be expressed as in Equation (3.13), where the specific interfacial area is the function of liquid flow rate (Q_L), the relative droplet velocity (u_E), droplet diameter (d_D), and the column cross-sectional area (A).

$$a = \frac{6}{d_D} \frac{Q_L}{u_E A} \tag{3.13}$$

Both approaches were used in order to determine the specific interfacial area of the spray system.

Packing spray condition

The specific interfacial area when the packing was presenting consisted of two areas: the free-settling droplet interfacial area and the liquid covered the packing surface area. In order to determine both interfacial areas, the fraction between the free-settling droplets and wetting surface area needed to be investigated. The volume fraction of the free-settling droplets was determined by determining droplet sizes and their velocities at the bottom of the packing. It was found that the droplets that collided with the packing formed the liquid film around the packing and consequently gravitated down to the bottom of the packing. Eventually, the liquid film formed large droplets settling down from the packing bottom end. By utilizing the fact that the droplets

formed at the bottom of the packing had low velocities and large sizes, the use of the high-speed camera to separate the large and slow droplets from the normal droplets that did not impact with the packing is possible. The example of captured droplets at the bottom of the packing is shown in Figure 3.8.
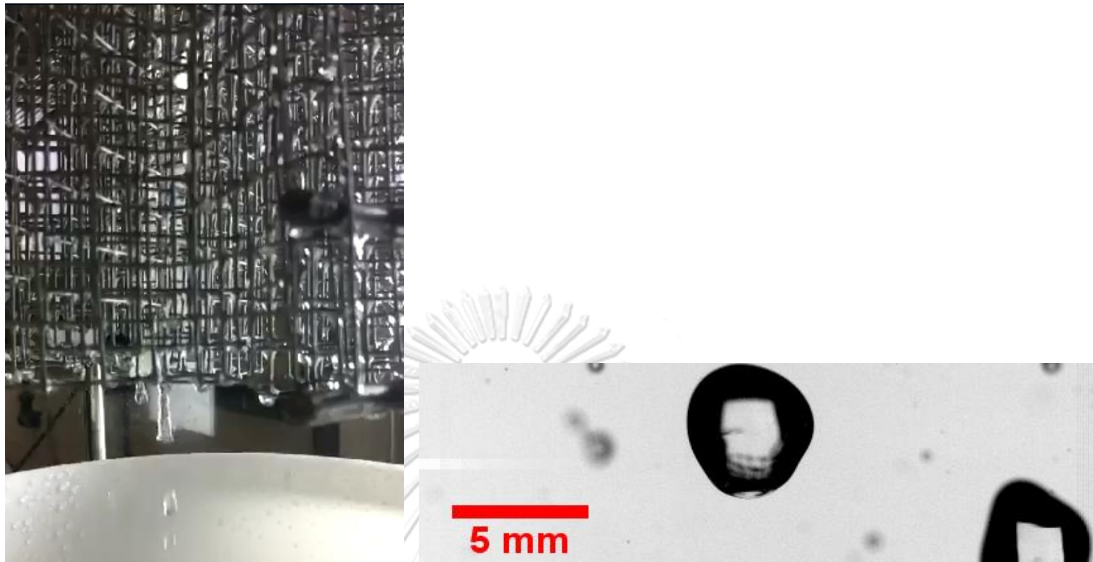
Figure 3.8 Droplet formed at the bottom of packing comparing to non-collision droplets

When the droplet velocity – size distribution is illustrated, there two types of droplets, which are the impacted and none impact ones, can be statistically separated using droplet size and velocity data filter. Equation (3.14) expresses the volume fraction of non-collision droplets that could be determined by the fraction of non-collision droplets to the total volume of droplets that is the summation of non-collision droplets and collision droplets.

$$\text{Volume fraction of non-collision droplets } (\varepsilon_d) = \frac{\text{Volume of non-collision dr}}{\text{Total volume of droplet}} \quad (3.14)$$

The specific interfacial area of non-collision droplets is calculated using same equation as normal spray condition, Equation (3.13). Note that Equation (3.12) is not used in the calculation when the packing is presenting as it is not possible to measure the liquid fraction inside the packing.

For the specific interfacial area of packing, although the total specific interfacial area of the packing is 31.69 m^{-1}, the effective area is not the same value since the liquid does not cover all the packing surface. In order to estimate the effective area of packing, the Onda's method is used (Onda et al., 1968) as can be expressed in Equation (3.15).

$$\frac{a_w}{a_p} = 1 - \exp[-1.45\left(\frac{\sigma_c}{\sigma_L}\right)^{0.75}\left(\frac{L_w^*}{a\mu_L}\right)^{0.1}\left(\frac{L_w^{*2}a}{\rho_L^2 g}\right)^{-0.05}\left(\frac{L_w^{*2}}{\rho_L\sigma_L a}\right)^{0.2} \tag{3.15}$$

Where L_w^* is liquid mass flow per unit cross-sectional area (kg/m^2.s), ρ_L is liquid density (kg/m^3), μ_L is liquid viscosity (Pa s), σ_L is liquid surface tension (N/m), σ_C is critical surface tension of packing material, which equals to 75 mN/m for steel packing, a is actual specific interfacial area (m^{-1}), and a_w is effective specific interfacial area (m^{-1}). After calculated the effective specific interfacial area of packing (a_w) and non-collision droplets (a_d), the total interfacial area (a_{Total}) can be determined using Equation (3.16).

$$a_{Total} = \varepsilon_w a_w + \varepsilon_d a_d \tag{3.16}$$

Where the ε_w and ε_d refer to the volume fraction of packing and non-collision droplets, respectively. The ε_w can be calculated from Equation (3.17).

$$\varepsilon_w = (1 - \varepsilon_d) \tag{3.17}$$

(v) Power consumption

The total specific power consumption (*P/V*) is the power consumption per unit volume of liquid in the reactor (*V*), where the same equation as bubble column, Equation (3.9), were used.

3.4 Result and discussion

3.4.1 Two-phases columns

(a) Bubble column

(i) Average bubble diameter

Figure 3.9 shows the effect of gas flow rates and orifice sizes on the Sauter mean diameter of bubble in the column. The Sauter mean diameter increased when the orifice size was larger. This incident was due to the formation of bubbles at the orifice where large bubbles were typically formed when large orifice size was used due to the smaller surface tension force at the orifice (Hernandez-Aguilar et al., 2006).
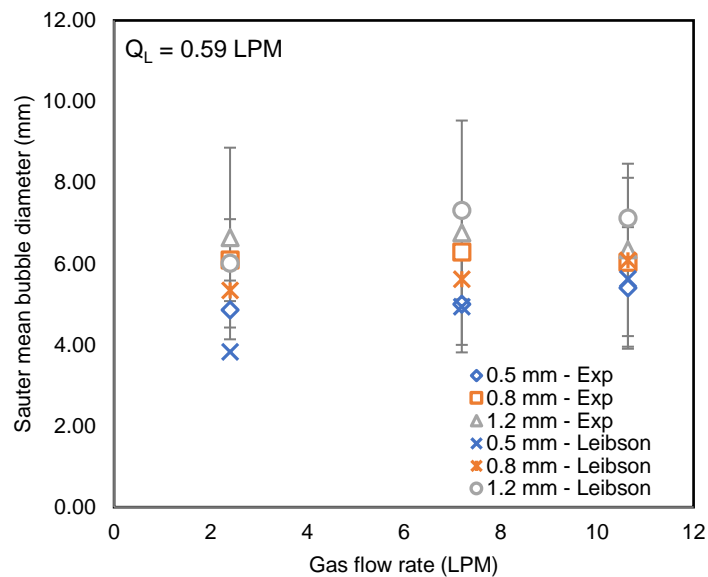
Figure 3.9 Effect of gas flow rate on average bubble size at different orifice sizes for bubble column without solid

The effect of gas flow rate on the Sauter mean diameter was different for each orifice size. For the orifice size of 0.5 mm, the Sauter mean diameter rose with the increase of gas flow rate. However, for the 0.8 mm and 1.2 mm orifice, the changes of Sauter mean diameters were not significant. This incident was due to the fact that all of the orifices in case of 0.5 mm were entirely used to produce bubbles. However, for the cases of 0.8 mm and 1.20 mm orifices, there were some orifices which did not produce any bubbles as shown in Figure 3.10
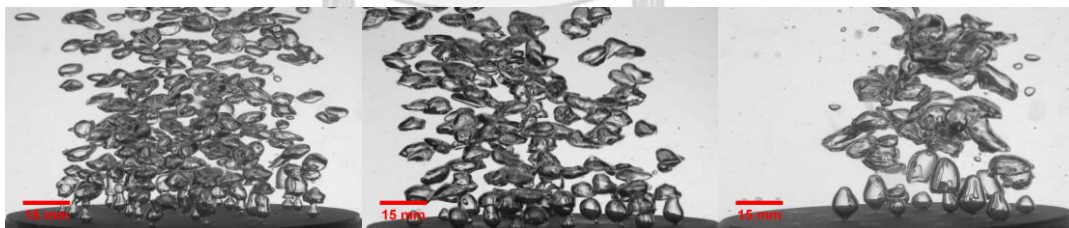
Figure 3.10 Bubbles produced at different orifice sizes at gas flow rate of 7.2 LPM (Left) 0.5 mm (Middle) 0.8 mm (Right) 1.2 mm

As shown in Figure 3.10, the increase in the gas flow rate only increased the number of orifices used but not the gas velocity. The finding was in consistent with the work of Loubière et al., (2003) which observed no change of bubble diameters according to the increase of gas flow rate when rigid orifices were used. The bubble frequency generated at the orifice was the one that changed from the increase of gas flow rate. In addition, when using the correlation of Leibson et al., (1956) to calculate bubble sizes for any cases, it was found that the bubble size calculated by the model had a good agreement with the experiment, where the average error between the model and experiment was 8.93 %. The clarification supported the finding in Figure 3.9 when

0.8 mm and 1.2 mm orifice sizes were used where no significant increase of bubble size was found. Note that the calculation using Leibson's correlation had already taken into account of the number of orifices that produced bubbles in each condition.

(ii) Bubble rising velocity

Figure 3.11 shows the average bubble rising velocity as a function of gas flow rate and orifice sizes. For the case of 0.5 mm orifice, bubbles produced by the orifice gave smaller bubble rising velocity in comparing with 0.8 and 1.2 mm due to the fact that the bubble sizes produced at the orifice was smaller leading to lower terminal rising velocity of bubbles. In addition, the increase of gas flow rate also responded in the same behavior since increasing gas flow rate also gave larger bubble sizes.
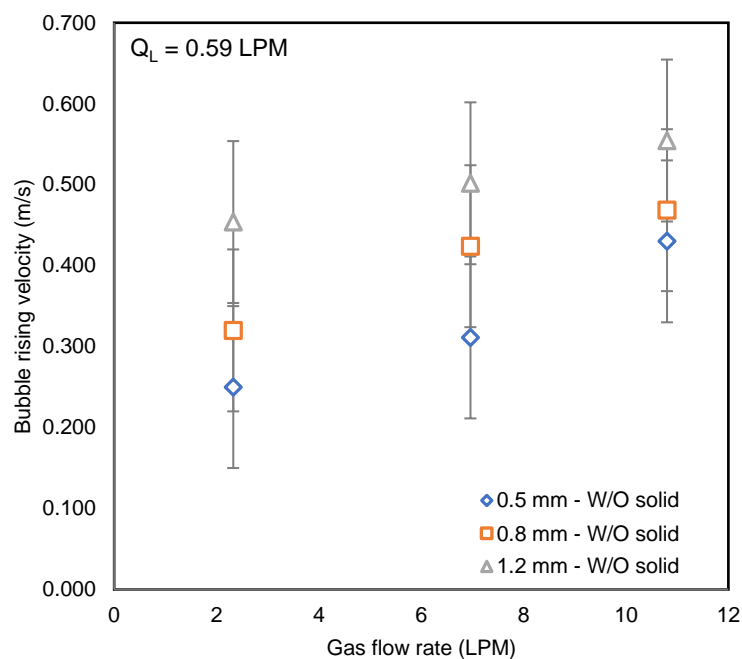
Figure 3.11 Average bubble rising velocity as a function of gas flow rate and orifice sizes

However, when considering the bubble rising velocity produced from the orifice sizes of 0.8 mm and 1.2 mm, it can be clearly seen in the figure that the bubble velocities were in the range of 0.3-0.5 m/s, but their bubble sizes were in the range of 5-7 mm where their terminal velocities should be approximately 0.25 m/s (Longo, 2006). The deviation from the terminal velocities indicated that the liquid velocity inside the column had a high influence on the bubble velocity in the column. It was occurred due to the fact that the gas sparger equipped at the bottom of the column for this experiment was located in the center position of the column and did not occupied the full section of the column. The airlift phenomenon that induced the liquid circulation was promoted. By using the fact that the bubble terminal velocity was calculated using the relative velocity between the bubble velocity and liquid velocity, it can be presumed that the liquid velocity can be calculated using the difference between the bubble

terminal velocity and its velocity measured by the high-speed camera. Figure 3.12 shows the result of the calculation using the mentioned methodology. Note that the liquid velocity inside the column was dominated by the shear-force from rising bubbles. The effect of liquid flow rate to the liquid velocity was insignificant as the liquid flow rate was 0.59 LPM which corresponding to the liquid superficial velocity of 0.0003 m/s.
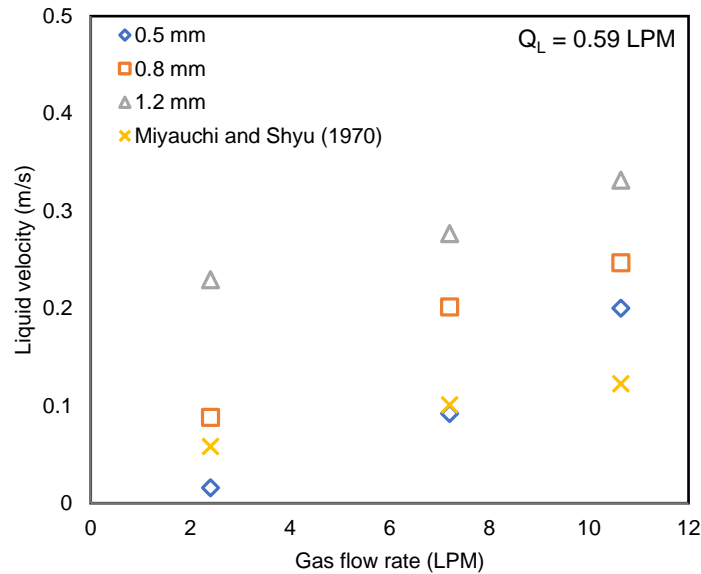
Figure 3.12 Investigation of liquid velocity in the bubble column as a function of gas flow rate and orifice sizes

In the figure, the liquid velocity rose with the increase of gas flow rate because the higher number of bubbles had higher shear force acting on liquid phase, resulting in larger liquid velocity which leading to higher bubble velocities. For the effect of gas sparger orifice size, the same effect was achieved when the orifice size of 1.2 mm was used because large bubble sizes produced at the orifice resulted in higher shear force acting on the liquid phase and highly increased the liquid velocity. The liquid velocity obtained by this calculation was compared with the correlation of Miyauchi and Shyu (1970), where the same order of liquid velocity was achieved. However, Miyauchi and Shyu's correlation does not consider the effect of different bubble sizes on the liquid velocity. Therefore, in order to further modelling purpose a correlation of liquid velocity was developed where the equation was expressed in Equation (3.18), where the average deviation of this equation to the experiment was 16.9%. Noted that the units of V_g, D_c and D_0 were in m/s, m and mm, respectively.

$$U_l(0) = 5.4 \cdot V_g^{0.5} D_c^{0.28} D_o^{1.17} \tag{3.18}$$

(iii) Gas holdup

Figure 3.13 shows the effect of gas flow rate on gas holdup for different orifice sizes. It can be seen that the increase of gas flow rate increased the gas hold up for any orifice sizes. In addition, the small orifice size yielded higher gas hold up. The result was consistent with the bubble rising velocities shown in Figure 3.11 since the low bubble rising velocity typically gave the higher gas holdup. As the height of the liquid level in the small column was not significantly changed, the bubble having smaller rising velocity would spend longer time in the bubble column, leading to a larger number of bubbles stayed inside the column where corresponding to higher gas hold up. Therefore, the orifice size of 0.5 mm gave the highest gas holdup followed by 0.8 mm and 1.2 mm according to their bubble rising velocities.
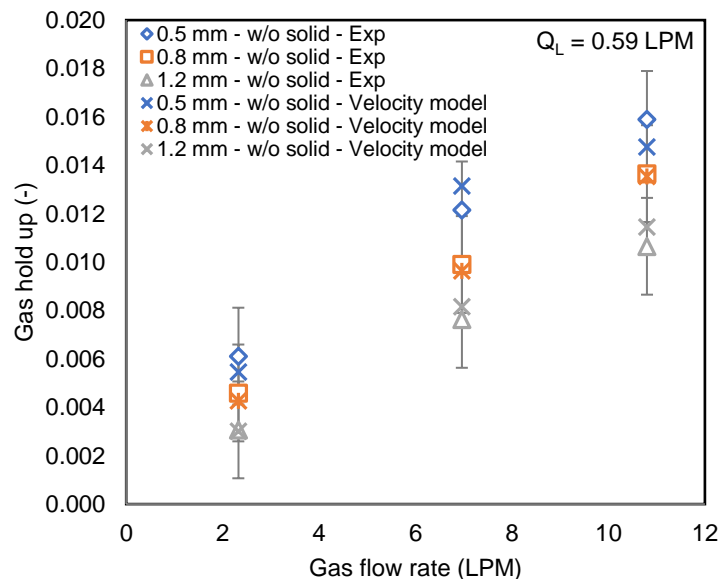
Figure 3.13 Effect of gas flow rate on gas holdup at different orifice sizes for bubble column without solid

For the effect of liquid flow rate, Figure 3.14 shows the effect of liquid flow rate on gas hold up for the orifice size of 0.5 mm. As can be seen in the figure, the gas holdup did not change with the change of liquid flow rate for the whole gas flow rates used. It indicated that the liquid flow rate used in this experiment was too low and the hydrodynamics of bubbles was not changed within the range of used liquid flow rates. Although the liquid flow rate did not influence with the hydrodynamics of bubbles, the fact that the mass transfer would change with different amount of liquid to gas ratio should be noted. The detail of liquid flow rate effect on mass transfer will be discussed in Chapter 5.
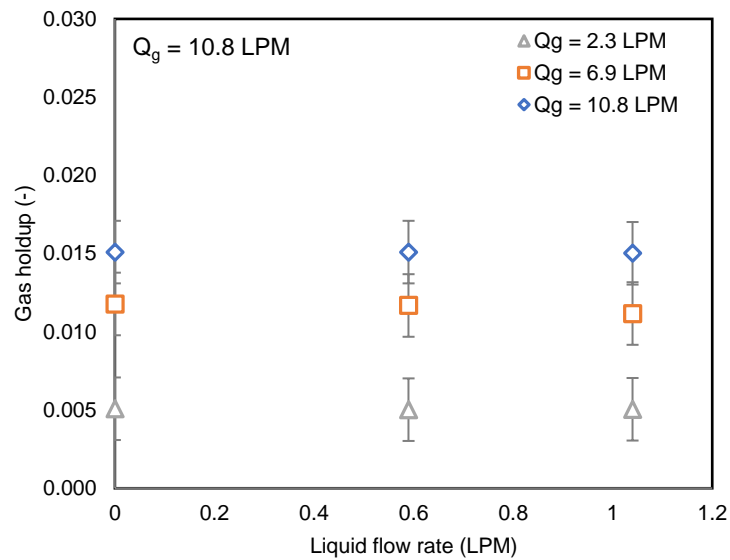
Figure 3.14 Effect of liquid flow rate on gas holdup for different gas flow rate with 0.5 mm orifice size

In order to model the gas holdup in the bubble column, two approaches were test. The first is one developed using bubble rising velocity along with the gas velocity inside the bubble column. By using Equation (3.6), the gas holdup can be estimated, and the results are shown in Figure 3.13. In the figure, it can be seen that the estimation and experiment were in the same trend. Hence, the utilization of Equation (3.6) was a reliable method for the estimation of gas holdup.
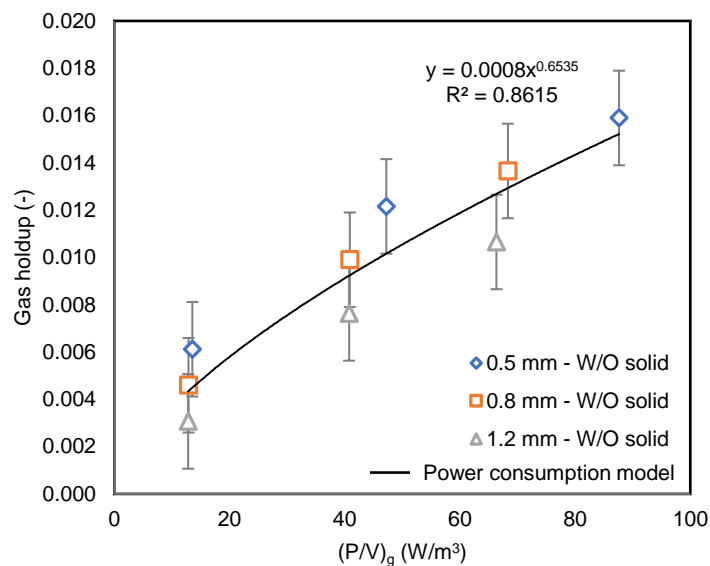
Figure 3.15 Gas holdup as a function of power consumption $(P/V)_g$

The other approach was one with the presumption that the gas holdup is a strong function of power consumption as mentioned by various literatures (Bouaifi et al., 2001). The equation developed using the presumption is expressed in Equation (3.19), where the result of the equation was plotted in Figure 3.15. The equation shows the same trend with the experiment, but a slight deviation was also obtained with the average error of 16.17 %.

$$\varepsilon_g = 8x10^{-4} \left(\frac{P}{V}\right)_g^{0.65} \tag{3.19}$$

(iv) Pressure drop and power consumption

Figure 3.16 shows the effect of gas pressure drop on gas flow rate in the bubble column. It can be seen in the figure that at the same pressure, when the small orifice size, 0.5 mm was used, the gas flow rate produced at the gas sparger was lower in comparing with the 0.8 and 1.2 mm spargers. In addition, the 0.8 mm and 1.2 mm orifice sizes did not give a significant different gas flow rate at the same pressure drop due to the fact that all of the orifices were not used at low pressure as mentioned earlier. Note that the relation between liquid flow rate and pressure drop followed the same trend as the gas pressure drop but the range of liquid flow rate achieved were significantly lower comparing with the gas flow rate. It was due to the fact that the liquid phase was injected at the top of the column directly from the pump and there is no orifice used for the liquid injection.
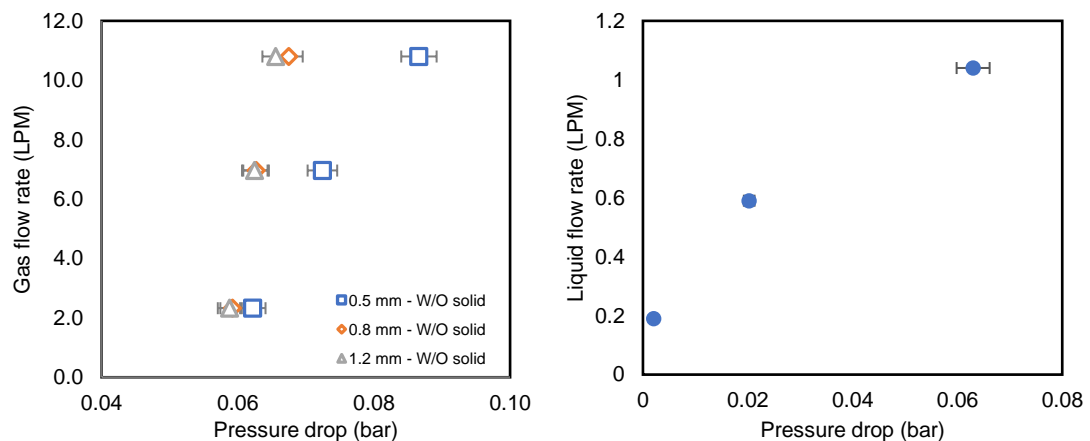
Figure 3.16 Effect of pressure drop at different orifice sizes on
(Left) Gas flow rate (Right) Liquid flow rate

When using the pressure drop data to calculate power consumption using Equation (3.9), the result can be shown in Figure 3.17. The results followed the same trend as the pressure drop; the gas flow rate increased with the increase of power consumption for both liquid and gas flow rate. However, for the gas flow rate, in order to obtain the same gas flow rate, a larger power consumption was required for 0.5 mm orifice when comparing with 0.8 and 1.2 mm. The orifice size of 0.8 and 1.2 mm gave

almost the same value due to the fact that the orifices were not entirely used since the orifice sizes were too large.
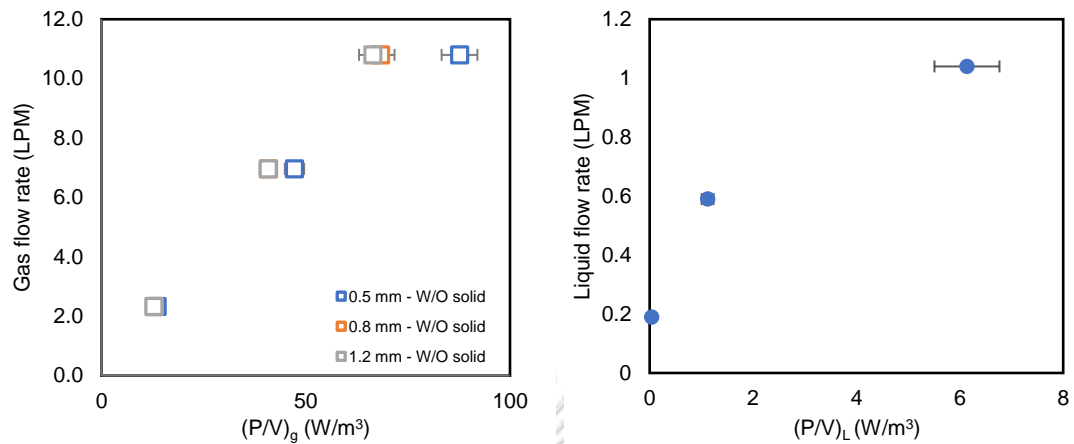
Figure 3.17 Effect of power consumption at different orifice sizes on (Left) Gas flow rate (Right) Liquid flow rate

(v) Specific interfacial area
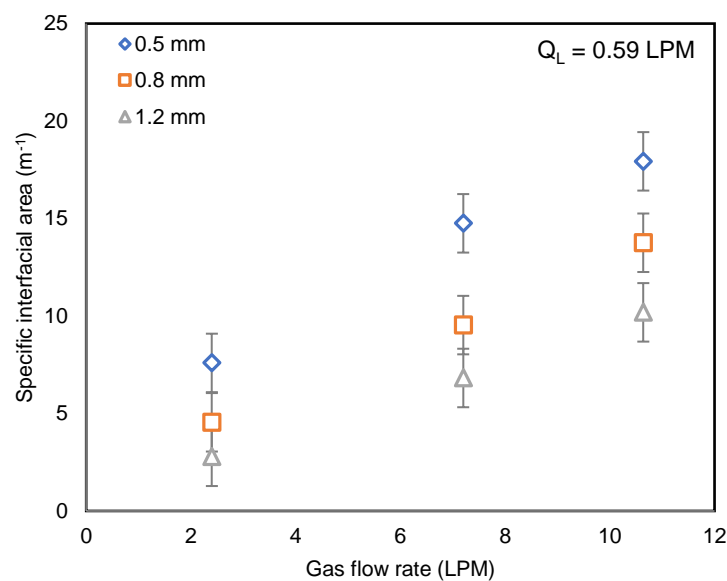
Figure 3.18 Effect of gas flow rate on specific interfacial area at different orifice sizes

The specific interfacial areas (a) of two-phases bubble column as a function of gas flow rates and orifice sizes are shown in Figure 3.18. The interfacial area increased with the gas flow rate due to the fact that the higher gas holdup was achieved for larger gas flow rate. In addition to the gas flow rate, since the small orifice size gave higher number of gas holdup, a larger value of specific interfacial area was also obtained. Moreover, for the consideration of specific interfacial area, smaller size of bubbles also affects the specific interfacial area since a smaller size of bubbles had larger interfacial

area for the same volume of bubbles. Therefore, it can be concluded that the best orifice size for bubble column was one with the smallest size where small bubble sizes was produced, and higher gas holdup was achieved. However, it should be noted that, a smaller orifice size and high gas flow rate also required a larger pressure, where a higher power was consumed. Figure 3.19 shows the relation between the power consumption and the interfacial area obtained at different orifice sizes.
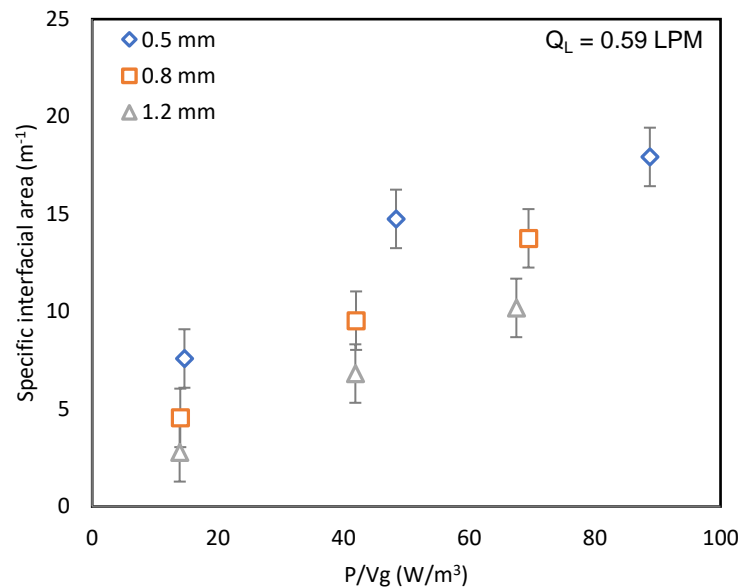
Figure 3.19 Effect of power consumption on the specific interfacial area

Figure 3.19 shows that the specific interfacial area raised with the power consumption. Although the small orifice, 0.5 mm, required higher pressure and power consumption to produce bubble at the same gas flow rate, the highest specific interfacial area was still achieved with the 0.5 mm orifice. The finding indicated that for the range of orifice used in the work, the suitable orifice size in terms of specific interfacial area was the smallest one, which was the 0.5 mm size.

(b) Spray column

(i) Average droplet size

Figure 3.20 shows the effect of liquid flow rate on the Sauter mean diameter of droplets produced with different sizes of orifice at 5 and 25 cm linear distance from the nozzle. It can be seen that the increase of liquid flow rate decreased the Sauter mean diameter of droplets regardless of the orifice size of nozzle. When the orifice size of nozzle was decreased, droplets produced by nozzle were decreased as can be seen in the figure that, the smaller size of orifice gave a smaller value of Sauter mean diameter at the same liquid flow rate. Note that the gas flow rate used in this experiment did not affect the Sauter mean diameter since the values of gas flow rate were not tremendously high.
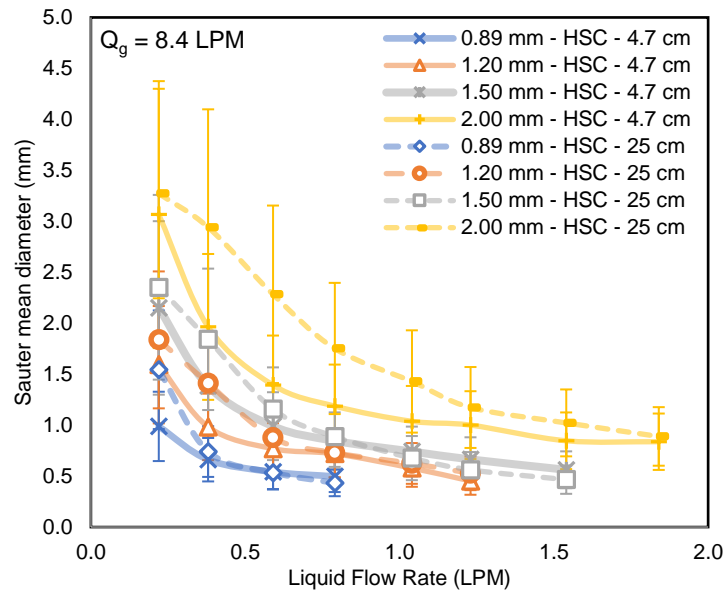
Figure 3.20 Sauter mean diameter produced by different orifice sizes at different distances from nozzle as a function of liquid flow rate

As droplets traveled from 5 cm to 25 cm, it can be seen in Figure 3.20 that the Sauter mean diameters were increased mostly for the large size orifice and small liquid flow rate. It was due to the fact that at the large orifice size, the angle of spray was narrow comparing to small orifice sizes. Hence, a chance of droplet coalescence was large. In addition to the size of orifice, the decrease of liquid flow rate also affected the angle of spray, where the low flow rate of liquid normally gives the small angle of spray cone. Therefore, high possibilities of droplets coalescence could be achieved.

In order to assure the experiment precision, the optical fiber probe was used to determine the same conditions of sprays, as shown in Figure 3.21. The optical fiber probe gave the same trend as the high-speed camera except the fact that the optical fiber probe had a lower limit of detectable droplets comparing with the high-speed camera, which had the limit at 0.1 mm of droplets. Therefore, the Sauter mean diameters determined by the optical fiber probe were slightly smaller comparing to the high-speed camera. Note that the slightly larger of Sauter mean diameter at the distance of 25 cm comparing with at 5 cm, were also found with the optical probe.
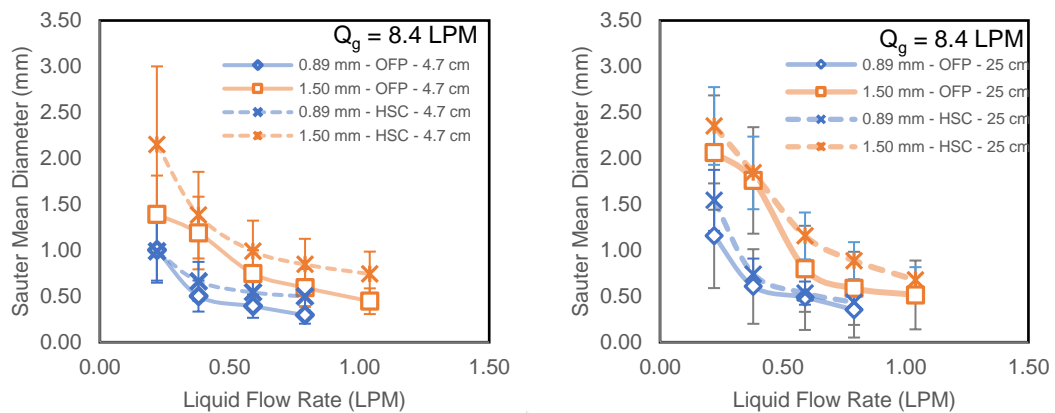
Figure 3.21 Comparison of Sauter mean diameter of droplet characterized by the
high-speed camera (HSC) and the optical fiber probe (OFP)
(Left) at 5 cm from nozzle (Right) at 25 cm from nozzle

For further purpose of modeling, a mimic of Murty's correlation was applied for the modelling approach (Roustan, 2003). The following equation was developed in order to represent the Sauter mean diameter of droplets, where the unit of d_D and D_{Nozzle} are both in mm.

$$d_D = 44Re^{-0.48}We^{-0.18}D_{Nozzle}^{0.44} \tag{3.20}$$

Where $Re = \frac{U_{Nozzle}D_{Nozzle}\rho_{water}}{\mu_{water}}$ and $We = \frac{U_{Nozzle}\cdot\mu_{water}}{\sigma_{water}}$.
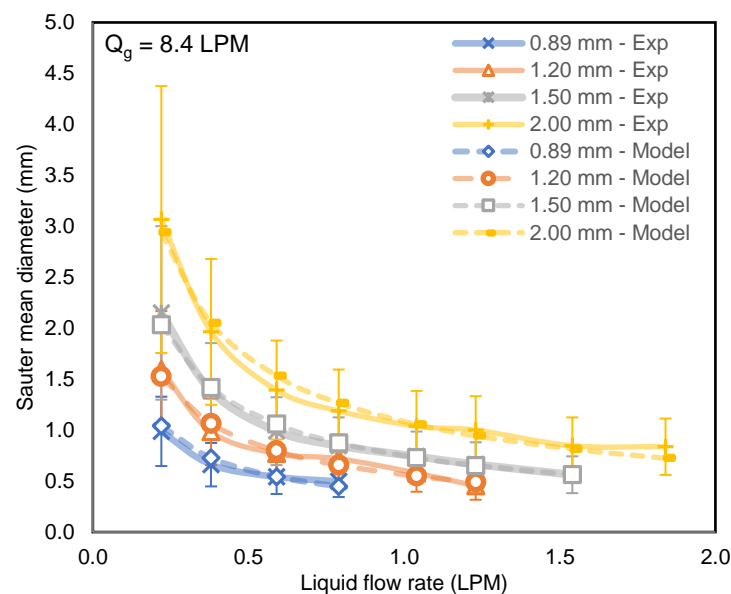
Figure 3.22 Murty's correlation results at different liquid flow rates and orifice sizes
in comparing with the experimental data

Figure 3.22 shows the result of Sauter mean diameter at different liquid flow rates and nozzle orifice sizes calculated with Equation (3.20). The calculation results were clearly in the same trend as the experiment with the average error of 5.41 %. Note that the coefficient and exponents in the equation was slightly modified from the original Murty's equation in order to achieve a good consistence between the equation and the experiment.

(ii) Droplet size – velocity distribution
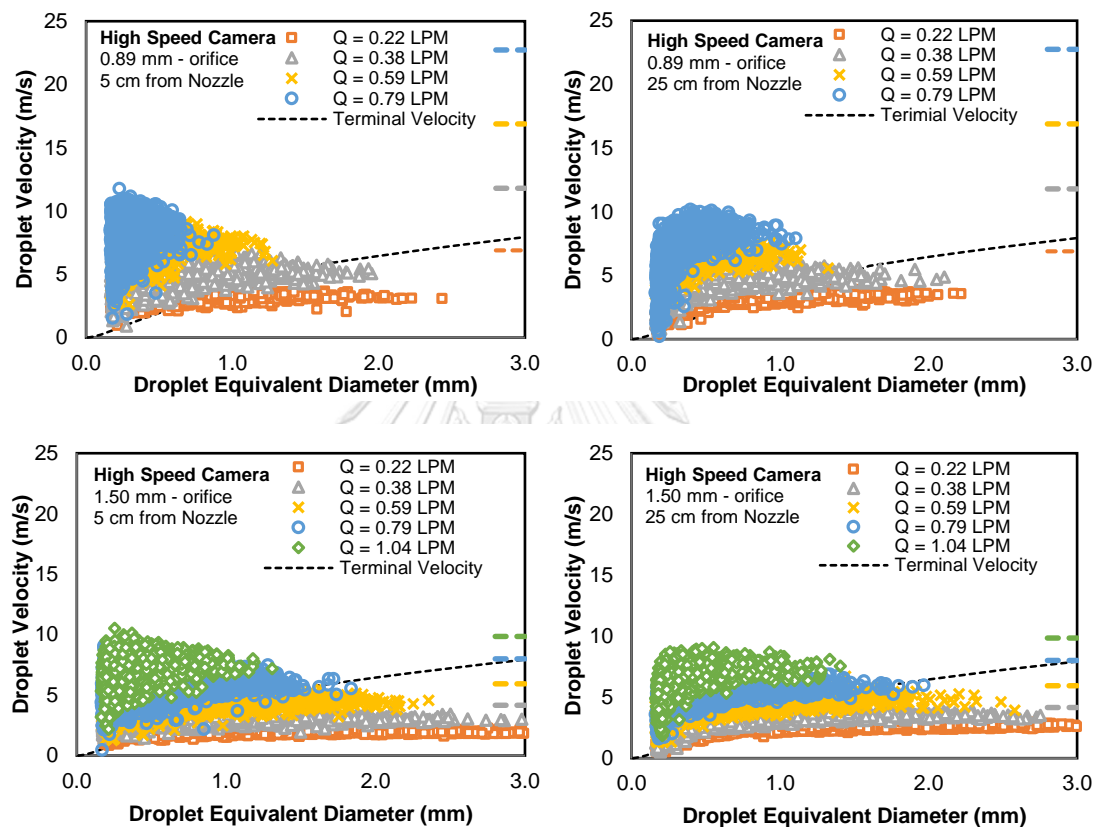
Figure 3.23 Droplet velocity – size distribution at different liquid flow rate, orifice sizes, and distance from nozzle determined using the high-speed camera

The droplet velocity – size distributions at different orifice sizes, liquid flow rates, and distances from nozzle are shown in Figure 3.23 when determined with the high-speed camera and in Figure 3.24 when determined using the optical probe. In the figures, the horizontal axis shows the droplet equivalent diameter while the vertical axis shows the droplet velocity. Higher droplet velocities and smaller droplet sizes are clearly seen when the liquid flow rate increased. In addition, when considering the effect of nozzle orifice sizes, the increase of orifice size lowered droplet velocities produced by the orifice as well as larger sizes of droplets were obtained.

The different distances from nozzle also affected the droplet velocity as well as droplet sizes. In Figure 3.23, it can be seen that at longer distance from nozzle, there were larger droplet detected by the high-speed camera in every condition. This incident

supported the fact that droplet coalescence occurred during the different distances as mentioned earlier. Moreover, as the distance increased, the droplet velocities changed according to the terminal velocity (dash line in the figure), where the closer to the terminal velocity at certain droplet sizes were accomplished. It was due to the initial velocities of droplets produced by the nozzle that was different from their terminal velocity. The droplets having larger initial velocities than their terminal velocities trended to decrease their velocities while the droplet with slower velocities than their terminal velocities raised their velocity according to the distance travel. This change of velocity can be clearly explained by the force balance on a single droplet, where the detail is mentioned in Appendix C. Noted that, the time that droplets requires to reach its terminal velocity is so-called "relaxation time".
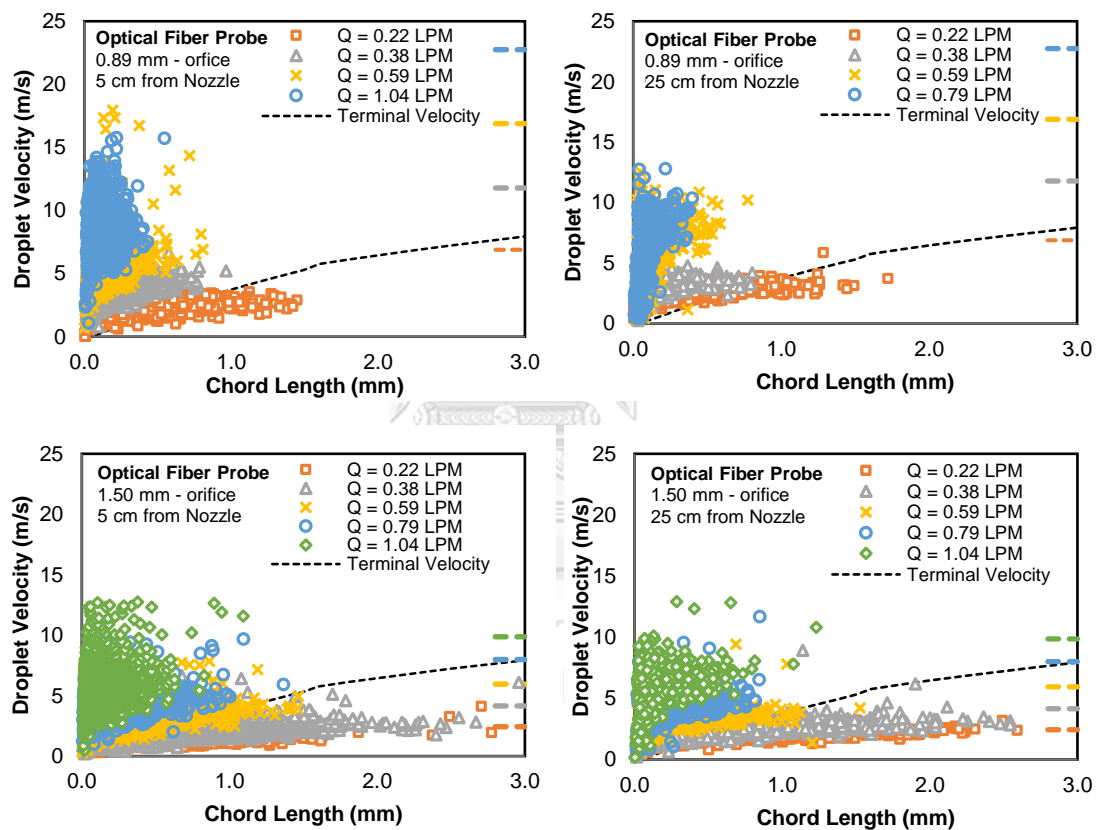
Figure 3.24 Droplet velocity – chord distribution at different liquid flow rate, orifice sizes, and distance from nozzle determined using the optical fiber probe

When comparing the results between the high-speed camera and the optical probe in Figure 3.23 and Figure 3.24, the same effects obtained by the high-speed camera were accomplished. Two small differences between the high-speed camera and the optical probe was that the de-wetting type optical probe were not able to determine the droplet size directly and the chord length had to be represented the droplet sizes instead of droplet diameter. Another difference was the smaller sizes of droplets were able to be investigated. However, regardless of the fact that two techniques gave

different results due to the limitation of each one. It can be seen that both techniques gave the same trend of the results.

$$U_{jet} = \frac{Q_L}{A_{orifice}} \tag{3.21}$$

In order to understand the initial velocities of droplets, the calculation of jet velocities in the studied conditions were done as plotted in both Figure 3.23 and Figure 3.24 as the dash line at the right-end of each figure. The same colors of the dash lines indicate the same liquid flow rate. In both figures, it can be seen that large differences of jet velocities (U_{jet}), which calculated using Equation (3.21), were acquired especially when the 0.89 mm orifice nozzle was used. However, in the case of the large orifice of 1.50 mm, the deviation was not evidently observed. In addition to the orifice sizes, the liquid flow rates also gave the same trend especially for the 0.89 mm orifice nozzle. The loss of energy due to sudden contraction was presumed to responsible for this effect, where the detail is described in Appendix B. From the methodology, the calculation results are shown in Table 3.4.

Table 3.4 Jet velocity of liquid at the orifice and the estimated droplet initial velocity using Bernoulli equation

Flow Rate (LPM)	Jet Velocity (m/s)				Estimated Droplet Initial Velocity (m/s)			
	0.89 mm	1.2 mm	1.5 mm	2.0 mm	0.89 mm	1.2 mm	1.5 mm	2.0 mm
0.22	5.89	3.24	2.07	1.17	3.62	3.21	1.99	1.05
0.38	10.18	5.60	3.58	2.02	6.54	5.49	3.48	1.87
0.59	15.81	8.69	5.56	3.13	8.84	7.66	5.29	3.04
0.79	21.16	11.64	7.45	4.19	13.84	9.21	7.34	4.07
1.05	-	15.40	9.86	5.55	-	13.23	9.80	5.54
1.23	-	18.13	11.60	6.53	-	16.10	11.55	6.25
1.54	-	-	14.52	8.17	-	-	14.47	8.11
1.84	-	-	-	9.76	-	-	-	9.75

Table 3.4 shows the estimated droplet initial velocities at different flow rates and nozzle orifice sizes calculated according to the methodology described in Appendix B. When the orifice sizes were large, 1.5 or 2.0 mm for instance, the estimate droplet velocities were close to those jet velocities calculated using Equation (3.21). However, when the smaller size of orifices was used, 0.89 and 1.2 mm for example, the differences between jet velocity and the estimated droplet initial velocities were large. This finding supported the experiment data in Figure 3.23 and Figure 3.24 that discussed earlier.

By using the droplet initial velocities in Table 3.4 along with the relaxation time calculation, Appendix C, the theoretical droplet velocities are shown in Figure 3.25 at different orifice sizes and distances from nozzle. As the distance traveled increased, droplet velocity trended to be closer to their terminal velocity, which was a function of droplet size. Moreover, the trends of droplet velocity as a function of droplet diameter can be clearly seen to be the same behavior as the Figure 3.23 and Figure 3.24. Therefore, it can be indicated that the initial velocity calculated according to Appendix

B can be further used for the calculation of initial velocity of droplets formed at the orifice of nozzle.
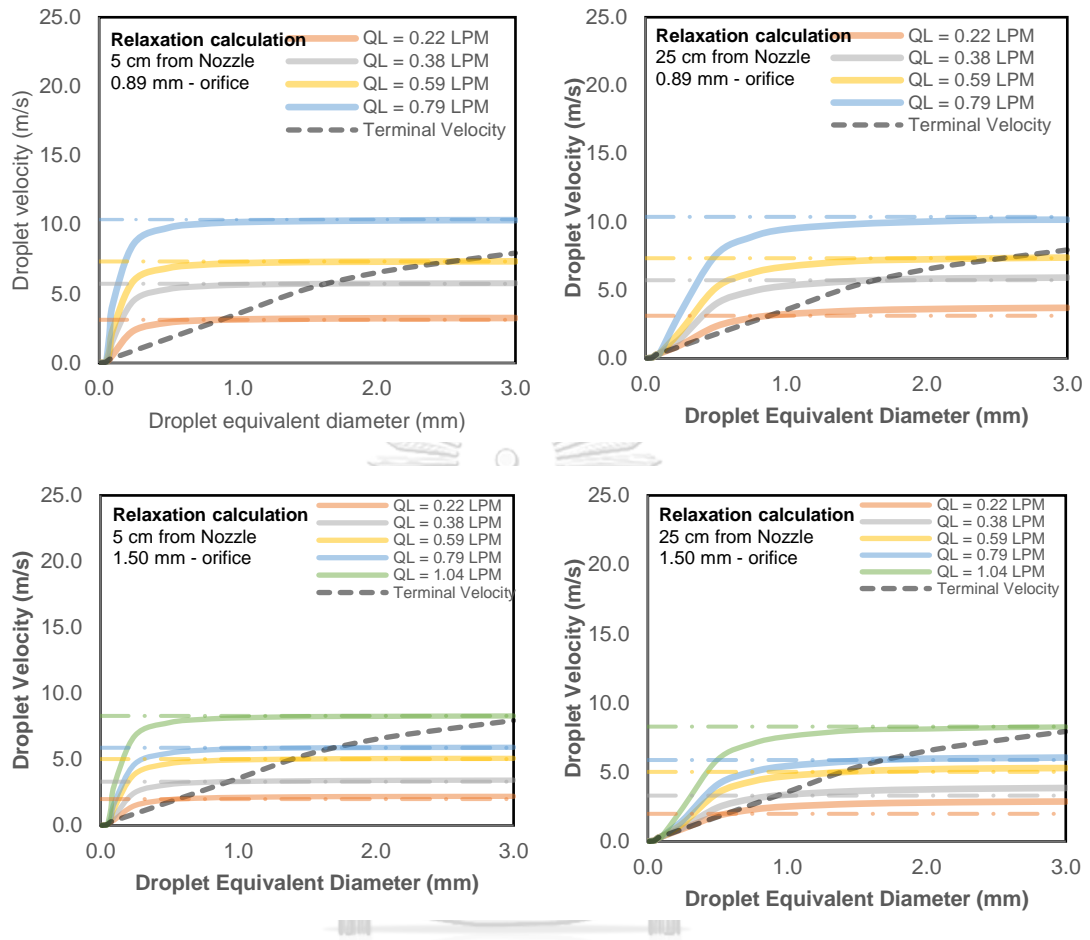
Figure 3.25 Droplet velocity – size distribution calculated with the relaxation time equation
(See detained in Appendix B and Appendix C)

Nevertheless, in order to simplify the calculation, the empirical equation was developed for modelling purpose. Since the Bernoulli's equation gave the droplet initial velocity according the loss of energy due to sudden contraction, the power consumption, which calculated using Equation (3.9), can be used to determine the initial velocity of droplets. Figure 3.26 shows the droplet velocity as a function of power consumption.
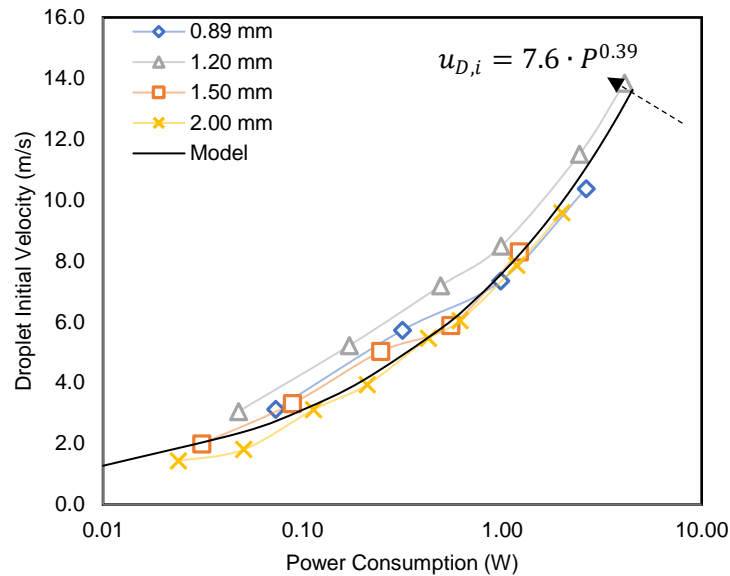
Figure 3.26 Droplet initial velocity as the function of power consumption

It can be seen in the figure that the relation between pressure drop and droplet initial velocity ($u_{D,i}$) followed the power law regardless of the orifice sizes. It was due to the fact that the power consumption is the multiplication result between liquid flow rate and pressure drop across the nozzle. The combination was already the effect of liquid flow rate and orifice diameter size instantaneously since the pressure drop was highly depended on the orifice size. Therefore, from the finding, Equation (3.22) was developed using the non-linear regression method, as shown in the following:

$$u_{D,i} = 7.6 \cdot P^{0.39} \tag{3.22}$$

The droplet initial velocity calculated using Equation (3.22) is also illustrated in Figure 3.26. The average deviation between the experiment and the model was at 9.85 %. Although there is a minor deviation between model and the experiment, it can be concluded that the power consumption (P) can be used to estimate the initial velocity of droplets. The equation is confident to be used in the modelling purpose further.

(iii) Average velocity

From the velocity distribution in the previous section, the average velocities of droplets at every condition were calculated. Figure 3.27(Left) shows the effect of liquid flow rate, orifice sizes and distances from nozzle on the average velocity of droplets. The figure indicates that the average droplet velocity increased with the liquid flow rate regardless of orifice size. The smaller size of orifice yielded higher average droplet velocity comparing at the same liquid flow rate. In addition, the distance from nozzle also affected the average velocities of droplets, the longer distance traveled, lower average droplet velocities obtained. This decrease followed the same behavior explained in the previous section that the droplets produced at the orifice of nozzle had higher velocities than their terminal velocity and after a certain distance, the droplets

decreased their velocities in order to get close to their terminal velocities. This fact was also confirmed with the optical probe where the same trends of the results were obtain as shown in Figure 3.27(Right).
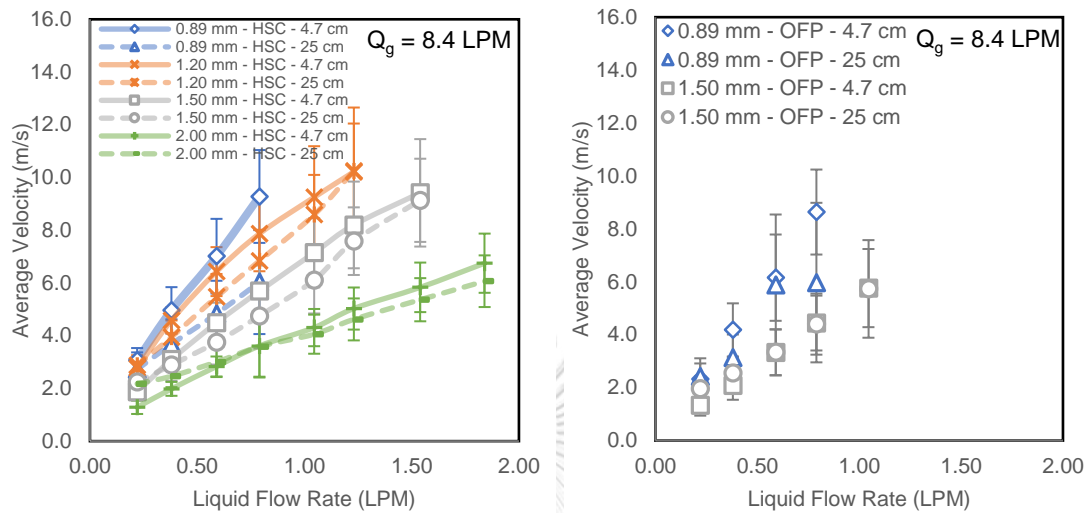
Figure 3.27 Droplet average velocity as the function of liquid flow rate at different orifice sizes and distance from nozzle determined by the high-speed camera

For modeling purpose, the relaxation time calculation was performed at the distance 5 cm and 25 cm from nozzle. The droplet size used for the calculation followed the result obtained from the droplet Sauter mean diameter as mentioned in Figure 3.20. The result of relaxation time calculation, Appendix C, are shown in Figure 3.28(Left) and Figure 3.28(Right), for the distance of 5 cm and 25 cm from nozzle respectively.
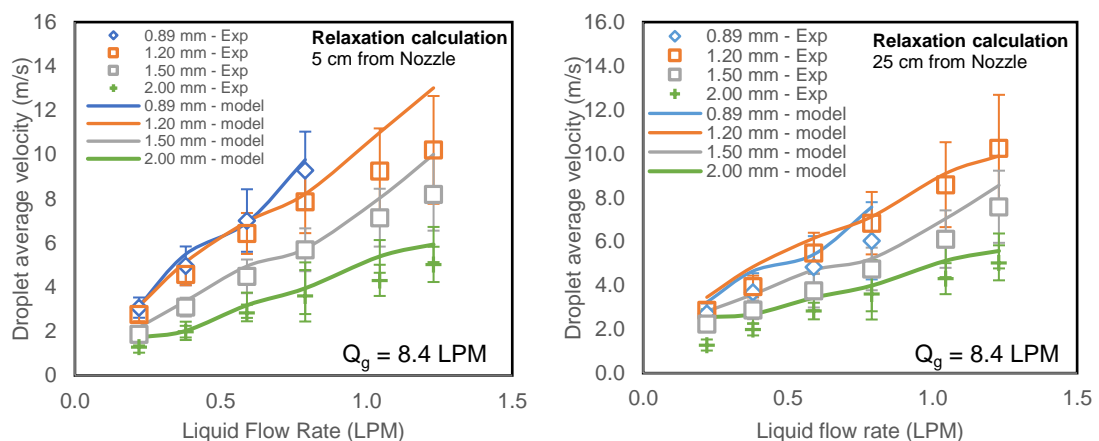
Figure 3.28 Droplet average velocity determined using relaxation time calculation

The result of relaxation time calculation indicated that the average velocity gave the same trend according to the experiment data as shown in Figure 3.28. The droplet average velocity of both distances at 5 and 25 cm can be estimated accurately at 12.6 and 16.6 % average deviation. The effect of orifice size was also included. Therefore, by using the relaxation time calculation, Appendix C, along with the droplet initial

velocity estimation, Equation (3.22), and the droplet average size in Equation (3.20), the hydrodynamics properties of droplet can be modelized. However, in order to understand the behavior of spray comprehensively, the liquid fraction study of spray cone should be considered.

(iv) Liquid fraction

The local liquid fraction was investigated using the optical probe by the methodology mentioned in Chapter 2. It was measured at each 2 cm interval from the center of the cone for the vertical distance of 25 cm from nozzle. The results are shown in Figure 3.29 where 2 sizes of nozzle orifices were considered.
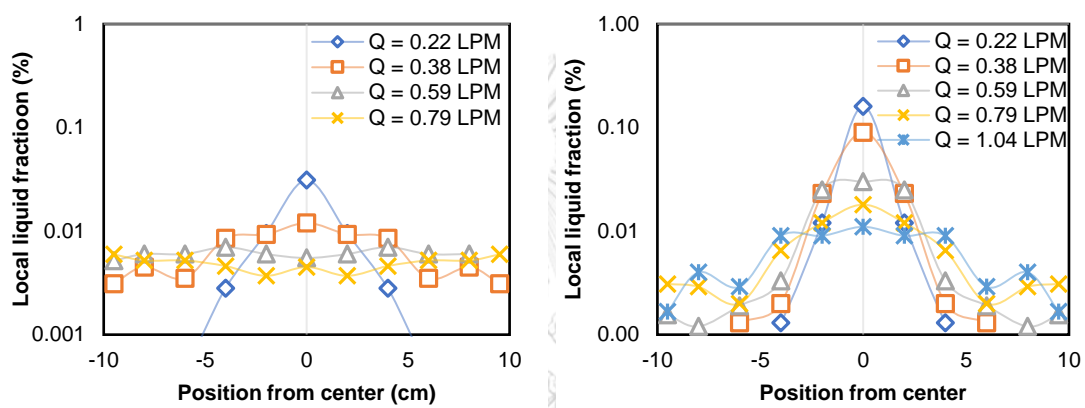
Figure 3.29 Liquid fraction at different position from the center of the spray cone at
different orifice size at the position of 25 cm from nozzle
(Left) 0.89 mm (Right) 1.50 mm

For the orifice size of 0.89 mm, it can be seen that the local liquid fraction was high at the very center of the cone and sharply reduced when the distance from the cone increased. It was due to the fact that the spray angle was small at low flow rate of liquid. Therefore, most of the droplet trajectories were in the center. However, at larger liquid flow rates, the spray of angle increased, leading to lower number of droplets at the center and the local liquid fraction was expanded to the farther position from the cone center. Hence, it can be seen that at the larger flow rate, the higher local liquid fraction obtained at the farther positions. Note that the same behavior was also obtained in the case of 1.50 mm orifice size. However, at the same liquid flow rate, the angle of spray of 1.50 mm orifice was smaller. Therefore, the local liquid fraction of the same liquid flow rate for the center of the cone was higher for the 1.50 mm orifice but smaller at the far side of the cone when in comparing with the 0.89 mm nozzle.

Nevertheless, according to the calculation of the specific interfacial area, the liquid fraction was one of the variables that can be used to estimate the specific interfacial area as described in Equation (3.12). It is mandatory to calculate global liquid fraction that represents the column liquid fraction. Equation (3.11) was used to calculate the global liquid fraction and its results are shown in Figure 3.30.
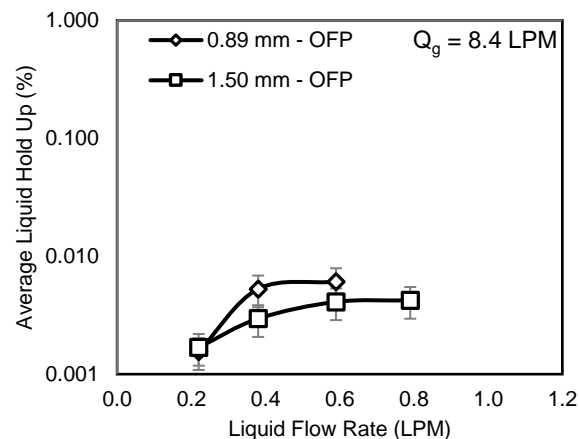
Figure 3.30 Average liquid fraction at 25 cm distance from nozzle for different flow rates and orifice sizes

Figure 3.30 shows the average liquid fraction among the column at 25 cm away from nozzle. For both orifice sizes, the average liquid fraction trended to increase with the liquid flow rate regardless of the orifice sizes. However, when considering at the same liquid flow rate, the average liquid fraction for the 0.89 mm nozzle was slightly larger in comparing with the 1.50 mm orifice. It was due to the fact that the smaller size of the orifice gave a larger angle of spray cone. Thus, the average values of the liquid fraction were certainly higher as it covered larger areas of the column.

(v) Pressure drop and power consumption

Pressure drop and power consumption are ones of the parameters that should be studied in order to economically determine the performance of the spray column. There are two pressure drops for consideration: liquid pressure drops, and gas pressure drop. The pressure sensors were used to determine the differences of pressure. Figure 3.31 shows the relation of pressure drop and flow rate of each phase.
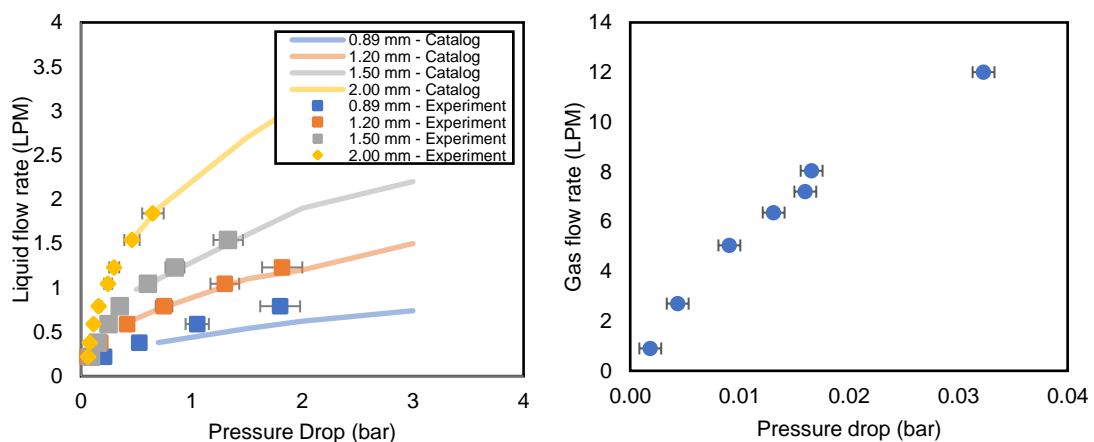
Figure 3.31 Pressure drop of fluid dispersed to the column
(Left) liquid phase (Right) gas phase

In the figure, the experiment data was consistent with the data provided by the spray nozzle manufacturer. Large liquid pressure is required especially for small size of the orifice, 0.89 mm for instance, where 2 bars of pressure can produce only 0.9 LPM of liquid flow rate. However, at the same pressure, the liquid flow rate can be produced up to 3 LPM when using the 2.00 mm orifice size. This fact indicated that the larger pressure was required in order to operate at a certain liquid flow rate for the smaller size orifice. The loss due to the sudden contraction at the nozzle orifice was responsible for the incident.

For the case of gas phase, since the inlet of gas phase to the reactor was the 6 mm pipe without any contraction, the gas pressure drop and gas flow rate relation, as shown in Figure 3.31(Right) was not depended on the orifice size. The gas pressure drops increased as the gas flow rate increased. However, the order of magnitude for the gas pressure drop was significantly lower than the liquid phase.

When using the fluid flow rate and its pressure drop to calculate the power consumption following Equation (3.9), the result can be illustrated as in Figure 3.32.
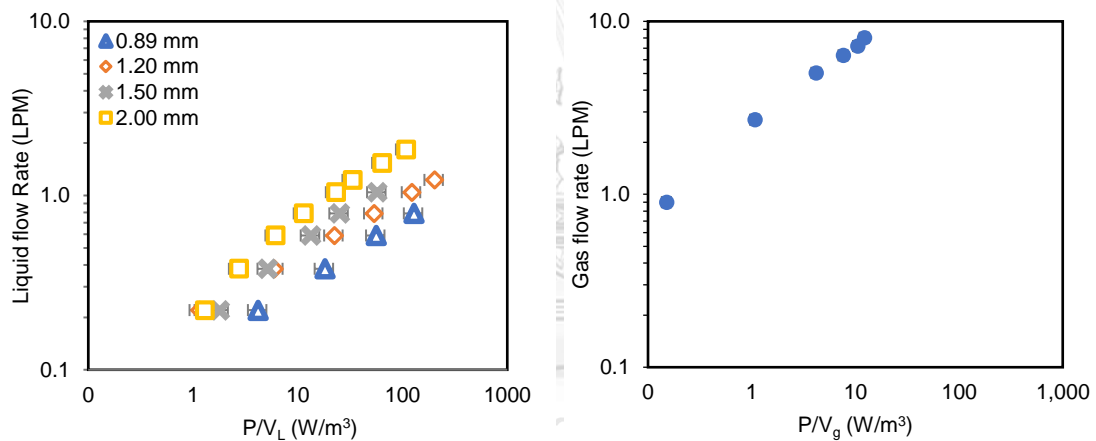
Figure 3.32 Power consumption of fluid dispersed to the column
(Left) liquid phase (Right) gas phase

In the figure, larger liquid flow rate required a larger power consumption especially for the small orifice size case. Since, the pressure occurring at the nozzle was used to calculate the power consumption, the power consumption needed for operating at a certain liquid flow rate followed the same trends as the pressure drop. It should be noted that although a larger power consumption is required for a small size orifice, its specific interfacial areas were significantly larger. Therefore, in order to obtain the optimal value for spray operation, both power consumption and interfacial area should be instantaneously considered.

(vi) Specific interfacial area

The specific interfacial area is one of the important parameters used in the mass transfer aspect. For the spray regime, it is possible to apply two cases of the equations used to determine the specific interfacial area, Equation (3.12) and (3.13). Both

equations used different approaches of calculations, Equation (3.12) utilizes the Sauter mean diameter of droplet and the average velocity to calculate the interfacial area, while Equation (3.13) uses the liquid fraction instead of the average velocity. Note that the Sauter mean diameter, average droplet velocity, and liquid fraction at the center of the column were used to represent the whole column value in order to simplify the calculation of the specific interfacial area.

When using different equations to calculate the interfacial area, it can be seen in Figure 3.33 that both equations gave the same tendency of the results. The specific interfacial area increased as the liquid flow rate increased. In addition, the effect of the orifice sizes on the specific interfacial areas calculated by both equations resulted in the same trend. Therefore, it can be concluded that the determination of the specific interfacial area can be done by both equations. Note that the discrepancy between both approaches was statistically at 20.7 %.
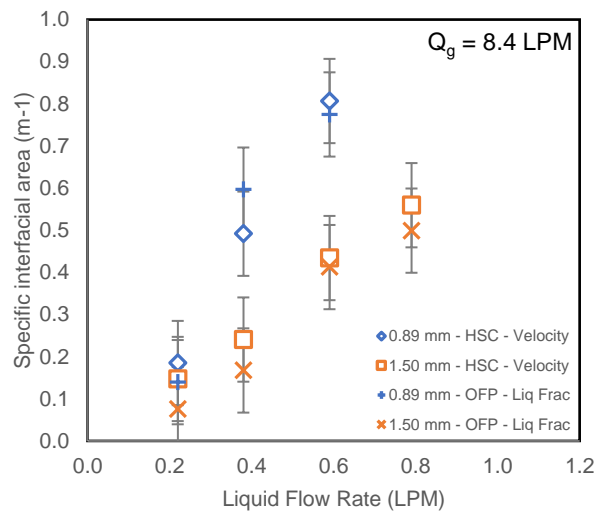
Figure 3.33 Specific interfacial area of mass transfer as the function of liquid flow rate for different orifice sizes of nozzle calculated with different equations

Figure 3.34 shows the specific interfacial area as a function of liquid flow rate and orifice sizes of nozzle calculated using droplet velocity approach, Equation (3.12). As the liquid flow rate increased, the specific interfacial area rose regardless of the orifice sizes. In addition, the smaller size of the orifices yielded the higher specific interfacial area.
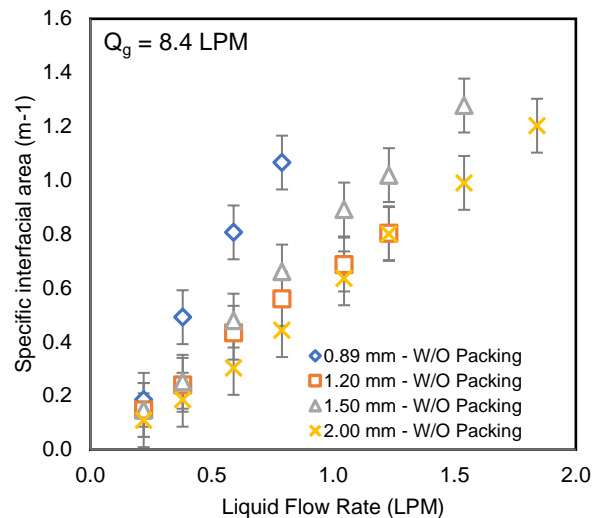
Figure 3.34 Specific interfacial area of mass transfer as the function of liquid flow rate for different orifice sizes of nozzle

In the mass transfer purpose of spray, small diameter of droplets as well as slow droplet velocities were recommended since the specific interfacial areas were highly depending on the value of Sauter mean diameter and droplet average velocity, Equation (3.12). However, as mentioned earlier, to create a small droplet, the small size of nozzle orifice was required and consequently the high velocity of droplets could not be avoided. Therefore, in order to obtain the great value of specific interfacial area, the balancing between the droplet size and velocity should be considered. Here, it can be seen for the orifice size of 0.89 mm that, the specific interfacial area of mass transfer was the greatest among all other orifices. Hence, it can be concluded that although high velocity droplets were produced, the small size of droplets were recommended as the small droplets reduced its velocity rapidly after leaving the nozzle. Although, the small size of the orifice was the best one in terms of the interfacial area of mass transfer, its liquid side mass transfer coefficient (k_L), pressure drop and power consumption should also be considered as the k_L was normally low for the small and low velocity droplets. In addition, a large power consumption would lead to inappropriate condition in terms of economical aspect. Figure 3.35 shows the results of specific interfacial area as a function of power consumption calculated with Equation (3.9).
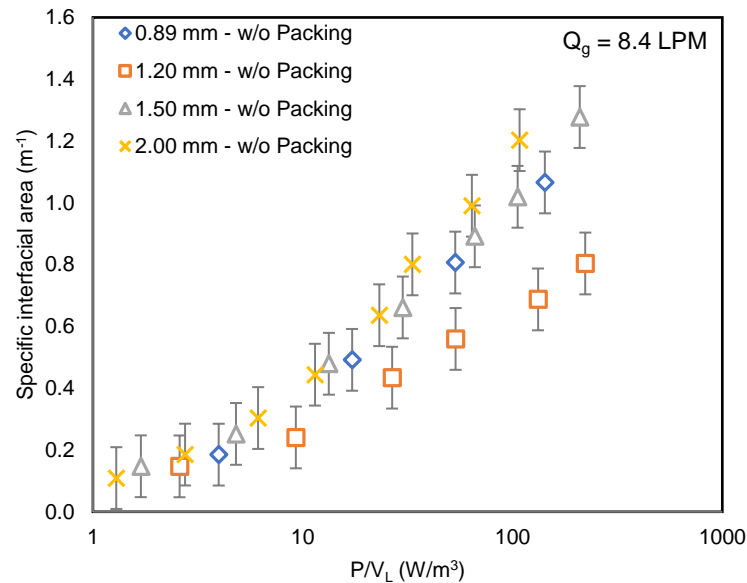
Figure 3.35 Specific power consumption as a function of power consumption for different sizes of nozzle orifices

According to the figure, the specific interfacial area increased when the power consumption increased due to the fact that the power consumption was large at high liquid flow rate where large number of droplets were produced. In addition, when comparing between each orifice size, the smallest orifice size (0.89 mm) was not the best one to give the highest specific interfacial area at the same power consumption. The high pressure drop occurred during sudden contraction of the small orifice was responsible for the effect. The optimum one for the specific interfacial area was the 2.00 mm orifice nozzle that yielded the highest interfacial among all other orifices. However, it should be noted that the highest specific interfacial area of 2.0 mm nozzle came from the high liquid flow rate at low pressure drop of the nozzle. Although the high specific interfacial area could be achieved, the amount of liquid consumed should also be considered. Thus, the cost of raw material of chemicals using for absorption was recommended to simultaneously be considered with the power consumption.

(c) Bubble – spray columns comparison

Figure 3.36 shows the comparison of the specific interfacial area between the bubble and spray columns in terms of specific power consumption (P/V_{Total}). The increase of power consumption of both equipment gave higher values of their specific interfacial area. However, it can be clearly seen that the specific interfacial areas of bubble column were significantly larger to those spray ones regardless of the orifice sizes. It was due to the fact that the disperse phase of bubble column was the gas phase while the continuous phase was the liquid phase. High density and viscosity of liquid phase resulted in the slow moving of disperse phase, where can be evidently seen in Figure 3.17 that the bubbles moving in the liquid phase had their velocities in the range of 0.2-0.5 m/s. In contrast with the spray, the droplets moving inside the column had

the range of velocities between 2-10 m/s, Figure 3.27, which was significantly larger than those of the bubble column. Hence, the residence time of the disperse phase for the bubble column was clearly smaller leading to the major cause of the significant different of specific interfacial area. Although the specific interfacial area is a function of both velocity and size, the small droplet sizes for the spray cases were not compensate with their high velocities. Thus, eventually, the specific interfacial areas of spray were lower when comparing with those of the bubble column. Nevertheless, it should be noted that, when considering the mass transfer, the specific interfacial area is not the only parameter that control the mass transfer. The mass transfer coefficient (k_L) is mandatory to take into account the mass transfer performance. The details of the mass transfer parameters of both bubble column and spray column are described in Chapter 5.
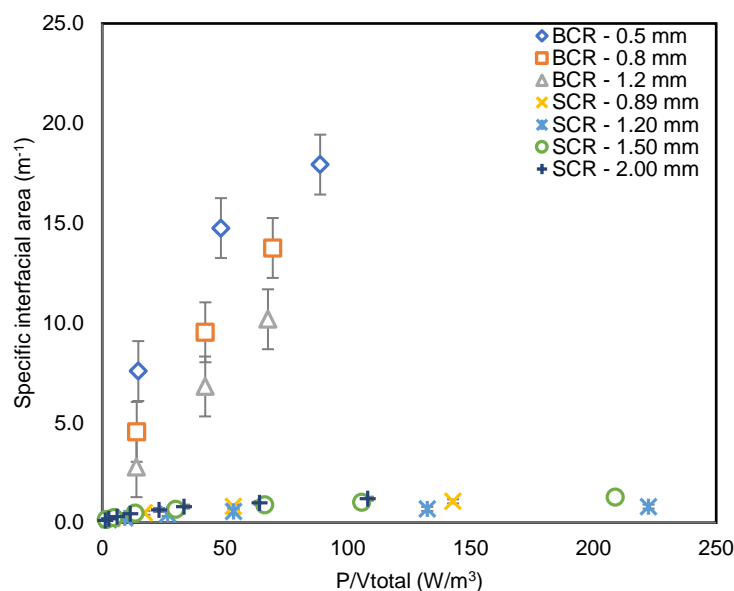
Figure 3.36 Comparison of the specific interfacial area between bubble column and spray column as a function of total specific power consumption

3.4.2 Three-phases columns

(a) Bubble column

(i) Average bubble diameter

Figure 3.37 shows the effect of packing and ring-shaped particles on the average bubble sizes of bubble column at different gas flow rates and orifice sizes. The presence of solid phase reduced the size of the average bubble diameter regardless of the solid types. However, the stronger effect was obtained when using the large size orifice as can be seen that the average bubble size was reduced from 6.77 mm to 5.09 and 4.44 mm for 1.2 mm orifice while the reductions from 5.02 mm to 4.44 and 4.35 mm were achieved for 0.5 mm orifice for the ring-shaped particles and packing, respectively.
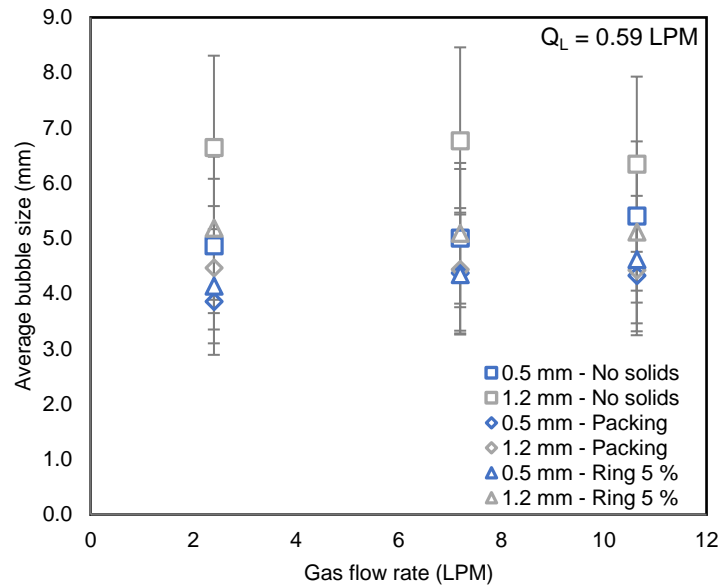
Figure 3.37 Effect of gas flow rate, orifice size, and solid phase on Sauter mean diameter

So far, the phenomenon of the bubble size reduction, due to the presence of solid, is still unclear. Normally, the addition of solid phase has three major impacts: increasing the breaking rate, acceleration of the coalescence rate, and slowing down bubbles (De Swart et al., 1996; Livingston and Zhang, 1993; Zhang et al., 2005). Here, both packing and solid particles gave the same effect, the addition of solids favored the breaking rate more than coalescence; therefore, the average bubble size decreased with the presence of solids. However, the promotion of breaking rate for the case of 0.5 mm orifice was not as strong as the 1.2 mm orifice. It probably occurred because there was a limitation of size reduction when solid phase was added (Moo-Young and Blanch, 1981). The turbulence around the solids may be responsible for the effect (Pang et al., 2011).

(ii) Average bubble rising velocity

Figure 3.38 shows the effect of packing on the average bubble rising velocity at different orifice sizes and gas flow rates. The packing increased the bubble rising velocity except for the 1.2 mm orifice. Although the size of bubble reduced after the presence of packing, the increase of bubble rising velocity was existed.
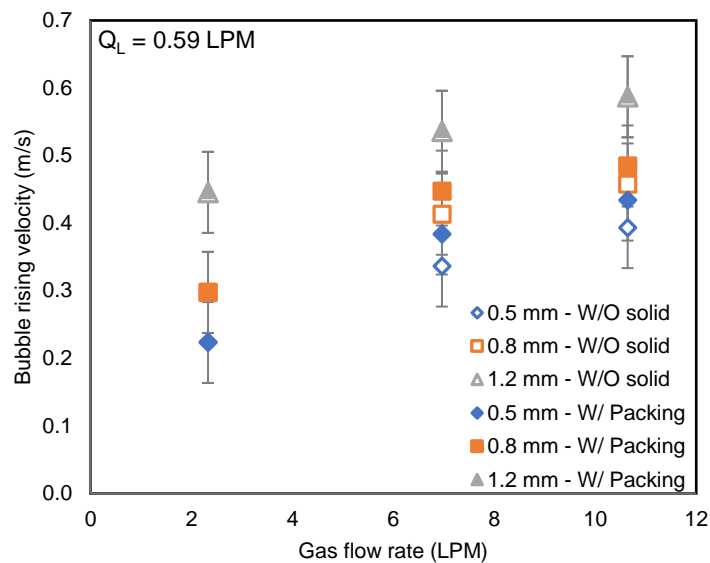
Figure 3.38 Effect of packing on bubble rising velocities at different gas flow rates
and orifice sizes

The arrangement of gas sparger at the bottom of the column was a major cause
for the occurrence where most of bubbles were not able to disperse in radial direction
due to the obstruction of packing. Therefore, the air lift regime was achieved leading to
create a restriction area of flowable zone for bubbles, leading to high liquid velocity
inside the column. Eventually, the bubble rising velocities rose in most of the
conditions. Note that for the case of 1.2 mm orifice, the presence of packing did not
significantly affect its bubble rising velocities. It indicated that for the case of 1.2 mm
orifice, bubbles rose to the liquid surface with the same regime as when the packing
presence. This incidence was due to the number of bubbles was low and each bubble
had high velocities. Consequently, most of the bubbles accumulated at the vertical
centerline of the column, which was the same regime as the center airlift column.
Hence, in order to develop a better regime, the gas sparger having orifices distributed
throughout the column bottom should be developed in the future since it can reduce the
effect of the bubble obstruction by the packing and still able to utilize the advantage of
the bubble size reduction of bubbles.

For the ring-shaped particles, as shown in Figure 3.39, the presence of the
particles could increase or reduce bubble rising velocities based on the orifice size used.
When the small orifice sizes, 0.5 and 0.8 mm were used, the bubble rising velocties
were not significantly changed while the bubble rising velocity sharply reduced when
the orifice size of 1.2 mm was applied. The same incident was occurred in the work of
Wongwailikhit et al., (2018). The bubbles obtruction, the increase of gas phase
dispersion as well as reduction of liquid velocity were presumed to resposible for the
effect.
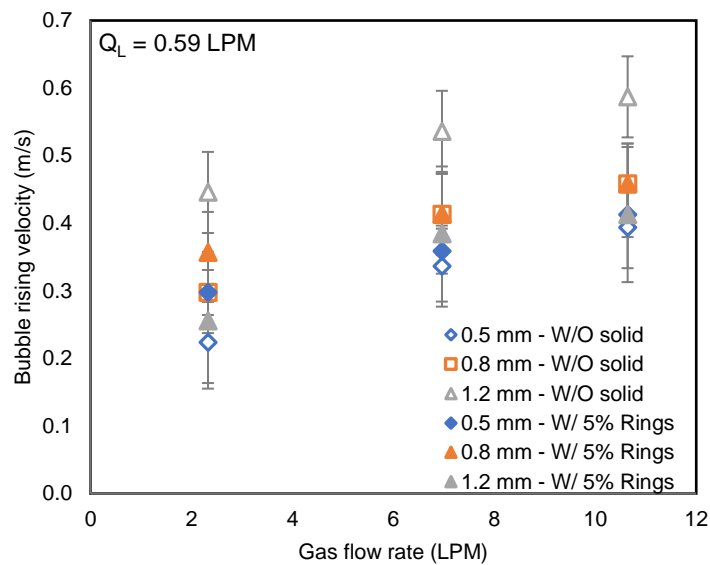
Figure 3.39 Effect of ring-shaped particles on bubble rising velocities at different gas flow rates and orifice sizes

When bubbles collided with the particles, the velocities of the bubbles decreased due to the loss of their kinetic energy. In addition, the trajectories of the bubbles were modified. Hence, for the case of 1.2 mm orifice size, the dispersion of gas phase increased, leading to higher numbers of bubbles dispersed to the radial direction of the column. Accordingly, since the airlift regime was diminished, the liquid velocity inside the column reduced. Therefore, the bubble velocity moving in the column were significantly lower. It should be noted that the reduction of liquid velocity was accomplished only in for the case of 1.2 mm since the promising gas dispersions in the cases of 0.5 mm and 0.8 mm were already achieved. Hence, it can be concluded that the addition of the ring-shapedparticles improved the gas dispersion in the bubble column espectially when the gas dispersion in the liquid phase was low.

(iii) Gas holdup

The results of gas holdup as a function of gas flow rates and orifice sizes are shown in Figure 3.40. The presence of packing slightly reduced the gas holdup in the case of 0.5 mm and 0.8 mm orifices while no significant effect was obtained when the orifice size of 1.2 mm was used except for ring-shaped particles. The influence of gas flow rates and orifice sizes on the gas holdup was in the same trend with the bubble rising velocities obtained in the earlier part since these two variables are strongly related. Recall that typically the gas holdup increases when the bubble rising velocity reduced.
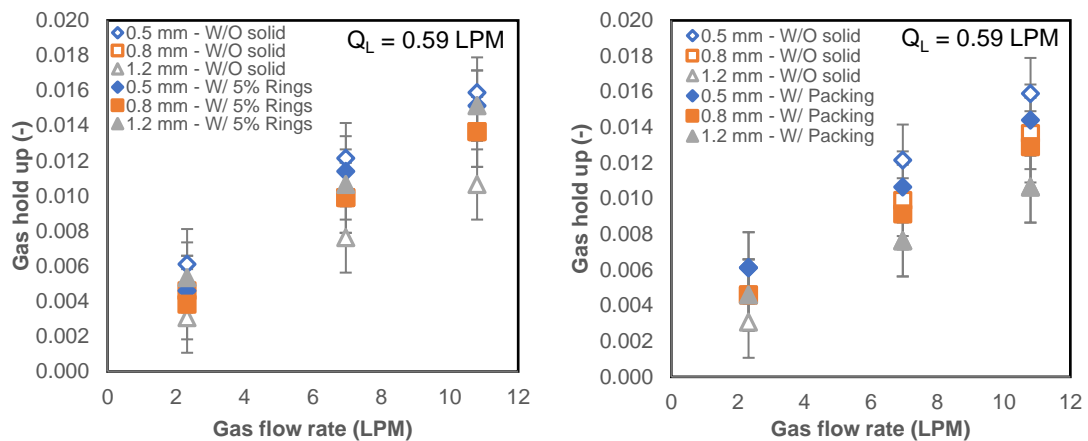
Figure 3.40 Effect of gas flow rate, orifice sizes, and solid phase on gas holdup
(Left) Movable particles (Right) Packing

The consistent results of gas holdups with the bubble rising velocities were also attained when the ring-shaped particles where the gas holdup increased when the orifice size of 1.2 mm was applied, but no significant effect were obtained when 0.5 and 0.8 mm orifices were used. Note that of all the liquid flow rate range used in this work, there was no significant effect of liquid flow rate on the gas holdup.

(iv) Pressure drop and power consumption
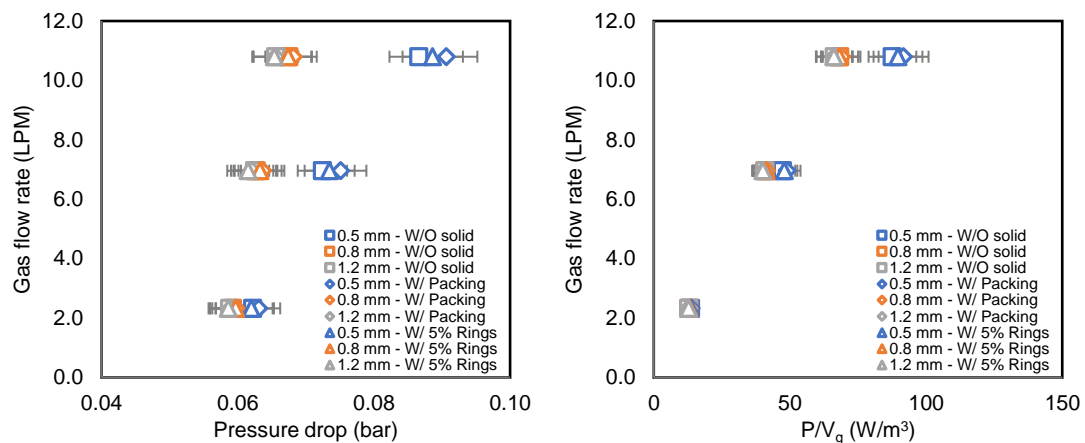
Figure 3.41 Effect of solid phases and different orifice sizes on
(Left) Pressure drop (Right) Specific power consumption

When considering the gas pressure drop required for a gas flow rate, the presence of packing as well as ring-shaped particles increased the pressure required to reach the same gas flow rate, which can be clearly seen in the case of 0.5 mm orifice. The inclusion of pressure required was due to the gravity force from mobile solid weight that increased the static pressure at the bubble formation position. For the packing effect, the liquid circulation promoted by the packing was responsible for the higher pressure required at the same gas flow rate. Note that for the specific power consumption, the same trend as the relation between pressure drop and gas flow rate

was obtained as those were calculated using Equation (3.9) where the power consumption was a function of pressure and gas flow rate.

(v) Specific interfacial area

When considering the specific interfacial area as a function of gas flow rate, orifice sizes, and solid types, Figure 3.42 shows that the addition of packing slightly increased the specific interfacial area. Although the gas holdup when the packing presented was diminished, the fact that the average bubble sizes reduced with the addition of packing should be noted. Therefore, the reduction of bubble sizes raised the specific interfacial area especially for the case of 1.2 mm orifice, where the significant reduction of bubble sizes was achieved.
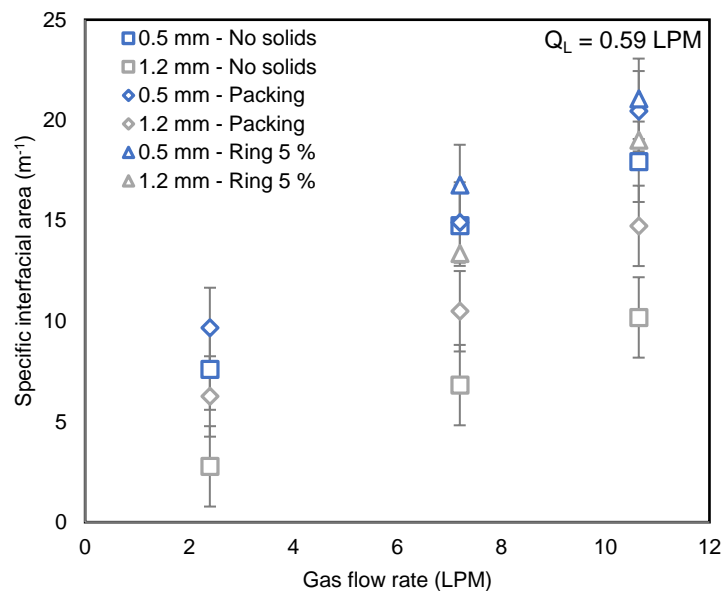
Figure 3.42 Effect of solid phases on the specific interfacial area as a function of gas flow rates and orifice sizes

The same effect was occurred to the specific interfacial area when the ring-shaped particles were added into the column. The specific interfacial area increased due to the smaller size of bubbles. However, a very strong increase of specific interfacial area was accomplished when the 1.2 mm orifice was used. The combination between the bubble size reduction and increase in gas holdup highly elevated the specific interfacial area. The elevation was clearly beyond the packing since the particles promoted the gas dispersion in the column. However, in order to conclude the optimal one, the specific interfacial area as a function of specific power consumption should be investigated, where the result is shown in Figure 3.43.
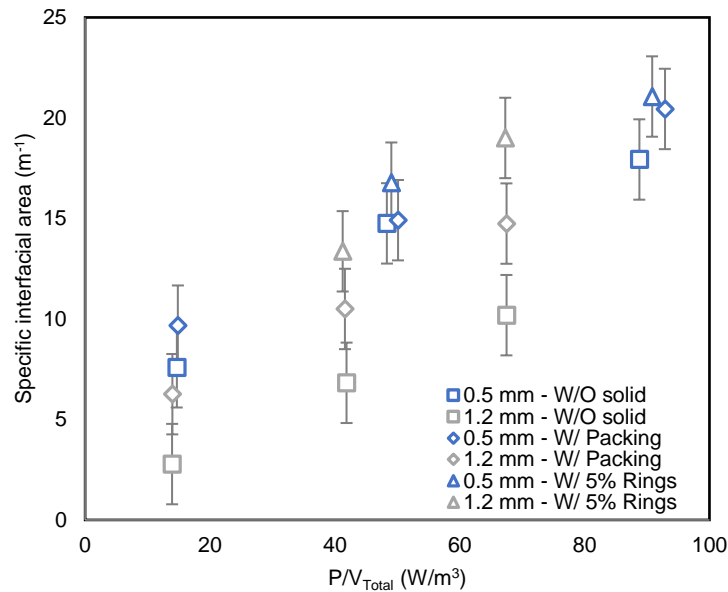
Figure 3.43 Specific interfacial area as a function of power consumptipn at different gas flow rates and orifice sizes

From Figure 3.43, the presence of packing and ring-shaped particles reduced the power consumption used to reach the same specific interfacial area comparing when there was no solid in presence. Among all conditions, it can be seen that the presence of ring-shaped particles for both 0.5 and 1.2 mm orifice sizes gave the highest value of specific interfacial area at a specific power consumption. As mentioned earlier, the increase of gas dispersion as well as reduction of bubble size were responsible for the effect.

Here, it can be concluded that, the addition of solid phases used in the work raised the specific interfacial area regardless of solid types. The best solid type was the ring-shaped particles where the highest specific interfacial area was achieved. It should be noted again here that, it might be able to increase effect of packing on the inclusion of specific interfacial area by the further experiment setup using a gas sparger that fully covers the cross-sectional area of the column in order to avoid the bubble dispersion obstruction to hinder the gas dispersion in the column.

(b) Spray column

(i) Average diameter

Figure 3.44 shows the effect of liquid flow rate, orifice sizes and presence of packing on the Sauter mean diameter of droplets at distance of 25 cm from nozzle. It should be noted here that the droplets determined in the figure were the non-collision droplets that did not contact with the packing. From the figure, it can be seen that, when considering only non-collision droplets, the Sauter mean diameters with the presence of packing were significantly smaller without packing conditions regardless of orifice sizes and liquid flow rates. Noted that the optical probe was not used for the

determination of droplet sizes; when the packing was presenting, it was not possible to safely equip the probe within the packing.
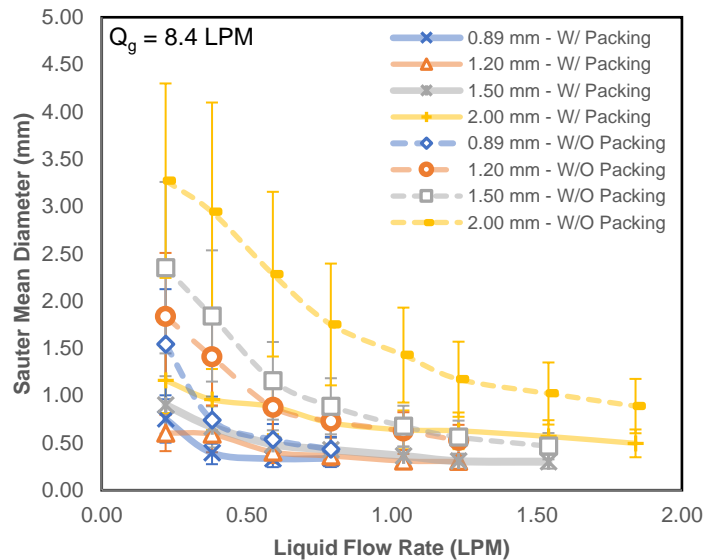
Figure 3.44 Sauter mean diamter of droplets at different flow rates, orifice sizes with and without the presence of high-void packing

The Sauter mean diameters with the presence of packing reduced due to the fact that, large diameter droplets had a higher chance to contact with the packing comparing with small ones. Figure 3.45 shows an example of image captured in a spray condition, where most of the droplets that settling freely at 25 cm distance from nozzle were mostly small. However, it should be noted that the Sauter mean diameters with the presence of packing did not entirely represent the interfacial area of mass transfer. The liquid film at the packing should also be considered when determining the specific interfacial area of the spray.
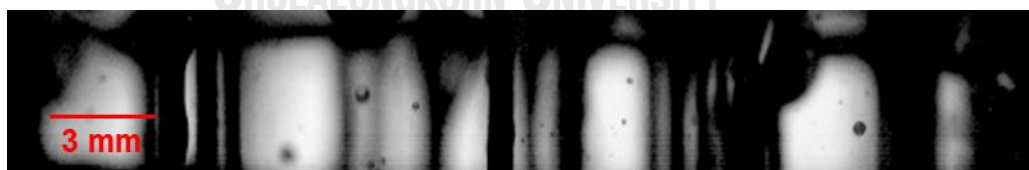
Figure 3.45 Non-collision droplets at the void of packing at 25 cm distance from nozzle

(ii) Droplet size – velocity distribution

When considering the effect of packing on the droplet velocity – size distribution, as can be seen in Figure 3.46. The same trend as without the presence of packing was obtained. Liquid flow rates increased the droplet velocity regardless of the orifice sizes while the smaller size of the orifice produced smaller size and higher

velocity of droplets. The difference between the presence of packing and without the packing was that some of the droplets had lower velocities than their usual regimes.
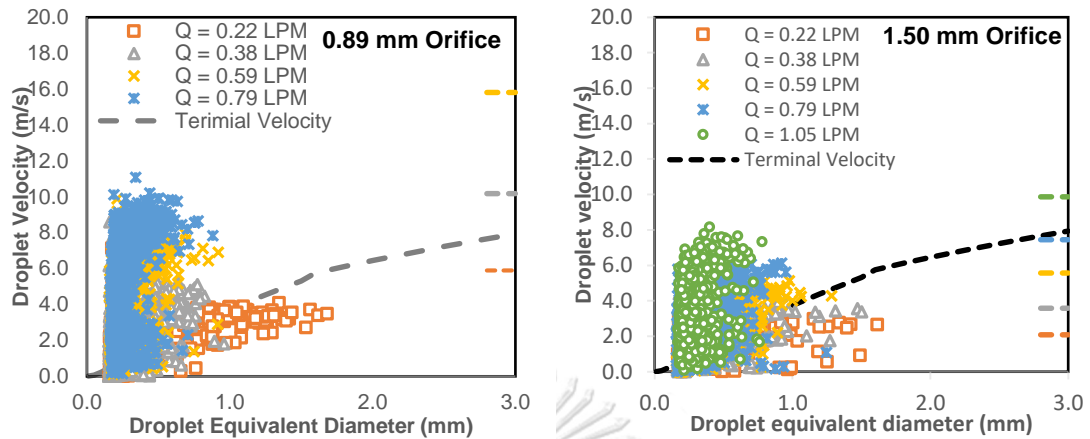
Figure 3.46 Droplet velocity – size distribution at different liquid flow rate, orifice sizes, and distance from nozzle determined using the high-speed camera at 25 cm from nozzle

This incident occurred due to the impact between droplets and high void packing. The collision between some droplets and the packing sharply reduced the velocities of droplets. Therefore, when determining the velocities of non-collision droplets when the packing was presenting, there were two regimes of droplets. The first regime was the normal regime of droplet where droplets did not contact with the packing and their velocity followed the same regime as the no packing condition. The other regime was the droplet that impacted with the packing. These droplets had slower velocities than those without the impact. In addition, when considering the droplets size and velocity at the bottom of the packing as can be shown in Figure 3.8.

Figure 3.8 shows that the droplets can be categorized into two different sizes; large and small ones. The small droplets were the droplets that produced at the nozzle orifice and did not contact with the packing. However, in the case that droplets contacted with the packing, it would form a liquid film covering the surface of packing. This liquid film was then gravitated to the bottom of the packing, condensed and formed larger-sized droplets. Hence, when determining the velocity and size distribution of droplets at the bottom of the packing, it can be sorted into two regimes as shown in Figure 3.47.
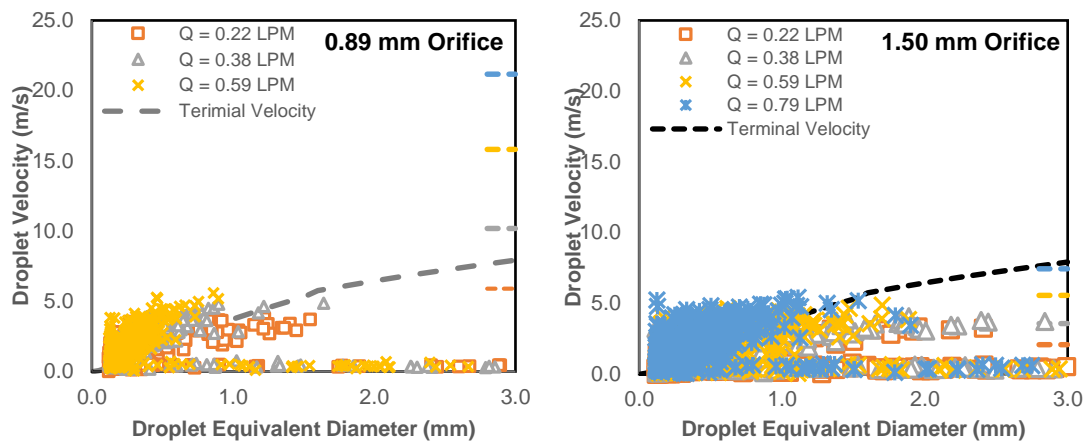
Figure 3.47 Droplet velocity – size distribution at different liquid flow rate, orifice sizes, and distance from nozzle determined using the high-speed camera at the bottom of packing (65 cm from nozzle)

According to the droplet velocity distribution, the droplets that didn't collide with the packing would have a velocity closer to the terminal velocity at a distance between the nozzle and the high-speed camera of 65 cm than those at a distance of 25 cm. Also, some droplets at a distance of 65 cm appeared to have much larger sizes when compared to those at a distance of 25 cm. In this case, they were identified as the droplets formed by the condensation of the liquid film at the bottom of the packing as in Figure 3.8. Note that the velocity and size distribution of the large droplets in Figure 3.47 were not included in the interfacial area calculation because they were at the bottom of the packing where the area from here onwards has significantly less influence on the mass transfer than the upper part of the packing. Nevertheless, the proportion of the large and small droplets can be used to determine the ratio of the fluid that still exists in a droplet form and the fluid that condenses as a film surrounding the packing by using Equation (3.14), which calculated the fraction of non-collision droplets by determining the volume fraction of small droplets to the total volume of droplets, where the result of the calculation is shown in Figure 3.48.
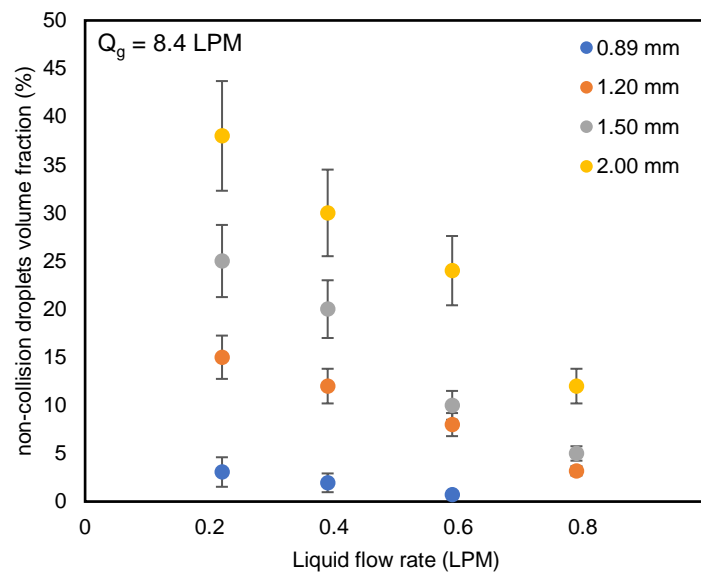
Figure 3.48 Non-collision droplets volume fraction as a function of liquid flow rates and orifice sizes

From the figure, the volume fraction of non-collision droplets to the total liquid volume decreased over the increase of liquid flow rate. It was due to the fact that as the liquid flow rate increased the angle of spray rose as well as the number of droplets produced at the nozzle. Hence, the chance of droplets to contact with the packing was larger when at higher liquid flow rates. In addition, when using the small size orifices, it can be seen in the figure that the volume fraction of non-collision droplets reduced dramatically. The decrease occurred because the angle of spray of the small orifice size was larger than the larger ones. Hence, the chance of wetting the packing was significantly larger as can be seen in Figure 3.48.

(iii) Average velocity

Figure 3.49 shows the effect of packing, liquid flow rates, and orifice sizes on the average velocity of non-collision droplets. According to Figure 3.49, the effect of liquid flow rates to the average droplets velocities were in the same trend as without packing; the velocity increased with the liquid flow rate. The smaller orifice sizes also produced higher average velocity of droplets regardless of the presence of the packing. In addition, as described in the droplet velocity – size distribution, the velocities of some droplets decreased with the presence of packing because some of the droplets collided with the packing and reduced their velocities.
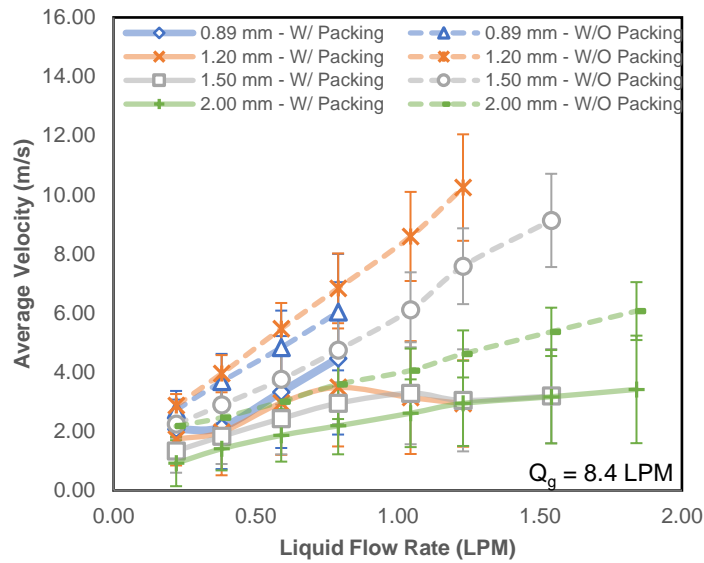
Figure 3.49 Droplet average velocity at different orifice sizes and liquid flow rates with and without the presence of packing

(iv) Pressure drop and power consumption

For this section, the pressure drop and power consumption when the packing was presented are analyzed. It should be noted that the liquid pressure drop was insignificantly changed as most of the pressure drop for the liquid phase was from the sudden contraction of the spray nozzle. Therefore, in this section, only the effect of gas flow rate, its pressure drop and power consumption will be discussed.
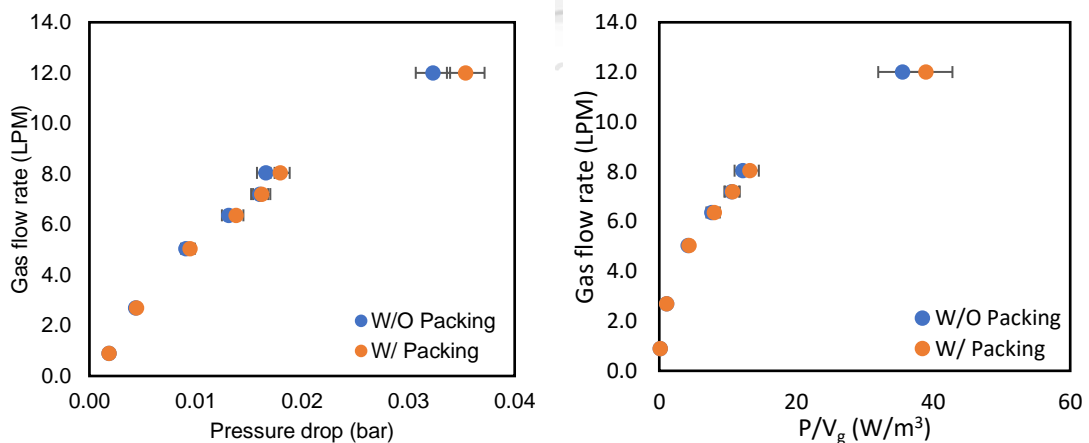
Figure 3.50 (Left) Effect of pressure drop on the gas flow rate (Right) Effect of power consumption on the gas flow rate

When determining the relationship between pressure drop and gas flow rates when the packing was presenting, it can be seen in Figure 3.50 that in order to obtain high gas flow rate, the pressure consumption was also large. The same trend was achieved between with and without the presence of packing. However, in order to

obtain the same gas flow rate, a slightly higher pressure was required in the case of packing. It was due to the presence of packing increased the shear surface that could reduce the velocity of gas flow inside the column. Therefore, when the shear force increased, a higher pressure was mandatory in order to obtain the same gas flow rate. Fortunately, only small portion of pressure needed to be risen as the packing was the high-void packing where the pressure drop across the packing was low comparing with other types of packing. Note that the relation between the gas flow rate and power consumption followed the same trend as the pressure drop and gas flow rate relation since it calculated directly via the pressure drop and gas flow rate using Equation (3.9).

(v) Specific interfacial area

The specific interfacial area when the packing was presenting consisted of two areas: the non-collision droplets interfacial area and the liquid flow that covered the packing surface area. In order to determine both interfacial areas, the fraction between the non-collision droplets and wetting surface area needed to be investigated. The volume fraction of the non-collision droplets was determined using Equation (3.14) as shown the result in Figure 3.48. The volume fraction was then used to determine the actual interfacial area by multiplying with each interfacial area as mentioned in Equation (3.15) and (3.16). From the equations, the effective specific interfacial area of packing was estimated (Equation (3.15)) and the total interfacial areas were calculated and shown the results in Figure 3.51.
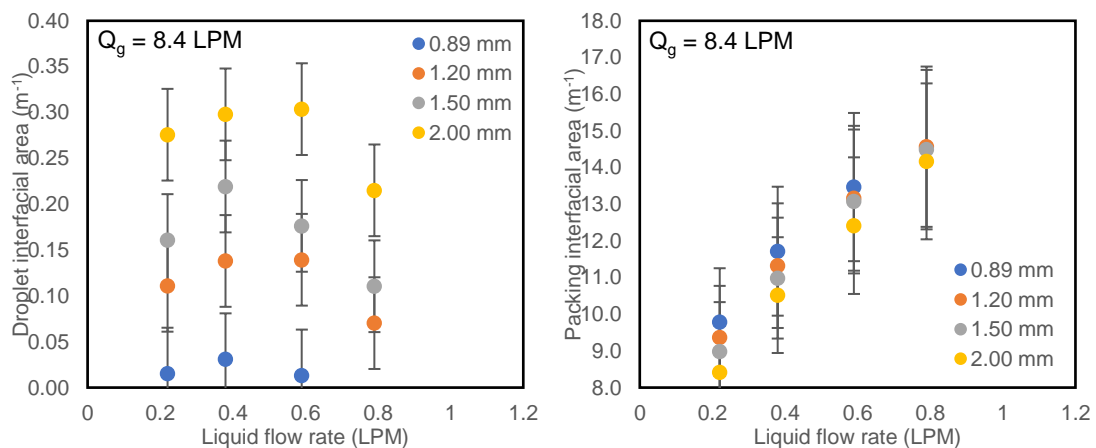
Figure 3.51 Effect of liquid flow rates and orifice sizes on the specific interfacial area of spray column with the presence of high-void packing
(Left) Droplet interfacial area (Right) Packing interfacial area

Figure 3.51(Left) and (Right) shows the effect of liquid flow rates and orifice sizes on the specific interfacial area of droplets and packing, respectively. Note that the vertical axis of both figures is not in the same magnitude. The range of the droplet interfacial areas was between $0 - 0.35$ m^{-1} while the packing interfacial area was range between 8-15 m^{-1}. Therefore, by comparing between both interfacial areas, it can be seen that the interfacial area of packing had higher impact than the droplet interfacial

areas. In addition, the orifice sizes had a strong effect on both interfacial areas since the droplet interfacial areas of 0.89 mm was the lowest of the droplet interfacial area but the highest for the packing interfacial area. It was due to the fact that the small size of the orifice produced a larger angle of spray when comparing with the large ones. Therefore, the chance of droplets in contacting with the packing was higher, leading to lower number of non-collision droplets left in the system. This result was already mentioned in Figure 3.48. Thus, it can be concluded that with the presence of packing, the higher specific interfacial area of mass transfer was achieved. Figure 3.52 shows the total specific interfacial area, which is the summation of packing and droplet interfacial area, in comparing with the conventional spray condition without the presence of packing.
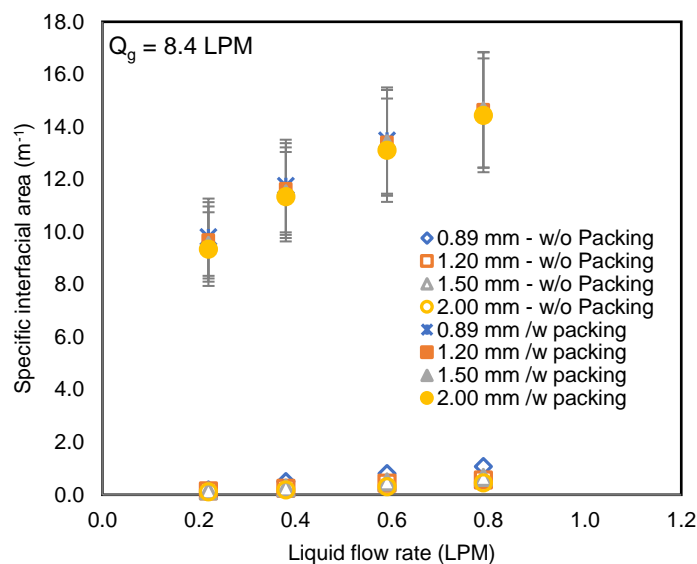
Figure 3.52 Effect of high-void packing on the specific interfacial area at different flow rates and orifice size

Figure 3.52 shows the effect of packing, liquid flow rates and orifice sizes to the specific interfacial area of mass transfer. It can be seen in the figure that, with the presence of packing, the specific interfacial area increased dramatically. The increase was clearly around 3-4 folds of the interfacial area without the presence of packing. The best condition of the interfacial area was the one with the orifice size of 0.89 mm where the total interfacial area was the highest among all other conditions. The angle of spray as well as small size of droplets responsible for the finding as descried earlier. From this figure, it can be clearly seen the advantage of using the high-void packing in the spray condition since it significantly increased the interfacial area and only small portion of pressure needed to be increased. However, in order to understand the finding comprehensively, the comparison with the bubble column in terms of the interfacial area and the power consumption should be investigated.
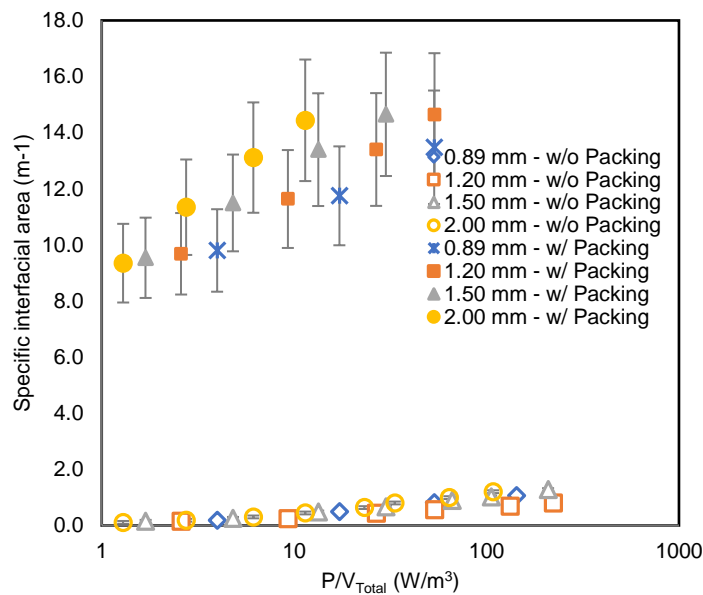
Figure 3.53 Effect of packing on the specific power comsumption at different orifice sizes

Figure 3.53 shows the effect of packing on the specific power consumption. The presence of packing significantly increased the specific interfacial area for the same power consumption. It indicated that the presence of packing promoted the specific interfacial area without further power consumption required. In addition, the 2.00 mm orifice size gave the highest trend of power consumption to the specific interfacial area. Hence, it can be concluded that the optimum orifice size in terms of power consumption was 2.00 mm. However, it should be noted that the high liquid flow rate is required in order to acquire high specific interfacial area. Hence, the cost of chemical or substance used for the liquid phase should also be considered as one of the operating costs in the spray system.

(c) Bubble – spray column comparison

Figure 3.54 shows the comparison between the bubble column and the spray column in terms of specific interfacial area with the addition of solid phases. With the increase of specific power consumption, both equipment gave a higher value of specific power consumption regardless of their orifice sizes.
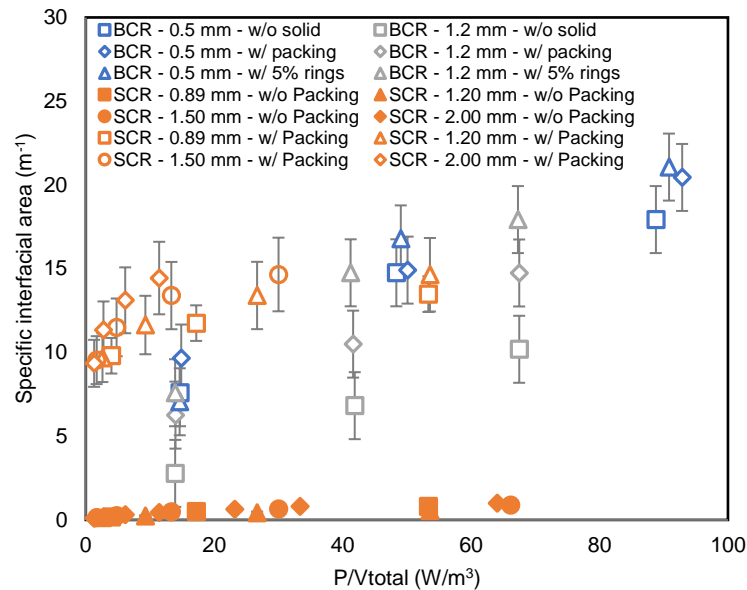
Figure 3.54 Comparison of three-phases bubble column and spray column in terms of specific power consumption and specific interfacial area

Despite the specific interfacial areas of two-phase spray column which were extremely low, the presence of packing in the spray column increased the specific interfacial area to be compatible with the bubble column especially at low specific power consumption. Without the presence of solid phase on the bubble column, the specific interfacial areas of spray were even higher for some conditions. However, at high specific power consumption, the specific interfacial area attained by the bubble column was larger especially with the cases where the ring-shaped particles were added. From this point, it can be concluded that when considering the specific interfacial area, the bubble column with the addition of ring-shaped particles achieved the highest value of specific interfacial area especially at high interfacial area.

3.5 Conclusion

In this chapter, the hydrodynamics of both bubble and spray columns were investigated, including the addition of solid phase. The disperse phase of bubble column, which was in bubble form, had significantly lower velocities than the droplets in the spray column. Although the droplet generated at the orifice were smaller than the bubbles, the fact that the residence time of the droplets was extremely lower than bubbles was unavoidable since the droplet velocities were very large. Hence, without the presence of solid phases, the specific interfacial areas of spray at any conditions were much inferior than the bubble column ones. However, with the addition of packing in the spray, the specific interfacial area increased dramatically due to the wetting effect on the packing surface. These specific interfacial areas of packing spray were slightly higher than the bubble column without the addition of solid.

The presence of the packing or the ring-shaped particles affected the hydrodynamics in the bubble column differently. Although the smaller sizes of bubbles were accomplished with the addition of both packing and ring-shaped particles, the gas holdup was reduced with the presence of packing. It was in contrast to the presence of the ring-shaped particles where gas holdup was increased. The lower of gas dispersion in the liquid phase was responsible to the effect when the packing was presenting due to the obstruction of bubbles from dispersion to the radial direction by the packing wires. In contrast, the ring-shaped particles promoted the gas dispersion especially for the large orifice size case. The promotion resulted in the strong increase of specific interfacial area without significant addition of power consumption. This addition of the ring-shaped particles increased the specific interfacial area to be higher than those of the spray with the packing. Hence, it can be concluded that, when considering only the specific interfacial area, the bubble column with the addition of ring-shaped particles was the best one among all the other conditions. However, it will be very important to consider the mass transfer behavior in both systems with or without packing to be able to conclude on which reactor is the best one for the mass transfer of few soluble molecule as carbon dioxide.

In the next chapter, the effect of solid on the mass transfer in a bubble column will be determined locally using the colorimetric method. The finding was the one crucial for the explanation for the presence of solids inside the bubble column in term of mass transfer effect.

Chapter 4

Colorimetric method for characterizing mass transfer in bubble column

4.1 Abstract

In this chapter, two colorimetric methods were used to investigate the mass transfer in bubble columns with the presence of solids. The first method was developed for the determination of $k_L a$ in bubble columns with the colorimetric without using any probe or equipment rather than a camera. The advantages of the method are that, firstly, the modification of fluid flow due to the probe or other instruments equip inside the column can be avoid. Secondly, the mass transfer can be seen visually where it can be used as a very good example for the education in mass transfer purpose for students to visually understand the phenomena. This methodology is planned to publish in Chemical Education journal.

The colorimetric method achieved a good explanation for the effect of moving particles on the mass transfer of the three-phase bubble column. Small bubbles and large bubbles interacted with particles differently in terms of hydrodynamics and mass transfer since the small bubbles lost their velocity sharply after collision with solids while the large ones did not significantly change their velocity after collision. The change of bubble velocity after collision was the main cause of the change of mass transfer coefficient since it depends on the bubble velocity. This finding is planned to conduct a further experiment in order to acquire a better image in order to ensure the results and therefore submit for a chemical engineering field journal.

4.2 Introduction

In this section, two procedures that applied the colorimetric method of "red bottle" has been used in bubble columns. Firstly, a procedure used for determination of the overall liquid side mass transfer coefficient ($k_L a$) was developed in a small bubble column. The technique can be further used as an alternative method for determining both local and global mass transfer in a reactor. It also can be used in education purpose, due to its outstanding advantage as the mass transfer of oxygen can be seen visually. Secondly, the other procedure developed by Dietrich and Hébrard, (2018) was used to investigate the effect of solid-bubble collision on the local mass transfer of bubbles. The experiment virtually clarified the effect of solid-bubble collision on the different sizes of bubbles, which until now have not been comprehensively investigated.

4.3 Overall mass transfer coefficient determination using colorimetric method

In this section, a new method using colorimetric for determination of the overall mass transfer coefficient in a bubble column was developed. The methodology and results are expressed as follow.

4.3.1 Methodology

(a) Colorimetric method principle

The colorimetric principle is based on the utilization of an oxygen-sensitive dye, where an oxidation/reduction reaction occurs when oxygen presents in the solution. With the reaction, a change of colors happened, leading to different colors after the reaction. The "blue bottle" experiment is one of the well-known reactions where the methylene blue is reduced from blue color to colorless after the reaction. Various literatures used the properties of these reactive dyes to visualize their experiment (Cook et al., 1994; Engerer and Cook, 1999; Wellman et al., 2003). The main advantage of this colorimetric is that it is a non-intrusive method; the experiment can be conducted without disturbing of any sensors that can lead to a discrepancy. However, the main drawback to the colorimetric using the methylene blue is the slow kinetics of the reactions (Wellman et al., 2003). Therefore, in order to select the suitable reactive dye, two factors should be considered: the kinetic of the reactions and the intensity of color generated due to the reaction. According to the study of Dietrich et al., (2013), the resazurin was the appropriate one due to a good compromise between kinetics and color.

Figure 4.1 shows the reduction reaction of resazurin to resorufin which changes the color from dark blue to pink by the glucose and sodium hydroxide. The further reaction can be occurred with the presence of remaining glucose and sodium hydroxide where the resorufin can be reduced to dihydroresorufin, which is the colorless substance. The dihydroresorufin can be re-oxidized when the oxygen is presenting in the solution. The substance converts back to resorufin that has pink color. Thanks to the change of the color, these overall reactions can be used to identify the oxygen mass transfer in the solution. The summary of the reaction can be expressed as in Equation (4.1), where the colorless solution changed from colorless to pink solution with the presence of dissolve oxygen. However, the pink solution can be converted back to colorless solution via the reduction of remaining glucose and sodium hydroxide. Note that the reaction rate of reaction (4.2) is slow when compared with the re-oxidation reaction, reaction (4.1).

$$O_2 + 2 \cdot \text{Dihydroresorufin} \rightarrow 2 \cdot \text{Resorufin} + 2 \cdot H_2O \tag{4.1}$$

$$\text{Resorufin} + \text{Dextrose} \rightarrow \text{Dihydroresurufin} + \text{gluconic acid} \tag{4.2}$$
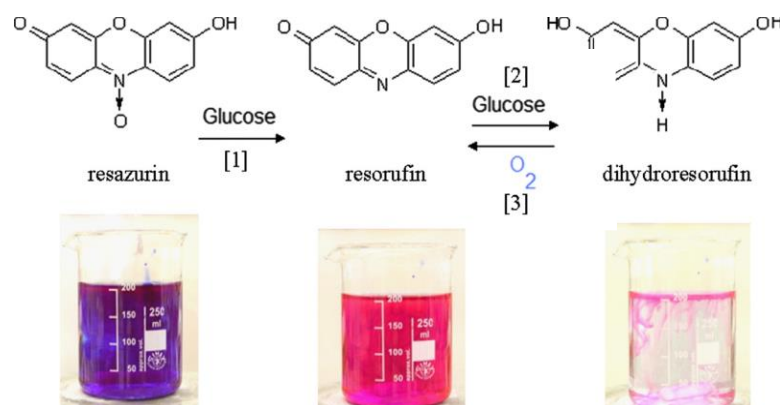
Figure 4.1 Reduction reaction of resazurin to resorufin by glucose and sodium hydroxide
(step 1), futher reduction to dihydroresorufin (step 2), and reoxidation of dihydroresorufin to resorufin with the presense of oxygen.

According to the experiment of Dietrich et al., (2013), the best concentration of resazurin (Sigma Aldrich, CAS 62758-13-8), d-glucose anhydrous (Fisher Scientific, CAS 50-99-7), and sodium hydroxide (VWR, CAS 1310-73-2) were 0.1 g/L for resazurin and 20 g/L for both glucose and sodium hydroxide. Note that at this condition none acceleration of mass transfer is observed corresponding to the enhancement factor (E) is close to one; hence, the phenomenon observed in this experiment represents the physical transfer of oxygen (Yang et al., 2017). The solution was prepared before used in the experiment by the addition of the 3 substances into 250 mL of de-ionized water. After stirred for 30 minutes, the solution converted from blue solution into pink and colorless respectively. The properties of the liquids are showed in Table 4.1. It should be noted that the surface tension of the colorimetric solution was less than those of de-ionized water. Hence, bubble characteristics might slightly change due to this different property.

Table 4.1 Properties of colorimetric solution at 20°C (Dietrich and Hébrard, 2018)

Liquid phase	Concentration (g/L)	Surface tension (mN/m)	Viscosity (mPa.s)	Density (kg/m³)
De-ionized water	-	73.4	1.003	996.8
Glucose	20	75.5	1.1179	1005.2
NaOH	20			
Glucose	20	45.4	1.1179	1005.3
NaOH	20			
Resazurin	0.1			

(b) Experimental setup
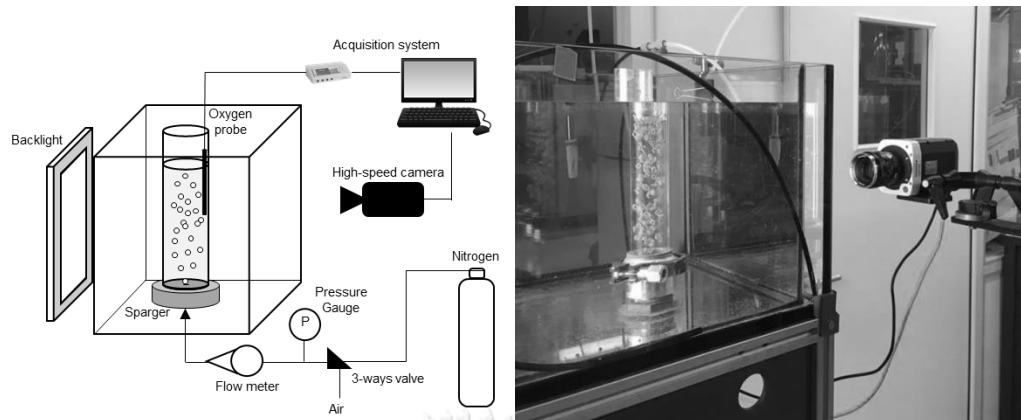
Figure 4.2 Experimental setup of overall mass transfer coefficient determination using a colorimetric method

Figure 4.2 shows the experimental setup used for the overall mass transfer coefficient determination using the colorimetric method. A bubble column having 4.5 cm in diameter was filled with the 250 mL of the colorimetric solution prepared following the method described earlier. A perforated plate gas sparger containing 5 orifices was positioned underneath the column, connecting to the gas inlet line that regulated its flow rate by a flow meter. Air or nitrogen can be selected to purse into the column using a 3-ways valve. The interval distance between each orifice is 1 cm. The diagram of the orifice can be illustrated as in Figure 4.3.
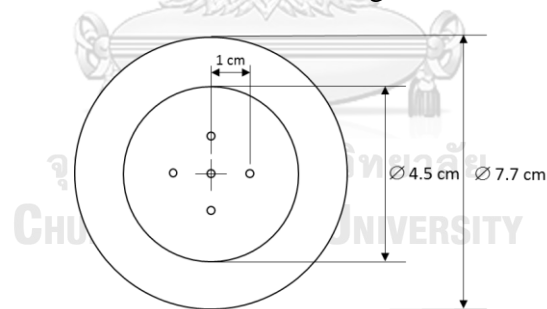
Figure 4.3 Diagram of perforated plate

The gas flow rate of 0.6 LPM (corresponding to the superficial velocity of 0.59 cm/s) was used throughout the experiment. Two sizes of orifice were studied: 0.5 and 0.8 mm. A high-void packing as shown in Figure 4.4 was also introduced into the bubble column in order to study its effect on the oxygen mass transfer. The packing had the same diameter as the column with the height of 15 cm. The overall volume of the dry was 6.25 mL, hence it consumed only 2.5 % of the total liquid volume in the column.
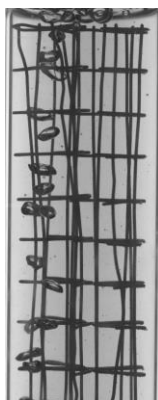
Figure 4.4 A high-void packing in the bubble column

(c) Global overall mass transfer coefficient determination using colorimetric method

(i) Image acquisition and processing

A high-speed camera (Vision Research, Miro – M110, USA) was used as the image acquisition equipment connecting to a computer. A backlight from PHLOX with a luminance of 30383 cd/m^2 and a uniformity of 93.65 % was set up as the image background. The Carl Zeiss 50mm f/1.4 Planar was equipped as a lens of the camera and the acquisition rate of 100 fps was used. Figure 4.5 shows the sample photos captured by the image acquisition system at different time.

In the figures, it can be seen that the color of the solution was bright and clear at the beginning corresponding to the color of the dihydroresorufin. After a certain time, the color of the solution became darker and finally the captured image was mostly dark throughout the column. The gray level at the center of the column was used to determine the overall liquid side mass transfer coefficient ($k_L.a$) by recording the gray level as a function of time. Note that the assumption of perfect mixed can be assumed since the homogenous gray level throughout the column was obtained.
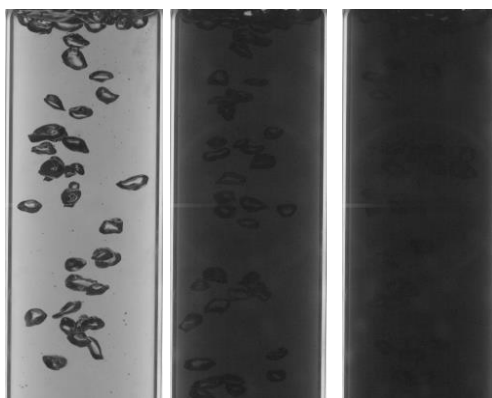
Figure 4.5 Image captured by the high-speed camera at different times
(Left) At the beginning (Center) 47 seconds from the beginning (Right) At the end
point

(ii) Calibration curve

In order to convert the level of gray obtained from the high-speed camera to oxygen equivalent concentration, a calibration curve had to be developed. The term "equivalent" represented the quantity of real dissolved oxygen that transferred per unit volume and reacted with the reactive dye. By assuming that none acceleration of the oxygen transfer was induced from the chemical reaction, the physical absorption of oxygen can be assumed. The stoichiometry of the reaction between oxygen and dihydroresorufin is expressed in Equation (4.1), where its number of moles reacted with each other can be expressed as in Equation (4.3).

$$n_{O_2,transferred} = n_{O_2,reacted} = \frac{n_{dihydroresorufin}}{2} = \frac{n_{resazurin}}{2} \tag{4.3}$$
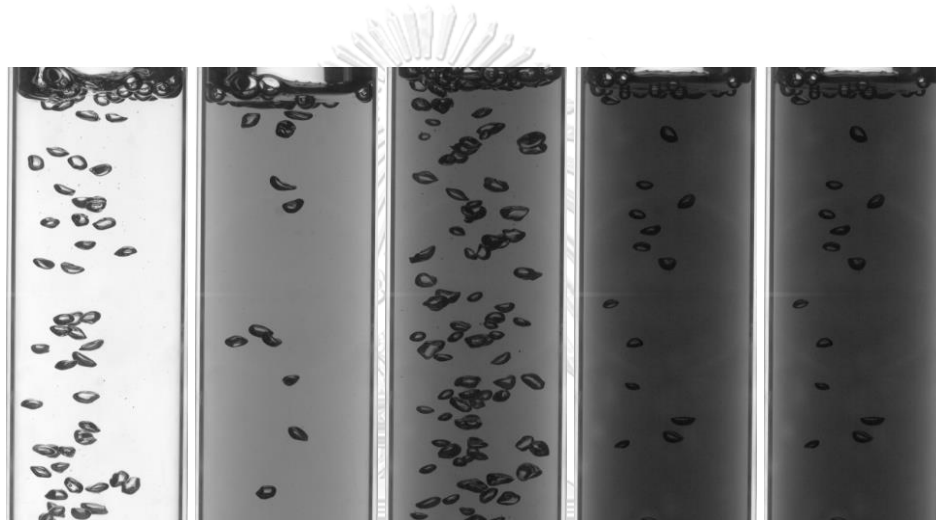
Figure 4.6 Variation of gray level used for at different amount of resazurin
(Left to right) 0, 12.5, 25, 50, 100 mg/L

Several colorimetric solutions were prepared at different concentrations of resazurin (from 0 to 100 mg/L). Air was fed through each solution in order to make every solution saturated with oxygen. The levels of gray at the saturated point of each concentration were recorded more than 100 images; the average values were used as the representative value for each condition. Figure 4.6 shows the images captured in order to develop the calibration curve. It can be seen in the images that, the higher concentration of resazurin prepared in the solution, the darker level of gray it obtained. After using Equation (4.2) to determine the amount of oxygen transferred and determine its concentration, the calibration curve was achieved as shown in Figure 4.7.

$$Absorbance = A_L = 1 - \frac{I}{I_0} \tag{4.4}$$

Figure 4.7 shows the calibration curved plotted at different concentration of resazurin that saturated with oxygen from Figure 4.6. The absorbance value calculated by Equation (4.5) was plotted as a function of oxygen equivalent concentration calculated with Equation (4.3). I_0 and I in the equation represent the light intensity

captured by the camera for the based solution (0 mg/L of resazurin) and for the certain concentration of resazurin, respectively. The relation between the absorbance and the oxygen equivalent concentration can be clearly seen as non-linear function as expressed in Equation (4.5). From the various functions, the exponential function was the best function matched with the experimental values. The non-linear relation was obtained due to the fact that the light had to travel pass through the layers of fluid equal to the diameter of the column. The light absorbed as it passed through the layers and reduced its intensity as it travels. The reduction of the intensity followed the explanation of the famous Beer-Lambert law (Mayerhöfer et al., 2016), which is a non-linear function. It should be noted that all the experimental was set up at the same condition in order to ensure the calibration of the system, which changes with the different setup.

$$C_{e,O2} = 0.174 \exp(4.129 A^{1.089} - 1) \tag{4.5}$$
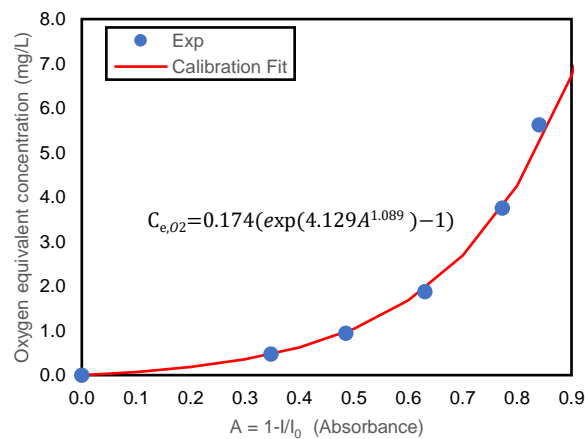
Figure 4.7 Calibration curve between absorbance of dye and oxygen equivalent concentration

(iii) Global overall liquid mass transfer coefficient

According to the mass transfer equation in batch operation and perfect mixed assumption, the mass transfer of oxygen can be expressed as in Equation (4.6), where C_{O2} is the concentration of oxygen dissolved in liquid, $C_{e,O2}$ is the equivalent oxygen concentration calculated according to Equation (4.3), $k_L a$ is the overall mass transfer coefficient, and C^* is the saturated concentration of oxygen in water. Noted that the $C_{e,O2}$ was obtained by the value of gray in each experiment and the calibration curve, Equation (4.5).

$$\frac{dC_{e,O_2}}{dt} = k_L a \left(C^* - C_{O_2}\right) \tag{4.6}$$

Since the actual oxygen concentration is zero due to the reduction reaction, Equation (4.6) becomes:

$$\frac{dC_{e,O_2}}{dt} = k_L a C^* \tag{4.7}$$

After integration, Equation (4.7) can be expressed as in Equation (4.8).

$$\frac{C_{e,O_2}}{C^*} = k_L a \cdot t \tag{4.8}$$

At the saturated condition, the concentration of oxygen should be equal to the C^*. Hence, Equation (4.8) can be written as follow; where t_f and t_i are the time at the beginning of the reaction and at the time at the saturated concentration, respectively.

$$\frac{C^*}{C^*} = 1 = k_L . a \cdot (t_f - t_i) \tag{4.9}$$

Therefore, the overall mass transfer coefficient ($k_L.a$) can be easily determined by the reaction time spends until reaches the saturated concentration as shown in Equation (4.10).

$$k_L a = \frac{1}{(t_f - t_i)} \tag{4.10}$$
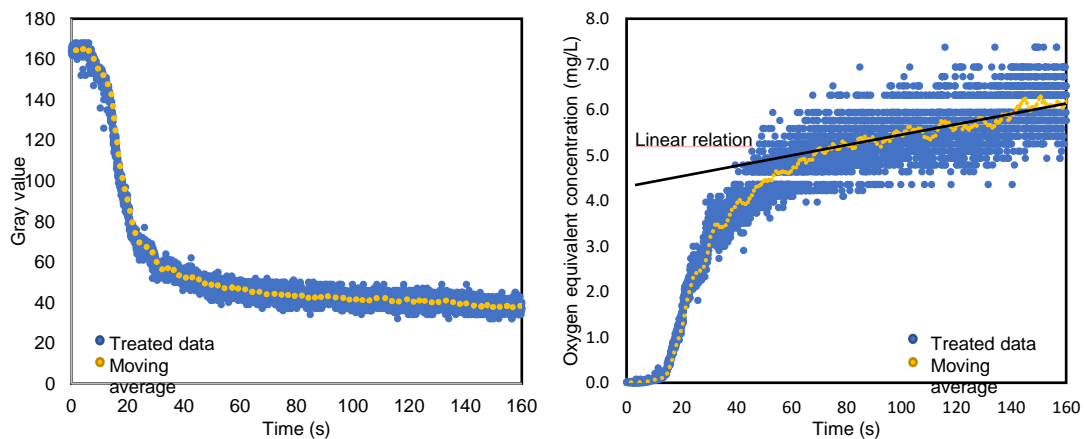
Figure 4.8 (Left) Gray value as a function of time (Right) oxygen equivalent concentration from mass transfer as a function of time

According to the raw data shown in Figure 4.8(Left), An example of the results for the oxygen concentration as a function of time is shown in Figure 4.8(Right). In the figure, the saturated concentration was not able to determine as the gradual increase of the oxygen concentration was observed when the time increased. The further research is needed to well understand this phenomenon. For the moment, it was presumed that this occurrence was caused by the calibration sensitivity due to the exponential function between gray value and oxygen equivalent concentration, Equation (4.5). The cylinder shape of the column was presumed to responsible for the occurrence.

However, it can be seen in the figure that the oxygen equivalent concentration rose linearly as a function of time. By using this fact, it is possible to normalize the data to obtain the raw data trend and acquire the initial time of reaction (t_i) and the saturated time (t_f). The linear regression of the experiment data after the oxygen equivalent concentration reached its linear function was performed and consecutively used to normalize the data by subtracted the experiment data by the slope of the linear function. Figure 4.9(Right) shows the oxygen concentration as a function of time after subtraction

of further oxidation reaction. It can be seen that, the initial time of reaction (t_i) and the saturated time (t_f) can be visually determined after the subtraction.
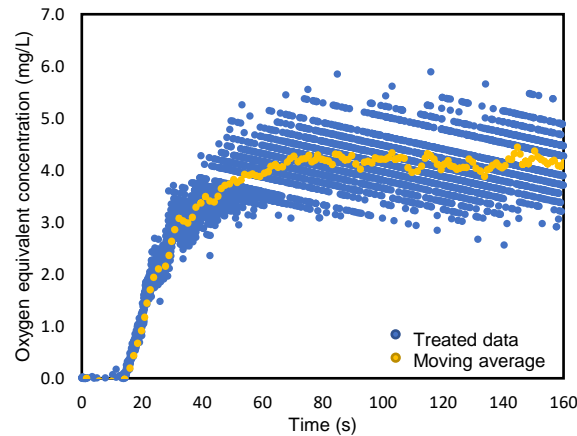
Figure 4.9 Linear subtraction technique used for determination of oxygen equivalent concentration from mass transfer as a function of time

In order to evaluate the method performance, another experiment was conducted. An oxygen sensor (Unisense A/S, Denmark) was equipped in the bubble column. The oxygenless water was prepared by pursing nitrogen gas until the concentration of oxygen reached zero. Afterward, air was fed through the column at the flow rate of 0.6 LPM. The concentration of oxygen was measured as a function of time (t) along the experiment until the concentration of oxygen (C) reached the saturated value (C^*). When the perfect mixed was assumed, the overall liquid mass transfer coefficient can be calculated according to Equation (4.11).

$$\frac{dC}{dt} = k_L a (C^* - C) \tag{4.11}$$

The integration form of the Equation (4.11) can be expressed as in Equation (4.12), where the $k_L.a$ can be determined from the slope between linear relation of $\ln(C^*-C)$ and t.

$$\ln(C^* - C) - \ln(C^* - C_0) = -k_L a \cdot t \tag{4.12}$$

4.3.2   Results and discussion

Figure 4.10 shows the oxygen equivalent concentration as a function of time for different orifice sizes. For the orifice size of 0.5 mm represented by Figure 4.10(Left), the oxygen equivalent concentration started to increase at the time of 13 second and reached the saturated concentration at 83 second. Therefore, the total time spent in order to reach its saturated concentration was 70 seconds, which corresponding to the $k_L.a$ of 0.0143 s^{-1} by the calculation using Equation (4.10). For the orifice size of 0.8 mm, the total time spent until reached saturated was 97 seconds where its $k_L.a$ was equal to 0.0105 s^{-1}.
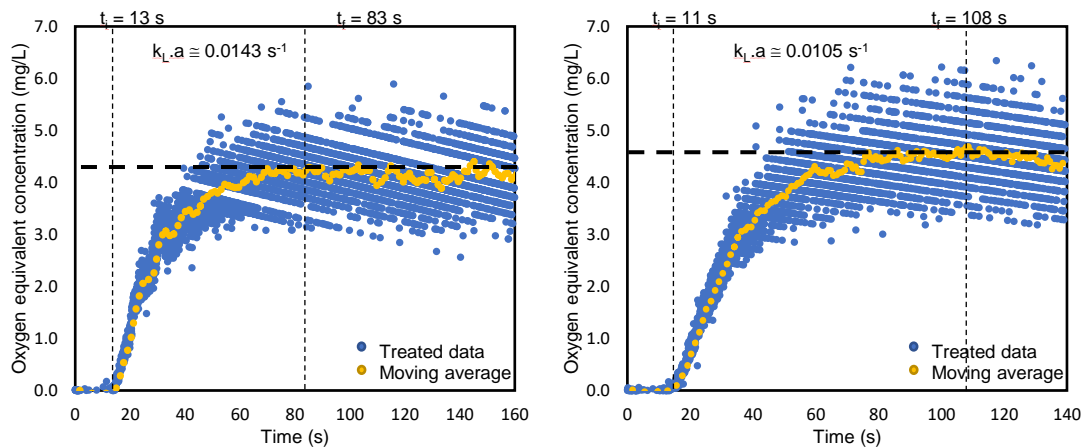
Figure 4.10 Oxygen equivalent concentration as a function of time without the presence of packing (Left) 0.5 mm orifice (Right) 0.8 mm orifice

With the presence of packing, the results of the oxygen equivalent concentration as a function of time are shown in Figure 4.11. The time spent for the cases of 0.5 and 0.8 mm orifices were 73 and 82 seconds, which corresponding to the $k_L.a$ values were 0.0137 and 0.0122 s^{-1}, respectively. When comparing with results without the presence of packing, the $k_L.a$ was slightly lower when the packing presented in the column for the case of 0.5 mm orifice. However, when the 0.8 mm orifice was used. The slightly increase of $k_L.a$ was achieved. This occurrence confirmed the finding of Wongwailikhit et al., (2018).
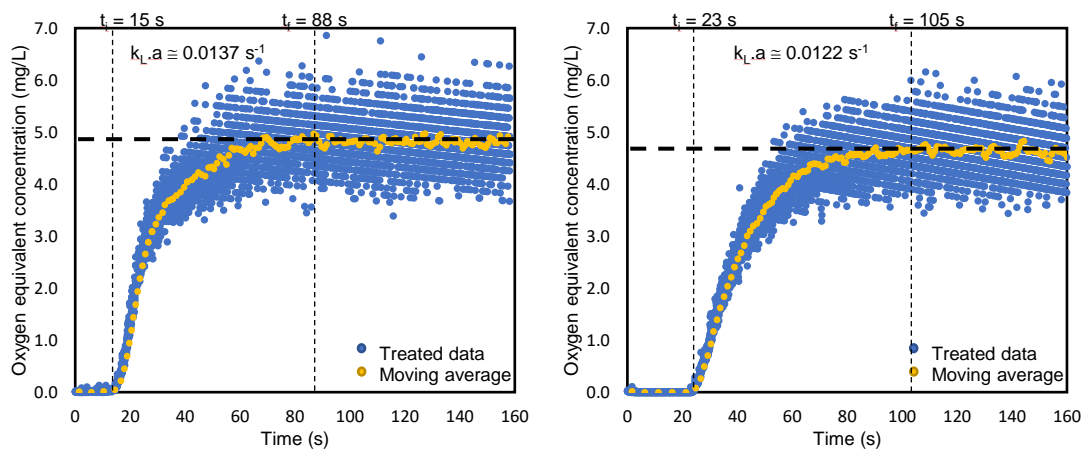
Figure 4.11 Oxygen equivalent concentration as a function of time with the presence of packing (Left) 0.5 mm orifice (Right) 0.8 mm orifice

Table 4.2 shows the value of $k_L.a$ determined by both oxygen probe and the colorimetric method at the same operating conditions. Noted that the $k_L.a$ obtained from the oxygen probe was determined from different set up than the colorimetric method due to the fact that the actual concentration in the colorimetric solution normally had zero concentration of oxygen as it reacted with the dihydroresarufin. In the table, the $k_L.a$ obtained from both techniques shows the same trend; almost equal in

values from both techniques were achieved. The consistent results from both techniques indicated that the colorimetric technique using for determination of global $k_L.a$ is efficient. This technique can be further used to characterize mass transfer in the bubble column system. Note that the error scale for the colorimetric method calculated from the ±5 seconds possible to read the curve by the observer.

Table 4.2 $k_L.a$ determined by the colorimetric method comparing with an oxygen probe

Orifice size	Superficial velocity (cm/s)	Solids	$k_L.a$ (s^{-1})	
			Oxygen probe	Colorimetric
0.5 mm	0.59 cm/s	No solid	0.0135 ± 0.000065	0.0143 ± 0.001
		Packing	0.0136 ± 0.000100	0.0137 ± 0.001
0.8 mm	0.59 cm/s	No solid	0.0102 ± 0.000036	0.0105 ± 0.001
		Packing	0.0122 ± 0.000059	0.0122 ± 0.001
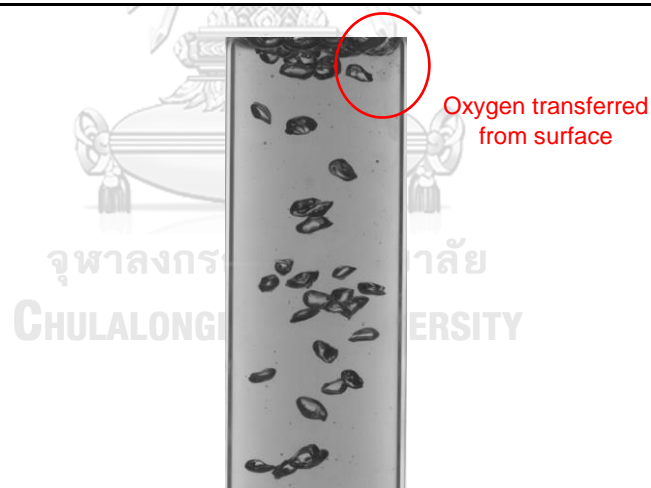
Figure 4.12 Effect of oxygen saturated surface on the mass transfer mechanism in the bubble column

The advantage of the colorimetric is that the mass transfer can be seen virtually and the further understand of the mass transfer mechanism in bubble column can be accomplished. For example, the surface of the liquid, which always saturated with dissolve oxygen from the contact with air, also affected the mass transfer in the bubble column. As can be seen in Figure 4.12, the oxygen transfer from the surface can be seen clearly. Normally, when considering the mass transfer and the interfacial area of aeration, the liquid surface area at the top of the column is not included as the area of

oxygen transfer. Only the interfaces of bubbles in the column were considered for the interfacial area (Bouaifi et al., 2001; Painmanakul et al., 2005). Therefore, the further and comprehensive consideration can be achieved using colorimetric method. Furthermore, it can be clearly seen that the perfect-mixed behavior was occurred in the column. Figure 4.5 shows that the gray level in the column excluded the bubbles were the same throughout the column. Therefore, the perfect mixed assumption can be confirmed using the colorimetric method, which cannot be understood using only an oxygen probe. These benefits confirmed the potential of the colorimetric method, which also can be further used in an education purpose for visual explanations of mass transfer to students for better understand. The only drawbacks of the colorimetric method are that, the preparation of the colorimetric solution is moderately complicated, and it requires the calibration curve to accurately identify the equivalent concentration in the column.

4.3.3 Summary

The colorimetric method used for determination of global mass transfer of oxygen was developed successfully. Accurate values of the liquid side mass transfer coefficients were achieved when comparing with the results obtained from the oxygen probe. The advantages of the colorimetric method are visualization of the mass transfer mechanism that can be used to understand the mass transfer in the bubble column comprehensively. The only drawback of the method is the complexity of the colorimetric solutions including the calibration curve preparation.
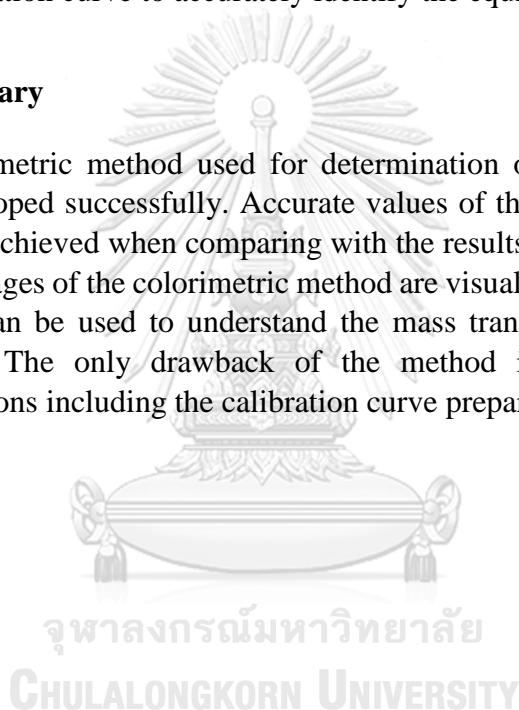
4.4 Determination of solid-bubble collision effect on mass transfer coefficient using colorimetric method

The purpose of this section is to identify the effect of solid collision with bubbles on the mass transfer at the interface of bubbles. According to several literatures (Freitas and Teixeira, 2001; Khare and Joshi, 1990; Kim and Kim, 1990; Pandit and Joshi, 2011), it was found that the presence of solid particles in bubble column leading to different results depending on the size of solids and bubbles. Hence, this experiment was set up to determine the effect visually thanks to the colorimetric method developed by Dietrich and Hébrard, (2018).

4.4.1 Methodology

(a) Experimental setup
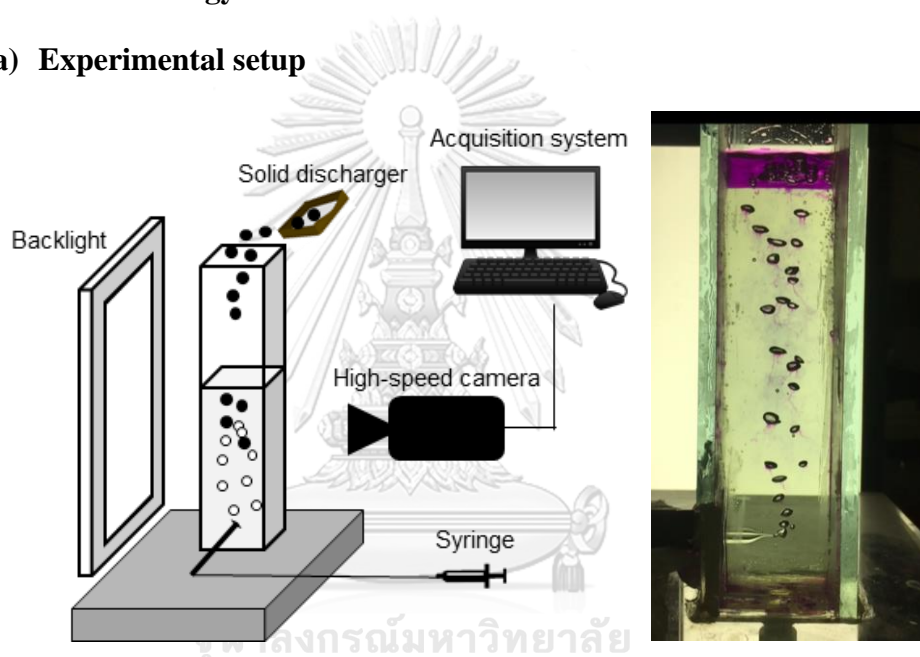
Figure 4.13 Experimental setup for the effect of bubble-solid collision on the mass transfer

The experiment was setup as shown in Figure 4.13. A 4 cm-square column was filled with 250 mL of a colorimetric solution prepared from 100 mg/L of resazurin. A needle connected to a syringe was equipped at the bottom of the column in order to produce bubbles. Bubble sizes range of 2-4 mm can be produced with this method.
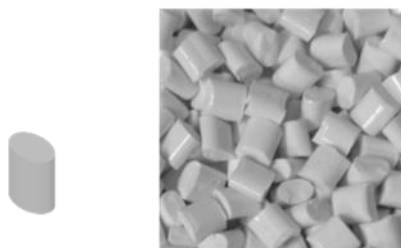
Figure 4.14 Characteristic of solid particles used in the experiment

A solid discharger was positioned above the column containing solid particles that can be illustrated in Figure 4.13. The particles were made from Acrylonitrile butadiene styrene (ABS) having the density of 1,050 kg/m^3. This material was selected as it was slightly heavier than the liquid phase due to the fact that particles only settle when their density was higher than the liquid phase. Table 4.3 summarized the properties of particles used in this experiment.

Table 4.3 Properties of solid particles colliding with bubbles

Properties	Value
Material	Acrylonitrile butadiene styrene (ABS)
Density (kg/m^3)	1,050
Shape	Cylinder
Particle Equivalent Diameter (mm)	2.95
Bulk Porosity (-)	0.39
Shape Factor (-)	0.5

(b) Local overall mass transfer coefficient determination

(i) Image acquisition

A high-speed camera (Vision Research, Miro – M110, USA) along with its acquisition system and a backlight (PHLOX with a luminance of 30383 cd/m^2 and a uniformity of 93.65 %) were position at the front and the back of the column, respectively. The determination of bubble size, velocity, as well as the gray level from colorimetric method were performed by the setup. In this experiment, a green filter was equipped at the lens (Carl Zeiss 50mm f/1.4) of the high-speed camera and 500 frames per second was used to record the trajectories of bubbles. An example of a bubble moving in the column with its dissolved oxygen concentration around the bubble is shown in Figure 4.15. The oxygen concentration wake behind the bubble can be clearly seen in the figure. This plume was used to further determine the local mass transfer coefficient around the bubble.
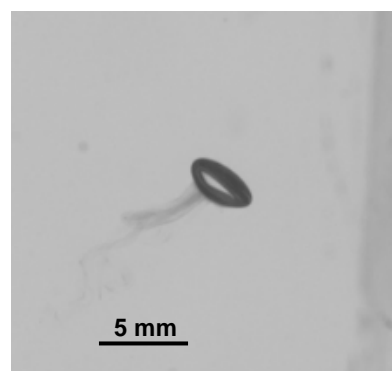
Figure 4.15 Image acquisition of a bubble and its visualized oxygen concentration

(ii) Bubble size and velocity determination

To determine droplet size and velocity using image processing, the "wrmtrack" plugin of ImageJ® was used. Each bubble size velocity was determined using the same methodology for droplet velocity determination, which detailed in Chapter 2. The velocity of bubbles was studied throughout their trajectories in order to acquire the relation between bubble velocity and mass transfer coefficient according to the moving position.

(iii) Calibration

In order to identify the concentration of dissolved oxygen around a bubble, a calibration has to be performed. In this experiment, the Beer-Lambert law of absorbance, Equation (4.13), was used as a calibration of the oxygen concentration. The term log I/I_0 refers to the light absorbance from the colorimetric solution that changes its color from colorless to pink with the presence of oxygen, while C, ε, and L represent concentration (mol/L), molar absorptivity (L/mol.cm) and path length of light travel which equal to the column width (cm), respectively.

$$\log_{10}\frac{I}{I_0} = -\varepsilon CL \qquad (4.13)$$
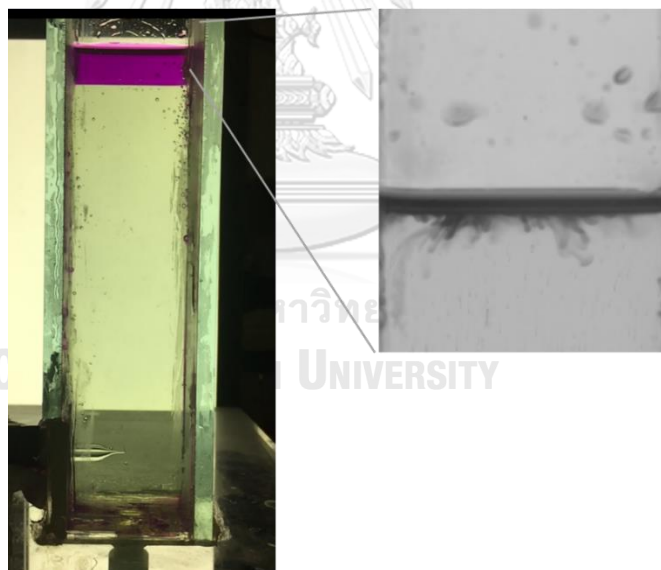
Figure 4.16 Surface oxygen saturated solution for calibration of oxygen concentration

According to the equation, when the light transmits through the column and passes the dye having the color of pink from the dissolved oxygen, the intensity of light is partially absorbed. Therefore, when considering at the position that the path length of the light and the concentration of the solution are known, the molar absorptivity (ε) can be calculated using Equation (4.13). Hence, the surface of the solution, that saturated with the dissolved oxygen and completely turned into a pink layer, as illustrated in Figure 4.16, can be used as a calibration since its concentration of the solution was known. The value of ε calculated in this experiment was 266.3 L/mol.cm.

After identified the value of ε, the relation between gray level in each image and the equivalent concentration was developed. The concentrations of oxygen at any pixel were identified using Equation (4.14), which directly developed from Equation (4.13), where the path length is equal to the column width.

$$C = -\frac{\log_{10}\frac{I}{I_0}}{(266.3\ x\ 4.0)} \tag{4.14}$$

(iv) Image processing methodology

An image processing method needs to be done in order to determine the concentration of oxygen accurately. After obtained an acquisition image of a bubble, the background of the image was subtracted from the raw image. The background was taken from the average of images that did not contain bubbles in the images. After the subtraction, the edge of the bubble was detected and the bubble itself was then removed in order to avoid the interpretation of gray level of the bubble. Consequently, Equation (4.14) was used to point out the concentration of oxygen of every pixel in the image. Figure 4.17 shows the results of each steps mentioned earlier. The image was then used to calculate the local liquid side mass transfer coefficient (k_L), where the method is detailed in the next section. Noted that for the case of the bubble that collided with solids, the suitable bubble was selected in order to avoid the error due to other bubble wakes in the area.
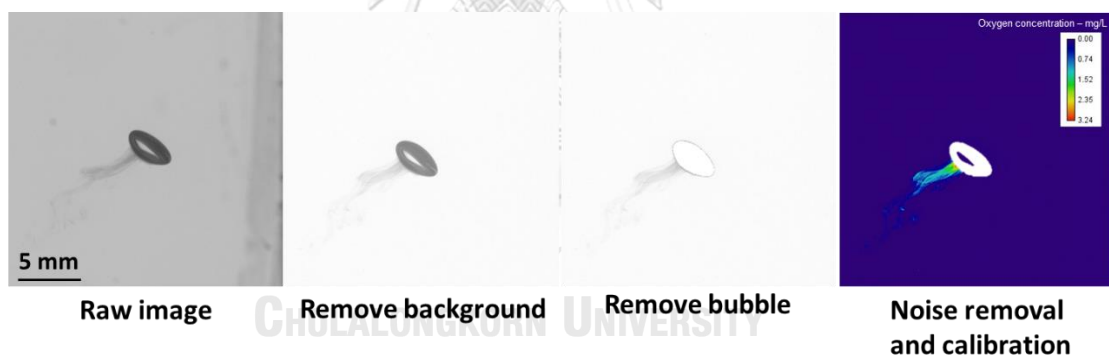
Figure 4.17 Image processing procedure

(v) Determination of local liquid side mass transfer coefficient

From the image processed with the image processing procedure, the local liquid side mass transfer coefficient around a single bubble can be determined using the following method.

At the beginning the total mass of oxygen transferred around the bubble can be determined by Equation (4.15), which is the integration of the concentration around the bubble. The x, y, and z in the equation represents the cartesian coordinate, while C(x,y) is the concentration of each pixel around the bubble obtained from the image.

$$m = \iiint C(x,y)\,dx \cdot dy \cdot dz \tag{4.15}$$

Therefore, the average oxygen concentration in the section can be calculated via the following equation, where z is the width of the column. Noted that, for this study, the oxygen concentration fields visualized were the result of all the different fields existing in all the vertical locations. Equation (4.16) does not take the dimension z, related to the channel width, into account when integrating C. This is because the present colorimetric technique is not able to discriminate the visualizations at different planes along the channel width.

$$\bar{C} = \frac{\iiint C(x,y)\,dx \cdot dy \cdot dz}{x \cdot y \cdot z} \tag{4.16}$$

According to mass transfer flux of oxygen when the bubble is rising up with the rising velocity of u_B along the x-axis, neglecting the transfer at the bubble formation. The mass flux of oxygen can be expressed as in Equation (4.17) (Dietrich and Hébrard, 2018). Noted that the concentration of dissolved oxygen in the liquid is assumed to equal to zero due to its consumption by the chemical reaction. In the equation, the k_L is the liquid-side mass transfer coefficient (m/s), a is the interfacial area between gas and liquid phases (m^2/m^3) and C^* is the dissolved oxygen saturation concentration ($C^* \sim$ 8.15 mg/L)

$$\varphi = u_B \frac{d\bar{C}}{dx} = k_L a C^* \tag{4.17}$$

Hence, from the integration, k_L can be determined using the following equation;

$$k_L = \frac{\bar{C} \cdot u_B}{y \cdot C^* \cdot a} \tag{4.18}$$

Where the interfacial area (a) can be calculated from the ratio of the surface area of the bubble and the volume considered for the mass transfer as shown in Equation (4.19).

$$a = \frac{\pi D^2}{x \cdot y \cdot z} \tag{4.19}$$

Therefore, in summary, the local liquid side mass transfer coefficient can be determined using Equation (4.20).

$$k_L = \frac{m \cdot u_B}{y \cdot C^* \cdot \pi D^2} \tag{4.20}$$

In order to verify the technique, the Higbie's penetration model was used to compare the result from the colorimetric methodology. The model was selected due to the fact that the bubbles used in this experiment were larger than 2 mm, where the Higbie model is applicable. The calculation using Higbie model is based on Equation (1.45)

4.4.2   Results and discussion

There are 3 cases of bubbles considering in this part. Firstly, a small bubble (2.7 mm in diameter) that raised freely without collision with any solid particle. Secondly, another small bubble (2.7 mm) that collided with a solid particle. Lastly, a larger bubble (3.7 mm) that collided with a particle. All the cases represent the effect of solid-bubble collision on the local mass transfer of a single bubble.

(a) Case I: Small bubble with no collision

In this case, a small bubble that did not collide with any particles was considered. The trajectory of the bubble is illustrated as in Figure 4.18. The bubble rose as a swirl motion during its trajectory while the wake of the bubble can be seen clearly in the figure. After applying the calibration mentioned in Equation (4.14), Figure 4.19 illustrated the oxygen concentration field after applied the calibration methodology.
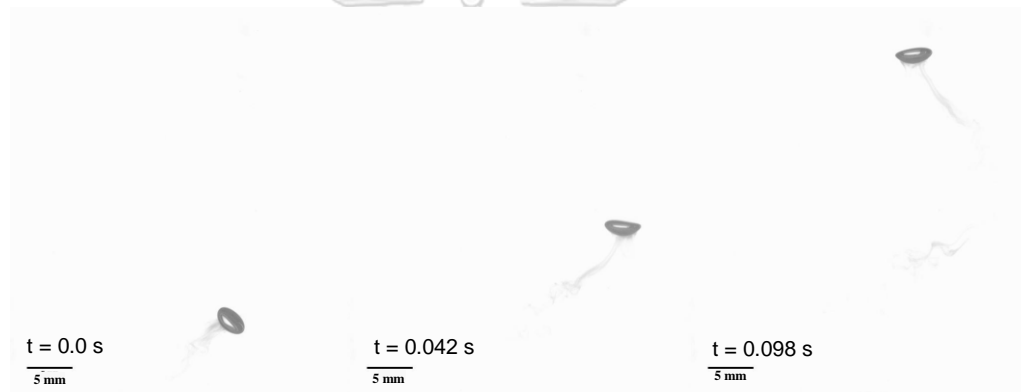
Figure 4.18 Trajectory of a small bubble without collision with particles and its oxygen transferred regime

It can be seen in Figure 4.19 that, the oxygen concentration was seen mostly in the bubble surrounding and the bubble wake. The closer to the bubble, the higher concentration of the oxygen. This concentration field was then used to calculate the mass transfer coefficient (k_L) according to the equation (4.20).
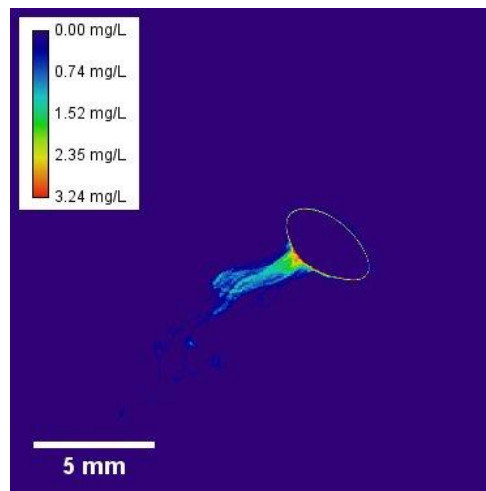
Figure 4.19 Oxygen concentration field around the small bubble without collision with particles

Before considering the mass transfer coefficient (k_L), the bubble velocity throughout its trajectory had to be investigated. It can be seen in Figure 4.20 that, the bubble velocity fluctuated around the average velocity of 29.6 cm/s, the k_L of the bubble calculated via the Higbie model was also almost constant at around 5×10^{-4} m/s. According to the colorimetric calculation of k_L, the results at different position are also plotted in the same figure. The k_L measured by the colorimetric technique results were consistent with the Higbie penetration model as the results were fluctuated around 5×10^{-4} m/s at the considered position. Hence, it can be summarized that, both colorimetric and Higbie penetration gave the same trend of the results where the mass transfer coefficients were constant throughout its trajectory without the collision with a solid.

Figure 4.20 (Left) Bubble velocity throughout its trajectory and (Right) local mass transfer coefficient calculated by Higbie model for the small bubble without collision with particles

Table 4.4 shows the result of both hydrodynamics and mass transfer parameters of the bubble in Figure 4.20. The bubble had the diameter of 2.75 mm with its average velocity of the bubble equaled to 29.6 cm/s. The average Higbie model resulted in the

value of 5.18 x 10^{-4} m/s whilst the k_L from the colorimetric method was averagely 4.95 x 10^{-4} m/s, indicating that the good agreement between the model and the experiment value was achieved. This comparison supported a good agreement between the model and the colorimetric experiment.

Table 4.4 Hydrodynamics and mass transfer parameters of the small bubble without collision

Variable	Value
Diameter (mm)	2.751
Average velocity (cm/s)	29.6
Average k_L (m/s) [Experiment]	4.95 x 10^{-4}
Average k_L (m/s) [Higbie]	5.18 x 10^{-4}

(b) Case II: Small bubble with a collision with particle

Figure 4.21 Trajectory of a small bubble with a collision with a particle and its oxygen transferred regime

Figure 4.21 shows the trajectory of a bubble that collided with a particle once in its path. The bubble moved freely and swirl before collision with the particle. After the collision, the bubble velocity was reduced due to the loss of its momentum. Consecutively, the bubble increased its velocity, and after a certain distance, the bubble reached its terminal velocity as the velocity was nearly constant.
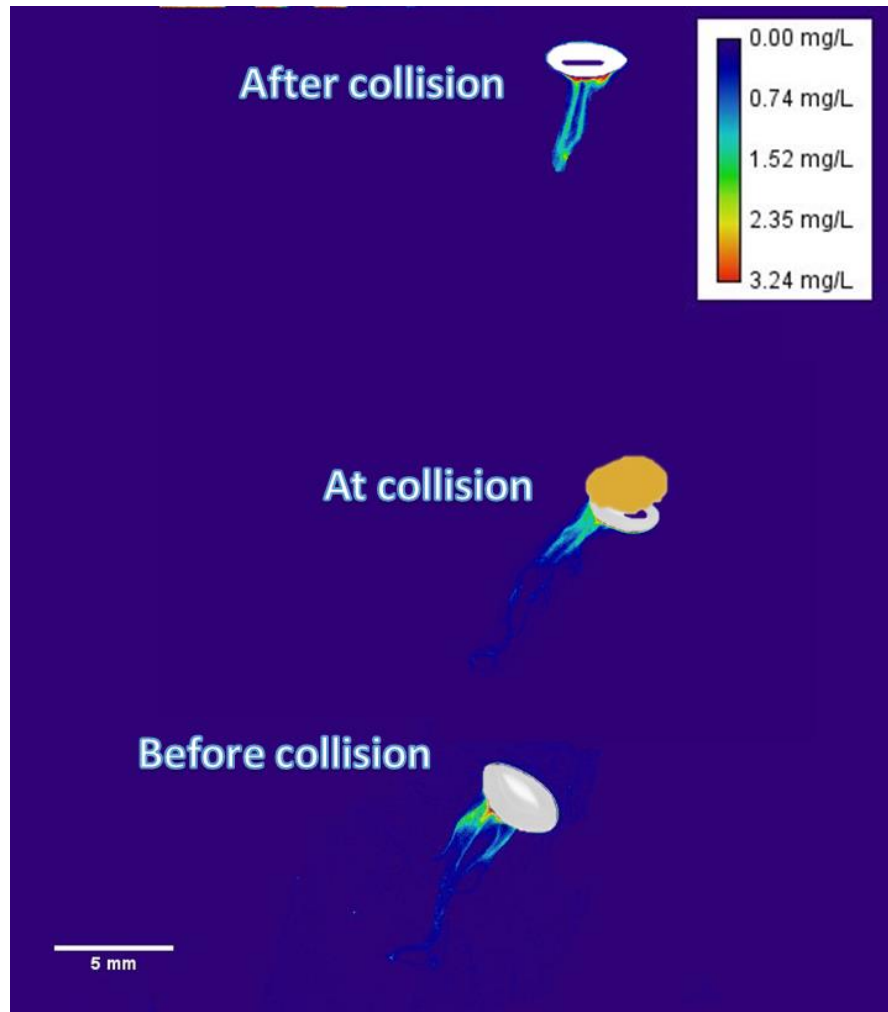
Figure 4.22 Oxygen concentration field around the small bubble before and after collision with a particle

The calibration of oxygen concentration and the gray level was then applied to the images. Noted that the suitable images were selected in order to avoid the error due to the wake of other bubbles as can be clearly seen in Figure 4.21. The oxygen fields before, at collision, and after collision are shown in Figure 4.22. The oxygen concentration field in Figure 4.22 shows a significant change of oxygen concentration around the bubble at the collision with the solid. The reduction of the bubble velocity was responsible for the finding due to the fact that, the slower velocity of the bubble, the lower mass transfer coefficient was attained corresponding to the Higbie model.

The velocity and mass transfer coefficient calculated using Higbie model in comparing with the colorimetric method are shown in Figure 4.23. In the figure, the bubble velocity dropped sharply after the collision with the particle, leading to abruptly decrease of k_L after the collision regarding the Higbie model. The k_L determined by the colorimetric method also gave the same trend of the result as the model, where the k_L sharply reduced when the bubble collided with the solid and consequently increased after a certain time of collision.
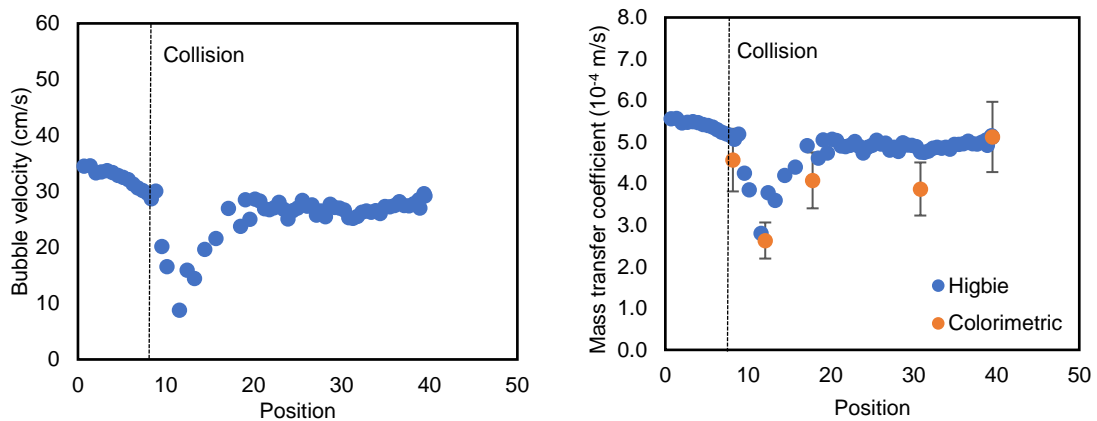
Figure 4.23 (Left) Bubble velocity throughout its trajectory and (Right) local mass transfer coefficient calculated by Higbie model for the small bubble before and after collision with a particle

In order to summarize, Table 4.5 shows the hydrodynamics and mass transfer parameters of the bubble before, at collision, and after collision. The k_L before collision and at collision, and after collision were changed significantly from 4.57×10^{-1} to 2.63×10^{-1} to 4.08×10^{-1} m/s, respectively. It was in consistence with the calculation from the Higbie model to where the k_L reduced dramatically from 5.16×10^{-4} to 2.81×10^{-4} and 4.92×10^{-4} m/s, respectively. Therefore, it can be summarized that, the collision between a small bubble and particles reduced the mass transfer ability of a bubble because its velocity reduced intensely. This finding support the experiment of Wongwailikhit et al., (2018), reporting that the small bubbles in the column containing solids particles had lower mass transfer coefficient than without solid.

Table 4.5 Hydrodynamics and mass transfer parameters of the small bubble with collision

Variable	Before collision	At collision	After collision
Diameter (mm)		2.798	
Average velocity (cm/s)	28.7	16.0	29.4
k_L (m/s) [Experiment]	4.57×10^{-4}	2.63×10^{-4}	4.08×10^{-4}
k_L (m/s) [Higbie]	5.16×10^{-4}	2.81×10^{-4}	4.92×10^{-4}

(c) Case III: Large bubble with a collision with solid

Figure 4.24 illustrates the trajectory of a larger bubble along its trajectory. The bubble collided with a particle at the edge of the acquisition images. It should be noted that, the image processing was not able to precisely apply for the oxygen concentration field of the bubble since its bubble wake was hidden by the solid particles. However, when considering the bubble velocity throughout its trajectory and applying the Higbie model, the effect of solid-bubble collision can be determined as well as the other bubbles mentioned earlier. Figure 4.25 shows the velocity and the local mass transfer coefficient of the large bubble that collided with the particle of both Higbie model and from the colorimetric method.
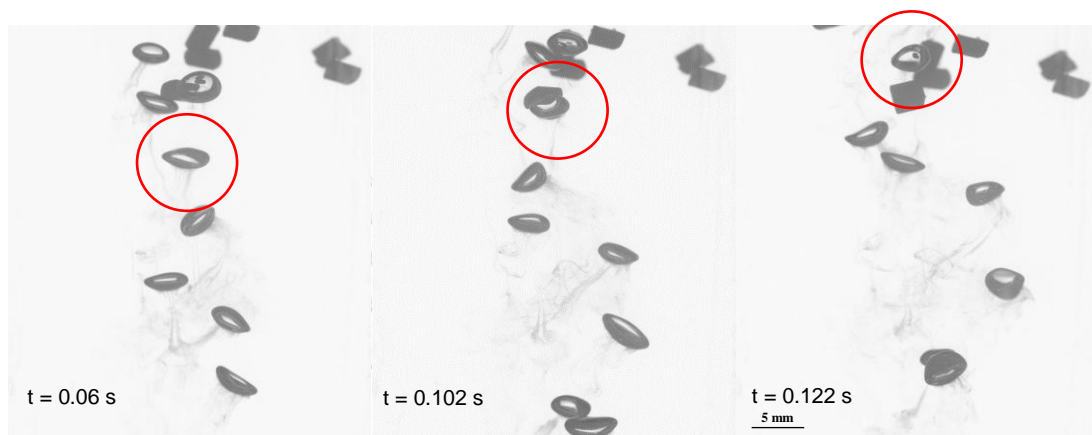
Figure 4.24 Trajectory of a large bubble with a collision with a particle and its oxygen transferred regime

Figure 4.25 shows that the velocity both before and after the collision with the particle slightly affect the bubble velocity. The bubble velocity only oscillated around the same value after the collision. Therefore, when using the value to determine the k_L using the Higbie model, the k_L of the bubble did not significantly reduce after the collision, which was in contrast with the previous small bubble in section 4.4.2(b). For the colorimetric method, there was a slight deviation between Higbie model and the colorimetric method due to the fact that the accuracy of colorimetric method was reduced since bubble wake was hidden by the solid particles or stacked of wake between adjacent bubbles. Although the deviation existed, the reduction of k_L according to the collision with solid were not clearly seen. The summary of the k_L for the large bubble case is shown in Table 4.6, where the change of k_L was not evidently observed for its entire trajectory.
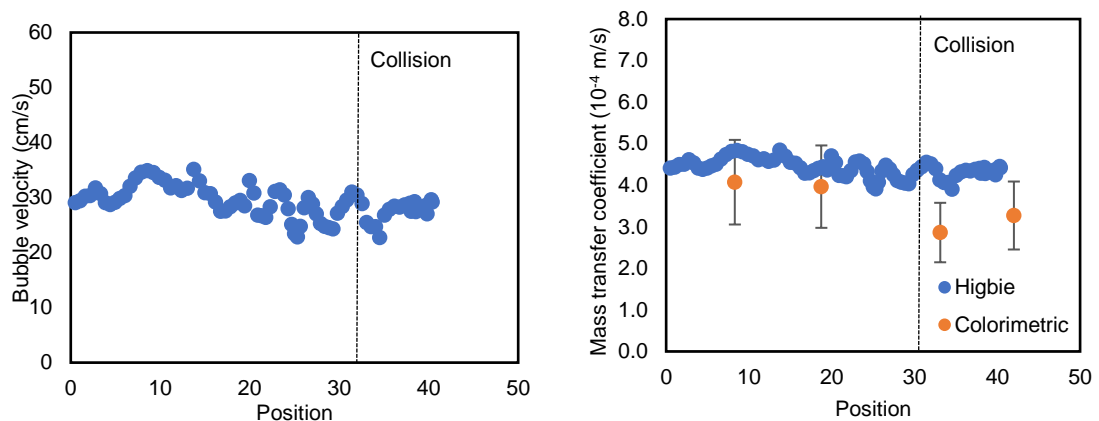
Figure 4.25 (Left) Bubble velocity throughout its trajectory and (Right) local mass transfer coefficient calculated by Higbie model for the large bubble before and after collision with a particle
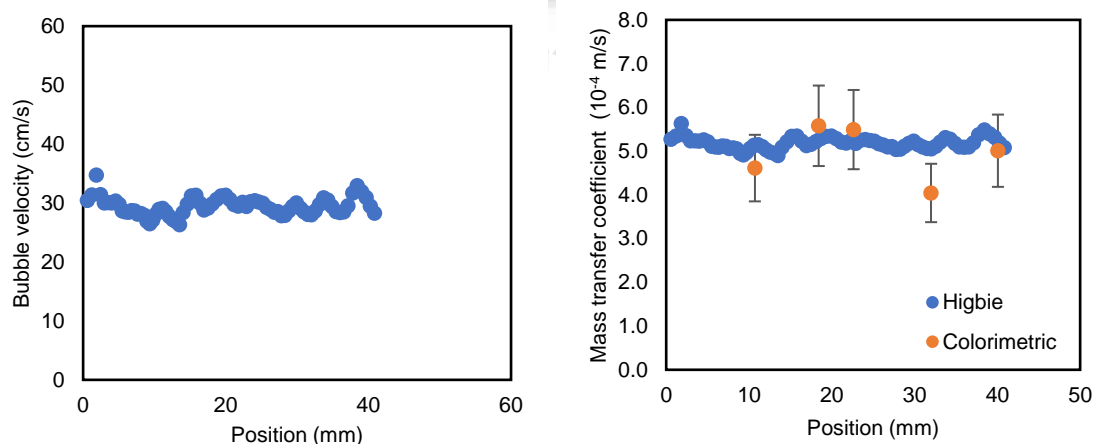
Table 4.6 Hydrodynamics and mass transfer parameters of the small bubble with collision

Variable	Before collision	At collision	After collision
Diameter (mm)		3.75	
Average velocity (cm/s)	28.0	25.0	29.2
k_L (m/s) [Experiment]	3.97×10^{-4}	2.86×10^{-4}	3.27×10^{-4}
k_L (m/s) [Higbie]	4.44×10^{-4}	4.07×10^{-4}	4.42×10^{-4}

When observing the large bubble that collided with a particle, the velocity of the bubble did not change sharply since the bubble itself contained higher momentum than the small one. In addition, the larger bubble also contained higher buoyancy force itself and, therefore, spent shorter time to recover its velocity back to its terminal velocity comparing with the smaller bubble. Consequently, the mass transfer coefficient of the large bubble did not reduce significantly due to the fact that the mass transfer of a bubble depends on the bubble velocity regarding the Higbie model. While in the case of the small bubble, the bubble velocity could be easily dropped as it contained less amount of momentum than the large one. This fact confirms the finding of Wongwailikhit et al., (2018), where the mass transfer coefficient increased with the presence of solid particles in the case that used a large orifice size, which produced large bubbles, but reduced when a small orifice size was used. The increase of the overall liquid mass transfer ($k_L.a$) was due to the slightly reduction of the bubble rising velocity. The slower rising velocity of bubbles leads to the longer contact time between the bubble and liquid phase and, consecutively, the interfacial area of the mass transfer increased. Therefore, for the case of large bubbles, the interfacial area rose whilst its

mass transfer coefficient did not significantly change leading to increase the $k_L.a$. However, in the case of small bubbles, although the interfacial area increased intensely as its velocity reduced, the mass transfer coefficient dropped dramatically. Consequently, the overall $k_L.a$ decreased.

It should be noted that the effect of the collision on the mass transfer in bubble columns is a part of the overall effect of solid particles in the column. The effect of size ratio between bubbles and particles is also one of the parameters that should be included in the further study. Moreover, the effect of bubble breaking up as well as coalescence should be further investigated in order to comprehensively understand the occurrence. In addition, this experiment can be further improved by designed a column where a single bubble and a single particle can be collided with each other where the discrepancy of due to the wake of other solids and bubbles can be removed.

4.4.3 Summary

In summary, the collision between bubbles and particles affected the mass transfer in the bubble column. The effect of presenting solids on the mass transfer can be improved or reduced depending on the size of the bubble produced by the orifice. For the case that bubbles are large enough to maintain its velocity, the overall mass transfer coefficient ($k_L.a$) trended to increase since the bubble velocity is slightly decreased leading to the increase of its interfacial area since the time spend in the reactor is increased. Although its interfacial area increased, the mass transfer coefficient is not reduced sharply from the collision as it contained high momentum. However, for the case of the small bubble, the mass transfer coefficient decreased dramatically comparing to the increase of the interfacial area due to the intensively reduction of the bubble velocity from collision. Therefore, the solid particles trended to raise the overall mass transfer coefficient only for the case that the bubble sizes are large enough to conserve its mass transfer ability.

In the future, the further experiment can be conducted by making a specific column that a particle and a bubble can be collided. An improvement can be accomplished in order to make clear image for image processing and avoid error from wakes of other bubbles. In addition, the effect of solid collision on bubble breaking and coalescence should be considered.

4.5 Conclusion

In this chapter, two procedures using the "red bottle" colorimetric technique were applied to use in bubble column. Firstly, a procedue used to determine the global liquid side mass transfer coefficient in a bubble column was developed. The methodology had the same trend when determined the $k_L.a$ comparing with the oxygen sensor. The advantage of the method is that the mass transfer in the bubble column can be seen visually; the further analysis can be developed.

The other procedure was the one used to determine the effect of bubble-solid collision in a bubble column. It was found that, with the different size of the bubble,

the mass transfers were affected differently. The small bubble changed its velocity dramatically after the collision with a particle, leading to a large change of mass transfer coefficient. This incident was not found when a large bubble collided with a particle due to the fact that the large bubble contains higher momentum than the small one. Therefore, its velocity did not change sharply. This experiment confirmed the finding of various experiment in bubble columns with the presence of solid particles. However, the further experiment should be conducted in order to reduce the error due to adjacent bubbles and solids.

The application of the colorimetric method to the spray system should also be developed in order to comprehensively understand the effect of solid to the spray system.

Chapter 5

Three-phases spray and bubble columns: Mass transfer

5.1 Abstract

This chapter describes the mass transfer of both three-phase bubble and spray columns that already mentioned their hydrodynamics performances in Chapter 3. The comparison was made between both columns in terms of mass transfer coefficient and specific power consumption in order to develop a guideline for industrial usages. The combination between this chapter 5 and chapter 3 will be used for a publication in the aspect of comparison in terms of power consumption.

5.2 Introduction

The mass transfer in bubble column and spray column were investigated in this chapter. The performance of gas-liquid bubble column and spray column including the gas-liquid-solid ones were investigated. The same experimental setups in Chapter 3 were used. The high-void packing as well as the ring-shaped particles was also studied their effects in this chapter. The absorption efficiencies of each absorber were analyzed, compared, and discussed in terms of the flow rate and specific power consumption. Lastly, the advantages and drawbacks of the bubble column and spray column were summarized.

5.3 Methodology

5.3.1 Experimental setup

(a) Bubble column

The experiment was setup according to the same condition as the hydrodynamics studied as shown in Figure 3.1. The CO_2 was selected as the medium of mass transfer due to its impact on the global warming and climate change. In this work, the absorption of CO_2 was performed using the solution of NaOH at 0.05%wt as the absorption agent. The dilute concentration was selected in order to investigate the performance of CO_2 absorption using as least chemical as possible. However, the utilization of only water could not yield a promising result. Therefore, the base solution was used in order to accelerate the mass transfer rate as well as its capacity.

The concentration of CO_2 at the inlet was regulated constantly at 15.5%vol, which mimicking the concentration of fuel combustion for electrical production. As far as the mass transfer of CO_2 is concerned, a gas sensor (Emerson - Rosemount Binos 100, USA) was equipped at the outlet of the bubble column while a pH meter (Meterlab - PHM210) was placed at the outlet of the liquid phase for measuring the change of pH regarding the absorption of CO_2 in the liquid phase.

(b) Spray column

The experiment setup for gas-liquid absorption via spray column was setup according to Figure 3.3. Most of the experimental setup was the same as the bubble column including gas and liquid concentrations of CO_2 and NaOH, respectively. A gas sensor (Fresenius – Biobasic, Germany) was used to detect the concentration of CO_2 at the outlet while a pH meter (Meterlab - PHM210) was used for measuring the change of pH at the liquid outlet. Furthermore, a portion of liquid phase having a height of 1 cm was continually preserved at the bottom of the column to avoid the gas phase to leak out

(c) Liquid phase

(i) Physical properties

The physical properties of the NaOH solution in comparing with tap water are shown in Table 5.1. The liquid densities were measured using a weigh scale while the surface tension and viscosity were determined using Wilhelmy plate method and viscometer (RM180 Rheomat Rheometric Scientific), respectively. For the alkalinity, the titration method was performed.

Table 5.1 Physical properties of NaOH solution comparing with tap water at room temperature (20°C)

Property	Tap water	NaOH 0.05%wt
Density (kg/m^3)	994.73	996.26
Surface Tension (mN/m)	71.4 ± 0.5	71.7 ± 0.5
Viscosity (mPa s) @ 20°C	0.965	0.975
pH	7.7	12.15
Alkalinity (mg/L as CaCO$_3$)	100.0	100.0

(ii) Mass transfer properties

When investigate the mass transfer of CO_2 in the NaOH solution, two parameters needed to be considered: Henry's constant (H_{CO2}) and CO_2 diffusion coefficient (D_{CO2}). According to Duan and Sun, (2003), Henry's constant of CO_2 increased when the concentration of OH^- ion rose. Figure 5.1(Left) shows the effect of OH^- concentration on the Henry's constant of CO_2 which was one of the parameters used to calculate mass transfer coefficient ($k_L.a$). The γ_{CO2} is defined as expressed in Equation (5.1), where $H_{CO2,0}$ is Henry's constant of pure water while H_{CO2} is Henry's constant of NaOH solution.
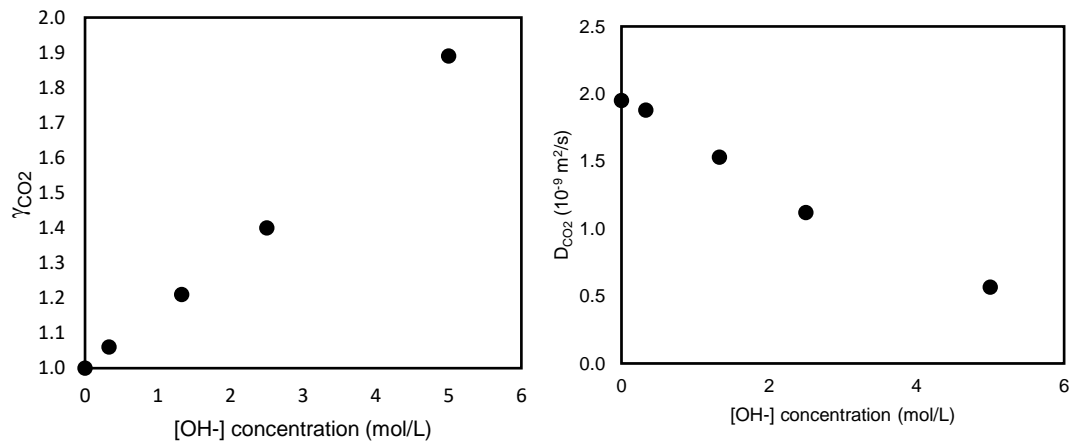
Figure 5.1 Effect of hydroxide ion concentration
(Left) Henry's constant in term of γ_{CO2} (Right) diffusion coefficient of CO_2 in water

$$\gamma_{CO_2} = \frac{H_{CO_2}}{H_{CO_2,0}} \tag{5.1}$$

It can be seen that in Figure 5.1(Left), at the dilute concentration of 0.05%wt, which equivalent to 0.0125 mol/L of OH^- concentration, γ_{CO2} was approximately equal to 1. Hence, the Henry's constant used in this experiment can be assumed as equal to pure water 29.24 L.atm/mol at 20°C.

The other parameter to be concerned is the diffusion coefficient of CO_2 in solution, since it is required to calculate several variables for mass transfer of CO_2. According to Hayduk and Laudie, (1974), the diffusion coefficient of CO_2 decreased with the increase of OH^- concentration as illustrated in Figure 5.1(Right). From the trend, it can be interpolated that at the concentration of OH^- equal to 0.0125 mol/L, the diffusion coefficient of CO_2 is approximately 1.95×10^{-9} m^2/s. This value is very close to that of pure water since the concentration of CO_2 in water was very low.

(d) Solid phase

(i) Moving particles

The same ring-shaped particles, as shown in Figure 3.5, were used in the study. The physical properties of the particles are expressed in Table 3.2. The concentration of the particles was specified as 5 % by volume.

(ii) Packing

The packing, Figure 3.6, used in the hydrodynamics study was also used in the mass transfer study. Its characteristic of the high void packing using in this experiment are shown in Table 3.3.

5.3.2   Mass transfer parameters

(a) CO₂ transferred rate

One of the parameters to quantify the mass transfer of CO_2 is the CO_2 transferred rate. It shows the amount of CO_2 transferred from the gas phase to the liquid phase. The calculation of the transfer rate can be done using the different concentrations between inlet and outlet of gas phase. By multiplying the difference with the gas flow rate, the CO_2 transferred rate can be calculated as shown in Equation (5.2)

$$CO_2 \text{ transferred rate} = Q_g \cdot \left(C_{CO_2,in} - C_{CO_2,out}\right) \tag{5.2}$$

The transferred rate will be used in this study as a dependent variable in order to understand the effect of independent variables on the mass transfer. Moreover, the CO_2 transferred rate will be used for the comparison between experiment and model for determining the accuracy of the mathematic model used in mass transfer purpose.

(b) Liquid side overall mass transfer coefficient ($k_L.a$)

In this work, since the CO_2 has low solubility in water and the mass transfer is limited at the liquid phase. The overall liquid side mass transfer coefficient ($k_L a$) was studied. The calculation of the mass transfer coefficient is based on the mass balance equation of continuous equipment. As the accumulation term is equal to zero, the inlet, outlet, and mass transfer of CO_2 on the gas phase can be expressed as in Equation (5.3).

$$Q_g \left(C_{CO2,in} - C_{CO2,out}\right) = E \, k_L.a \, \Delta C_{ln,mean} \, V_{Total} \tag{5.3}$$

In the equation, Q_g refers to the gas flow rate (LPM), C_{CO2} is the concentration of CO_2 at the inlet and the outlet depending on the subscripts (mol/L), and the last term represents the mass transfer rate per unit volume between gas phase and liquid phase of CO_2. The mass transfer rate per unit volume is the function of mass transfer coefficient (k_L, m/s), specific interfacial area (a, m⁻¹), enhancement factor (E, -), and log-mean difference of concentration (ΔC_{ln}, mol/L). The mean difference of the concentration is the log-mean different concentration between the saturated concentration of CO_2 in the liquid (C^*_{CO2}) and the actual CO_2 concentration (C_{CO2}) at the inlet and the outlet. Since the mass transfer is limited in the liquid phase, it is more convenient to determine the log-mean different concentration in the liquid phase where the concentration of CO_2 can be identified by the pH and alkalinity in the liquid phase. It should be noted that the log-mean different concentrations in the spray column and the bubble column have to be calculated with different approaches. As the bubble column has the perfect mixed regime of liquid phase. The equation using to determine the ΔC_{ln} is Equation (5.4) where the concentration of CO_2 is equal throughout the column for the liquid phase and equal to the concentration of CO_2 at the outlet. Whilst, the concentrations of liquid phase at the inlet and outlet of the spray column are not identical and follow the plug flow regime where the log-mean concentrations can be calculated using Equation (5.5).

$$\Delta C_{ln,mean} = \frac{(C^*_{CO_2,in} - C_{CO_2,out}) - (C^*_{CO_2,out} - C_{CO_2,out})}{\dfrac{C^*_{CO_2,in} - C_{CO_2,out}}{C^*_{CO_2,out} - C_{CO_2,out}}} \tag{5.4}$$

$$\Delta C_{ln,mean} = \frac{(C^*_{CO_2,in} - C_{CO_2,out}) - (C^*_{CO_2,out} - C_{CO_2,in})}{\dfrac{C^*_{CO_2,in} - C_{CO_2,out}}{C^*_{CO_2,out} - C_{CO_2,in}}} \tag{5.5}$$

It should be well noted that the saturated concentration of CO_2 at the inlet and the outlet are not equal because the saturated concentration (C^*_{CO2}) is the function of CO_2 partial pressure (P_{CO2}) in the gas phase followed the Henry's las as shown in Equation (5.6). Once the CO_2 transferred from gas phase to liquid phase, the concentration of CO_2 changed according to the inlet and outlet positions leading to lower partial pressure of CO_2. Therefore, from the Henry's law, the saturated concentration of CO_2 changed from the inlet to the outlet of both spray and bubble column. Note that H_{CO2} is the Henry's constant of CO_2 which equal to 0.034 mol/L/atm at 20°C.

$$C^*_{CO2} = H_{CO2} P_{CO2} \tag{5.6}$$

Nevertheless, the CO_2 concentration in the liquid phase is required to be considered as the dissolved CO_2, represented as CO_2 (aq), can react with water to form bicarbonate (HCO_3^-) and hydrogen ion (H^+) as shown in Equation (5.7). The HCO_3^- can further dissociate into CO_3^{2-} and H^+ as shown in Equation (5.8). In order to calculate the log-mean different concentration in Equation (5.4) and (5.5), these chemical reactions are needed to be considered which means that the concentrations of all compounds (i.e. CO_2, HCO_3^-, CO_3^{2-}, and H^+) are mandatory.

$$CO_2 \ (aq) + H_2O \ \leftrightarrow \ HCO_3^- + H^+ \tag{5.7}$$

$$HCO_3^- \ \leftrightarrow \ CO_3^{2-} + H^+ \tag{5.8}$$

To calculate each concentration, the equilibrium concentrations of each component according to Equation (5.7) and (5.8) are assumed. Hence, the relation between each component according to Equation (5.7) and (5.8) can be expressed as in Equation (5.9) and (5.10), respectively.

$$\frac{[HCO_3^-][H^+]}{[CO_2]} = K_1 \tag{5.9}$$

$$\frac{[CO_3^{2-}][H^+]}{[HCO_3^-]} = K_2 \tag{5.10}$$

In these equations, the concentrations of each component are in the unit of molar. K_1 and K_2 are equilibrium constants of the reactions which equal to 4.47×10^{-7} and 4.68×10^{-11} mol/L, respectively. By utilizing the equilibrium relations, the concentrations of each component can be achieved. However, in order to calculate each component concentration, the extend of reaction variables (δ_i) are introduced. The (δ_i) represents the quantity that measures the extent in which the reaction proceeds. By

assuming that the chemical reactions occur in the system involve only the reactions represented in (5.7) and (5.8), the initial and final concentrations of each components can be summarized as in Table 5.2.

$$\frac{[(HCO_3^-)_{initial} + \delta_1 - \delta_2][(H^+)_{initial} + \delta_1 + \delta_2]}{[CO_{2,initial} - \delta_1]} = K_1 \qquad (5.11)$$

$$\frac{[(CO_3^{2-})_{initial} + \delta_2][(H^+)_{initial} + \delta_1 + \delta_2]}{[(HCO_3^-)_{initial} + \delta_1 - \delta_2]} = K_2 \qquad (5.12)$$

Table 5.2 Initial and final concentrations of each component involving CO_2 absorption

Component	Initial concentration (mol/L)	Final concentration (mol/L)
CO_2	2.40×10^{-10} (Calculated from Equation (5.9))	$CO_{2,initial} - \delta_1$
HCO_3^-	6.78×10^{-5} (Calculated from Equation(5.10))	$(HCO_3^-)_{initial} + \delta_1 - \delta_2$
CO_3^{2-}	2.00×10^{-3} (From alkalinity measurement)	$(CO_3^{2-})_{initial} + \delta_2$
H^+	1.58×10^{-12} (Measured from pH meter)	$(H^+)_{initial} + \delta_1 + \delta_2$

Consequently, by knowing the initial concentrations of each component that obtained by direct measurements of pH and alkalinity integrating with the equilibrium calculations by Equation (5.9) and (5.10), the final concentrations of each component can be calculated by the substitution of the concentrations in Table 5.2.

to Equation (5.9) and (5.10) where the substitutions are expressed in Equation (5.11) and (5.12). The final concentrations can be determined by solving the δ_1 and δ_2 from the equations and the final concentrations can be acquired. Eventually, the log-mean different concentration is obtained and from Equation (5.3), the $E.k_La$ can be calculated.

(c) Enhancement factor (E)

In order to achieve the k_La individually, the Enhancement factor (E) is obligatory to be estimated. The E is the factor represents the improvement of mass transfer according to the chemical reaction occurred in the system because the reaction involving with the transferring component affects the concentration of the component in the liquid phase where the mass transfer is different.

In the NaOH solution, the reaction of CO_2 with the solution can be written as in Equation (5.13). The dissolved CO_2 reacts with the hydroxide ion (OH^-) in the solution and formed the bicarbonate component. It can be noted here that this equation is the same equation as Equation (5.7) but changing the reactant to OH^- instead of H_2O for the convenience of the E estimation.

$$CO_2(g \to l) + OH^-(l) \ \to \ HCO_3^-(aq) \qquad (5.13)$$
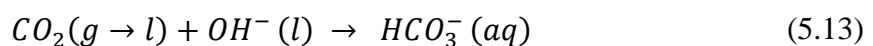
Krevelen and Hoftijzer, (1948) described the reaction rate of the chemical equation as in Equation (5.14) which is the second order reaction depending on the concentration of CO_2 and OH^- in the system, where the reaction constant (k_r) is equal to 5157.43 L/mol.s at 18°C.

$$-R_A = k_r[CO_2][OH^-] \qquad (5.14)$$

In order to estimate E, there are two factors needed to be determined, E_{AL} and M_H. Both factors can be computed using Equation (5.15) and (5.16), respectively

$$E_{AL} = 1 + \frac{D_{OH}C_{OH}}{D_{CO_2}C^*_{CO_2}} \qquad (5.15)$$

$$M_H = \sqrt{\frac{k_r C_{OH} D_{CO_2}}{k_L^2}} \qquad (5.16)$$

In the equations, D_{OH} and D_{CO2} are the diffusion coefficient of OH^- and CO_2 in the liquid phase, respectively. k_r is the reaction constant and k_L is the mass transfer coefficient. Lastly, the C_{OH} is the concentration of OH^- in the liquid phase. After obtained the M_H and E_{AL}, the enhancement factor (E) can be calculated using Equation (5.17).

$$E = \frac{Ha.\sqrt{\dfrac{E_{AL} - E}{E_{AL} - 1}}}{tanh\left[Ha.\sqrt{\dfrac{E_{AL} - E}{E_{AL} - 1}}\right]} \qquad (5.17)$$

It should be noticed that in order to calculate M_H, the k_L is required. However, to achieve the k_L, it is mandatory to know the E factor. Therefore, the trial and error methodology is introduced here. By first trial the value of E, the k_L can be estimated using Equation (5.18) along with the specific interfacial area acquired in Chapter 3. Afterwards, the M_H factor in Equation (5.16) can be computed and, eventually, E can be estimated. The value of first trial E and the estimated E will be compared. By changing the value of trail E until the final and the trail E is identical, the actual value of E can be obtained. In this study, the trial and error methodology were performed using by non-linear solving method.

$$k_L = \frac{Ek_L a}{E \cdot a} \qquad (5.18)$$

5.3.3   Modeling

In this study, only two-phase spray and bubble columns are modelized since the three-phase columns were complicated and needs further investigation in order to acquire the accurate model.

(a) Bubble column

(i) Bubble hydrodynamics

The correlation of Leibson et al., (1956) was used to estimate the bubble diameter in order to determine the specific interfacial area. For its rising velocity, the force balance as mentioned in Appendix C was used with the drag coefficient correlation of Tomiyama et al., (1999). in order to estimate the bubble rising velocity. The bubble velocity was then used to determine the gas holdup in the reactor using Equation (5.19). After acquired the gas holdup and the bubble size, the specific interfacial area was calculated using Equation (5.20).

$$\varepsilon_g = \frac{Q_g}{U_B A} = \frac{V_g}{U_B} \tag{5.19}$$

$$a = \frac{6}{d_B} \cdot \frac{\varepsilon_g}{1 - \varepsilon_g - \varepsilon_s} \tag{5.20}$$

(ii) Liquid side mass transfer coefficient (k_L)

$$k_L = 2\sqrt{\frac{D_{CO_2} U_B}{\pi d_B}} \tag{5.21}$$

Since the CO_2 has low solubility in water, mass transfer rate was limited at the liquid interface and bulk liquid, then the mass transfer coefficient was equal to the liquid side mass transfer coefficient. In this study, the Higbie penetration model was used to estimate the k_L of the bubbles.

(b) Spray column

(i) Droplet hydrodynamics

The droplet diameter was determined using the correlation developed in Chapter 3. The equation is shown here as Equation (5.22). Consequently, the droplet velocity was estimated using the initial velocity estimation and relaxation time as described in Appendix B and Appendix C, respectively. The specific interfacial area was eventually calculated using Equation (5.23)

$$d_D = 44Re^{-0.48}We^{-0.18}D_{Nozzle}^{0.44} \tag{5.22}$$

$$a = \frac{6}{d_d} \frac{Q_L}{U_E A} \tag{5.23}$$

(ii) Liquid side mass transfer coefficient (k_L)

In order to estimate the liquid side mass transfer (k_L), the correlation of Hadamart et al. was used. The k_L can be determined from the Sherwoord Number (*Sh*) which expressed in Equation (5.24), where the *Sh*, *Re*, *Sc*, and *Pe* can be determined using Equation (5.25) - (5.28).

$$Sh = 1.13 \left(1 - \frac{2.9}{Re^{0.5}}\right)^{0.5} Pe^{0.5} \tag{5.24}$$

$$Sh = \frac{k_L d_d}{D_{CO_2}} \tag{5.25}$$

$$Re = \frac{\rho_L V_D d_d}{\mu} \tag{5.26}$$

$$Sc = \frac{\mu}{\rho D_{CO_2}} \tag{5.27}$$

$$Pe = Sc \cdot Re \tag{5.28}$$

5.4 Result and discussion

5.4.1 Two-phases columns

(a) Bubble column

Figure 5.2 (Left) shows the effect of the gas flow rate and the orifice size on the CO_2 transferred rate, which calculated via Equation (5.2). The figure shows the increase of CO_2 transferred rate as the gas flow rate increased regardless of the orifice sizes. This increase was due to the escalation of bubble numbers that rose with the gas flow rate as mentioned in Chapter 3 where the specific interfacial area enlarged. Moreover, since the bubble sizes generated by the 0.5 mm orifice size were smaller than those of 0.8 and 1.2 mm, the specific interfacial were larger, leading to higher mass transfer rate of CO_2. Hence, it can be seen in Figure 5.2 that the 0.5 mm orifice gave higher CO_2 transfer rate when comparing with 0.8 and 1.2 mm, accordingly.
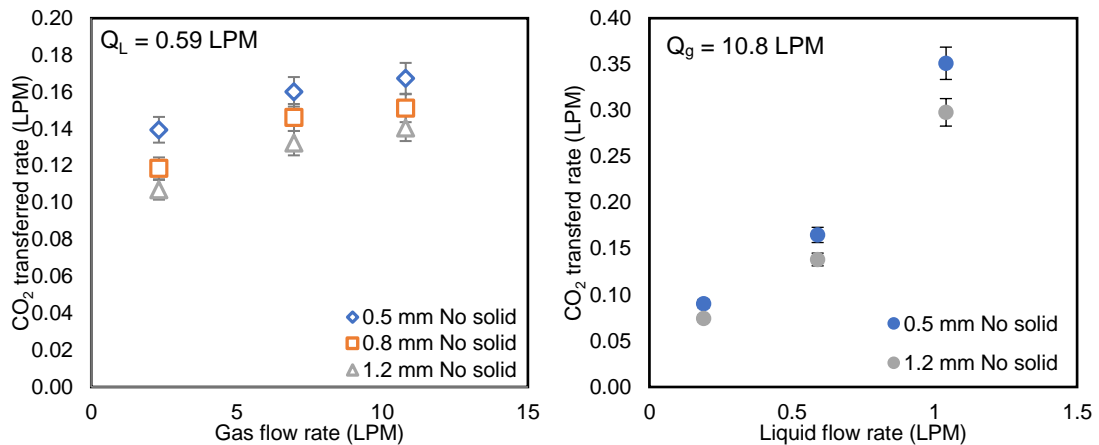
Figure 5.2 Amount of CO_2 transferred in two-phases bubble column as a function of (Left) gas flow rate and (Right) liquid flow rate for different orifice sizes

For the effect of liquid flow rate, according to Figure 5.2 (Right), the increase of liquid flow rate sharply raised the CO_2 transfer rate nonetheless of the orifice size. The larger liquid flow rate did not only reduce the residence time of the liquid phase but also reduced gas to liquid ratio. The decrease of gas liquid ratio affected the mass transfer of CO_2 since there was a larger portion of liquid that could absorb the CO_2, leading to lower CO_2 concentration in liquid and increased the driving force. Therefore, it can be seen that, the mass transfer increased intensely with the liquid flow rate.

By using the CO_2 transferred rate acquired in Figure 5.2 to calculate $k_L a$ according the methodology mentioned in Section 5.3.2, the $k_L a$ results at different gas flow rates and orifice sizes can be illustrated as in Figure 5.3.
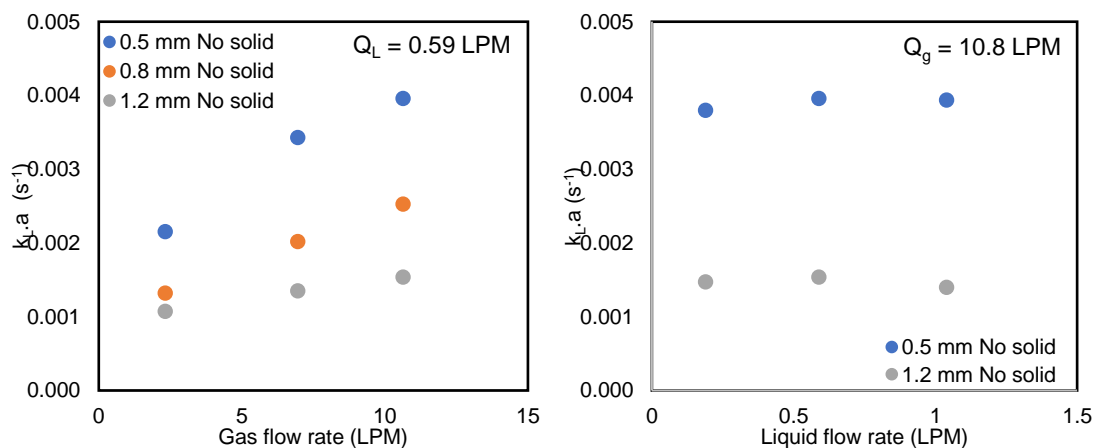
Figure 5.3 $k_L a$ in two-phases bubble column as a function of (Left) gas flow rate and (Right) liquid flow rate at different orifice sizes

According to Figure 5.3(Left), the $k_L a$ increased with the increase of gas flow rate for every orifice size; the result was consistent with the CO_2 transferred rate. As mentioned earlier, the increase of the $k_L a$ was responsible by the increase of the specific interfacial area as the gas flow rate rose. The reduction of bubble sizes and inclusion of

the gas holdup increased the specific interfacial area (a) and, therefore, increased the $k_L.a$. Note that the detail of the effect of gas flow rate on the specific interfacial area of the bubble column is described in Chapter 3. When considering the effect of liquid flow rate as shown in Figure 5.3(Right), it can be seen that the $k_L.a$ was not the function of the liquid flow rate even though the CO_2 transferred rate increased with the liquid flow rate. It was according to the fact that, the increase of liquid flow rate reduced the concentration of CO_2 in the liquid phase, leading to lower the log-mean concentration difference of CO_2. Therefore, it can be concluded that the $k_L.a$ did not depend on the liquid flow rate. This fact supported the finding of the gas hold up and specific interfacial area in Chapter 3. Although the liquid flow rate increased, the gas holdup and the bubble sizes did not be affected; the specific interfacial area was consequently not changed with the liquid flow rate in this range of variation. As the specific interfacial area (a) was not changed as well as the bubble hydrodynamics, the k_L should also be the same according to the Higbie's penetration model.

When considering the k_L of the system as the function of gas flow rate as shown in Figure 5.4, it can be seen that the k_L reduced with the gas flow rate. This decrease was according to two incidences. Firstly, the increase of gas flow rate slightly increased the bubble sizes but not significantly affected the relative bubble rising velocities. According to the terminal velocity of bubbles (Guet and Ooms, 2006), the bubble velocity of the bubble size in the range of 5-8 mm does not change significantly. Therefore, the k_L reduced due to the larger size of bubbles according to the Higbie penetration model. The other incidence was that, the mass transfer occurred from the bubble swarms and the mass transfer of large bubble swarm was less than the small ones due to the fact that the concentration of CO_2 liquid film around each bubble was interfered by the adjacent bubbles. This finding also supported by several works as the mass transfers in a single bubble and bubble swarms were significantly different (Colombet et al., 2015; Hughmark, 1967).
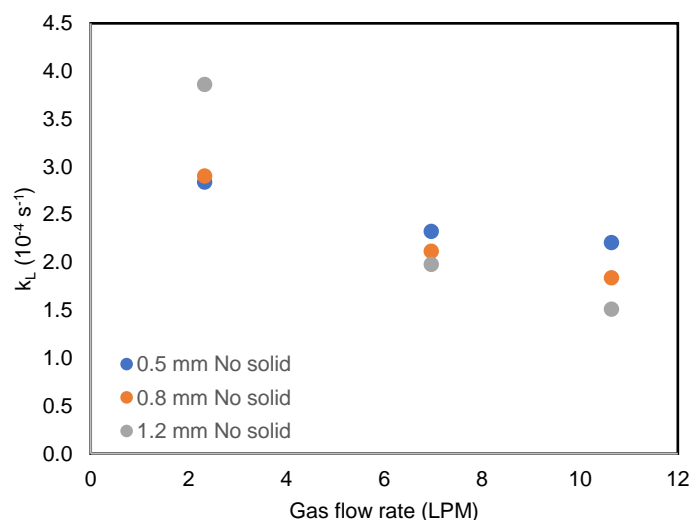
Figure 5.4 k_L as a function of orifice sizes and gas flow rate in two-phases bubble column

Nevertheless, in order to comprehensively understand the performance of the bubble column, the $k_L.a$ is plotted as a function of the specific power consumption (P/V_{total}) in Figure 5.5.
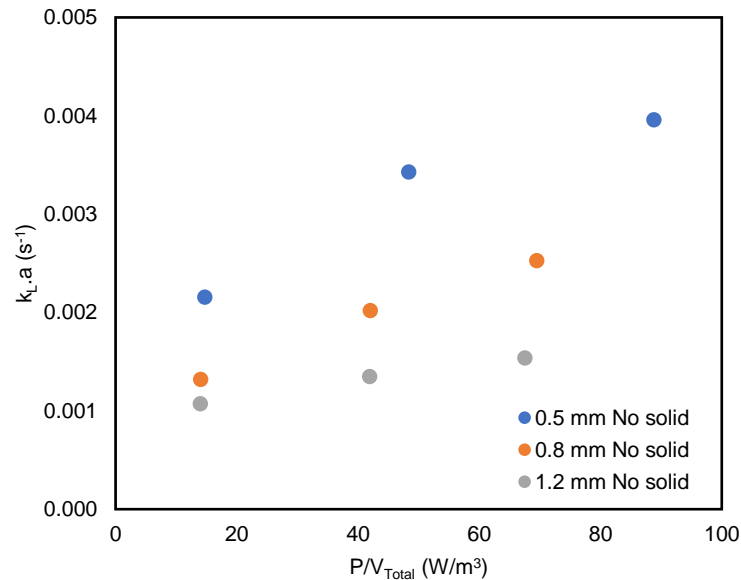
Figure 5.5 $k_L.a$ as a function of specific power consumption for different orifice sizes in two-phase bubble column

In the figure, it can be seen that the 0.5 mm orifice size was the best one giving the highest $k_L.a$ for a certain P/V_{total} value among the other orifice sizes. Although the large specific power consumption was required for the operation of the small orifice size, it was compensated with the high $k_L.a$ achieved by the orifice size. The highest specific interfacial area was the one responsible for this finding. Hence, for the case of the bubble column, it can be concluded that the best condition for the mass transfer is the smallest orifice size as it generated the highest $k_L.a$ in the range of studied P/V_{total}.

(b) Spray column

Figure 5.6(Left) and (Right) show the effect of liquid flow rate and gas flow rate on the CO_2 transferred rate in the spray column. The increase of both liquid and gas flow rate increased the CO_2 transfer rate for every orifice size used. However, the liquid flow rate had much effect than the gas flow rate as can be seen in both figures that their slopes were larger because the mass transfer of CO_2 was limited in the liquid phase due to the low solubility of CO_2 in the liquid phase. The increase of liquid flow rate not only raised the capability to absorb the CO_2, but also affected the droplet hydrodynamics especially for the reduction of droplet sizes. Therefore, it can be concluded that for the spray column, the liquid flow rate was the one controlling the mass transfer rate of the system. In addition, when considering the effect of orifice sizes, the smallest orifice size (0.89 mm in this study) gave the best mass transfer rate of CO_2. The smaller droplet sizes were responsible for this trend as the small droplet sizes yielded higher specific interfacial area as mentioned in Chapter 3.
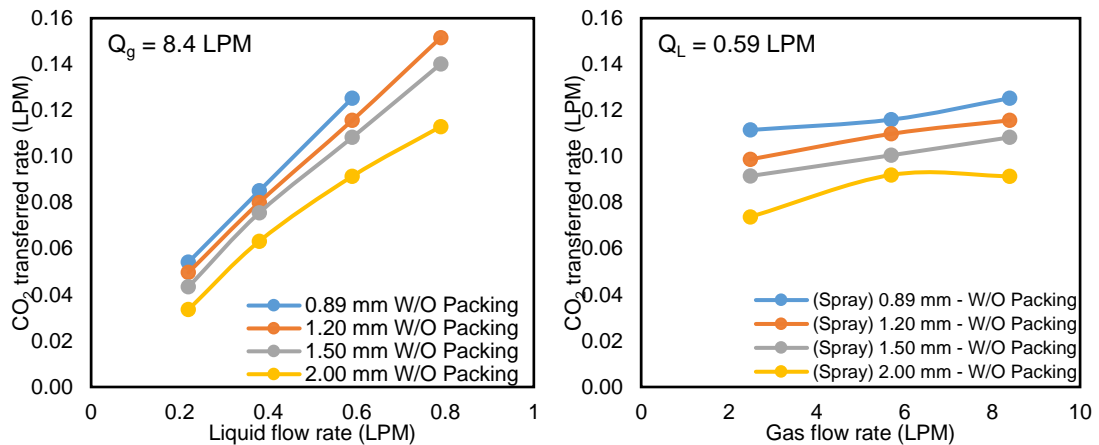
Figure 5.6 CO_2 transferred rate as a function of liquid flow rate and orifice sizes for two-phase spray column

When investigating the $k_L.a$, the same trends as the CO_2 transferred rate were achieved for both liquid and gas flow rate, as shown in Figure 5.7. The increase of the specific interfacial area as the liquid flow rate increased was the major cause. As mentioned in Chapter 3, the specific interfacial area increased with the liquid flow rate because the higher flow rate it was, the smaller sizes of droplets produced by the orifice, leading to higher specific interfacial area. Although the larger liquid flow rate gave higher droplet settling velocities, the smaller sizes of droplets dominated the change. For the gas flow rate, as mentioned earlier, the effect was not as strong as the liquid flow rate since the increase of gas flow rate did not affect the specific interfacial area. A small increase of the $k_L.a$ was due to the minor inclusion of k_L. The increase of gas flow rate affected the gas velocity inside the column, leading to higher effective droplet velocity (which was the relative velocity between gas phase and liquid phase) and consequently raised the mass transfer coefficient (k_L).
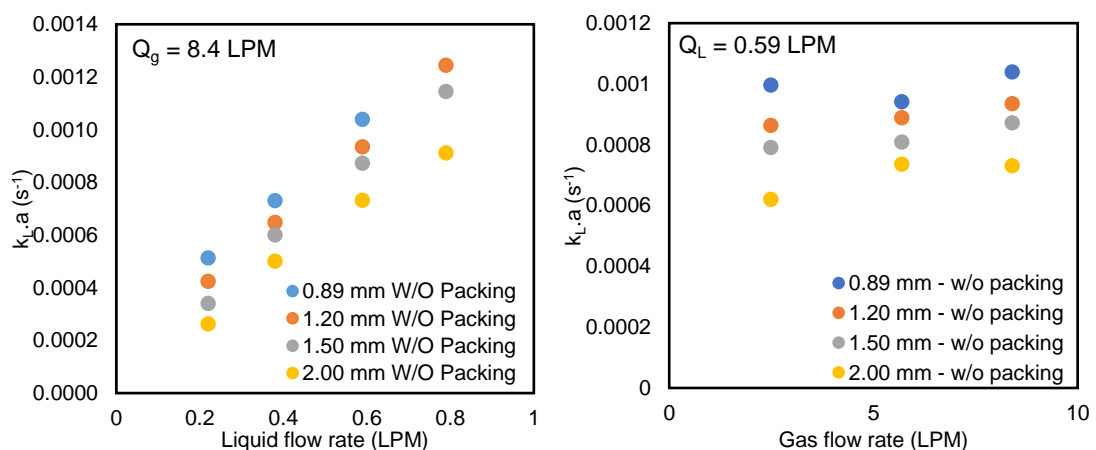
Figure 5.7 Effect of liquid flow rate and orifice sizes on $k_L.a$ for two-phases spray column

Nevertheless, the orifice sizes played an important role for the change of $k_L.a$ in the column. As mentioned in Chapter 3, the smaller size of the orifice gave the higher specific interfacial area. Therefore, it can be seen that, when using the smaller size of the orifice, the larger $k_L.a$ was obtained. Although the small orifice sizes gave higher specific interfacial areas as described in Chapter 3. Figure 5.8 indicates that when using the small orifice sizes, the k_L especially at high liquid flow rate were the smallest one. It was due to the fact that, the small orifice produced the small droplets and their Reynolds number was smaller comparing with the large droplets. Although their velocities were larger, the smaller of droplet sizes dominated the effect as mentioned earlier. The decrease of the k_L over the liquid flow rate was also responsible for the same effect since the increase of liquid flow rate decreased the droplet sizes where the k_L was reduced.
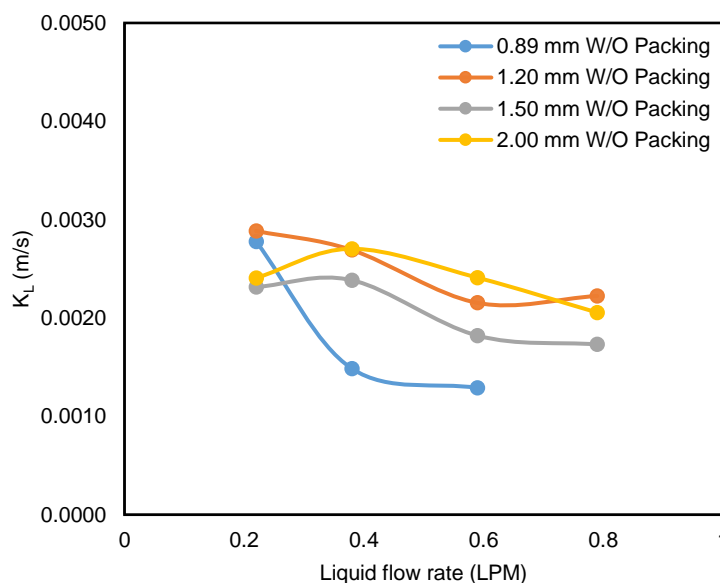
Figure 5.8 k_L of spray column as a function of orifice size and liquid flow rate for two-phases spray column

Nevertheless, the $k_L.a$ as the function of the specific power consumption of the spray column at different orifice sizes were also determined and illustrated as in Figure 5.9. It can be seen in the figure that the increase of the P/V_{total} increased the $k_L.a$ regardless of the orifice sizes. When considering the orifice sizes, the 2.00 mm orifice yielded the best $k_L.a$ for the same specific power consumption due to the lower significant pressure drop when comparing with the larger orifice. However, it could not be concluded that the best orifice size for the two-phase spray column was the one with the largest orifice size since the specific power consumption did not consider the liquid loading used in the column. Therefore, for practical usage, the balance between the cost due to the power requirement and the cost of liquid phase should be together taken into an account.
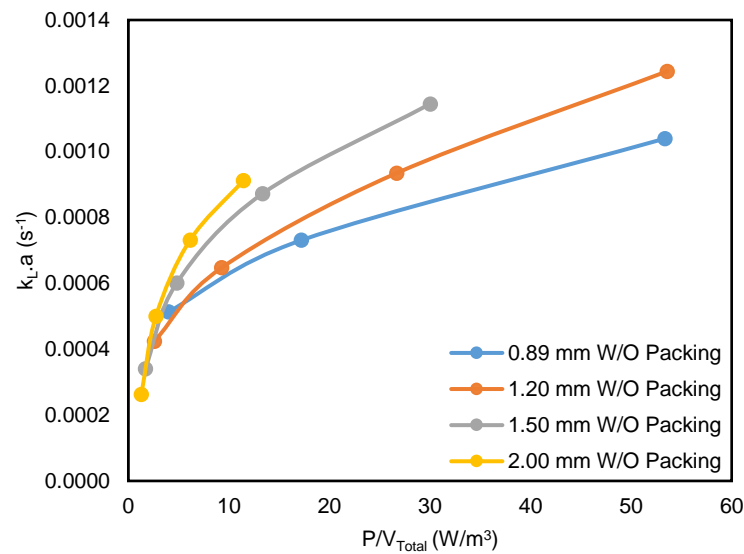
Figure 5.9 $k_L.a$ as a function of specific power consumption for different orifice sizes in two-phases spray column

(c) Bubble – spray columns comparison

Figure 5.10 shows the comparison of the $k_L.a$ between the bubble and spray columns as the function of P/V_{total} at different orifice sizes of bubbles or droplets production. In the figure, the $k_L.a$ of the bubble column were significantly higher than those of the spray column especially for the case of the smallest orifice size of the bubble column, 0.5 mm. The $k_L.a$ of the spray column were in the same range as the bubble column when the orifice size of the bubble column was 1.2 mm.
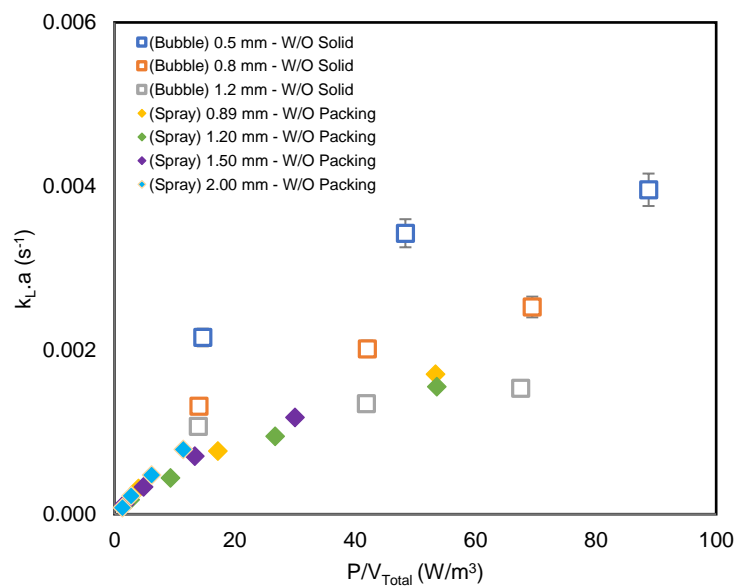
Figure 5.10 Comparison of $k_L.a$ between two-phase bubble column and spray column as a function of specific power consumption

The significant difference between the bubble column and spray column was due to the significant larger of the specific interfacial area of the bubble column, where the bubbles in the bubble column had significant lower velocities comparing with the droplets in the spray column. Hence, for the two-phase bubble column and spray column, it can be concluded that, the bubble column was the better one in terms of the $k_L.a$ when considering at the same specific power consumption in this range of kinetic reaction, Hatta number (M_H) < 3, and operating conditions of gas and liquid flow rates. It should be noted that when considering at higher kinetic reaction (M_H > 3) where higher concentration of NaOH was used, the consequence might be different. According to the fluid dynamics in the spray column where both gas and liquid phases can be considered as nearly plug flow, the dilution of the liquid phase that occurred in the well-mixed regime as the bubble column is not occurred. Therefore, for the absorption that required very high kinetic reaction rate, the spray system is the one that should be taken into account. Moreover, when the absorption process encounters very high gas loading, (e.g. carbon dioxide capture from combusted air etc.), it might be convenient to use the spray column instead of the bubble column due to the fact that the hydrodynamics and power consumption of the bubble column are very dependent on the gas flow rate. However, the droplet entrainment in the spray should also be considered as the superficial velocity of gas should not excess than half of droplet velocities in the column in order to avoid the liquid entrainment.

5.4.2 Three-phases columns

(a) Bubble column

Figure 5.11 CO_2 transferred rate as a function of gas flow rate and orifice sizes in the bubble column when solid phase presented (Left) Ring-shaped particles (Right) High-void packing

Figure 5.11 (Left) and (Right) shows the effect of solid phase, gas flow rate and liquid flow rate on the CO_2 transferred rate, respectively. The effect of solid phases was different depending on the orifice sizes and the types of solid phase. The addition of packing increased the CO_2 transferred rate only for the cases with the 1.2 mm orifice size. However, for the 0.5 and 0.8 mm orifice sizes, the addition of packing decreased

the CO_2 transfer rate. The same effect was also found when the ring-shaped particles were presented in the column except for the ring-shaped particles that also gave the positive effect for the 0.8 mm orifice size.

When used these transferred rates for the calculation of $k_L.a$, the results are depicted in Figure 5.12(Left) and (Right) for the effect of gas flow rate and liquid flow rate, respectively.
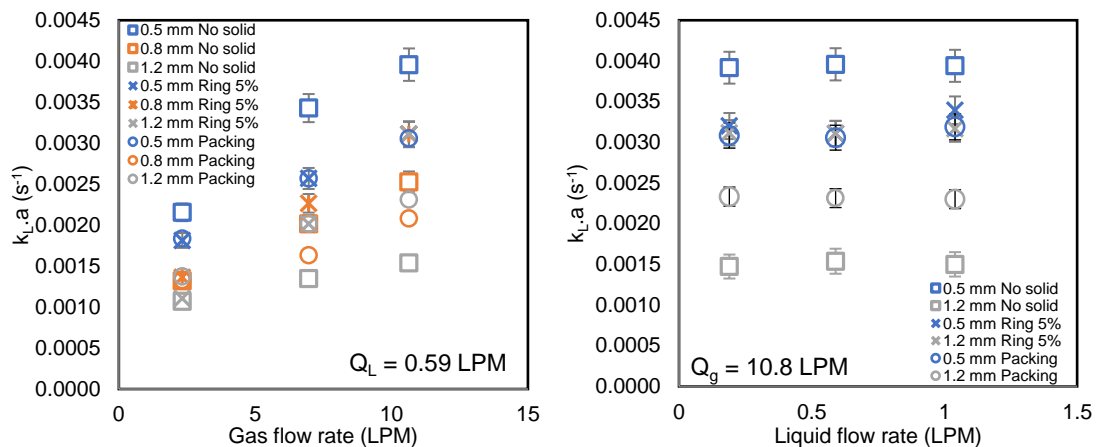
Figure 5.12 $k_L.a$ as a function of gas flow rate and orifice sizes in the bubble column when solid phase presented (Left) Ring-shaped particles (Right) High-void packing

When considering the $k_L.a$, the liquid flow rate did not have any effects even though when the solid phase was presented. It was due to the fact that the hydrodynamics of the bubbles in the column was not significantly changed in the operating liquid flow rate. Hence, the specific interfacial area as well as the mass transfer coefficient did not be affected by the liquid flow rate. However, when considered the gas flow rate, the volumetric mass transfer coefficient $k_L.a$ increased with the gas flow rate due to the enlargement of the amount of bubbles in the column. The addition of solid phase in the column had the same effect throughout the range of the gas flow rate used in this study.

For the effect of solid phase, the $k_L.a$ was lower when the orifice size of 0.5 mm was used for both packing and ring-shaped particle conditions. The reduction up to 22.5 % was achieved when the packing and the particles were introduced. However, when using the orifice size of 1.2 mm, the addition of solid phase in the column had a positive effect where the $k_L.a$ of the column was increased. The increase of the $k_L.a$ was up to 47 % for the packing whilst 113 % was achieved for the ring-shaped particles. It should be noticed that the same effect was also found when considering only the specific interfacial area as mentioned in Chapter 3. Hence, it can be concluded that for the presence of packing, the change of the specific interfacial area dominated the mass transfer in the system.

In order to understand the effect of solid phase on the mass transfer in the bubble column, the mass transfer coefficient (k_L) was individually investigated as shown in

Figure 5.13. Here, it can be seen that, the k_L in the case of solid presented, were lower when comparing for the case without solid phase. It was due to the effect of the solid phase that reduced the velocities of bubbles. According to the Higbie's penetration theory, the decrease of the bubble velocity diminished the k_L as it reduced the liquid film changing time around each bubble, where the detail can be seen in Chapter 4. Therefore, the increase of the specific interfacial area had to be overcome the reduction of the k_L in order to enhance the mass transfer in the three-phase bubble column system. Note that the enhancement can only be acquired when the orifice size of 1.2 mm was used.

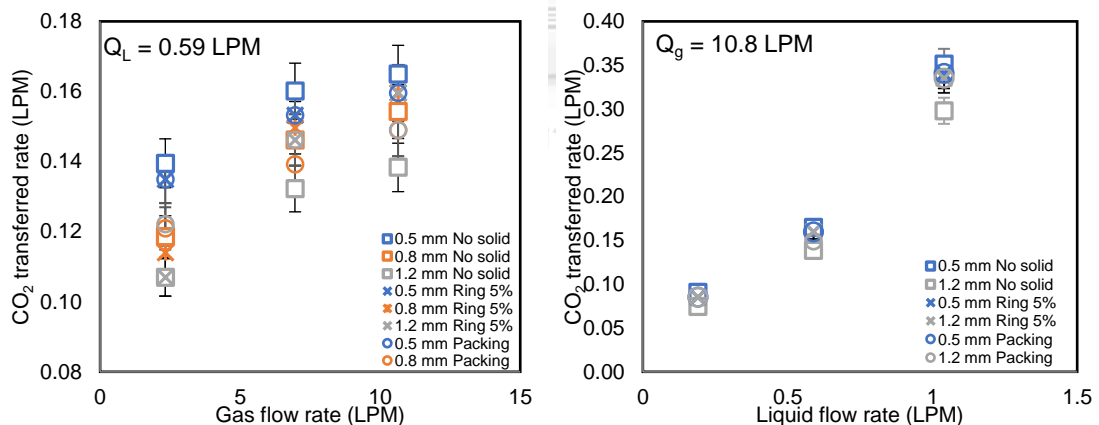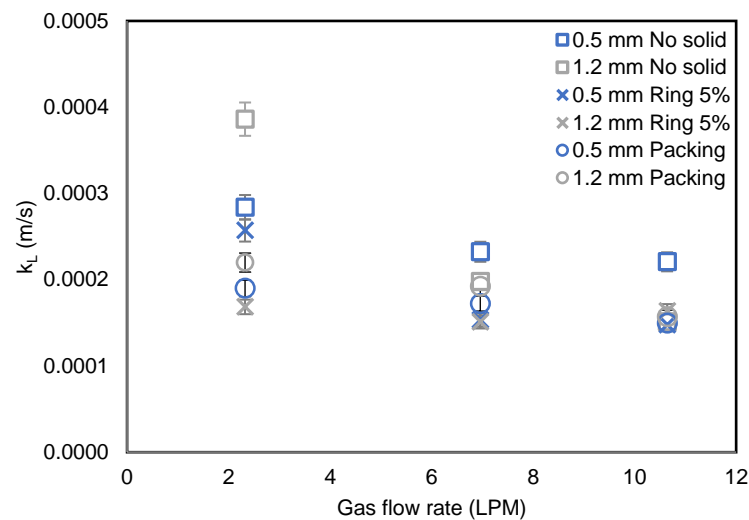Figure 5.13 k_L as a function of gas flow rate and orifice sizes in the bubble column when solid phase presented (Left) Ring-shaped particles (Right) High-void packing

When considering the specific power consumption with the change of the $k_L.a$ due to the presence of the solid as shown in Figure 5.14, for the case of 1.2 mm orifice size, the addition of solid phase gave the better $k_L.a$ for the same P/V_{total}. The same effect was found for the 0.8 mm orifice size when the ring-shaped particles were used but not with the packing. The reduction of the $k_L.a$ was also achieved for the 0.8 mm with the presence of packing and 0.5 mm for all the presenting solid phase. It should be noticed that, the addition of ring-shaped particles for the case of 1.2 mm orifice size could overcome the $k_L.a$ for the case of 0.8 mm without the addition of solid. However, it cannot overcome the $k_L.a$ of the 0.5 mm orifice without the presence of any solid.
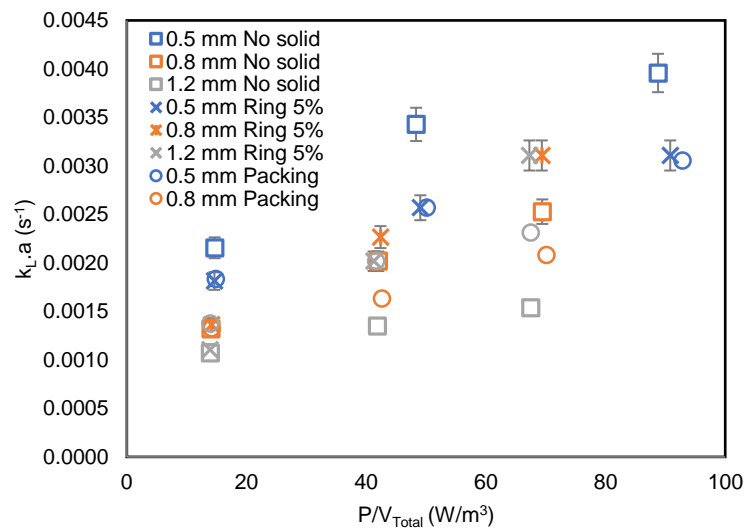
Figure 5.14 $k_L.a$ as a function of specific power consumption for different orifice sizes in the bubble column when solid phase presented

Hence, it can be summarized that the addition of packing did not have a positive effect unless the orifice size was large. The ring-shaped particles gave a better improvement when comparing with the packing especially for the large orifice size. However, the improvement of the $k_L.a$ with the presence of solid cannot overcome the small orifice size (0.5 mm orifice in this case) because the k_L of the bubbles decreased even though the specific interfacial area increased. Hence, there was a limitation using the solid phase for the improvement of mass transfer since it had to balance between the increase of the specific interfacial area and the decrease of the mass transfer coefficient.

(b) Spray column

The CO_2 transferred rate of the spray column with the presence of packing as the functions of liquid flow rate and gas flow rate are shown in Figure 5.15(Left) and (Right), respectively. When the packing was presented, slightly larger CO_2 transferred rates were obtained for every case. The effect of the liquid flow rate and gas flow rate followed the same trend as without the packing presented where the increase of CO_2 transferred rates were achieved.
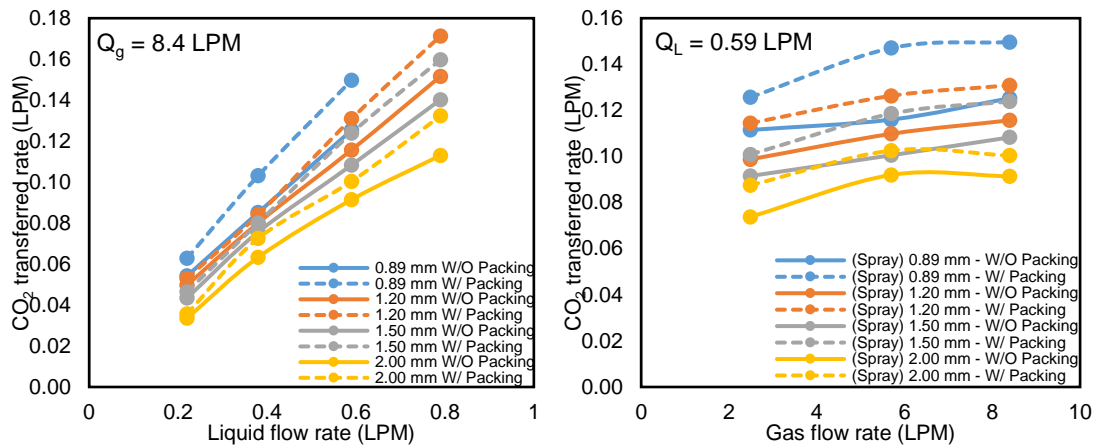
Figure 5.15 CO_2 transferred rate as a function of liquid flow rate, orifice size, and presence of packing in the spray column

When determining the $k_L.a$ using the CO_2 transferred rate for the calculation, Figure 5.16 indicates that the presence of packing gave the same trend as the case without packing but with the increase of the $k_L.a$ especially for the case of the 0.89 mm orifice size that improved up to 50 %. It can be clearly seen that the 0.89 mm orifice size was the one that had the highest improvement among the others since its angle of spray was larger and had higher chance to contact with the packing that provided the additional specific interfacial area that described already in Chapter 3. Note that the liquid flow rate controlled the mass transfer of CO_2 in the system since the solubility of CO_2 was very low. Therefore, even with the presence of packing, the increase of liquid flow rate increased the $k_L.a$ more effective than the gas flow rate. It is one of the great advantages of the spraying system since its performance does not depend on gas flow.
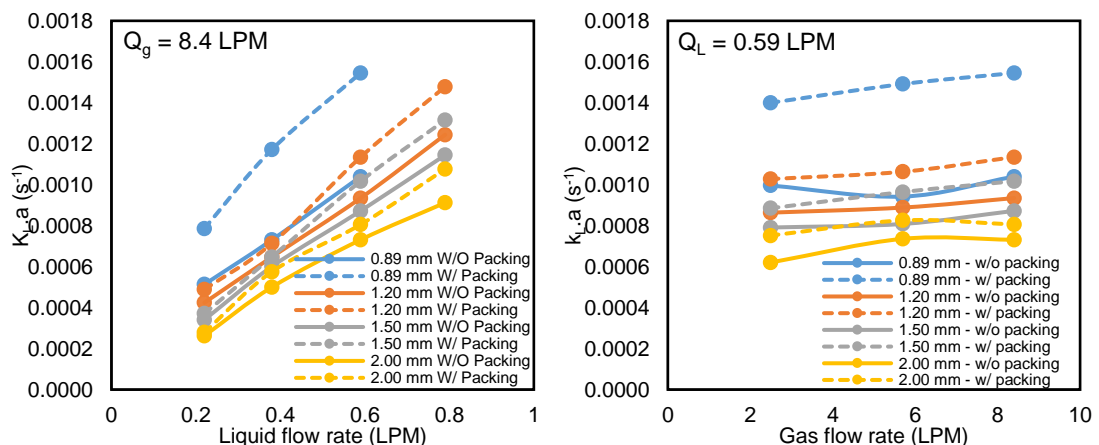
Figure 5.16 Effect of liquid flow rate and orifice sizes on $k_L.a$ with and without the presence of packing in the spray column

When considering the k_L for the spray system, Figure 5.17(Left), the significant reduction of k_L was achieved due to the fact that the droplet settling velocities when droplets did not collide with the packing was significantly larger. After droplets collided

with the packing and form a larger droplet, the velocity of the new formed droplets was slower leading to lower Reynolds number and low k_L.
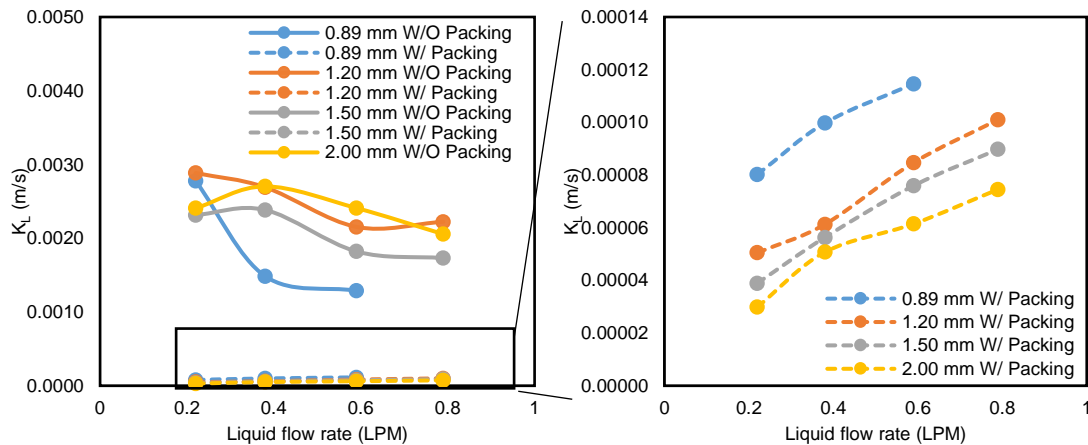
Figure 5.17 k_L of spray column as a function of orifice size and liquid flow rate with and without the presence of packing in the spray column

Figure 5.17(Right) shows the k_L of the spray column in the cases when the packing presented. The increase of k_L was achieved when the liquid flow rate increased due to the higher frequency of droplets were formed on the packing surface at the higher liquid flow rate. In addition, the film of the liquid had higher velocities. Moreover, the 0.89 mm orifice yielded the highest k_L among the other orifice sizes. The same explanation of the film velocity was still valid for this case since the 0.89 mm orifice produced much higher droplet velocities than the smaller ones. Therefore, the liquid film would have higher kinetic energy, leading to higher Reynolds number and the k_L.
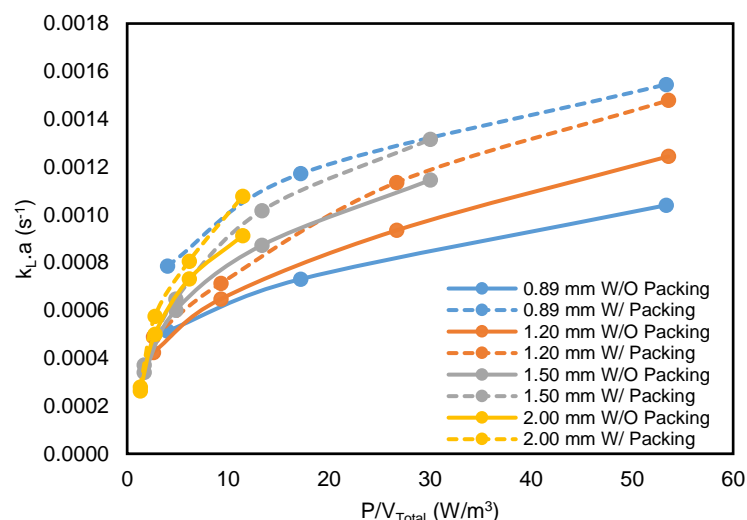
Figure 5.18 $k_L.a$ as a function of specific power consumption for different orifice sizes with and without the presence of packing in the spray column

When considering the $k_L.a$ as the function of the specific power consumption and the orifice size, Figure 5.18 shows the increase of the $k_L.a$ when the P/V_{total}

increased which was the same trend as when the packing was not presented. However, with the presence of packing, the sharp increase of the $k_L.a$ of the 0.89 mm orifice was obtained; the $k_L.a$ of the 0.89 mm orifice were compatible with the 2.00 mm orifice when considering at the same P/V_{total}. Unfortunately, the range of the $k_L.a$ and P/V_{total} for the 2.00 mm was narrow due to its low pressure drop. Therefore, it could not clearly conclude that which ones were the best for the three-phases spraying system. Though, it can be summarized that the presence of packing increased the $k_L.a$ without spending the significant extra power consumption.

(c) Bubble – spray columns comparison

Figure 5.19 shows the comparison between the bubble column and the spray columns in terms of the $k_L.a$ as the function of the P/V_{total} for both two-phases and three-phases ones. The increase of the $k_L.a$ via the presence of the packing overcame the $k_L.a$ of the bubble column without the presence of solid phase in the case of the orifice size of 1.2 mm. Although the addition of the packing increased the $k_L.a$ of the spray column, the increase was not overcome the $k_L.a$ of the bubble column with the 0.5 mm orifice size. Hence, it can be concluded here that, the bubble column had an advantage over the spray column when considering the global specific power consumption. The addition of the specific interfacial area by the presence of packing did not overcome the specific interfacial area and the mass transfer of the bubble column. However, it should be noted that the comparison was considered only the global specific power consumption of the columns. If both systems were compared assuming that the major issue is the high gas loading rate as in the CO_2 absorption from combustion processes, the conclusion could be different when considering the gas specific power consumption. In addition, when the Hatta number is taken into account, this statement can also be changed. The cost due to the chemical or raw material should also be considered when determining the total cost of the operation.
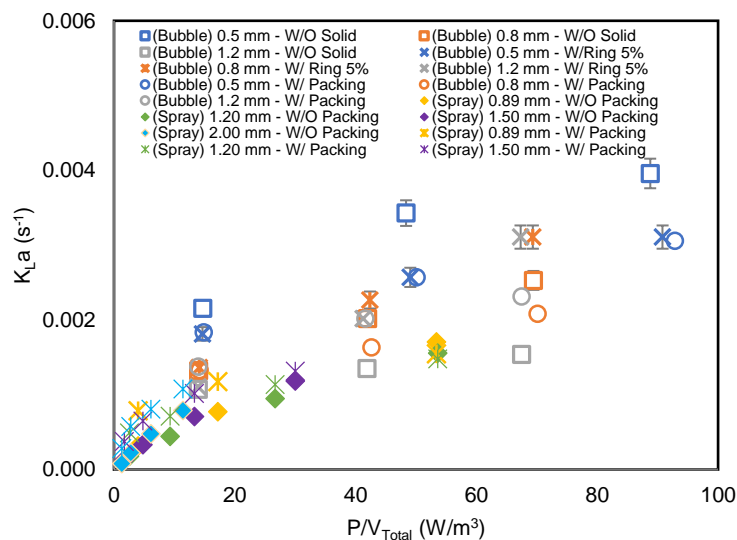
Figure 5.19 Comparison of $k_L.a$ between three-phases bubble column and spray column as a function of specific power consumption

In order to sum up, Table 5.3 shows the summarized comparison between the bubble column and spray column for the absorption in the column. The discrete phase of the bubble column (i.e. bubbles) had significant lower velocity than the discrete phase of spray column (i.e. droplets). Although the sizes of droplets were smaller, the velocities of bubbles were much lower leading to significant higher of the specific interfacial area. One of the advantages of the higher velocity of droplets was the high Reynolds number that yielded the higher k_L. However, it was not compensated with the low specific interfacial area leading to overall lower the $k_L.a$ of the spray column in comparing with the bubble column.

Table 5.3 Summary of the comparison between bubble column and spray column in terms of mass transfer

Operation	Bubble column	Spray column
Discrete characteristic	Bubbles	Droplets
Discrete size	Large (3-8 mm)	Small (<0.1 – 3 mm)
Discrete velocity	Low (0.1-0.2 m/s)	High (1-10 m/s)
Discrete phase holdup	Higher (0.5-2.0 %)	Lower (0.01-0.1 %)
Specific interfacial area	Higher ($10\text{-}25 \text{ m}^{-1}$)	Lower ($0.1\text{-}2.0 \text{ m}^{-1}$)
K_L	Lower (10^{-4} m/s)	Higher (10^{-3} m/s)
Overall mass transfer coefficient ($K_L.a$)	Higher ($1.0\text{-}4.0 \times 10^{-3} \text{ s}^{-1}$)	Lower ($0.3\text{-}1.5 \times 10^{-3} \text{ s}^{-1}$)
Absorption rate	Higher	Lower
Pressure drop	Lower	Higher
Specific power consumption	Lower	Higher
Control variable of mass transfer	Gas flow rate, orifice characteristics	Liquid flow rate, nozzle characteristics
Control variable of specific power consumption	Gas flow rate, orifice characteristics	Liquid flow rate, nozzle characteristic
Enhancement of mass transfer with solid phase	Possible for larger orifice sizes than 1.0 mm with movable particles	Improvable with packing

The spray column also had another drawback as their pressure drop was high in the liquid phase leading to higher power consumption than the bubble column. However, the major difference between both columns was that the control variable of the spray column was the liquid flow rate while the gas flow rate was for the bubble column. Therefore, the suitable condition should be selected based on the use condition of the absorption. For example, as shown in Figure 5.20(Left), when operating at very

low gas flow rate (low gas to liquid ratio), the $k_L.a$ for the bubble column would be very low in comparing with the spray column. Therefore, in this condition, the spray column should be selected. In contrast, when using at the large gas to liquid ratio, the bubble column is recommended. Note that the $k_L.a$ of both columns can be improved by the addition of solid phase. The ring-shaped particles are recommended for the bubble column than the packing one due to the better specific interfacial area achieved. In addition, when determining the specific power consumption used for both process, it can be seen in Figure 5.20(Right) that, for a certain $k_L.a$, the bubble column spent high power consumption when gas to liquid ratio was large while the spray column highly spent the power when the gas to liquid ratio was small. It indicated that the specific power consumption was highly depended on the selected process and should also be taken into account when preliminary select the process for absorption purpose.
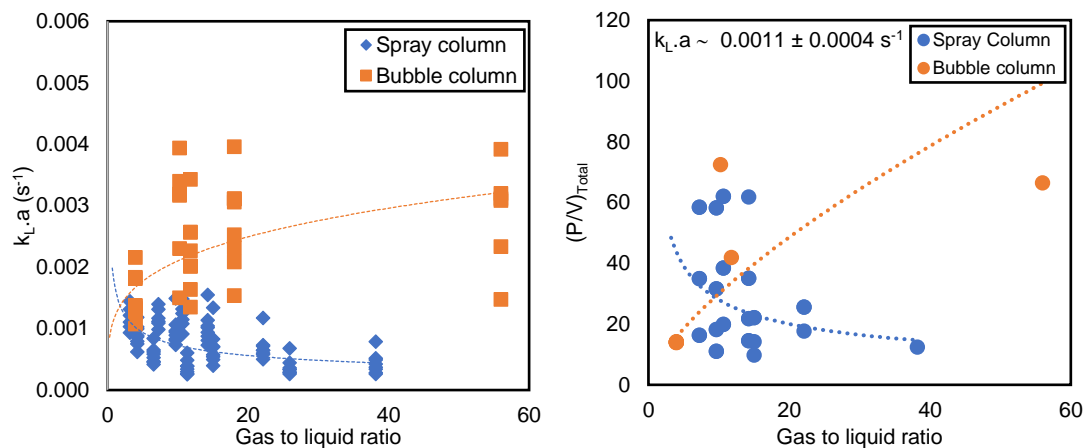
Figure 5.20 (Left) Comparison of the $k_L.a$ as the function of gas to liquid ratio for the bubble and spray columns and (Right) comparison of the specific power consumption as the function of gas to liquid ratio in the range of $k_L.a$ 0.0011 ± 0.0004 s^{-1}

Furthermore, a comparison of the $k_L.a$ as a function of the specific power consumption that included other gas-liquid contactors, a packed bed and a stirred tank, was achieved. The $k_L.a$ of the packed bed using the 1.5-inch metal Pall-like rings packing was simulated using the rate-based method according to Seader et al., (2010), while the stirred tank was the results researched by Bouaifi et al., (2001). It can be seen in the figure that, the packed bed and the stirred tank provided larger $k_L.a$ than the spray column, but in the same range as the bubble column.
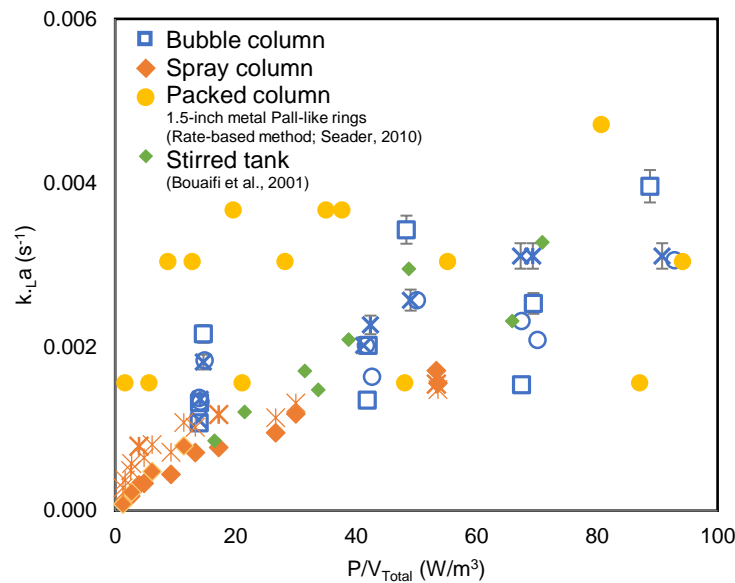
Figure 5.21 Comparison of $k_L.a$ between bubble column, spray column, packed column (Rated-based method; Seader, 2010), and stirred tank (Bouaifi et al., 2001)

In detail, the packed bed gave the same range of the $k_L.a$ as the bubble column for the P/V_{total} larger than 40 W/m^3 but significantly larger for lower P/V_{Total} due to the fact that the bubble column for the small P/V_{Total} produced small amounts of bubbles and could not compete with the interfacial area of wetted packing, whilst for the larger P/V_{Total}, there were more bubbles and their specific interfacial areas were more comparable. For the stirred tank, its $k_L.a$ was slightly lower than the bubble column using the 0.5 mm orifice gas sparger due to the slightly lower specific power consumption. This result is consistent with the comparison done by Bouaifi et al., (2001). Moreover, the mass transfer parameter between the contactors was compared for the range of P/V_{Total} less than 100 W/m^3 where the result is shown in Table 5.4.

Table 5.4 Comparison between contactors in terms of mass transfer for low specific power consumption (< 100 W/m^3)

Operation	Bubble column (Experiment)	Spray column (Experiment)	Packed column 1.5-inch metal Pall-like rings (Rate-based method; Seader et al., 2010)	Stirred tank (Bouaifi et al., 2001)
Discrete characteristic	Bubbles	Droplets	Wetted packing	Bubbles
Discrete phase holdup (%)	0.5-2.0	0.01-0.1	0.5-1.0	0.5-2.0
Specific interfacial area (a, m^{-1})	10-25	0.1-2.0	15-40	10-22
K_L (m/s)	$1\text{-}4 \times 10^{-4}$	$1\text{-}4 \times 10^{-3}$	$1\text{-}2 \times 10^{-4}$	$1\text{-}3 \times 10^{-4}$
Overall mass transfer coefficient ($K_L.a$, s^{-1})	$1.0\text{-}4.0 \times 10^{-3}$	$0.3\text{-}1.5 \times 10^{-3}$	$1.5\text{-}4.0 \times 10^{-3}$	$1.0\text{-}3.5 \times 10^{-3}$
Control variable of mass transfer	Gas flow rate, orifice characteristics	Liquid flow rate, nozzle characteristics	Liquid flow rate, packing characteristics	Gas flow rate, stirred speed, types, impellers types, orifice characteristic
Power consumption-dominated phase	Gas	Liquid	Gas	Gas
Control variable of specific power consumption	Gas flow rate, orifice characteristics	Liquid flow rate, nozzle characteristic	Gas flow rate, packing characteristics, liquid distributors	Gas flow rate, stirred speed, types, impellers types, orifice characteristic

From the table, the discrete holdups for all the contactors are between 0.01-2.0 %. The bubble column and the stirred tank gave the highest holdup among other contactors. Slightly smaller holdup was achieved by the packed bed while the spray provided the lowest one. These different ranges are caused by the different discrete characteristics and their velocity. As droplets have the highest velocity, the holdup was the smallest while for the bubble column and the stirred tank, their holdups are in the same range due to their discrete phases are identical. The specific interfacial areas are also in the same order for the bubble column, stirred tank, and the spray column since they were directly affected by their holdups. However, for the packed column, its interfacial area is the highest among the others because of the interfacial area that

provided by the packing. The overall mass transfer coefficient ($k_L.a$) are as mentioned earlier, the packed column, stirred tank, and the bubble column are very close especially for the bubble column and the packed column. Although the specific interfacial area of the bubble column is lower than the packed bed, its mass transfer coefficient (k_L) is slightly higher. Hence, the mass transfer performances of both contactors are in the same range and are the highest ones among the other types. However, the packed column and the bubble column have a major difference in terms of the variables that control their $K_L.a$. The mass transfer of the bubble column is controlled by the gas flow rate and the orifice characteristics which are the important factors controlling bubble characteristics. Whilst, the $k_L.a$ of the packed column is dominated by the liquid flow rate and the packing characteristics as these variables are directly related to the creation of liquid layer on the packing interface.

In addition to the mass transfer, the phase and variables that control the power consumption are included in the table. For the spray and bubble column, the variables that affect the power consumption are also the same ones that control the mass transfer. This relation is also the same for the stirred tank, where the stirred speed, types of impellers, and gas flow rate are the ones contributing the power consumption (Bouaifi et al., 2001). However, for the packed bed, the power consumption is highly related to the pressure drop of gas flow rate not the liquid one (Seader, 2010). The gas phase pressure drop is caused by the internal packing and also the flow contraction due to the liquid distributors (Rix and Olujic, 2008). Hence, the packed column should not be used with very high gas throughput as it causes high power consumption and, moreover, also causing the flooding regime (Ray, 1994). In this case, the spray column might be more appropriate as its power consumption is controlled by the liquid phase.

Nevertheless, it should be emphasized that these results and discussions covered a limited range of possible configurations. This information can be used for a preliminary guideline for the equipment selection and design. The actual design and optimization require further information than this comparison. When considering the huge number of parameters that can be optimized, some other conclusion could emerge in other conditions.

5.4.3   Modeling
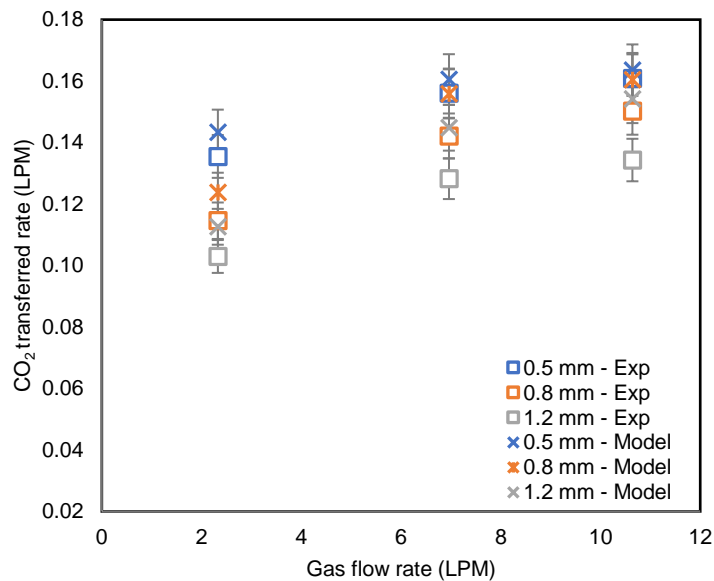
Figure 5.22 Experimental and modelling comparison of CO_2 transfer rate of two-
phases bubble column

Figure 5.22 shows the CO_2 transferred rate as the function of gas flow rate
estimated using the methodology described in Section 5.3.3. The CO_2 transferred rate
of the model was rose with the gas flow rate, which was consistent with the result from
the experiment. Moreover, the model was able to determine the change of CO_2 transfer
rate when using different orifice sizes, where it can be seen that the 0.5 mm orifice
yielded larger CO_2 transfer rate. The average error between the experiment and the
modeling was 7.75 %, indicating a very good promising agreement.

In addition, it can be seen that, the accuracy of the model was high when the
small orifice size was used. A larger deviation was obtained when calculating the CO_2
transferred rate of the 1.2 mm orifice size. The error was due to the overestimation of
the k_L of the small orifice size because the small orifice size did not provide a good
dispersion of bubbles throughout the column, as mentioned in Chapter 3.
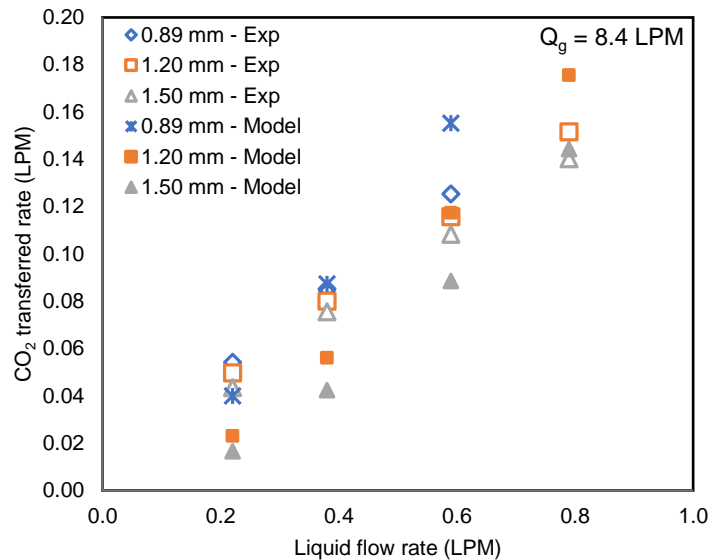
Figure 5.23 Experimental and theoretical mass transfer rate of two-phases spray column

Figure 5.23 shows the comparison between the experiment and the model of the spray column at different liquid flow rates and orifice sizes where the average error was at 25.5 %. The result of the model was consistent with the experiment especially for the small orifice sizes, 0.89 and 1.20 mm. However, when determining the CO_2 transferred rate of the 1.50 mm orifice, a larger deviation was obtained particularly at low liquid flow rate. The overestimation of the CO_2 transferred was due to the overestimated of the k_L at low liquid flow rate of the model since the correlation used in the studied was normally used for a single droplet; therefore, for the droplet swarm, the k_L was changed.

5.5 Conclusion

In this chapter, the mass transfer parameters in terms of CO_2 transferred rate, $k_L.a$ and k_L were investigated for bubble and spray columns. The gas flow rate was the one controlling the mass transfer rate in the bubble column because the change of gas flow rate also changed the bubble hydrodynamics in the column. However, the increase of the liquid flow rate did not significantly affect the hydrodynamics and the $k_L.a$ in the column was steady. It was in contrast with the spray column where the liquid flow rate was the major variable controlling the mass transfer. The same reason for the bubble column can also be applied for the spray system, since the change of the liquid flow rate dramatically changed the hydrodynamics of droplets in the column while the gas flow rate did not. This difference was due to the similarity of the disperse phase in each column. In addition, the mass transfer rates of both columns were at their highest when the smallest sizes of their orifices were used. When comparing between both columns, the bubble column gave the higher mass transfer rate approximately 30 % over the mass transfer rate of the spray column. Nevertheless, the bubble column was also the optimal one giving higher mass transfer rate in terms of the specific power consumption.

However, it cannot be concluded that the bubble column was better than the spray column since the suitable condition needed to be considered depending on the substances used in the system. At low gas to liquid ratio, the spray column trended to give higher value of the mass transfer coefficient; while at the high gas to liquid ratio, the bubble column yielded larger mass transfer coefficient.

For three-phases columns, the presence of the high-void packing increased the mass transfer rate for the spray column as it raised the specific interfacial area. However, the mass transfer coefficient (k_L) was decreased due to the lower velocity of the liquid phase. Although the mass transfer rate increased, the three-phases spray column could overcome only the bubble column using the large orifice size. However, with the addition of the ring-shaped particles, the mass transfer rate of the large orifice size increased, and the inclusion was larger than the mass transfer rate of the three-phases spray column. The increase of the mass transfer rate in the bubble column was due to the elevation of the specific interfacial area in the bubble column as the bubbles in the column reduced their sizes, lower rising velocity, and increased bubble dispersion in the column. This effect was significantly found when the large orifice size was used in the bubble column since their bubbles would normally be in the center of the column when the ring-shaped particles were not presented. However, when using the high-void packing, mass transfer rate reduced since the packing diminished the bubble dispersion as it obstructed bubbles and accumulated them only at the center of the column. Hence, for the bubble column, the movable ring-shaped particles were the optimal one that can improve the mass transfer rate without significantly spends extra power consumption.

Research conclusion

Bubble column and spray column are ones of the crucial equipment for gas absorption in industrial processes. So far, information regarding hydrodynamics and mass transfer of bubble and spray columns has been studied. However, the comparison between spray and bubble column when the specific power consumption and addition of solid phase are taken into account has not been investigated. Hence, this research aims to fill the gap by setting up the experiment that both bubble and spray columns were compared in terms of hydrodynamics and mass transfer where the specific power consumption was also included in the study. Moreover, the addition of solid phase was introduced into the columns with the objective to enhance the specific area and thus mass transfer in the column. Both local and global investigations were performed in this research.

For local investigation of sprays, optical fiber probes were used to determine the hydrodynamics of sprays. The performances of the optical fiber probes, de-wetting probe and light interference probe were initially investigated by comparing their characterization results with a high-speed camera. The comparison indicated that the optical fiber probes, which are novel techniques, has a promising result when comparing with the result from the high-speed camera. Although there were deviations according to the droplet oscillation and coalescence on the probe, the optical fiber probes were able to characterize droplet hydrodynamics accurately. The advantages of the probe over other techniques are the simplicity to setup, the ability to use in moderate dense spray regime, and the capability to determine local liquid fraction. However, the drawback of the de-wetting should be considered as it requires a complicated post-processing or data treatment in order to achieve a good accuracy result.

For the local investigation of bubble column, the effect of movable particles added into a bubble column was inspected using the red-bottle colorimetric method. Liquid side mass transfer coefficient (k_L) was estimated using the change of the color from colorless to red when oxygen was transferred from bubbles to the liquid solution. It was found that the bubble-particles collision diminished the mass transfer of bubbles due to the collision slowed down the bubbles where its k_L decreased dramatically as described by Higbie model. This decrease in k_L was obviously found when bubbles were small due to the fact that the small bubble simply lost their velocities from the collision. Nevertheless, the research also developed a new technique used for determination of the overall liquid side mass transfer coefficient ($k_L.a$) of oxygen transfer using the colorimetric method where the $k_L.a$ can be estimated without using other equipment rather than measuring the time which color of the solution changed from colorless to saturated red. This technique is very useful in the aspect of education since it is very simple to demonstrate the mass transfer in bubble columns.

For the global investigation, the comparison of bubble and spray columns was achieved. In hydrodynamics aspect, the bubble column was superior to the spray

column due to bubbles had lower velocity when comparing with droplets. Therefore, the bubbles stayed in the column longer than the droplets resulting in higher holdup and therefore the specific interfacial area. The bubble column also had a greater performance in terms of mass transfer since its $k_L.a$ were larger than those of spray columns. However, this comparison was made when small gas loading rate was used. When considering the large gas loading rate, the spray column was more appropriate since the mass transfer and the hydrodynamics of spray column were greater than the spray column. The addition of the solid phase in both bubble and spray columns promoted the mass transfer rate in the columns. It was due to the increase of the specific interfacial area which modified when the solid was presented. However, there was appropriate conditions for which solid promoted the mass transfer rate. Especially for bubble column, the enhance of mass transfer rate was occurred when the movable ring-shaped particles were introduced into the column that had large orifice sizes of gas sparger.

In order to continue the research, the experimental setup where the gas phase is very soluble in the liquid should be considered in order to combine the result with this research to comprehensively cover the range of use of absorption process. Moreover, the chemical reaction also needed to be included in the study.
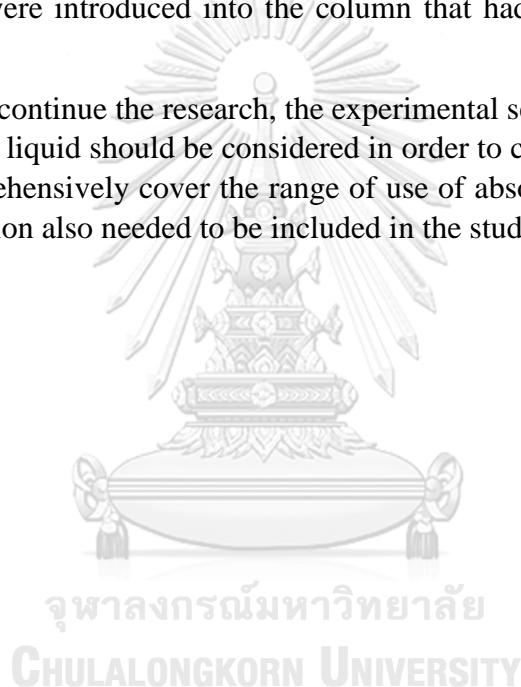
REFERENCES

Abuaf, N., Jones, O.C., Zimmer, G.A., 1978. Optical probe for local void fraction and interface velocity measurements. Rev. Sci. Instrum. 49, 1090. https://doi.org/10.1063/1.1135524

Agency, F.S., n.d. Current EU approved additives and their E Numbers | Food Standards Agency [WWW Document]. URL https://www.food.gov.uk/science/additives/enumberlist (accessed 7.8.17).

Bandyopadhyay, A., Biswas, M.N., 2007. Modeling of SO2 scrubbing in spray towers. Sci. Total Environ. 383, 25–40. https://doi.org/10.1016/j.scitotenv.2007.04.024

Behkish, A., Men, Z., Inga, J.R., Morsi, B.I., 2002. Mass transfer characteristics in a large-scale slurry bubble column reactor with organic liquid mixtures. Chem. Eng. Sci., Jean-Claude Charpentier Festschrift Issue 57, 3307–3324. https://doi.org/10.1016/S0009-2509(02)00201-4

Bhaduri, G.A., Šiller, L., 2013. Nickel nanoparticles catalyse reversible hydration of carbon dioxide for mineralization carbon capture and storage. Catal. Sci. Technol. 3, 1234–1239. https://doi.org/10.1039/C3CY20791A

Bhatia, B., Nigam, K.D.P., Auban, D., Hebrard, G., 2004. Effect of a new high porosity packing on hydrodynamics and mass transfer in bubble columns. Chem. Eng. Process. Process Intensif. 43, 1371–1380. https://doi.org/10.1016/j.cep.2003.10.009

Bhavaraju, S.M., Mashelkar, R.A., Blanch, H.W., 1978a. Bubble motion and mass transfer in non-Newtonian fluids: Part I. Single bubble in power law and Bingham fluids. AIChE J. 24, 1063–1070. https://doi.org/10.1002/aic.690240618

Bhavaraju, S.M., Russell, T.W.F., Blanch, H.W., 1978b. The design of gas sparged devices for viscous liquid systems. AIChE J. 24, 454–466. https://doi.org/10.1002/aic.690240310

Bird, R.B., Stewart, W.E., Lightfoot, E.N., 2007. Transport Phenomena. John Wiley & Sons.

Bouaifi, M., Hebrard, G., Bastoul, D., Roustan, M., 2001. A comparative study of gas hold-up, bubble size, interfacial area and mass transfer coefficients in stirred gas–liquid reactors and bubble columns. Chem. Eng. Process. Process Intensif. 40, 97–111. https://doi.org/10.1016/S0255-2701(00)00129-X

Boys, C.V., 1890. Soap-bubbles, and the forces which mould them. Cornell University Library.

Bridgewater, L.L., Baird, R.B., Eaton, A.D., Rice, E.W., American Public Health Association, American Water Works Association, Water Environment Federation (Eds.), 2017. Standard methods for the examination of water and wasterwater, 23rd edition. ed. American Public Health Association, Washington, DC.

Calderbank, P.H., Moo-Young, M.B., 1961. The continuous phase heat and mass-transfer properties of dispersions. Chem. Eng. Sci. 16, 39–54. https://doi.org/10.1016/0009-2509(61)87005-X

Cartellier, A., Achard, J.L., 1991. Local phase detection probes in fluid/fluid two-phase flows. Rev. Sci. Instrum. 62, 279–303. https://doi.org/10.1063/1.1142117

Castle, W.F., 2002. Air separation and liquefaction: recent developments and prospects for the beginning of the new millennium. Int. J. Refrig. 25, 158–172. https://doi.org/10.1016/S0140-7007(01)00003-2

Centi, G., Perathoner, S., 2009. Opportunities and prospects in the chemical recycling of carbon dioxide to fuels. Catal. Today, Special Issue of the 10th International Conference on CO Utilization, Tianijn, China, May 17-21, 2009 148, 191–205. https://doi.org/10.1016/j.cattod.2009.07.075

Chaudhari, R.V., Hofmann, H., 1994. COALESCE OF GAS BUBBLES IN LIQUIDS. Rev. Chem. Eng. 10. https://doi.org/10.1515/REVCE.1994.10.2.131

Chen, Y.-M., Liang-Shin, F., 1989. Bubble breakage mechanisms due to collision with a particle in liquid medium. Chem. Eng. Sci. 44, 117–132. https://doi.org/10.1016/0009-2509(89)85238-8

Choi, K.H., Chisti, Y., Moo-Young, M., 1996. Comparative evaluation of hydrodynamic and gas—liquid mass transfer characteristics in bubble column and airlift slurry reactors. Chem. Eng. J. Biochem. Eng. J. 62, 223–229. https://doi.org/10.1016/0923-0467(96)03085-0

Clark, N.N., Turton, R., 1988. Chord length distributions related to bubble size distributions in multiphase flows. Int. J. Multiph. Flow 14, 413–424. https://doi.org/10.1016/0301-9322(88)90019-5

Clift, R., Grace, J.R., Weber, M.E., 2013. Bubbles, drops, and particles. Dover Publ, Mineola, NY.

CO2 for Enhanced Oil Recovery Needs - Enhanced Fiscal Incentives [WWW Document], n.d. URL https://web.archive.org/web/20120207071349/http://www.touchoilandgas.com/enhanced-recovery-needs-enhanced-a423-1.html (accessed 7.8.17).

Colombet, D., Legendre, D., Risso, F., Cockx, A., Guiraud, P., 2015. Dynamics and mass transfer of rising bubbles in a homogenous swarm at large gas volume fraction. J. Fluid Mech. 763, 254–285. https://doi.org/10.1017/jfm.2014.672

Cook, A.G., Tolliver, R.M., Williams, J.E., 1994. The Blue Bottle Experiment Revisited: How Blue? How Sweet? J. Chem. Educ. 71, 160. https://doi.org/10.1021/ed071p160

Darake, S., Hatamipour, M.S., Rahimi, A., Hamzeloui, P., 2016. SO2 removal by seawater in a spray tower: Experimental study and mathematical modeling. Chem. Eng. Res. Des. 109, 180–189. https://doi.org/10.1016/j.cherd.2015.11.027

De Swart, J.W.A., van Vliet, R.E., Krishna, R., 1996. Size, structure and dynamics of "large" bubbles in a two-dimensional slurry bubble column. Chem. Eng. Sci. 51, 4619–4629. https://doi.org/10.1016/0009-2509(96)00265-5

Deckwer, W.-D., Field, R.W., 1992. Bubble column reactors. Wiley New York.

Dietrich, N., Hebrard, G., 2018. Visualisation of gas-liquid mass transfer around a rising bubble in a quiescent liquid using an oxygen sensitive dye. Heat Mass Transf. 54, 2163–2171. https://doi.org/10.1007/s00231-018-2297-3

Dietrich, N., Loubière, K., Jimenez, M., Hébrard, G., Gourdon, C., 2013. A new direct technique for visualizing and measuring gas–liquid mass transfer around bubbles moving in a straight millimetric square channel. Chem. Eng. Sci., 11th International Conference on Gas-Liquid and Gas-Liquid-Solid Reactor Engineering 100, 172–182. https://doi.org/10.1016/j.ces.2013.03.041

198

Dixon, T., Greaves, A., Christophersen, O., Vivian, C., Thomson, J., 2009. International marine regulation of CO2 geological storage. Developments and implications of London and OSPAR. Energy Procedia, Greenhouse Gas Control Technologies 9 1, 4503–4510. https://doi.org/10.1016/j.egypro.2009.02.268

dsong, 2013. Post-combustion capture – an efficient way to ameliorate global warming. Energy Technol. Policy.

Duan, Z., Sun, R., 2003. An improved model calculating CO2 solubility in pure water and aqueous NaCl solutions from 273 to 533 K and from 0 to 2000 bar. Chem. Geol. 193, 257–271. https://doi.org/10.1016/S0009-2541(02)00263-2

Engerer, S.C., Cook, A.G., 1999. The Blue Bottle Reaction as a General Chemistry Experiment on Reaction Mechanisms. J. Chem. Educ. 76, 1519. https://doi.org/10.1021/ed076p1519

Experts in Spray Technology | Spraying Systems Co. [WWW Document], n.d. URL https://www.spray.com/ (accessed 1.5.19).

Fanchi, J.R., Fanchi, C.J., 2016. Energy in the 21st Century. World Scientific Publishing Co Inc.

Felder, S., Chanson, H., 2015. Phase-detection probe measurements in high-velocity free-surface flows including a discussion of key sampling parameters. Exp. Therm. Fluid Sci. 61, 66–78. https://doi.org/10.1016/j.expthermflusci.2014.10.009

Felder, S., Pfister, M., 2017. Comparative analyses of phase-detective intrusive probes in high-velocity air–water flows. Int. J. Multiph. Flow 90, 88–101. https://doi.org/10.1016/j.ijmultiphaseflow.2016.12.009

Ferreira, A., Ferreira, C., Teixeira, J.A., Rocha, F., 2010. Temperature and solid properties effects on gas–liquid mass transfer. Chem. Eng. J. 162, 743–752. https://doi.org/10.1016/j.cej.2010.05.064

Freitas, C., Teixeira, J.A., 2001. Oxygen mass transfer in a high solids loading three-phase internal-loop airlift reactor. Chem. Eng. J. 84, 57–61. https://doi.org/10.1016/S1385-8947(00)00274-6

FROSSLING, N., 1938. Uber die Verdunstung fallender Tropfen. Beitr Geophys Gerlands 52, 170–216.

Fukui, Y., Nakanishi, K., Okamura, S., 1980. Computer evaluation of sprinkler irrigation uniformity. Irrig. Sci. 2, 23–32. https://doi.org/10.1007/BF00285427

Gaddis, E.S., Vogelpohl, A., 1986. Bubble formation in quiescent liquids under constant flow conditions. Chem. Eng. Sci. 41, 97–105. https://doi.org/10.1016/0009-2509(86)85202-2

García-Abuín, A., Gómez-Díaz, D., Losada, M., Navaza, J.M., 2012. Bubble column gas–liquid interfacial area in a polymer+surfactant+water system. Chem. Eng. Sci. 75, 334–341. https://doi.org/10.1016/j.ces.2012.03.054

Garcia-Ochoa, J., Khalfet, R., Poncin, S., Wild, G., 1997. Hydrodynamics and mass transfer in a suspended solid bubble column with polydispersed high density particles. Chem. Eng. Sci. 52, 3827–3834. https://doi.org/10.1016/S0009-2509(97)00286-8

Green, D.W., Perry, R.H., 2007. Perry's Chemical Engineers' Handbook, Eighth Edition. McGraw Hill Professional.

Guet, S., Ooms, G., 2006. FLUID MECHANICAL ASPECTS OF THE GAS-LIFT TECHNIQUE. Annu. Rev. Fluid Mech. 38, 225–249. https://doi.org/10.1146/annurev.fluid.38.061505.093942

HADAMARD, J.S., 1911. Mouvement permanent lent d'une sphere liquid et visqueuse dans un liquide visqueux. C R Hebd Seances Acad Sci Paris 152, 1735–1738.

Hariz, R., del Rio Sanz, J.I., Mercier, C., Valentin, R., Dietrich, N., Mouloungui, Z., Hébrard, G., 2017. Absorption of toluene by vegetable oil–water emulsion in scrubbing tower: Experiments and modeling. Chem. Eng. Sci., 12th International Conference on Gas-Liquid and Gas-Liquid-Solid Reactor Engineering 157, 264–271. https://doi.org/10.1016/j.ces.2016.06.008

Hayduk, W., Laudie, H., 1974. Prediction of diffusion coefficients for nonelectrolytes in dilute aqueous solutions. AIChE J. 20, 611–615. https://doi.org/10.1002/aic.690200329

Hébrard, G., Bastoul, D., Roustan, M., 1996. Influence of the Gas Sparger on the Hydrodynamic Behaviour of Bubble Columns. Chem. Eng. Res. Des. 74, 406–414.

Herm, Z.R., Swisher, J.A., Smit, B., Krishna, R., Long, J.R., 2011. Metal−Organic Frameworks as Adsorbents for Hydrogen Purification and Precombustion Carbon Dioxide Capture. J. Am. Chem. Soc. 133, 5664–5667. https://doi.org/10.1021/ja111411q

Hernandez-Aguilar, J.R., Cunningham, R., Finch, J.A., 2006. A test of the Tate equation to predict bubble size at an orifice in the presence of frother. Int. J. Miner. Process. 79, 89–97. https://doi.org/10.1016/j.minpro.2005.12.003

Heyt, J., Diaz, J., 1975. Pressure drop in flat-oval spiral air duct. ASHRAE Trans. 81, 221–230.

Higbie, R., 1935. The rate of absorption of a pure gas into still liquid during short periods of exposure,. New York.

Hinze, J.O., 1955. Fundamentals of the hydrodynamic mechanism of splitting in dispersion processes. AIChE J. 1, 289–295. https://doi.org/10.1002/aic.690010303

Hong, M., Cartellier, A., Hopfinger, E.J., 2004. Characterization of phase detection optical probes for the measurement of the dispersed phase parameters in sprays. Int. J. Multiph. Flow 30, 615–648. https://doi.org/10.1016/j.ijmultiphaseflow.2004.04.004

Hong, T., Fan, L.-S., Lee, D.J., 1999. Force variations on particle induced by bubble-particle collision. Int. J. Multiph. Flow 25, 477–500. https://doi.org/10.1016/S0301-9322(98)00056-1

Hughmark, G.A., 1967. Holdup and Mass Transfer in Bubble Columns. Ind. Eng. Chem. Process Des. Dev. 6, 218–220. https://doi.org/10.1021/i260022a011

Husted, B.P., Petersson, P., Lund, I., Holmstedt, G., 2009. Comparison of PIV and PDA droplet velocity measurement techniques on two high-pressure water mist nozzles. Fire Saf. J. 44, 1030–1045. https://doi.org/10.1016/j.firesaf.2009.07.003

Isalski, W.H., 1989. Separation of Gases. Oxford University Press, Oxford.

Isbin, H.S., 1970. One-dimensional two-phase flow, Graham B. Wallis, McGraw-Huill, New York(1969). AIChE J. 16, 896–1105. https://doi.org/10.1002/aic.690160603

Jadhav, S.G., Vaidya, P.D., Bhanage, B.M., Joshi, J.B., 2014. Catalytic carbon dioxide hydrogenation to methanol: A review of recent studies. Chem. Eng. Res. Des. 92, 2557–2567. https://doi.org/10.1016/j.cherd.2014.03.005

Jones, D.P., Watkins, A.P., 2012. Droplet size and velocity distributions for spray modelling. J. Comput. Phys. 231, 676–692. https://doi.org/10.1016/j.jcp.2011.09.030

Kantarci, N., Borak, F., Ulgen, K.O., 2005. Bubble column reactors. Process Biochem. 40, 2263–2283. https://doi.org/10.1016/j.procbio.2004.10.004

Kataoka, I., Ishii, M., Mishima, K., 1983. Generation and Size Distribution of Droplet in Annular Two-Phase Flow. J. Fluids Eng. 105, 230–238. https://doi.org/10.1115/1.3240969

Khare, A.S., Joshi, J.B., 1990. Effect of fine particles on gas hold-up in three-phase sparged reactors. Chem. Eng. J. 44, 11–25. https://doi.org/10.1016/0300-9467(90)80050-M

Kheshgi, H., Coninck, H. de, Kessels, J., 2012. Carbon dioxide capture and storage: Seven years after the IPCC special report. Mitig. Adapt. Strateg. Glob. Change 17, 563–567. https://doi.org/10.1007/s11027-012-9391-5

Kim, J.O., Kim, S.D., 1990. Gas-Liquid mass transfer in a three-phase fluidized bed with floating bubble breakers. Can. J. Chem. Eng. 68, 368–375. https://doi.org/10.1002/cjce.5450680303

Kohl, A.L., Nielsen, R.B., 1997. Chapter 2 - Alkanolamines for Hydrogen Sulfide and Carbon Dioxide Removal, in: Gas Purification (Fifth Edition). Gulf Professional Publishing, Houston, pp. 40–186. https://doi.org/10.1016/B978-088415220-0/50002-1

Kothandaraman, A., 2010. Carbon dioxide capture by chemical absorption : a solvent comparison study (Thesis). Massachusetts Institute of Technology.

Krevelen, D.W. van, Hoftijzer, P.J., 1948. Kinetics of gas-liquid reactions part I. General theory. Recl. Trav. Chim. Pays-Bas 67, 563–586. https://doi.org/10.1002/recl.19480670708

Kulkarni, A.R., Sholl, D.S., 2012. Analysis of Equilibrium-Based TSA Processes for Direct Capture of CO2 from Air. Ind. Eng. Chem. Res. 51, 8631–8645. https://doi.org/10.1021/ie300691c

Kumar, A., Degaleesan, T.E., Laddha, G.S., Hoelscher, H.E., 1976. Bubble swarm characteristics in bubble columns. Can. J. Chem. Eng. 54, 503–508. https://doi.org/10.1002/cjce.5450540604

Kumar, R., Kuloor, N.K., 1970. The Formation of Bubbles and Drops, in: Drew, T.B., Cokelet, G.R., Hoopes, J.W., Vermeulen, T. (Eds.), Advances in Chemical Engineering. Academic Press, pp. 255–368. https://doi.org/10.1016/S0065-2377(08)60186-6

Kunesh, J.G., 1993. Direct-contact heat transfer from a liquid spray into a condensing vapor. Ind. Eng. Chem. Res. 32, 2387–2389. https://doi.org/10.1021/ie00022a023

Leibson, I., Holcomb, E.G., Cacoso, A.G., Jacmic, J.J., 1956. Rate of flow and mechanics of bubble formation from single submerged orifices. I. Rate of flow studies. AIChE J. 2, 296–300. https://doi.org/10.1002/aic.690020305

Levenspiel, O., 1999. Chemical reaction engineering. Wiley.

Livingston, A.G., Zhang, S.F., 1993. Hydrodynamic behaviour of three-phase (gas—liquid—solid) airlift reactors. Chem. Eng. Sci. 48, 1641–1654. https://doi.org/10.1016/0009-2509(93)80124-9

Longo, S., 2006. The effects of air bubbles on ultrasound velocity measurements. Exp. Fluids 41, 593–602. https://doi.org/10.1007/s00348-006-0183-0

Loubière, K., Hébrard, G., 2004. Influence of liquid surface tension (surfactants) on bubble formation at rigid and flexible orifices. Chem. Eng. Process. Process Intensif., Special Issue on Gas-Liquid and Gas-Liquid-Solid Reactor Engineering 43, 1361–1369. https://doi.org/10.1016/j.cep.2004.03.009

Loubière, K., Hébrard, G., Guiraud, P., 2003. Dynamics of Bubble Growth and Detachment from Rigid and Flexible Orifices. Can. J. Chem. Eng. 81, 499–507. https://doi.org/10.1002/cjce.5450810323

Luo, L., Liu, F., Xu, Y., Yuan, J., 2011. Hydrodynamics and mass transfer characteristics in an internal loop airlift reactor with different spargers. Chem. Eng. J. 175, 494–504. https://doi.org/10.1016/j.cej.2011.09.078

Luo, X., Lee, D.J., Lau, R., Yang, G., Fan, L.-S., 1999. Maximum stable bubble size and gas holdup in high-pressure slurry bubble columns. AIChE J. 45, 665–680. https://doi.org/10.1002/aic.690450402

Maldonado, J.G.G., Bastoul, D., Baig, S., Roustan, M., Hébrard, G., 2008. Effect of solid characteristics on hydrodynamic and mass transfer in a fixed bed reactor operating in co-current gas–liquid up flow. Chem. Eng. Process. Process Intensif. 47, 1190–1200. https://doi.org/10.1016/j.cep.2007.02.013

Marty, S., Matas, J.-P., Cartellier, A., 2013. Study of a liquid–gas mixing layer: Shear instability and size of produced drops. Comptes Rendus Mécanique, Combustion, spray and flow dynamics for aerospace propulsion 341, 26–34. https://doi.org/10.1016/j.crme.2012.10.009

Mayerhöfer, T.G., Mutschke, H., Popp, J., 2016. Employing Theories Far beyond Their Limits—The Case of the (Boguer-) Beer–Lambert Law. ChemPhysChem 17, 1948–1955. https://doi.org/10.1002/cphc.201600114

Mena, P., Ferreira, A., Teixeira, J.A., Rocha, F., 2011. Effect of some solid properties on gas–liquid mass transfer in a bubble column. Chem. Eng. Process. Process Intensif. 50, 181–188. https://doi.org/10.1016/j.cep.2010.12.013

Miller, D.N., 1974. Scale-up of agitated vessels gas-liquid mass transfer. AIChE J. 20, 445–453. https://doi.org/10.1002/aic.690200303

Montgomery, D.C., Runger, G.C., 2010. Applied Statistics and Probability for Engineers. John Wiley & Sons.

Moo-Young, M., Blanch, H.W., 1981. Design of biochemical reactors mass transfer criteria for simple and complex systems, in: Reactors and Reactions, Advances in Biochemical Engineering. Springer Berlin Heidelberg, pp. 1–69.

Morsi, S.A., Alexander, A.J., 1972. An investigation of particle trajectories in two-phase flow systems. J. Fluid Mech. 55, 193–208. https://doi.org/10.1017/S0022112072001806

Moustiri, S., Hebrard, G., Roustan, M., 2002. Effect of a new high porosity packing on hydrodynamics of bubble columns. Chem. Eng. Process. Process Intensif. 41, 419–426. https://doi.org/10.1016/S0255-2701(01)00162-3

Neal, L.G., Bankoff, S.G., 1963. A high resolution resistivity probe for determination of local void properties in gas-liquid flow. AIChE J. 9, 490–494. https://doi.org/10.1002/aic.690090415

Nicholas P. Cheremisinoff, 1986. Encyclopedia of Fluid Mechanics: Gas-Liquid Flows, Encyclopedia of Fluid Mechanics. Gulf Publ. Company.

Ogden, J.M., 2003. PROSPECTS FOR BUILDING A HYDROGEN ENERGY INFRASTRUCTURE [WWW Document]. http://dx.doi.org/10.1146/annurev.energy.24.1.227. URL http://www.annualreviews.org/doi/10.1146/annurev.energy.24.1.227 (accessed 7.8.17).

Onda, K., Takeuchi, H., Okumoto, Y., 1968. MASS TRANSFER COEFFICIENTS BETWEEN GAS AND LIQUID PHASES IN PACKED COLUMNS. J. Chem. Eng. Jpn. 1, 56–62. https://doi.org/10.1252/jcej.1.56

openCCS: Transport | Global Carbon Capture and Storage Institute [WWW Document], n.d. URL http://www.globalccsinstitute.com/publications/openccs-transport (accessed 7.8.17).

Oxy-fuel technology [WWW Document], 2014. URL https://www.newcastle.edu.au/research-and-innovation/centre/energy/research/low-emission-coal/oxy-fuel/oxy-fuel-technology (accessed 7.8.17).

Painmanakul, P., Loubière, K., Hébrard, G., Mietton-Peuchot, M., Roustan, M., 2005. Effect of surfactants on liquid-side mass transfer coefficients. Chem. Eng. Sci., 7th International Conference on Gas-Liquid and Gas-Liquid-Solid Reactor Engineering 60, 6480–6491. https://doi.org/10.1016/j.ces.2005.04.053

Pamperin, O., Rath, H.-J., 1995. Influence of buoyancy on bubble formation at submerged orifices. Chem. Eng. Sci. 50, 3009–3024. https://doi.org/10.1016/0009-2509(95)00140-Z

Pandit, A.B., Joshi, J.B., 2011. Three Phase Sparged Reactors — Some Design Aspects. Rev. Chem. Eng. 2, 1–84. https://doi.org/10.1515/REVCE.1984.2.1.1

Pang, M., Wei, J., Yu, B., 2011. Effect of particle clusters on turbulence modulations in liquid flow laden with fine solid particles. Braz. J. Chem. Eng. 28, 433–446. https://doi.org/10.1590/S0104-66322011000300009

Park, Y., Lamont Tyler, A., de Nevers, N., 1977. The chamber orifice interaction in the formation of bubbles. Chem. Eng. Sci. 32, 907–916. https://doi.org/10.1016/0009-2509(77)80077-8

Pierantozzi, R., 2000. Carbon Dioxide, in: Kirk-Othmer Encyclopedia of Chemical Technology. John Wiley & Sons, Inc. https://doi.org/10.1002/0471238961.0301180216090518.a01.pub2

Roustan, M., 2003. Transferts gaz-liquide dans les procédés de traitement des eaux et des effluents gazeux. Tec & Doc.

S. W. Park, J. K. Mitchell, G. D. Bubenzern, 1983. Rainfall Characteristics and Their Relation to Splash Erosion. Trans. ASAE 26, 0795–0804. https://doi.org/10.13031/2013.34026

Saboni, A., 1991. Contribution à la modélisation du transfert de masse entre un gaz et une goutte d'eau. Toulouse, INPT.

Saito, T., 2017. Optical Fibre Probing for Bubble/Droplet Measurement, and Its Possibility of the Application to Biotechnology, in: Recent Global Research and

Education: Technological Challenges, Advances in Intelligent Systems and Computing. Springer, Cham, pp. 231–246. https://doi.org/10.1007/978-3-319-46490-9_33

Sander, R., 2015. Compilation of Henry's law constants (version 4.0) for water as solvent. Atmospheric Chem. Phys. 15, 4399–4981. https://doi.org/10.5194/acp-15-4399-2015

Sardeing, R., Painmanakul, P., Hébrard, G., 2006. Effect of surfactants on liquid-side mass transfer coefficients in gas–liquid systems: A first step to modeling. Chem. Eng. Sci. 61, 6249–6260. https://doi.org/10.1016/j.ces.2006.05.051

Seader, J.D., Henley, E.J., Roper, D.K., 2010. Separation Process Principles with Applications using Process Simulators, 3 edition. ed. Wiley, Hoboken, NJ.

Spigarelli, B., 2013. A Novel Approach to Carbon Dioxide Capture and Storage. Diss. Masters Theses Masters Rep. - Open.

Stevenin, C., Tomas, S., Vallet, A., Amielh, M., Anselmet, F., 2016a. Flow characteristics of a large-size pressure-atomized spray using DTV. Int. J. Multiph. Flow 84, 264–278. https://doi.org/10.1016/j.ijmultiphaseflow.2016.05.004

Stevenin, C., Vallet, A., Tomas, S., Amielh, M., Anselmet, F., 2016b. Eulerian atomization modeling of a pressure-atomized spray for sprinkler irrigation. Int. J. Heat Fluid Flow 57, 142–149. https://doi.org/10.1016/j.ijheatfluidflow.2015.11.010

Sullivan, G.M., Feinn, R., 2012. Using Effect Size—or Why the P Value Is Not Enough. J. Grad. Med. Educ. 4, 279–282. https://doi.org/10.4300/JGME-D-12-00156.1

Tate, T., 1864. XXX. *On the magnitude of a drop of liquid formed under different circumstances*. Lond. Edinb. Dublin Philos. Mag. J. Sci. 27, 176–180. https://doi.org/10.1080/14786446408643645

Tatin, R., Moura, L., Dietrich, N., Baig, S., Hébrard, G., 2015. Physical Absorption Of Volatile Organic Compounds By Spraying Emulsion In A Spray Tower: Experiments And Modelling. Chem. Eng. Res. Des.

Treybal, R.E., 1980. Mass-Transfer Operations, 3rd Edition, 3rd edition. ed. McGraw-Hill Book Company, New York.

Valero, D., Bung, D.B., 2017. Artificial Neural Networks and pattern recognition for air-water flow velocity estimation using a single-tip optical fibre probe. J. Hydro-Environ. Res. https://doi.org/10.1016/j.jher.2017.08.004

Vázquez, G., Cancela, M.., Riverol, C., Alvarez, E., Navaza, J.., 2000. Application of the Danckwerts method in a bubble column. Chem. Eng. J. 78, 13–19. https://doi.org/10.1016/S1385-8947(99)00174-6

Walzel, P. (Bayer A., 1993. Liquid atomization. Int. Chem. Eng. Q. J. Transl. Russ. East. Eur. Asia U. S. 33:1.

Wei-rong, Z., Hui-xiang, S., Da-hui, W., 2004. Modeling of mass transfer characteristics of bubble column reactor with surfactant present. J. Zhejiang Univ.-Sci. A 5, 714–720. https://doi.org/10.1007/BF02840986

Wellman, W.E., Noble, M.E., Tom Healy, 2003. Greening the Blue Bottle. J. Chem. Educ. 80, 537. https://doi.org/10.1021/ed080p537

Winner: Clean Coal - Restoring Coal's Sheen - IEEE Xplore Document [WWW Document], n.d. URL http://ieeexplore.ieee.org/document/4428318/ (accessed 7.8.17).

Wongwailikhit, K., Warunyuwong, P., Chawaloesphonsiya, N., Dietrich, N., Hébrard, G., Painmanakul, P., 2018. Gas Sparger Orifice Sizes and Solid Particle Characteristics in a Bubble Column - Relative Effect on Hydrodynamics and Mass Transfer. Chem. Eng. Technol. 41, 461–468. https://doi.org/10.1002/ceat.201700293

Xiao, Xiao, Yan, B., Fu, J., Xiao, Xianming, 2015. Absorption and recovery of n-hexane in aqueous solutions of fluorocarbon surfactants. J. Environ. Sci. 37, 163–171. https://doi.org/10.1016/j.jes.2015.03.023

Yan, H.J., Bai, G., He, J.Q., Li, Y.J., 2010. Model of droplet dynamics and evaporation for sprinkler irrigation. Biosyst. Eng. 106, 440–447. https://doi.org/10.1016/j.biosystemseng.2010.05.008

Yang, G.Q., Du, B., Fan, L.S., 2007. Bubble formation and dynamics in gas–liquid–solid fluidization—A review. Chem. Eng. Sci. 62, 2–27. https://doi.org/10.1016/j.ces.2006.08.021

Yang, L., Dietrich, N., Hébrard, G., Loubière, K., Gourdon, C., 2017. Optical methods to investigate the enhancement factor of an oxygen-sensitive colorimetric reaction using microreactors. AIChE J. 63, 2272–2284. https://doi.org/10.1002/aic.15547

Zhang, G., Chanson, H., 2018. Application of local optical flow methods to high-velocity free-surface flows: Validation and application to stepped chutes. Exp. Therm. Fluid Sci. 90, 186–199. https://doi.org/10.1016/j.expthermflusci.2017.09.010

Zhang, T., Wang, J., Luo, Z., Jin, Y., 2005. Multiphase flow characteristics of a novel internal-loop airlift reactor. Chem. Eng. J. 109, 115–122. https://doi.org/10.1016/j.cej.2005.03.014

จุฬาลงกรณ์มหาวิทยาลัย

CHULALONGKORN UNIVERSITY

Appendix A

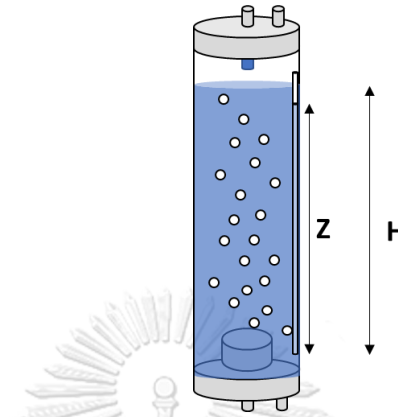# Gas holdup measurement with pressure method

Figure A.1 Liquid level in column (H) and liquid level in a single pipe (Z)

Due to the fact that the operation of the bubble column was in the continuous regime and the liquid level in the column was controlled to be constant. It was not possible to measure the change of liquid level before and after gas flow. Therefore, in order to determine the gas holdup in the column, a single pipe method was developed according to the assumption that the hydraulic pressure at the lowest level of the pipe is equivalent throughout the same liquid level as shown in Figure A.1. Therefore, hydraulic pressure of liquid above pipe and above liquid surface should be identical. The equal of hydraulic pressure can be expressed as in Equation (A.1), where ρ_i is the density of phase i, H is the liquid level in the column and Z is the liquid level in the pipe.

$$(\rho_g \varepsilon_g + \rho_L \varepsilon_L + \rho_s \varepsilon_s) gH = \rho_L gZ \qquad (A.1)$$

$$\varepsilon_g + \varepsilon_l + \varepsilon_s = 1 \qquad (A.2)$$

When combining Equation (A.1) with Equation (A.2) that described the summation of liquid fraction (ε_L) gas fraction or gas holdup (ε_g) and solid fraction (ε_s). The gas holdup can be derived as shown in Equation (A.3).

$$\varepsilon_g = \left[\frac{1 - \left(\frac{Z}{H}\right) - \varepsilon_s \left(1 - \frac{\rho_s}{\rho_L}\right)}{1 - \left(\frac{\rho_g}{\rho_L}\right)} \right] \qquad (A.3)$$

In order to validate the methodology, the result of gas holdup determination from the one-pipe technique was compared with the conventional different liquid level technique. Figure A.2 shows that both techniques gave the same trend of the result when both gas flow rate as well as different orifice sizes were varied. The result indicated

that the one-pipe technique is one of the method that can be used to determine the gas holdup of the bubble column.
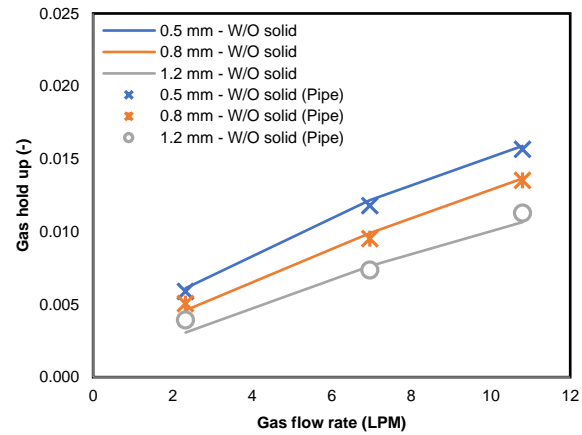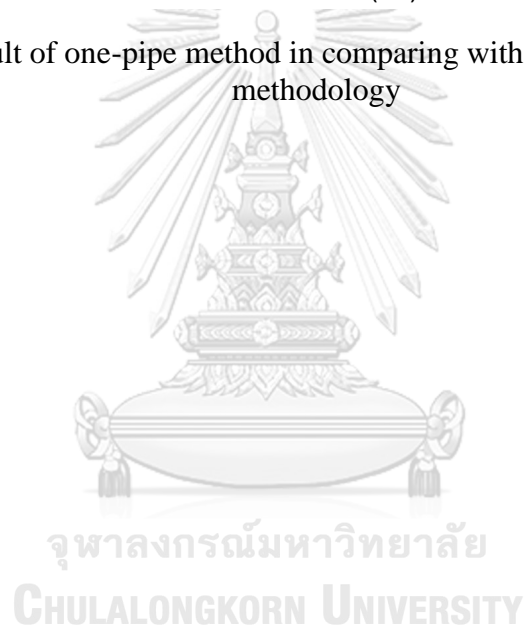

Figure A.2 Result of one-pipe method in comparing with the different water level methodology
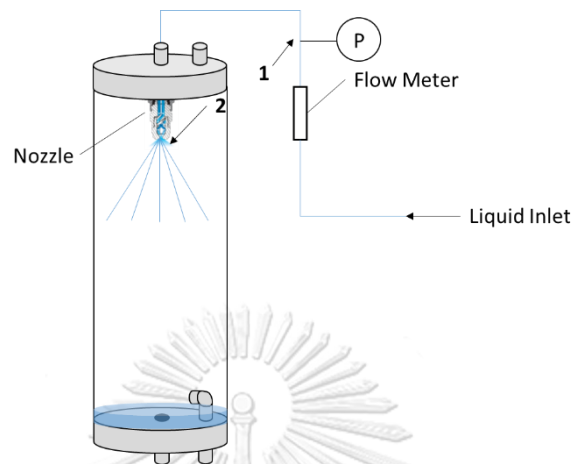
Appendix B

Initial droplet velocity estimation

Figure B.1 Bernoili's equation conceptual diagram for droplet velocity calculation

In order to confirm the presumption, the Bernoulli's equation was used to simulate the liquid velocity at the different positions. Figure B.1 shows the initial position and final position using in the Bernoulli's calculation. The initial position was the position at the pressure sensor where the pressure in the pipe can be known. The final position was at the outlet of the nozzle where could be assumed to be the initial velocities of droplets. The Bernoulli's equation is expressed in Equation (B.1) and the sudden contraction coefficient (K) is shown in Equation (B.2).

$$p_1 - p_2 = \frac{\rho V_2^2}{2} - \frac{\rho V_1^2}{2} + \rho g(z_2 - z_1) + \frac{K\rho V^2}{2} \tag{B.1}$$

$$K = 0.5\left(1 - \frac{A_2}{A_1}\right) \tag{B.2}$$

In the equation, p_i refers to the pressure at the certain position, where p_1 was obtained from the pressure gauge while p_2 was equal to the atmospheric pressure. The V_i represents liquid velocity at the considered position. The V_1 was equal to the liquid velocity in the pipe that calculated using the ratio of flow rate and cross-sectional area of the pipe whereas the V_2 was the initial velocity of the droplet. Other variables are ρ, z_i and A_i that represent the density of liquid, height from reference position, and cross-sectional area of flow. A_1 was the cross-sectional area of pipe while A_2 was the cross-sectional area of nozzle orifice.

Appendix C

Relaxation time and distance calculation of droplet

The force balance on a droplet was developed as shown in Equation (C.1). The equation consists of 3 terms: Accumulate momentum, gravity force along with buoyancy force, and drag force as shown in the equation below:

$$\left(\rho_D + \frac{1}{2}\rho_C\right)\left(\frac{\pi d_d^3}{6}\right)\left(\frac{dU_{rel}}{dt}\right) = \frac{\pi d_d^3}{6}\Delta\rho g - \frac{\pi d_d^2}{4}\frac{1}{2}\rho_C C_D U_{rel}^2 \tag{C.1}$$

Where ρ_D and ρ_C are the density of dispersed phase (liquid) and continued phase (gas), respectively, while d_d represents droplet diameter. After rearranging the terms, the droplet relative velocity (U_{rel}) can be written as shown in Equation (C.2).

$$\left(\frac{dU_{rel}}{dt}\right) = \frac{U_{rel,t+\Delta t} - U_{rel,t}}{\Delta t} = \frac{\frac{\pi d_d^3}{6}\Delta\rho g - \frac{\pi d_d^2}{4}\frac{1}{2}\rho_C C_D U_{rel,t}^2}{\left(\rho_D + \frac{1}{2}\rho_C\right)\left(\frac{\pi d_d^3}{6}\right)} \tag{C.2}$$

By using explicit differential equation solving method, the velocity droplets at the considered time can be calculated. However, in order to perform velocity and distance analysis, the relation between distance, time, and droplet velocity can be calculated using Equation (C.3).

$$U_{rel,t} = \frac{\Delta x}{\Delta t} \tag{C.3}$$

The drag coefficient (C_D) used in this calculation was followed the model of Yevgeny et al (1967) where the summary of the drag coefficient as a function of Reynolds number can be expressed as in Equation (C.4) (Yan et al., 2010). Note that the calculation using Equation (C.1) to (C.4) is called "Relaxation time calculation" in this manuscript.

$$C_D = \frac{24}{Re}\left(1 + 0.15Re^{0.687} + \frac{0.0175}{1+4.25x10^4 Re^{-1.16}}\right) \qquad \text{for Re} \leq 800$$

$$C_D = 0.5 \qquad\qquad\qquad \text{for } 800 < \text{Re} \leq 1600 \tag{C.4}$$

$$C_D = 3 \ x \ 10^{-4}Re \qquad\qquad\qquad \text{for Re} > 1600$$

Appendix D

Determination of optimal particle type

Publication

(Wongwailikhit et al., 2018)

Experimental setup

The experimental setup used in this study is depicted schematically in Fig. D.1. The experiments were carried out in a cylindrical acrylic column 0.14 m in diameter and 1 m in height. The column was filled with 10 L of tap water. A porous sparger was installed at the bottom of the column. Different sizes of porous sparger were used to determine the effects of orifice sizes on hydrodynamics and mass transfer. The small-orifice and large-orifice sparger consisted of various pores with diameter ranges between 0.1 – 0.2 mm and 0.5 – 1.0 mm respectively. An HP-12000 air compressor was used to inject air through the sparger. Gas flow rates (Qg) from 2.5 to 12.5 L min-1 were studied. This range corresponded to superficial gas velocities (Ug) of 0.27x10-2 – 1.3x10-2 m s-1. The gas flow rate was measured and adjusted by a rotameter and its pressure was measured with a pressure gauge.
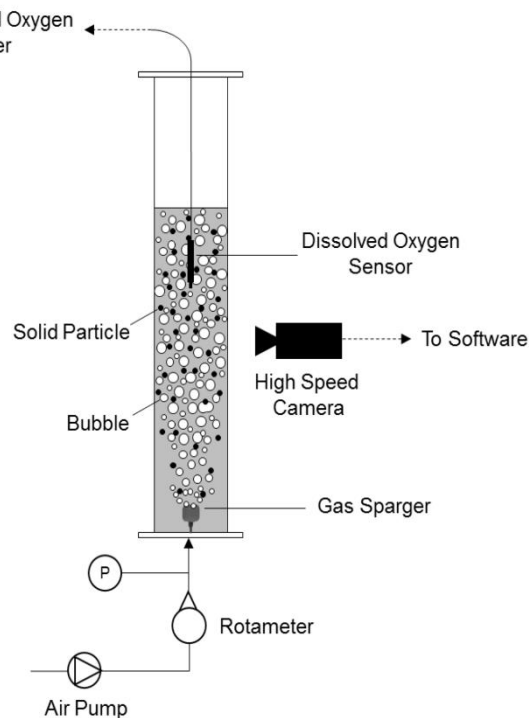

Fig. D.1 Experimental setup
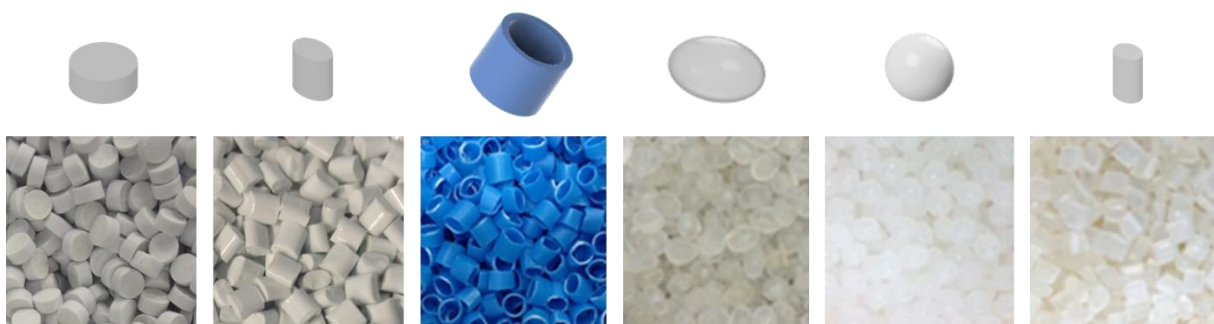
Solid particles

Figure D.2 Movable solid particles
(Left to right) PVC, ABS, PP ring shape, PP ellipsoid, PP sphere, and PP cylinder

Initially, the effect of 6 types of particles on mass transfer of oxygen and bubble hydrodynamics were investigated. The particles made of Polyvinylchloride (PVC), Acrylonitrile butadiene styrene (ABS), and Polypropylene (PP) were test in a 14-cm diameter bubble column and studied their effects on the mass transfer of oxygen in the column. The oxygenless water obtained by the reaction of Na_2SO_3 with water was used as the liquid phase in the column. The characteristic and their physical properties are shown in Figure D.2 and Table D.1, respectively.

Table D.1 Solid particles physical properties.

Material	Density (kg/m³)	Shape	Particle equivalent diameter (mm)	Void fraction (-)	Shape factor (-)	Terminal velocity* (cm/s)
PVC	1,380	Cylinder	4.34	0.43	0.79	+9.41
ABS	1,050	Cylinder	2.95	0.39	0.5	+1.81
PP	946	Ring	4.15	0.78	0.35	-1.66
		Ellipsoid	3.46	0.40	0.96	-1.98
		Sphere	4.00	0.40	1.00	-2.13
		Cylinder	3.08	0.43	0.85	-1.97

*Positive velocity value refers to velocity in the direction of gravity

Result and discussion

Effect of Solid Particles on Gas Phase Bubble Hydrodynamics and Mass Transfer

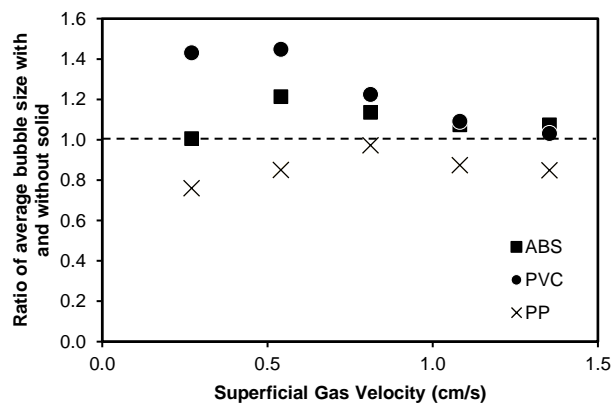*Effect of solid particles density*

Figure D.2 Effect of particles density and superficial gas velocity on ratio of average bubble diameter in presence of solid and without solid at concentration of 2 % v/v, for small orifice sparger

PVC, ABS and PP particles were added at a concentration of 2 % v/v and the effect of the density of the particles on bubble size was observed as in Figure D.2. The figure represents the ratio of average bubble diameter with presence of solid to bubble diameter without solid. It indicates that the bubble ratio rose above 1 after addition of PVC and ABS particles. Thus, with presence of PVC and ABS solid particles, the average bubble diameter increased.

According to their density (1380 and 1050 kg/m^3 for PVC and ABS respectively), the solid particles, which had a higher density than water, settled and accumulated at the bottom of the bubble column. Once the bubbles were generated by the gas sparger, they had to pass through the layer of accumulated solid, which acted as a packed bed, accumulating bubbles and causing them to coalesce. Thus, the bubble diameters were larger after PVC and ABS had been added. In contrast, the bubbles were smaller after the addition of the PP particles than they were with no particles. This was probably caused by collision of the solids with the bubbles or the inhibition of bubble coalescence. This will be discussed in detail later. The gas holdup and interfacial area observed consecutively to bubble diameter change are shown in Figure D.4.
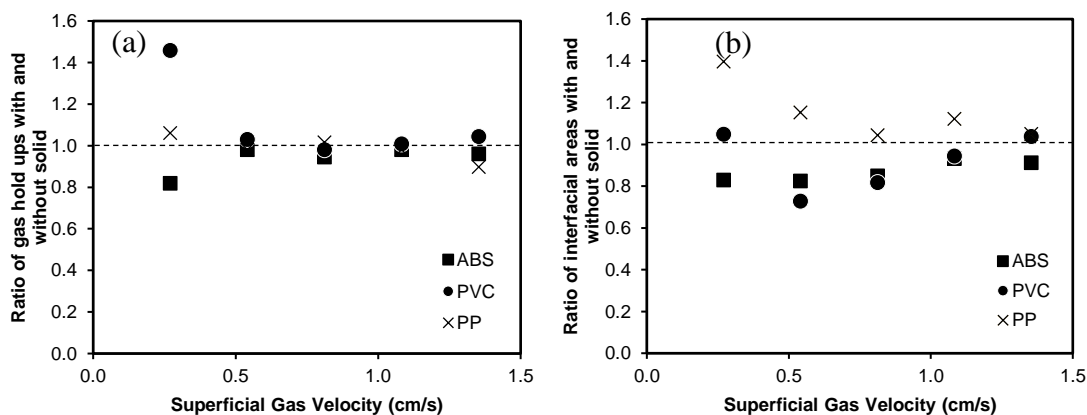
Figure D.4 Effect of the particles density at concentration of 2 % v/v with small orifice sparger and superficial gas velocity on (a) gas hold up ratio and (b) specific interfacial area ratio in presence of solid and without solid

Figure D.4(a) indicates that gas hold up was not affected by the addition of solid particles. However, the interfacial area in Figure D.4(b), was increased with PP and higher than without solid. Thus, PP particles were selected to determine the effect of the concentration and shape of the solid particles in the bubble column.

Effect of solid particles shapes and concentration

For the PP particles, 4 shapes of particles were tested with different solid loading amount and orifice sizes. It was found that the presence of solid particles reduced the mass transfer coefficient ($k_L.a$) when the small orifice size was used regardless of shape of solids. Among all the particles the ring shape provided the best $k_L.a$ since it did not dramatically reduce the $k_L.a$ comparing to the other ones. However, in the case of large orifice size, the improvement of $k_L.a$ was achieved for all of the particle shapes. Among all shapes, the ring particles can be concluded as the best one since it gave the highest value of $k_L.a$ for both cases, small and large orifice sizes. Hence, the ring shape solid was selected to determine its effect in comparing with the high void packing.
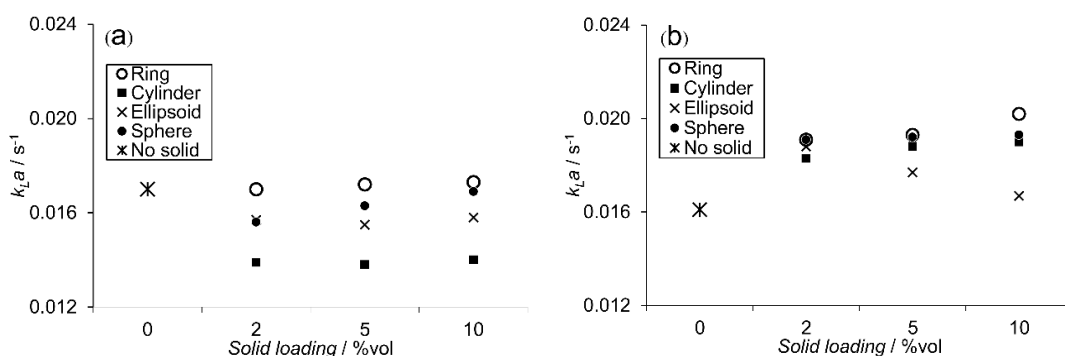

Figure D.5 Effect of particle shape and solid loading in volume fraction of mass transfer coefficient of oxygen in water. (Left) small size orifice (Right) large size orifice

VITA

NAME	Kritchart Wongwailikhit
DATE OF BIRTH	24 Dec 1989
PLACE OF BIRTH	Bangkok
INSTITUTIONS ATTENDED	Chulalongkorn University INSA Toulouse
HOME ADDRESS	16/181 Radchadapisek 36 Jankaseam Jatujak Bangkok, Thailand, 10900

PUBLICATION

⌉ Wongwailikhit, W, Warunyuwong, P., Chawaloesphonsiya, W, Dietrich, N., Hébrard, G., Painmanakul, P. Gas Sparger Orifice Sizes and Solid Particle Characteristics in a Bubble Column – Relative Effect on Hydrodynamics and Mass Transfer. Chemical Engineering and Technology. (2018)

⌉ Phanpa, K., Wongwailikhit, K., Dammee, R., Jamnongwong, M., Painmanakul, P. Study of aeration and CO2 absorption using filtration membranes in terms of physical properties and mass transfer parameters. Engineering Journal 22(4), pp. 83-95

⌉ Chawaloesphonsiya, N., Prommajun, C., Wongwailikhit, K., Painmanakul, P. Comparison of cutting-oil emulsion treatment by electrocoagulation–flotation in bubble column and airlift reactors. Environmental Technology 38(10), pp. 1295-1304

⌉ Chawaloesphosiya, N., Mongkolnauwarat, J., Prommajun, C., Wongwailikhit, K., Painmanakul, P. Treatment of cutting-oily wastewater by electrocoagulation-flotation (ECF) process: Modeling approach. Environmental Engineering Research 20(4), pp. 392-396 (2015)

⌉ Romphophak, P., Wongwailikhit, K, Chawaloesphonsiya, N, Samornkraisorakit, P , and Painmanakul, P. Study of Flow Pattern in Jet Clarifier for Removal of Turbidity by Residence Time Distribution Approach. Engineering Journal 20(2). ISSN: 0125-8281.